Plasmapolymerization and particle growth

DISSERTATION

zur Erlangung des Doktorgrades
der Mathematisch-Naturwissenschaftlichen Fakultät
der Christian-Albrechts-Universität zu Kiel

vorgelegt von
Erik von Wahl

Kiel, 2019

1. Gutachter: Prof. Dr. Holger Kersten

2. Gutachter: Dr. habil. Maxime Mikikian

Tag des Promotionskolloquims: 05.11.2019

Eidesstattliche Erklärung

Hiermit versichere ich an Eides Statt, dass die vorliegende Dissertation, abgesehen von der Beratung durch meine wissenschaftlichen Betreuer, nach Inhalt und Form meine eigene Arbeit ist. Die Arbeiten Dritter habe ich entsprechend gekennzeichnet. Des Weiteren versichere ich, dass diese Arbeit weder in Gänze noch in Teilen im Rahmen eines Prüfungsfervahrens vorgelegen hat, veröffentlicht worden ist oder zur Veröffentlichung eingereicht wurde. Zudem versichere ich, dass die Arbeit unter Einhaltung der Regeln guter wissenschaftlicher Praxis der Deutschen Forschungsgemeinschaft entstanden ist und dass mir kein akademischer Grad entzogen wurde.

Ort, Datum Unterschrift

"There has never been a democratic society in which citizens' influence over government policy was unrelated to their financial resources. In this sense, the difference between democracy and plutocracy is one of degree. But by this same token, a government that is democratic in form but is in practice only responsive to its most affluent citizens is a democracy in name only."

Gilens, Martin (2005): Inequality and Democratic Responsiveness
In: Public Opinion Quarterly 69 (5, Special Issue), pp. 778–796

Kurzfassung

Diese Doktorarbeit stellt verschiedene Experimente vor, die innerhalb des Projektes B13 des Sonderforschungsbereiches TR24-Grundlagen komplexer Plasmen an der Anlage ATILA am Institut für Experimentelle und Angewandte Physik in Kiel durchgeführt wurden. Es handelt sich dabei um Versuche an einem Nanopartikel bildenden Hochfrequenzplasma im Niederdruck unter der Verwendung von Acetylen als Präkursor.
Schwerpunkt der Arbeit ist die chemische und physikalische Wechselwirkung der sich elektrisch aufladenden Partikel mit dem Plasma. Um diese zeitlichen und räumlichen Phänomene zu Erfassen, wurden unterschiedliche Diagnostiken angewandt, wobei die Betonung auf insitu Techniken liegt. Um die zahlreichen Ergebnisse miteinander vergleichen zu können, wurde der Wachstumszyklus der Nanopartikel in drei Phasen unterteilt und alle diagnostischen Methoden zeitlich zueinander korreliert. Es handelt sich bei den Diagnostiken im Wesentlichen um die elektrische Charakterisierung der Entladung anhand der sich einstellenden Gleichspannung auf der kapazitiv gekoppelten Elektrode, Laserlichtstreuung an den Nanopartikeln, Langmuirsondenmessungen, HF-phasenaufgelöste Kameramessungen der Randschicht über der getriebenen Elektrode, energieaufgelöste Massenspektrometrie und Quartz-Mikrowägung zur Bestimmung der Schichtabscheidungsrate.
Als eine der Hauptthesen wurde dabei herausgearbeitet, dass die Nukleation und Koagulation des Nanostaubs zeitgleich und während der kompletten Phase I im Wachstumszyklus stattfindet, sodass folglich dessen Dauer die Breite der Partikelgrößenverteilung bestimmt. In den beiden darauf folgenden Phasen hingegen sinkt die Präkursorkonzentration in der Gasphase stark ab, sodass keine weitere Nukleation mehr stattfinden kann, weshalb in Sammelexperimenten meist eine monodisperse Partikelpopulation gefunden wird.
Stark vereinfachte Modelle wurden verwendet, um die Langmuirsondendaten zu interpretieren und um die Partikelladung und -dichte annhähernd zu errechnen. Des Weiteren konnten mithilfe einfacher Child-Langmuir Gesetze die Ionenstromdichte und die Randschichtdicke vor der getriebenen Elektrode analysiert werden.
Die massenspektrometrischen Untersuchungen erlaubten sowohl die Bestätigung bekannter Reaktionsschema in acetylenhaltigen Plasmen als auch Messung der zeitabhängigen Ionenenergie. Mithilfe einfachster Modellrechungen wurden die Diffusionskonstanten und Verlustraten für die Radikale C und CH_2 bestimmt.
Die Messung der Schichtabscheidungsrate lieferte schließlich interessante Hinweise auf den entscheidenden Beitrag der Kohlenwasserstoffionen zum Schichtwachstum. Dies mag ein Ansatz in Richtung zukünftiger Arbeiten sein.

Abstract

In this thesis various experiments are presented, that have been exercised in the frame of the project B13 of the Sonderforschungsbereich TR24, titled Fundamentals of Complex Plasmas. All of the presented experiments have been realized at the research vessel ATILA at the Institute for experimental and applied physics in Kiel. They deal with the synthesis of nanoparticles in a radio frequency plasma at low pressure with acetylene as precursor gas.
The focus of this work is the chemical and physical interaction between the electrically charged particles and the plasma. In order to understand the time-space phenomena, different techniques have been applied with emphasis on in-situ techniques. The nanoparticle growth cycle has been separated into three phases and all diagnostics have been time correlated, so that they become comparable. In more detail the applied diagnostics are the electrical characterisation of the discharge by the self-bias voltage at the powered electrode, laser light scattering at the dense dust cloud, Langmuir probe measurements, RF-phase resolved camera measurements of the plasma sheath region above the driven electrode, energy resolved mass spectrometry and quartz micro balance measurements for deposition rate determination.
As one of the main hypothesis it was brought out, that the nucleation and coagulation of the nanoparticles occurs simultaneously throughout the entire phase I of the growth cycle, and thus, its duration determines the width of the particle size distribution. In both of the following phases, however, the precursor concentration in the gas decreases strongly, so that no further nucleation can take place. Hence, in dust collection experiments often a mono disperse particle population is found.
Strongly simplified models have been used to interpret the Langmuir probe data and to calculate the particle charge and density approximately. Furthermore the ion current density and plasma sheath width in front of the powered electrode could be estimated by simple Child-Langmuir laws.
The mass-spectrometric investigations allowed for the confirmation of already known reaction schemes in acetylene containing plasmas as well as for the recording of the time dependent ion energies. By the help of simple calculations the diffusion constants and loss rates for the radicals C and CH_2 have been determined.
Finally, the measurement of the deposition rate, shows interesting indications for the importance of the contribution to the film growth by hydrocarbon ions. This may be interesting work to investigate further in future.

Contents

Chapter 1

Introduction

Being explained as mythical events, plasmas have been observed since ancient times in natural phenomena like the Aurora Borealis [1]. But it was not before Langmuir and Tonk, who, inspired by the transport of red and white blood corpuscles in the medical blood plasma, introduced this term in physics in the nineteen-twenties [2–4], that plasma physics became a separate discipline in science.
In a physical plasma, electrons and ions are transported through a neutral background gas instead of blood corpuscles through blood. Existing since primeval times as astrophysical appearances [5–7] like interstellar clouds, the sun, the ionosphere, but also closer on earth as lightning and Aurora Borealis, it was first produced and observed artificially by the French Jean Picard (1608 - 1647), who noticed a glow like appearance in his mercury barometer [8], without being able to understand the origin. With continously improving power supplies, the plasma experiments became more and more advanced, so that the Geissler tubes came up in the nineteenth century. It may have been the first useful application for plasmas, which not only evolved as a light source into neon lighting in the twentieth century but has also been used for tuning radio transmitters to resonance [9].
Nowadays plasmas are widely used in industry not only as light sources. They exist in various forms and shapes ranging from the micrometer range in micro-hollow-cathodes [10, 11] to several meters in fusion research reactors like ITER [12] or W7-X [13], from atmospheric pressure to high vacuum [14, 15]. This work deals with Low Temperature Plasmas, that nowadays are most commonly used in industry, for example for etching processes [16] or for surface treatments [17–19]. Materials can also be activated in order to change the surface energy and wetting behaviour or thin films can be deposited. In the semiconductor industry plasma advanced to the most important etching technique for the production of integrated circuits. For coating and etching technologies chemical processes are of great interest. In the so-called reactive plasmas, chemically reactive molecules or atoms are introduced, radicals and ions then formed, which finally can interact with a substrate surface.
This kind of plasma chemistry offers new possibilities to control chemical pathways and thermal stress to the substrate [20]. It is based on the fact, that energy is transmitted to the electrons but not directly to the ions and the neutral gas, so that an out of thermal equilibrium chemistry is created.

Not only can chemically reactive species be deposited to surfaces like the substrate or the chamber walls but also can they agglomerate in the gas phase and by doing so, they can form small clusters and particles. Firstly observed by Kobayashi *et al.* [21] when they studied an acetylene containing radio frequency discharge, they gained of interest when Gary Selwyn also found particles while etching silicon in 1989 [22]. These small grains, soon known as *killer particles*, short-circuit different conducting channels of the integrated circuit when deposited on it [23]. Also in sputter processes or during plasma enhanced vapor deposition particles can be formed unintentionally. They also pose a problem to fusion devices, where the contact of the hot plasma with the recipient walls can cause the ablation of small particles, which then essentially lead to an unfavoured cooling of the plasma [12, 24].
The formation of nano-particles is desired in only a few cases. Generally, so-called *dusty* or *complex plasmas* offer the possibility to study fundamental plasma properties by observing the particle behaviour, therefore micrometer sized dust containing plasmas gained some attention in the last decades [25–31]. The focus of research are the heating mechanisms of the immersed dust [32], their electrostatic charging [33] and also their influence on the plasma. Furthermore small particles can be used as a probe inside the plasma as a diagnostic tool [34]. Last but not least the growth mechanisms and properties of nano-particles in the gas phase are under discussion [35]. A good overview over dust containing plasmas can be found in the topical issue "Fundamentals of Complex Plasmas" in the European Physical Journal D from 2018.
Although this work is strongly dominated by an interest to do fundamental research on nano-dusty plasmas, the following paragraph shall give a short overview on the practical use and possible applications of nano-particles.
Since nano-materials have evolved as more and more promising new industry, research on complex plasmas also has grown [36]. Treating particles by plasma surface deposition [37] as well as depositing them for the structuring of surfaces and tuning of their properties like hydrophily or porosity [38] open new possibilities for material scientists. Key features of nano-sized spheres, flakes or rods are the high ratio of surface area to volume and thus little material consumption for high reactivity, the highly active surface after plasma immersion and also the small size itself, which is in the range of light wavelength and thus offering interesting electro-optical properties [39, 40]. Completely unexpected applications are the result of the entire package of properties, like for example the use as drug delivering system, where the active surface, that can easily attach to a drug, is combined with the small size, that enables the particles to penetrate the walls of living cells [41]. In another example zinc oxide nano-particles were tested as UV blocker on textiles [42]. Silver ions, which have antibacterial properties [43], can be released in a controlled amount by embedding silver nano-particles in metals, plastic or even glass [44, 45] and thus resulting in antimicrobial surfaces for medical devices and applications. Silver-gold alloy nano-particles were found to have synergistic effects for the catalysis of carbon-monoxide oxidation [46]. Many more applications can be found, like the use as perfect light absorber in a tunable frequency range [47] due to plasmon resonance, which makes them suitable for light adsorption in hybrid solar cells [48]. or as biosensors [49]. Making use of different materials, new applications come up and the combination of two materials, like in alloy or core-shell particles, opens up even

more possibilities. Thus the value of nano-particles in technology, medicine and life-science is yet to be fully explored.
Several methods for the synthesis of nano-particles exist. Besides unwanted fine dust production in combustion, which is a pyrolytic process, methods like attrition, chemical precipitation, ion implantation and more can form nano-scaled dust particles. Plasma processes however, are advantageous regarding little toxicity of the synthesis, little expenditure of work and often good control over the nano-particle size distribution [50]. For conducting materials, often sputtering of the desired material by the energetic ions of a plasma, called Magnetron sputtering, is utilized for their production.
In this study, however, dielectric nano-particles have been synthesized in the gas phase by plasma polymerization of acetylene. Making use of a low temperature radio frequency (RF) plasma, thermally sensitive polymers can not only be deposited as thin films, which is the common usage of plasma polymerization, but also lead to nano-particle formation by agglomeration of radicals and ions in the reactor volume. Here a capacitively coupled RF-driven electrode was on the bottom, igniting the discharge and delivering energy to free electrons without directly heating the background gas, which allows to form thermally sensitive hydrocarbons, that then ultimately form the nano-particles. Further-more, the plasma can trap negative ions, and thereby, increase the probability for the synthesis of clusters and particles, which is another advantage of plasma processes.
Understanding the interaction of the plasma with the forming carbonaceous nano-particles will be the main focus of this work as the plasma properties affect the chemistry and confinement of the particles and vice versa the particle size and consequent charge induces major changes in the plasma.
As it is impossible to achieve a full understanding of the discharge and the growth mechanisms by only one diagnostic method, several different analysis techniques were applied consecutively and combined in order to get an insight into the evolution of some basic plasma parameters like electron temperature and density as well as into the particle growth chemistry and physics. Only by observing both, the plasma and the nano-dust, can the impact of one on each other be uncovered.
Many studies have been conducted on the growth of nano-particles in plasmas during the past decades, especially for silane [51] due to its importance in semiconductor industry. Among the most commonly involved in situ techniques, there are electrical measurements of the discharge characteristics [52–58], laser light scattering at the dust cloud [59–61] or even more advanced Mie ellipsometry [62–66] in order to examine the dust distribution, investigations of the molecular chemistry by IR-absorption techniques [61, 67, 68], by optical emission spectroscopy [57, 69–71] and by mass spectrometry [61, 64, 67, 72–76], microwave interferometry for measuring the electron density [77–79] and last but not least Langmuir probe measurements in order to retrieve an entire set of information on the electron population [80–83]. However, all of these techniques do have their difficulties when applying to nano-particle forming polymerization plasmas. In this ever changing environment a suitable time resolution is crucial, surfaces quickly become covered not only by thin films but also by dust changing currents to Langmuir probes or affecting the transparency of windows and the electrostatic lenses of mass spectrometers, a suitable spatial resolution is necessary to take

distortions by an inhomogeneous particle cloud into account and finally the particles can only be directly detected from a certain size on by light scattering methods, which obviously limits their applicability to very small particle diameters.
The only way to obtain information on the exact morphology and size of the small nano-particles however, is by doing ex situ electron microscopy, e.g. SEM and TEM [84], or atomic force microscopy. Otherwise, XPS and NEXAFS [85, 86] can explore the chemical composition. Unfortunately this implies to extract the dust from the plasma chamber. Here new problems arise as various extraction methods also act like a filter, only picking out a certain size range of particles. A very common technique is to have the particles falling out of the plasma when they reach a certain size and thus overcome the trapping, elsewhere neutral drag was used to accelerate the particles towards a substrate [84], complicating the matter. As the particle size usually is not stable, the size also depends on the time of their extraction from the plasma.
Therefore, it is useful to combine various diagnostics in order to develop a proper understanding of the complicated growth mechanisms. In this work several techniques have been applied to the reaction chamber ATILA. The chamber itself with its plasma as well as the techniques will be introduced during this thesis after giving an overview over not only plasma theory but also its reactive and its dusty occurrence. On top of that an insight into current models of how the different steps of particle formation happen shall be given. The topics are divided into the following chapters: Chapter 2 will provide an overview over topic related plasma fundamentals, which will be completed by a proper chapter on reactive plasma in 3 containing basic sets of equations and ideas on PECVD processes, especially in acetylene and introducing current theory on particle growth in plasma chambers.
Then the reactor ATILA, at which most of the presented work has been done shall be presented in detail in chapter 4, followed by chapters concerning the experimental part of this thesis. They consist of electrical measurements of the discharge characteristics in chapter 5, laser light scattering at the dust particle cloud in chapter6 in order to retrieve the tempo-spatial dust distribution, Langmuir probe measurements in chapter 7 for the basic plasma parameters, phase resolved imaging of the near electrode sheath to obtain a better understanding of the heating mechanism in chapter 8, energy resolved mass spectrometry in chapter 9 with the aim to understand the effects, that dense dust clouds induce in the plasma in the plasma chemistry and finally the short chapter 10 is dedicated to deposition rate measurements done during the growth of nano-particles.
The last chapter, chapter 11, will finally summarize the experimental work, that has been done, and also the results and conclusions, that are the outcome of this thesis. Additionally a brief outlook, on what can be researched in future concerning the use of the reactor ATILA and nano-particle growth in plasmas in general.
The entire work was made possible by the financing through the project B13 in the frame of the *Sonderforschungsbereich Transregio 24*, in short SFB-TR24/B13, titled *Fundamentals of Complex Plasmas*. It was given by the Deutsche Forschungsgemeinschaft (DFG) and the results obtained here, have greatly benefited from the close collaboration with the project SFB-TR24/B15 in the same frame, that was financing the PhD-thesis of Alexander Martin Hinz at the chair of Prof. Dr. rer. nat. Franz Faupel for Multicomponent Materials of the

Technical Faculty at the University of Kiel [87].

Chapter 2

Plasma basics

The plasma state is characterized by several properties, which shall be discussed in the first part of this chapter. Then the formation of the plasma sheath in a RF reactor will be explained, because it separates not only the plasma from its surrounding surfaces but also the particles from the surrounding plasma, so the sheath characteristics are crucial to understand the embedding and trapping of nano-particles in a plasma, which will be further deepened in the ensuing section by introducing the basics of dusty plasmas. However, one focus of current research is, if the classical dusty plasma, that typically deals with micrometer sized dust grains, can correctly describe nano-dusty plasmas, or if some assumptions need to be thought over, especially concerning considerable changes in the plasma induced by a large quantity of dust particles. This issue will also be addressed before some aspects of reactive plasmas are presented in order to comprehend the importance of thermal non-equilibrium for chemical reactions, that produces fast electrons but slow and trapped negative ions and finally can lead to nucleation and consecutive particle genesis in the volume of the chamber.

2.1 Definition of a plasma

Besides the neutral atoms and molecules a plasma is marked by the presence of free ions and electrons. These populations, index n for neutrals, i for ions and e for electrons, can be described by their densities n and temperature T. The ions can be charged positively or negatively as single or multiple charge. However, the most common ion species in low temperature plasmas are single positively charged. If the background or neutral gas does not consist of one atom species like in an argon plasma, the different molecules or atoms can each form this bunch of negative and positive ions resulting in a zoo of different ions with charge $q_k = z_k e$, a multiple z_k of the elementary charge e. Each ion species, with index k, is then allocated a density $n_{\mathrm{i},k}$. On a macroscopic length scale a plasma needs to be *quasi-neutral*,

which means, that the sum of all charges must be zero:

$$\sum_k n_{\mathrm{i},k} q_k - e n_\mathrm{e} = 0 \tag{2.1}$$

$$\sum_k n_{\mathrm{i},k} z_k - n_\mathrm{e} = 0. \tag{2.2}$$

Assuming there were only single positive ions, the upper expression would be simplified to

$$n_\mathrm{i} \approx n_\mathrm{e}. \tag{2.3}$$

However, in many reactive plasmas, a non-negligible quantity of negative ions is formed as well, which violates the assumptions for equation 2.3, and thus, it is not true any longer. Also, the presence of dust particle can change this balance by the collection of electrons onto the particles, and hence, a reduction of the electron density n_e in the plasma. The charging of dust immersed in a plasma will be treated more extensively in chapter 2.3.
Obviously, on an inter atomic distance the quasi-neutrality cannot hold true neither. If a test charge is immersed in the plasma, ions and electrons group around it and build up an inverse space charge and thus diminish the electric field around it rapidly. The length scale at which the screening happens is the so called *linearized Debye length* λ_D or also *screening length*:

$$\lambda_\mathrm{D}^{-2} = \lambda_\mathrm{Di}^{-2} + \lambda_\mathrm{De}^{-2}. \tag{2.4}$$

It depends on the temperature T, that counteracts against the screening, and it is composed of the ion and electron Debye length:

$$\lambda_{\mathrm{D}j} = \sqrt{\frac{\varepsilon_0 k_\mathrm{B} T_j}{n_{j0} e^2}}; \qquad j = \mathrm{e}, \mathrm{i} \tag{2.5}$$

with $n_{\mathrm{i}0}$ and $n_{\mathrm{e}0}$ the ion and electron density respectively in the undisturbed plasma. This is a common model, that includes only positively charged ions at the temperature T_i but allows for several ion atom species and also for double charges z=2, where $\sum z_k n_{\mathrm{i},k0} = n_{\mathrm{i}0}$. Whereas for thermal plasmas, where $T_\mathrm{e} \approx T_\mathrm{i}$, the electron Debye length and the ion Debye length contribute similarly to its linearized form, most of the laboratory plasmas are low temperature plasmas. There the ions are fairly cold in comparison to the electrons, and thus, contribute much stronger. It is not by hazard, as the energy source usually is designed to only excite electrons but not the ions.
Due to the screening of any test charge Q, the potential formed by such is not a Coulomb potential diminishing with $1/r$ but decreasing even faster with distance r by the factor $\exp -r/\lambda_\mathrm{D}$:

$$\Phi(r) = \frac{Q}{4\pi\varepsilon_0 r} \exp\left(-\frac{r}{\lambda_\mathrm{D}}\right). \tag{2.6}$$

The radially symmetric *Debye-Hückel* or *Yukawa potential* is named after its explorers Peter Debye and Erich Hückel in plasma physics [88] and Hideki Yukawa in quantum physics [89].

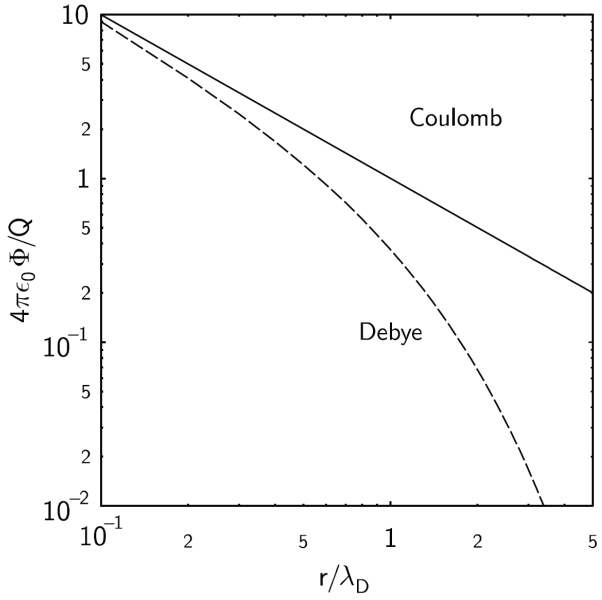

Figure 2.1: The Debye-Hückel potenial decays faster than the Coulomb potential. Taken from [90];

It resembles the Coulomb potential close to the charge $r < \lambda_D$ but at distance λ_D it decays to $1/e$ of its initial value and it is much weaker far away $r > \lambda_D$. The profile is shown in figure 2.1.
For low temperature plasmas, where $T_i < T_e$, the Debye length must be dominated by the shorter ion Debye length λ_{Di} according to 2.4 and 2.5. Hence the screening is mostly a result of the ion characteristics. In some experiments with dust particles, however, it was found, that particles arrange in a distance to each other, that agrees better with the electron Debye length [91–94]. It can be explained by a non-isotropic velocity distribution of the ions at the plasma sheath edge, where the particles were observed.
If the test charge is of infinitesimal size, then the screened volume around it becomes a sphere with a radius of the Debye length $V = 4/3\pi\lambda_D^3$, so that the number of ions and electrons in it, called *Debye number*, becomes

$$N_{Di,e} = n_{i,e}\frac{4}{3}\pi\lambda_{Di,e}^3 \tag{2.7}$$

respectively. In order to effectively screen the test charge, there have to be enough free charges in this sphere, that can group around it. So the critical number of ions is set to be $N_{Di,limit} = 1$ [90]. In case there are more ions, the plasma is considered to be *weakly coupled*, below one it is a *strongly coupled plasma*. Figure 2.2 gives an overview over different plasmas and where they have to be sorted to according to this criteria. The only force pushing charge carriers out of the Debye sphere against the electrostatic attraction is the thermal movement of the ions and electrons. So the number of ions in the sphere can also be described as a function of the ratio Γ_i between the potential energy of the ion interaction, assumed to be

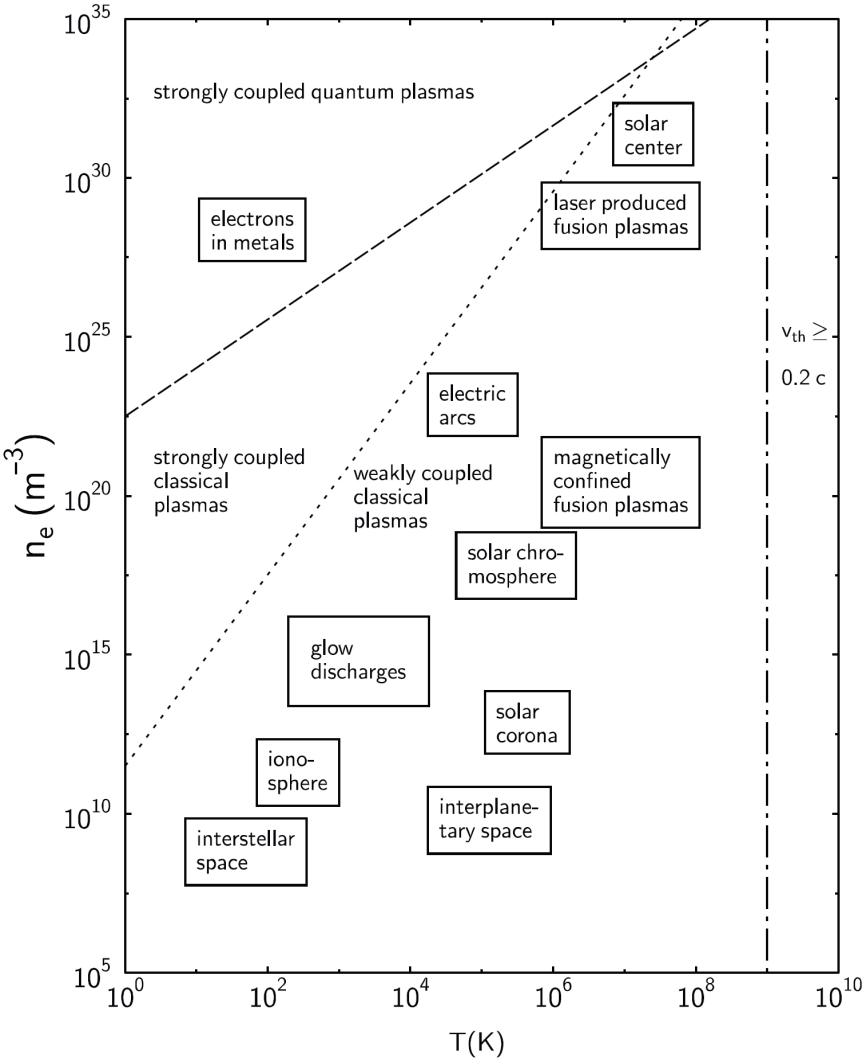

Figure 2.2: The dotted line corresponds to $N_{\mathrm{De}} = 1$. Taken from [90];

of Coulomb kind

$$W_{pot} = \frac{q^2}{4\pi\varepsilon_0 r}, \tag{2.8}$$

and their thermal energy $k_{\mathrm{B}}T_{\mathrm{i}}$. Exchanging ion to ion distance by measures of the Wigner-Seitz-radius $r = 2a_{\mathrm{ws}}$ the ratio becomes

$$\Gamma_{\mathrm{i}} = \frac{W_{\mathrm{pot}}}{W_{\mathrm{th}}} = \frac{e^2}{8\pi\varepsilon_0 a_{\mathrm{ws}} k_{\mathrm{B}} T_{\mathrm{i}}}. \tag{2.9}$$

Because the Wigner-Seitz-radius is related to the ion density by

$$\frac{4\pi}{3} a_{\mathrm{ws}}^3 n_{\mathrm{i}} = \frac{a_{\mathrm{ws}}^3}{\lambda_{\mathrm{Di}}^3} N_{\mathrm{i}} = 1, \tag{2.10}$$

a connection between the amount of ions in the Debye sphere and the coupling parameter Γ_i can be made using equation 2.5 for the ions:

$$\Gamma_\mathrm{i} = \frac{1}{6} N_\mathrm{Di}^{-2/3}. \tag{2.11}$$

So up to a factor the coupling parameter and the Debye number describe the same physical property and a similar definition for the limit between weakly and strongly coupled plasmas is to use $\Gamma_\mathrm{i} = 1$, so that $\Gamma_\mathrm{i} > 1$ corresponds to a cold and strongly coupled plasma and $\Gamma_\mathrm{i} < 1$ to a hot and weakly coupled one. The parameters Γ and N are equivalent for ions and electrons.
The coupling parameter can also be used to describe the dust inside the plasma Γ_d. Because it is arranged in an inter particle distance b_ws, that needs to consider the screening by ions and electrons, the Coulomb energy in equation 2.9 must be modified by the Debye-Hückel potential. Also the charge q is a multiple of the elementary charge $Q_\mathrm{d} = Ze$, which will be further explained in section 2.3.1. So the coupling parameter becomes [90]:

$$\Gamma_\mathrm{d} = \frac{Z^2 e^2}{4\pi\varepsilon_0 b_\mathrm{ws} k_\mathrm{B} T} \exp\left(-\frac{b_\mathrm{ws}}{\lambda_\mathrm{D}}\right). \tag{2.12}$$

For low values $\Gamma_\mathrm{d} < 1$ the dust cloud can be assumed to behave like a gas, whereas above it exhibits liquid like features. In experiments it was found that the dust cloud undergoes a transition to a crystal structure at the critical value of $\Gamma_\mathrm{d} = 175$ [95].

2.2 RF discharges

As already mentioned, low temperature RF plasmas are not in thermal equilibrium. This is due to the fact, that energy is fed externally to the electrons but not the ions nor the neutrals. As a consequence the electron temperature is far higher than the ion temperature, which in terms often can be assumed to be close to room temperature like the neutral gas. This is a wanted feature of many laboratory plasmas. It allows to use the energetic electrons for certain chemical and physical reactions without overheating a substrate or gas. It can not only be realized by RF plasmas, but for example also by microwave or inductive plasmas and even continuous or pulsed DC-discharges.
In principle the energetic imbalance is achieved by making use of different response times of electrons and ions on electric fields due to their different masses. As the electrons are much less heavy, they can pick up sudden changes in the electric field and thus be accelerated at high frequencies. The response time is described by

$$\tau_{\mathrm{p}j} = 2\pi \cdot \sqrt{\frac{\varepsilon_0 m_j}{n_j q_j^2}}, \qquad j = \mathrm{i}, \mathrm{e}. \tag{2.13}$$

Often, the according frequency is used instead:

$$\omega_{\mathrm{p}j} = \frac{2\pi}{\tau_{\mathrm{p}j}} = \sqrt{\frac{n_j q_j^2}{\varepsilon_0 m_j}}, \qquad j = \mathrm{i}, \mathrm{e}. \tag{2.14}$$

Taking a typical value of $n_\mathrm{i} = n_\mathrm{e} \approx 4 \cdot 10^{15}\mathrm{m}^{-3}$ the circular electron plasma frequency ω_pe is in the range of $3 \cdot 10^9\,\mathrm{s}^{-1}$, whereas the dominant argon ion has a frequency in the order of $1.3 \cdot 10^7\,\mathrm{s}^{-1}$. The RF generator frequency of 13.56 MHz, which is $8.52 \cdot 10^7\,\mathrm{s}^{-1}$ expressed as circular frequency, is chosen to be in between the electron and ion plasma frequency. Therefore the ions cannot react to the fast fluctuations in the electric field but see a time averaged field, which will be explained in the following section. However for the lightest existing ion, H^+, in this example the plasma frequency is of the same order $\omega_{\mathrm{pH}^+} = 8.4 \cdot 10^7\,\mathrm{s}^{-1}$ as the exciting frequency of the generator, assuming $n_{\mathrm{H}^+} = n_\mathrm{i}$. So if it was a pure hydrogen discharge, the heating of hydrogen ions might be important to consider. Here however, hydrogen ions are much rarer than argon ions, so ω_{pH^+} is a lot lower.
Free electrons, however, that are always present due to cosmic rays like UV light, pick up the electric field generated at the RF electrode. They are accelerated and consequently collide with the background gas. The inelastic collisions mainly lead to excitation of the neutrals but when the kinetic energy overcomes the ionization energy of the neutrals, new ion-electron pairs are created, which each delivers a new artificial electron to the discharge. This way electrons are multiplied and the plasma is ignited. However, the energy loss in elastic collisions is rather low due to the big mass difference between electrons and atoms and thus only little momentum transfer. That's why the electrons don't loose their energy easily and thus stay hot in the vicinity of cold neutrals and ions.
Similarly a plasma frequency for the dust can be defined:

$$\tau_\mathrm{pd} = \frac{2\pi}{\omega_\mathrm{pd}} = 2\pi \cdot \sqrt{\frac{\varepsilon_0 m_d}{n_d Q_\mathrm{d}^2}}. \tag{2.15}$$

For nano-particles the charge is a few elementary charges $Q_\mathrm{d} = -Ze$, whereas their mass is already much higher than that of atoms and molecules. So their plasma frequency is even lower than the ion plasma frequency. Calculations from Bilik *et al.* [83] give an approximate value of $\omega_\mathrm{pd} \approx 9 \cdot 10^3\,\mathrm{s}^{-1}$, which is far below the ion plasma frequency. The dust plasma frequency will be a crucial point for Langmuir probe measurements later on.

2.2.1 The plasma sheath

In contrast to cosmic plasmas, the size of low pressure laboratory plasmas is limited to the walls of the vacuum vessel. The transition from a bulk plasma to the wall happens through the so called *plasma sheath*. It is marked by a rarification of charge carriers, which is caused by absorption and conversion into neutrals at the walls. A detailed mathematical description can be found in various literatures, for example in [90]. For collision-less sheaths the first model was introduced by Child and Langmuir, which was later solved mathematically by Harrison and Thompson [96].
As the electrons carry energies in the order of a few electron volts, they can overcome potential barriers of a few volts by thermal motion. Usually it is assumed, that the electrons exhibit a Maxwellian energy distribution. Thus, even a few electrons from the highly energetic tail of the distribution can even reach repulsive potentials in the range of several electron volts. The ions, however, can only reach to potentials more negative than their

origin. So when a plasma is ignited, many electrons leave the plasma quickly due to their high velocities. That reduces the negative charges in the bulk and so the plasma settles at a higher potential than the enclosing walls, consecutively pushing ions out of the discharge. Finally an equilibrium is reached, where the outward ion current equals the loss of highly energetic electrons to the walls. Because a plasma tends to shield any charges, the walls are also being shielded resulting in a positive space charge in front of them. This positive space charge is the plasma sheath, that is generated around any surface, that can collect charges, also around nano-particles.
For an effective shielding it is necessary, that ions inside the bulk don't take any notice of the charges outside. Reconsidering this, another definition for the sheath edge would be, that at the edge ions travel just as fast enough, so that no distortion can propagate into the plasma. Hence, in this picture, ions are accelerated before reaching the sheath edge at $z = 0$ by picking up energy from a slowly decreasing potential. At the sheath edge they reach the speed of sound, called *Bohm velocity* 2.16, and here the distortion from the walls is brought to a standstill like a standing wave:

$$v_\mathrm{B} = \sqrt{\frac{k_\mathrm{B} T_\mathrm{e}}{m_\mathrm{i}}}. \tag{2.16}$$

Afterwards, for $z_\mathrm{wall} > z > 0$, the ions are strongly attracted by the relatively negative walls. Finally all the potential energy, that they carry from the plasma potential at their origin Φ_pl, is transformed into kinetic energy during a collisionless transit through the pre-sheath and sheath:

$$E_\mathrm{kin} = e\left(\Phi_\mathrm{pl} - \Phi_\mathrm{wall}\right). \tag{2.17}$$

Whereas quasi-neutrality still is valid in the pre-sheath, the plasma density already decreases. In an RF discharge the powered electrode alternates its current. While the ions can only see a time averaged electrode potential due to their inertia and thus are constantly flowing towards the electrode, the electrons need to do all the alternating of the current. During one half of the cycle they are attracted, during the other half they are repelled. So from an electron point of view the sheath in front of the electrode needs to collapse once per cycle, so that a considerable amount of them can reach it. The time averaged density profile of ions and the time dependent density of electrons in front of the electrode is shown in figure 2.3.
The exponential decrease of the averaged electron density $\bar{n}_\mathrm{e}$ is a direct consequence of the Maxwellian energy distribution. The further the electrons intrude into the sheath, the more energy they needed to have in the beginning [90]:

$$\bar{n}_\mathrm{e}(z) = n_\mathrm{e}(0) \exp\left(\frac{e\left(\Phi(z) - \Phi(0)\right)}{k_\mathrm{B} T_\mathrm{e}}\right). \tag{2.18}$$

As it is also demonstrated in figure 2.3, the electron density decreases drastically in the sheath, only close to the sheath edge a considerable amount can still be found. So for potential drops high enough, the sheath can be considered a pure ion sheath. Assuming

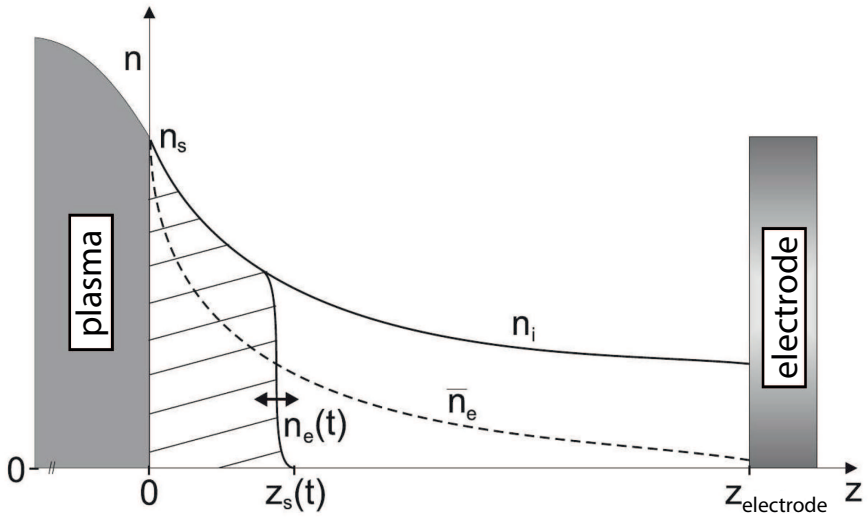

Figure 2.3: Due to highly energetic electrons a positive space charge builds up in front of walls and electrodes. The electron density $n_e(z)$ in front of the electrodes is time dependent due to a quickly alternating field. At the sheath edge the plasma density is decreased to n_s. After [15];

there are no collisions to occur, energy conservation is valid for the ions as already depicted in equation 2.17. Using energy conservation and continuity through the sheath

$$n_i(z)u_i = n_i(0)v_B \tag{2.19}$$

one obtains the ion density profile [90]

$$n_i(z) = n_i(0)\left(1 - \frac{2e\Phi(z)}{m_i v_B^2}\right)^{-1/2}. \tag{2.20}$$

Because the small amount of electrons can be neglected in Poisson's equation the potential profile $\Phi(z)$ now only depends on the ion density profile:

$$\frac{\partial^2\Phi}{\partial z^2} \approx -\frac{en_i(z)}{\varepsilon_0}. \tag{2.21}$$

Assuming further, that the Bohm velocity is small compared to the ion potential energy at the sheath edge and the electric field at this point also being small compared to the field strength at the wall, an expression for the potential profile across the sheath can be derived analytically [90]:

$$\Phi(z) = -\left(\frac{3}{2}\right)^{4/3}\left(\frac{m_i}{2e}\right)^{1/3}\left(\frac{j_i}{\varepsilon_0}\right)^{2/3} z^{4/3}, \tag{2.22}$$

where $j_i = en_i(0)v_B$ corresponds to the electric ion current density. Defining $\Phi(0) = 0$, one can use the electric voltage across the full sheath ($d = z_{wall}$) instead $U = \Phi(d) - \Phi(0) = \Phi(d)$

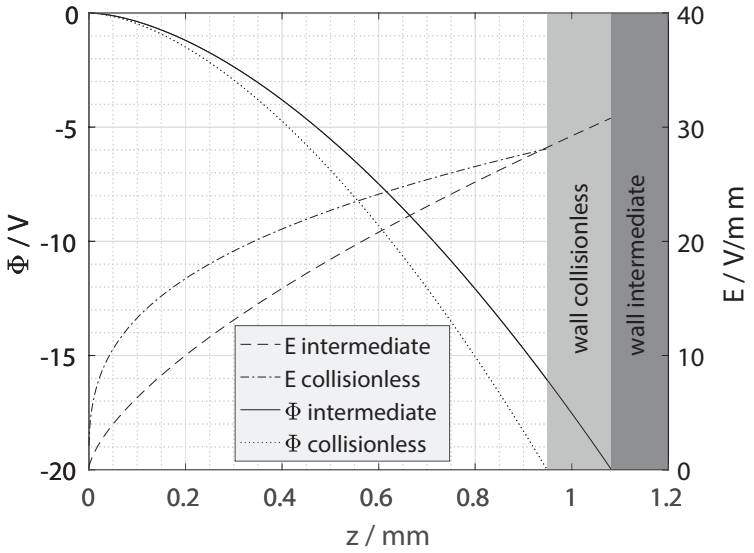

Figure 2.4: For the analytical solution of the potential distribution across the collisionless Child-Langmuir sheath ,Φ collisionless, the potential decreases towards the vessel walls. The electric field, E collisionless, is the strongest close to the walls and goes to zero close to the sheath edge. In the intermediate pressure model, which accounts for collisions, the sheath thickness d is slightly larger and the electric field, E intermediate, increases more linearly towards the vessel walls. The here presented curves refer to $n_\mathrm{i} = 4 \cdot 10^{15}\,\mathrm{m}^{-3}$, $T_\mathrm{e} = 2\,\mathrm{eV}$ and $U = \Phi_\mathrm{pl} = 20\,\mathrm{V}$.

and thus obtains

$$U^{3/2} = \frac{9}{4}\left(\frac{m_\mathrm{i}}{2e}\right)^{1/2} \frac{j_\mathrm{i}}{\varepsilon_0} \cdot d^2, \tag{2.23}$$

which, resolved for j_i is the famous Child-Langmuir law [97, 98] for the collisionless plasma sheath model:

$$j_\mathrm{i} = \frac{4}{9}\varepsilon_0 \left(\frac{2e}{m_\mathrm{i}}\right)^{1/2} \frac{U^{3/2}}{d^2}. \tag{2.24}$$

The sheath thickness d is in the order of one to hundred electron Debye lengths [15, 99]. For typical conditions of $n_\mathrm{i} = n_\mathrm{e} = 4 \cdot 10^{15}\,\mathrm{m}^{-3}$, $T_\mathrm{e} = 2\,\mathrm{eV}$ and a plasma potential of $\Phi_\mathrm{pl} = 20\,\mathrm{V}$ equation 2.23 yields a sheath thickness of $d \approx 950\,\mu\mathrm{m}$ in front of any grounded surface by setting $U = \Phi_\mathrm{pl}$, whereas the electron Debye length calculates to $\lambda_\mathrm{De} = 166\,\mu\mathrm{m}$. Moreover it was used, that the ion current density follows continuity through the sheath, so that it is determined by the flux at the sheath edge: $j_\mathrm{i} = 0.61 e n_\mathrm{i} v_\mathrm{B}$ with the ion density $n_\mathrm{i}(z = 0) = 0.61 n_\mathrm{i}$ at the sheath edge, as will be shown in section 2.2.2.
The sheath potential profile and its derivative, the electric field, are calculated for the above mentioned conditions and plotted in figure 2.4. It can be seen, that the electric field increases very drastically close to the plasma sheath edge but is the strongest close to the wall, here at $d = 950\,\mu\mathrm{m}$.
The Child-Langmuir sheath describes the potential fairly simply and is valid for very low

pressures, but not taking collisions into account is only valid where the ion mean free path l_i is larger than the sheath width d, $l_\mathrm{i} \gg d$, though. For a typical pressure of 6 Pa used during this study, as will be calculated in section 2.3.1, the ion mean free path for ion-neutral collisions is in the order of 550 μm. That is considerably lower than the sheath thickness calculated above but not far away neither. Therefore, an intermediate pressure model as provided in the book [15] shall be considered here, that may be used for the case $l_\mathrm{i} \approx d$. According to this model the potential profile in the sheath can be calculated to be

$$\Phi(z) = -\frac{3}{5}\left(\frac{3j_\mathrm{i}}{2\varepsilon_0}\right)^{2/3}\left(\frac{\pi m_\mathrm{i}}{2el_\mathrm{i}}\right)^{1/3} z^{5/3}. \tag{2.25}$$

Using the same steps as for the Child-Langmuir law an equal expression to equation 2.24 for the ion current density can be derived in the intermediate pressure regime:

$$j_\mathrm{i} = \frac{2}{3}\varepsilon_0\left(\frac{5}{3}\right)^{3/2}\left(\frac{2el_\mathrm{i}}{\pi m_\mathrm{i}}\right)^{1/2}\frac{U^{3/2}}{d^{5/2}}. \tag{2.26}$$

The two models are compared in figure 2.4 for the plasma values already used for the Child-Langmuir sheath. The resulting sheath thickness for the intermediate pressure model is $d \approx 1080\,\mu$m, which is actually quiet close to the collisionless model. Therefore, the Child-Langmuir model may provide a comprehensive picture nevertheless. However, as depicted in figure 2.4, the electric field in the sheath is much more linear in the intermediate pressure model.
For elevated pressures, where $d \gg l_\mathrm{i}$, the collisional model, called Mott-Gourney law, provides another approximation [99]:

$$j_\mathrm{i} = \frac{9}{8}\varepsilon_0\mu_\mathrm{i}\frac{U^2}{d^3}, \tag{2.27}$$

where μ_i is the ion mobility describing the drift velocity v_i of the ions in the sheath electric field $E = -\partial\phi/\partial z$ by

$$v_\mathrm{i} = -\mu_\mathrm{i}\frac{\partial\Phi}{\partial z}. \tag{2.28}$$

More models exist also accounting for an electron contribution in the Poisson equation 2.21, which is especially important for low voltage sheaths, because here electrons can penetrate deeply into the sheath. For an extensive knowledge the reader may refer to [99–102].
Furthermore, solutions for cylindrical and spherical geometries have been provided by Langmuir and Blodgett [98,103,104], where the continuity equation cannot be applied that easily.

2.2.2 The presheath

Ions, coming from the discharge center and reaching the sheath edge, need to be accelerated in order to obtain the bohm velocity. The accelerating force is the electrical force exerted by a decreasing potential towards the sheath edge. Considering quasi-neutrality in the presheath and making use of equation 2.18 it can be concluded, that

$$n_\mathrm{i}(z) = n_\mathrm{e}(z) = n_\mathrm{e0}\exp\left(\frac{e(\Phi(z) - \Phi_\mathrm{pl})}{k_\mathrm{B}T_\mathrm{e}}\right) \qquad \text{for } z < 0 \tag{2.29}$$

needs to be fulfilled, where $n_{e0} = n_{i0}$ and Φ_{pl} denote the electron density and plasma potential in the discharge center, respectively. This can be rewritten to

$$\Phi - \Phi_{pl} = \frac{k_B T_e}{e} \ln\left(\frac{n_i}{n_{i0}}\right). \tag{2.30}$$

The first derivative of that, considering continuity $n_i v_i = \text{const}$, and thus, $\mathrm{d}n_i/\mathrm{d}z = -n_i/v_i \cdot \mathrm{d}v_i/\mathrm{d}z$, therefore becomes

$$\frac{\mathrm{d}\Phi}{\mathrm{d}z} = -\frac{k_B T_e}{e}\frac{1}{v_i}\frac{\mathrm{d}v_i}{\mathrm{d}z}. \tag{2.31}$$

It can be inserted into the ion motion equation [90]

$$m_i v_i \frac{\mathrm{d}v_i}{\mathrm{d}z} + m_i \nu_{ni} v_i = -e\frac{\mathrm{d}\Phi}{\mathrm{d}z}, \tag{2.32}$$

which describes the acceleration by the field $\mathrm{d}v_i/\mathrm{d}z$ and the de-acceleration through ion-neutral collisions at the frequency ν_{ni}. Hence, a compact expression for the ion velocity is found

$$\frac{\mathrm{d}v_i}{\mathrm{d}z} = \frac{\nu_{ni} v_i^2}{v_B^2 - v_i^2}, \tag{2.33}$$

that clearly demonstrates, that the ion velocity needs to be smaller than v_B to obtain a positive acceleration.
Neglecting momentum loss through ion-neutral collisions the ions gain a kinetic energy $\frac{1}{2}m_i v_B^2 = \frac{1}{2}k_B T_e$ until the sheath edge, which is equal to the potential drop towards it:

$$e\left(\Phi_{pl} - \Phi(z=0)\right) = \frac{1}{2}k_B T_e. \tag{2.34}$$

Inserting this again into equation 2.29 it can now easily be found, that the plasma density reduces to 0.61 of its initial value in the discharge center through the presheath:

$$n_i(z=0) = n_{e0}\exp\left(-\frac{1}{2}\right) \approx 0.61\, n_{e0}. \tag{2.35}$$

This factor is found in various plasma formulas and has its origin in the continuity of the accelerating ion flux in the presheath.

2.2.3 The asymmetric RF plasma

Many RF discharges are asymmetric, meaning that the powered electrode doesn't have the same size A as the grounded one B. In this kind of RF discharges different sheath potentials $U = \Phi_{pl} - \Phi_{electrode}$ in front of the two different electrodes build up. Often the powered electrode is capacitively coupled, so it cannot support any DC currents. Therefore no DC current is conducted through the grounded electrode neither. However, due to geometrical reasons, locally the grounded electrode can draw some current, which overall needs to cancel out. This can be explained by geometrical dependence of the floating potential Φ_{fl}.

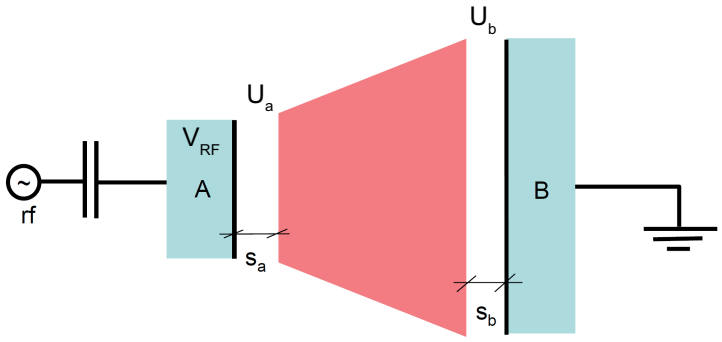

Figure 2.5: The sheaths in front of the electrode and in front of the grounded chamber walls may not be the same. Taken from [100];

It is known, that the measured floating potential differs for different shapes of Langmuir probes [105], which is caused by a geometrical dependency of the ion saturation current. The grounded electrode of a reactor is at the same potential everywhere, but also collects locally different ion currents depending on the local shape.
The principle of the electode size dependent sheath potential $U_{\mathrm{a,b}}$ and thickness $s_{\mathrm{a,b}}$ is depicted in figure 2.5. The smaller capacitively coupled powered electrode charges up negatively, so it must be $U_{\mathrm{a}} > U_{\mathrm{b}}$ and thus, according to 2.24 $s_{\mathrm{a}} > s_{\mathrm{b}}$. To be more precise, the RF period can be resolved like it was already shown in figure 2.3, so that $U_{\mathrm{a,b}}(t)$ and $s_{\mathrm{a,b}}(t)$ become a time dependent variable. This is shown in figure 2.6 for same sized electrodes $A = B$ and for unequal sized ones $B \gg A$. The average potential of the powered electrode, denoted as V_{bias} and called *self-bias voltage* from now on, is represented by the dashed line. It should also be mentioned, that the plasma potential varies much more in case of the symmetric configuration and thus, the sheath in front of the grounded electrode is subjected to high changes too.
As it is mathematically described in [106] the ratio of the two sheath voltages can be expressed as:

$$\frac{\bar{U}_{\mathrm{a}}}{\bar{U}_{\mathrm{b}}} = \left(\frac{B}{A}\right)^{q}. \tag{2.36}$$

Depending on the discharge conditions a value for q can be found. For typical RF discharges a value of $q = 2.21$ can be derived. In the chamber used during this study, the grounded electrode was represented by the entire chamber walls. In front of the grounded electrode the sheath potential must be equal to the plasma potential $U_{\mathrm{b}} \approx \Phi_{\mathrm{pl}} - 0 = \Phi_{\mathrm{pl}}$. Because the RF generator with the electrode V_{RF}, the sheath U_{a} and the sheath U_{b} form a closed circuit via the plasma, the sum of these voltages must be:

$$V_{\mathrm{RF}} + U_{\mathrm{a}} = U_{\mathrm{b}}, \tag{2.37}$$

So for the time average, V_{bias}, follows

$$V_{\mathrm{bias}} = -\left(\bar{U}_{\mathrm{a}} - \bar{U}_{\mathrm{b}}\right). \tag{2.38}$$

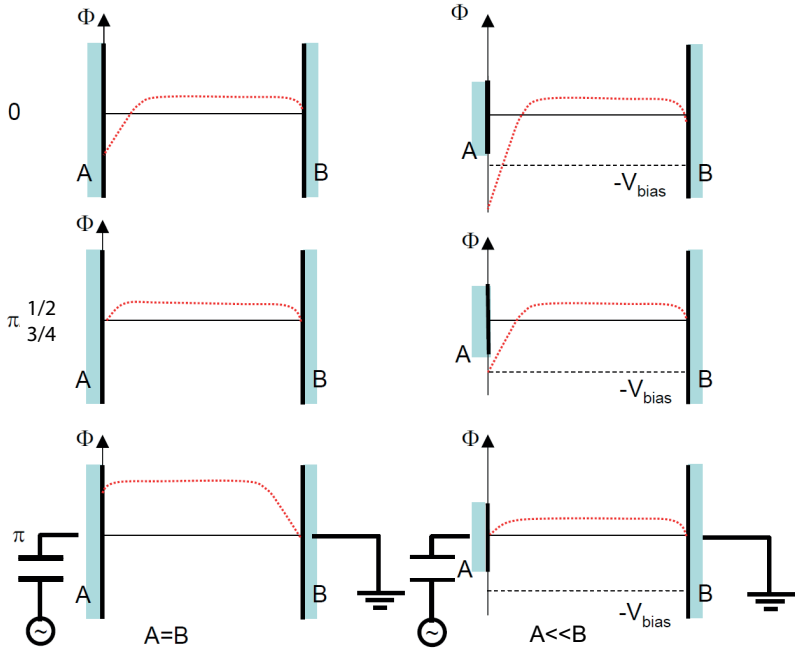

Figure 2.6: The sheath potentials vary as a function of the applied generator voltage. In capacitively coupled asymmetric discharges the powered electrode settles at a constant DC potential, the self-bias voltage, marked by the dashed line. Taken from [100];

Making use of equation 2.36 this can be rewritten to

$$V_{\text{bias}} = -\bar{U}_{\text{b}} \left(\left(\frac{B}{A} \right)^{q} - 1 \right) \approx -\bar{\Phi}_{\text{pl}} \left(\left(\frac{B}{A} \right)^{q} - 1 \right). \tag{2.39}$$

Hence, the self-bias voltage must be negative, because the plasma potential always is more positive than its surrounding, which is on ground and because $B/A > 1$. Also it can be concluded, that for a symmetric case, where $B/A = 1$, the self-bias voltage must be zero $V_{\text{bias}} = 0$. So, measuring V_{bias} can be a very useful tool, that contains information about the plasma potential and symmetry.
Another important relation can be derived by considering, that the sheath in front of the powered electrode needs to collapse shortly during each cycle, so that the electrons can reach it. A collapse marks the event, that the electrode potential V_{RF} becomes slightly positive for a short period. This way the constant ion current can be equalized by a high and short electron current. So the amplitude $1/2V_{\text{pp}}$ of the generator voltage must fulfil

$$\frac{1}{2} V_{\text{pp}} \geq -V_{\text{bias}}, \tag{2.40}$$

which by the use of equation 2.39 becomes

$$\frac{1}{2} V_{\text{pp}} \geq \bar{\Phi}_{\text{pl}} \left(\left(\frac{B}{A} - 1 \right)^{q} \right). \tag{2.41}$$

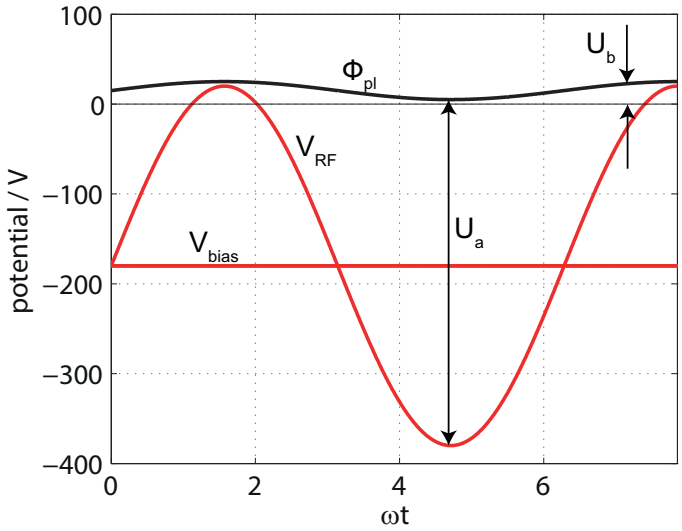

Figure 2.7: The self-bias voltage V_{bias} must be added onto the time varying applied RF voltage, resulting in an on average negative potential. Therefore the powered electrode is positively charged during only a very short period of the RF cycle. It is at that moment, that the electrons can reach to the electrode. The plasma potential Φ_{pl} always is the most positive throughout the RF cycle. From [101];

Because in this configuration B/A always is a positive factor greater than one we can conclude

$$\bar{\Phi}_{\text{pl}} \leq \frac{1}{2} \cdot \frac{V_{\text{pp}}}{(B/A)^q - 1} \tag{2.42}$$

as upper limit for the time averaged plasma potential. Its evolution together with the applied RF and self-bias voltage are shown in figure 2.7.
Because the self-bias voltage can be highly negative up to several hundreds of volts, high electric fields build up, which strongly accelerates positive charges onto the powered electrode. Therefore, substrates positioned on the electrode experience heavy ion bombardment, which can heat up the substrate and lead to significant sputtering. A lot of the discharge energy is dissipated here, which can be noticed from the hot electrode after an experiment.

2.3 Dusty plasmas

In dusty plasmas the neutral gas atoms and molecules, ions and electrons coexist together with additional microscopic particles. The dust can be added externally for example by a dust dispenser but it can also be produced inside the plasma chamber. In the industry during etching and polymerization processes the dust genesis mostly is an undesired side effect [35, 107], for example it can reduce the deposition rate in plasma-enhanced vapour deposition [108, 109] or disturb by producing killer particles [22, 110].
In order to understand the trapping, movement and growth of particles in a plasma and also

the effects on the plasma, the particle charging plays the most critical role. In laboratory plasmas the dust typically charges up negatively $Q_\mathrm{d} = -Ze$ to a floating potential and by collection ion and electron currents. By doing so it has an impact on the quasi-neutrality, which needs to be reformulated taking the overall dust charge $Q_\mathrm{d} n_\mathrm{d}$ into account:

$$\sum_k n_{\mathrm{i},k} q_k - e n_\mathrm{e} - Z e n_\mathrm{d} = 0. \tag{2.43}$$

In space the particles are also subject to energetic photons and particles, which can lead to photo emission or secondary emission of electrons and thereby the dust can also charge up positively [111]. Photo emission has a very low cross section and doesn't need to be considered in low-temperature plasmas. Secondary emission of ions and electrons can occur in laboratory plasmas. The energies of the ions and electrons coming to the dust surface is in the order of a few electron volt. The secondary electron emission yield is dependent on the material and has its maximum at relatively high energies of some hundreds of electron volts for the incident particles [112, 113]. Secondary ion emission can only occur in a sputtering regime, which is also at high energies for the incident particles, so it doesn't need to be considered neither. Therefore the charging of nano-particles in low temperature plasmas is dominated by the collection of primary ions and electrons, which will be discussed in the following section.

2.3.1 Dust charging

Different models to calculate the amount Z of elementary charges on the dust exist. Usually it is done by assuming, that the particles are a floating object as any other foreign body immersed in a plasma. They are surrounded by a plasma sheath and because they are not in contact with any other potential or current source, the ion and electron current must be equal once an equilibrium charge is established. Therefore it is accepted, that the particles charge up to floating potential Φ_fl. Whereas the electrons reach the dust grains by thermal motion, the ions are accelerated towards the particle, that is more negative than the plasma bulk.

A relatively simple model describing the currents onto a dust particle was introduced by Langmuir and Mott-Smith [114]. They assumed, that the ions are orbiting around the dust, whereas electrons are repelled. They called it Orbital Motion Limit (OML-) theory, in which the dust electric field is approximated by a Coulomb field and collisions in the sheath are neglected, yet, experiments show that this leads to higher charge numbers than in reality [91, 115, 116]. A parameter quantifying the amount of collisions ocurring in the sheath is the ratio of the mean free path for ion-neutral collisions with the Debye length: λ_D / l_i. It was found that collisions still effect the dust charge when this parameter is less than one [117, 118].

Taking the ideal gas law

$$p = n_\mathrm{n} k_\mathrm{B} T_\mathrm{n} \tag{2.44}$$

for the neutral argon gas and using an approximate value of $p = 6\,\mathrm{Pa}$ for the pressure mostly used during this work and further assuming the gas to be at room temperature $T = 300\,\mathrm{K}$ the

neutral gas density can be calculated to $n_\mathrm{n} = 1.45 \cdot 10^{21}\,\mathrm{m}^{-3}$. Setting this value together with the cross section for ion-neutral collisions to $\sigma_\mathrm{ni} = 125\,\mathrm{Å}^2$, taken from [119], into equation

$$l_\mathrm{i} = \frac{1}{n_\mathrm{n}\sigma_\mathrm{ni}}, \tag{2.45}$$

a mean free path of $l_\mathrm{i} \approx 550\,\mu\mathrm{m}$ can be estimated. As will be presented later in chapter 7 Langmuir probe measurements have been done in the dust forming plasma. For an undisturbed plasma an electron density of $n_\mathrm{e} \approx 4 \cdot 10^{15}\,\mathrm{m}^{-3}$ and an electron temperature of $T_\mathrm{e} \approx 2\,\mathrm{eV}$ were obtained. Hence, assuming an ion temperature of $T_\mathrm{i} \approx 0.03\,\mathrm{eV}$ and $n_\mathrm{i} = n_\mathrm{e}$ the linearised Debye length is determined by the help of equations 2.4 and 2.5 to be $\lambda_\mathrm{D} \approx 20\,\mu\mathrm{m}$. Therefore the collision parameter is estimated to be

$$\frac{\lambda_\mathrm{D}}{l_\mathrm{i}} \approx 0.04. \tag{2.46}$$

Because the Debye length is strongly dominated by the ion Debye length, a perturbation in the electron Debye length by a change of n_e or T_e due to nano-dust does not affect the collision parameter. So this result can still be used for dense dust clouds and it seems that a collisional model like proposed from Khrapak *et al.* [120] can be avoided here. In the following the model from Mott-Smith and Langmuir shall be introduced as described in [90]. By attractive or repulsive forces the sphere cross section of radius r_d is enlarged or reduced respectively to the OML-factor σ_c, a cross section described by the effective collection radius b_c:

$$\sigma_\mathrm{c} = \pi b_\mathrm{c}^2 = \pi r_\mathrm{d}^2 \left(1 - \frac{2q\Phi_\mathrm{d}}{mv^2}\right) \tag{2.47}$$

Here q, m and v are the orbiting particle mass, charge and velocity, respectively. If the force is attractive, then $q\Phi_\mathrm{d} < 0$, so that the effective cross section is enlarged. For a repulsive force the term is only valid for kinetic energies greater than the dust surface potential $mv^2 \geq mv_0^2 = 2q\Phi_\mathrm{d}$, so that the cross section cannot become smaller than zero. Assuming, that the velocities of the impinging particles are of Maxwellian distribution f_M, the overall current is the integral

$$\begin{aligned} I &= q \int v\sigma_\mathrm{c}(v) f_\mathrm{M}(v)\mathrm{d}v \\ &= qn\pi r_\mathrm{d}^2 \left(\frac{m}{2\pi k_\mathrm{B}T}\right)^{3/2} \int 4\pi v \left(v^2 \pm v_0^2\right) \exp\left(-\frac{mv^2}{2k_\mathrm{B}T}\right)\mathrm{d}v \end{aligned} \tag{2.48}$$

with $+$ for attractive forces and $-$ for repulsive ones. Because the ions are attracted, all of them, regardless of their velocity, cross the sheath and thus, the integral needs to be solved from 0 to ∞, yielding

$$I_\mathrm{i} = en_\mathrm{i}\pi r_\mathrm{d}^2 \left(\frac{8k_\mathrm{B}T_\mathrm{i}}{\pi m_\mathrm{i}}\right)^{1/2} \cdot \left(1 - \frac{e\Phi_\mathrm{d}}{k_\mathrm{B}T_\mathrm{i}}\right). \tag{2.49}$$

For the electrons, however, the minimum velocity v_0 must be used as lower limit, so that the integral gives:

$$I_\mathrm{e} = -en_\mathrm{e}\pi r_\mathrm{d}^2 \left(\frac{8k_\mathrm{B}T_\mathrm{e}}{\pi m_\mathrm{e}}\right)^{1/2} \exp\left(-\frac{e\Phi_\mathrm{d}}{k_\mathrm{B}T_\mathrm{e}}\right). \tag{2.50}$$

Once the dust has established an equilibrium charge no net currents can be drawn, which actually is the definition for the floating potential $\Phi_\mathrm{d} = \Phi_\mathrm{fl}$:

$$0 = \frac{\mathrm{d}Q_\mathrm{d}}{\mathrm{d}t} = I_\mathrm{i}(\Phi_\mathrm{fl}) + I_\mathrm{e}(\Phi_\mathrm{fl}). \tag{2.51}$$

In [90] it is now once more assumed, that $n_\mathrm{i} = n_\mathrm{e}$. In this study, however, for large dust densities the assumption may not be justified. Due to the modified quasi-neutrality 2.43 the electron density may be much lower than the ion density. So equation 2.51 becomes

$$\begin{aligned} n_\mathrm{e}\left(\frac{8k_\mathrm{B}T_\mathrm{e}}{\pi m_\mathrm{e}}\right)^{1/2} \exp\left(\frac{e\Phi_\mathrm{fl}}{k_\mathrm{B}T_\mathrm{e}}\right) &= n_\mathrm{i}\left(\frac{8k_\mathrm{B}T_\mathrm{i}}{\pi m_\mathrm{i}}\right)^{1/2}\left(1 - \frac{e\Phi_\mathrm{fl}}{k_\mathrm{B}T_\mathrm{i}}\right) \\ \exp\left(\frac{e\Phi_\mathrm{fl}}{k_\mathrm{B}T_\mathrm{e}}\right) &= \frac{n_\mathrm{i}}{n_\mathrm{e}}\left(\frac{m_\mathrm{i}T_\mathrm{e}}{m_\mathrm{e}T_\mathrm{i}}\right)^{-1/2}\left(1 - \frac{e\Phi_\mathrm{fl}}{k_\mathrm{B}T_\mathrm{i}}\right). \end{aligned} \tag{2.52}$$

The equation has to be solved numerically, which for $n_\mathrm{i}/n_\mathrm{e} = 10$, 4 and 1 exemplary, setting $T_\mathrm{i} = 0.03\,\mathrm{eV}$, $n_\mathrm{i} = 4 \cdot 10^{15}\,\mathrm{m}^{-3}$ and $m_\mathrm{i} = 40\,\mathrm{amu}$ for argon ions results in figure 2.8. As can be seen from the graph, high electron temperatures yield a highly negative dust surface, whereas a high ratio of $n_\mathrm{i}/n_\mathrm{e}$ brings the dust surface potential closer to the plasma potential, set to be zero in this case.
When the dust has charged up to its floating potential it carries a certain quantity Z of elementary charges on it. In order to estimate this quantity one usually treats each particle as a spheric capacitor. If the dust radius is in the same size range as the distance to its opposing charges, which is the plasma, meaning $r_\mathrm{d} \gtrsim \lambda_\mathrm{D}$, the capacitance is

$$C = 4\pi\varepsilon_0 r_\mathrm{d}\left(1 + \frac{r_\mathrm{d}}{\lambda_\mathrm{D}}\right). \tag{2.53}$$

As it has already been calculated in the beginning of this subsection, the Debye length is approximately $\lambda_\mathrm{D} \approx 20\,\mu\mathrm{m}$, so with particles of some tens of nanometres in radius the last term in equation 2.53 can be dropped and the particle is treated like a sphere in vacuum:

$$C = 4\pi\varepsilon_0 r_\mathrm{d}. \tag{2.54}$$

The dust charge then can be estimated to be

$$Q_\mathrm{d} = C\Phi_\mathrm{fl} = 4\pi\varepsilon_0 r_\mathrm{d}\Phi_\mathrm{fl} \tag{2.55}$$

or equivalently

$$Z = \frac{4\pi\varepsilon_0}{e} r_\mathrm{d}\Phi_\mathrm{fl}. \tag{2.56}$$

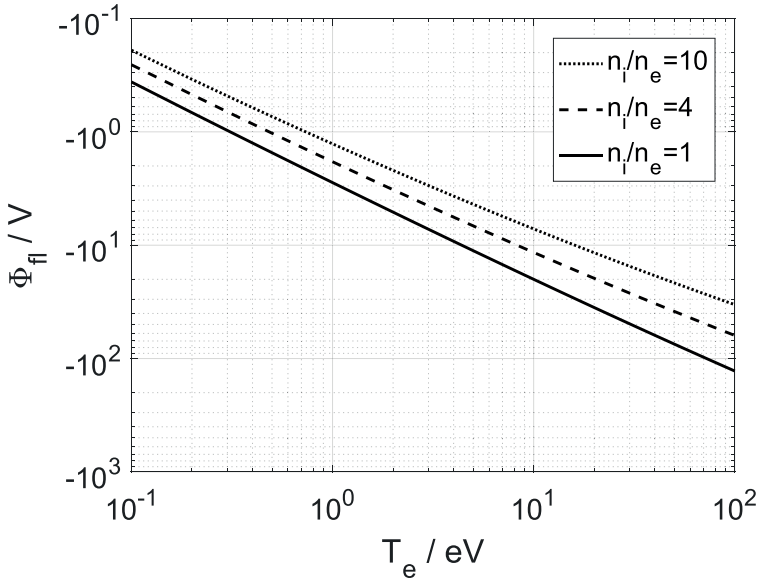

Figure 2.8: With increasing T_e the floating potential drops due to a higher electron current. For high ratios of $n_\mathrm{i}/n_\mathrm{e}$ the ion current counteracts, resulting in less negative floating potentials.

From figure 2.8 it can be taken, that for $n_\mathrm{i}/n_\mathrm{e} = 1$ and a moderate electron temperature of $T_\mathrm{e} = 2\,\mathrm{eV}$ the floating potential is $\Phi_\mathrm{fl} \approx -5\,\mathrm{V}$. Hence, the dust charge quantity can be calculated and simplified to be

$$Z \approx -3.5 \cdot \frac{r_\mathrm{d}}{[\mathrm{nm}]}. \tag{2.57}$$

Hence, a particle of 100 nm in diameter carries a charge of 175 electrons. Interestingly the charge might stay unaffected by an electron rarefaction due to high dust densities, if the electron temperature increases in the same time. Taking $n_\mathrm{i}/n_\mathrm{e} = 10$ as an example, an electron temperature of $T_\mathrm{e} = 6\,\mathrm{eV}$ would compensate the lower electron current and yield the same dust potential.
Like for any other capacitor connected via a resistance R, the dust particles have a finite charging time τ, that is the time it takes to reach $1 - e^{-1}$ of its equilibrium charge. The resistance in a dusty plasma is determined by the currents I_i and I_e through the sheath around the particle. However, the according sheath resistance R_s is not strictly ohmic but changing with the dust potential $R_\mathrm{s}(\Phi_\mathrm{d})$ and therefore the charging currents exhibit some non-linear behaviour. Nevertheless the common equation for the charging of a capacitor can be used by expanding the charging currents around any dust potential Φ_d:

$$\frac{\mathrm{d}\Phi}{\mathrm{d}t}(\Phi_\mathrm{d}) = \frac{1}{C}\frac{\mathrm{d}Q}{\mathrm{d}t} = \frac{1}{C}\left(I_\mathrm{i}(\Phi_\mathrm{d}) + I_\mathrm{e}(\Phi_\mathrm{d})\right) = -\frac{1}{CR_\mathrm{s}(\Phi_\mathrm{d})}(\Phi - \Phi_\mathrm{d}), \tag{2.58}$$

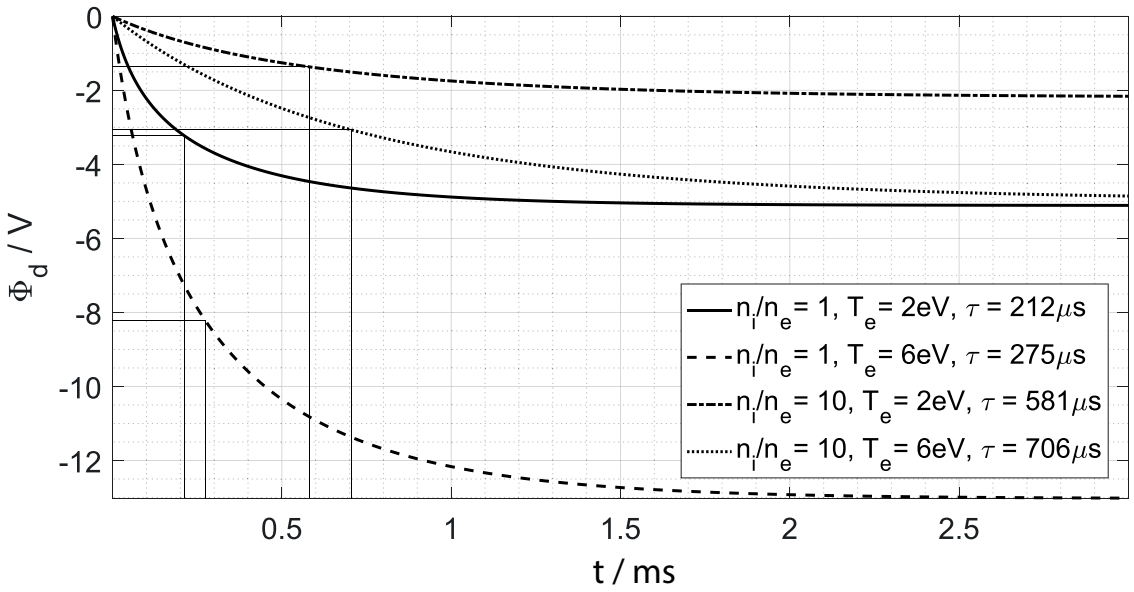

Figure 2.9: The charging time τ for a dust particle of 10 nm radius is in the order of several hundred microseconds. It increases with increasing T_e and decreases with lower n_e.

where, using equations 2.49 and 2.50

$$\begin{aligned} -\frac{1}{R_\mathrm{s}(\Phi_\mathrm{d})} &= \left.\frac{\mathrm{d}I_\mathrm{i}}{\mathrm{d}\Phi}\right|_{\Phi_\mathrm{d}} + \left.\frac{\mathrm{d}I_\mathrm{e}}{\mathrm{d}\Phi}\right|_{\Phi_\mathrm{d}} \\ &= -\frac{e^2\pi n_\mathrm{i} r_\mathrm{d}^2}{k_\mathrm{B}T_\mathrm{i}} \cdot \left(\frac{k_\mathrm{B}T_\mathrm{i}}{2\pi m_\mathrm{i}}\right)^{1/2} + \frac{e^2\pi n_\mathrm{e} r_\mathrm{d}^2}{k_\mathrm{B}T_\mathrm{e}} \cdot \left(\frac{k_\mathrm{B}T_\mathrm{e}}{2\pi m_\mathrm{e}}\right)^{1/2} \exp\left(-\frac{e\Phi_\mathrm{d}}{k_\mathrm{B}T_\mathrm{e}}\right) \propto r_\mathrm{d}^2 \end{aligned} \tag{2.59}$$

stands for the differential resistance $R_\mathrm{s}(\Phi_\mathrm{d})$, which is the inverse slope of I versus Φ around the potential Φ_d. We can see, that because $C \propto r_\mathrm{d}$ and $R_\mathrm{s} \propto r_\mathrm{d}^{-2}$ the charging time constant, defined like for a spheric capacitor $\tau = R_\mathrm{s}C \propto r_\mathrm{d}^{-1}$, becomes bigger for small particles. In order to investigate the charging time in more detail one can integrate the dust potential numerically by using the current in equation 2.58:

$$\Delta\Phi(\Phi_\mathrm{d}) = \frac{1}{C}\left(I_\mathrm{i}(\Phi_\mathrm{d}) + I_\mathrm{e}(\Phi_\mathrm{d})\right) \cdot \Delta t. \tag{2.60}$$

Figure 2.9 shows the result of it for $r_\mathrm{d} = 10\,\mathrm{nm}$, $n_\mathrm{i} = 4 \cdot 10^{15}\,\mathrm{m}^{-3}$, but different n_e and for different electron temperatures. The charging time τ increases with increasing electron temperature, because a higher floating potential needs to be reached. It also increases with increasing ratio $n_\mathrm{i}/n_\mathrm{e}$ due to electron rarefaction and consequently lower electron current. As already mentioned, the charging time is inversely proportional to the dust radius. So for a 1 nm radius particle the charging or discharging takes some milliseconds. If the plasma undergoes a sudden change, the nano-particles may take up or release electrons after the sudden change and by doing so they can influence a dynamic response of the plasma.
One of the first to describe the effect of electron depletion by high dust densities were Havnes

et al. [121]. They introduced the plasma paramter P, which divides a dusty plasma into two categories, $P > 1$, where the charge and dust potential is significantly diminished, and $P \ll 1$, where the particles are charged like a single dust grain and the plasma remains unaffected. The Havnes value is given by [122]

$$P = 695 T_{eV} r_{\mathrm{d}\mu m} \cdot \frac{n_{\mathrm{d}}}{n_{\mathrm{e}}} \tag{2.61}$$

with the electron temperature T_{eV} in eV and the dust radius $r_{\mathrm{d}\mu m}$ in μm. For $T_{eV} = 6$ and $r_{\mathrm{d}} = 10\,\mathrm{nm}$ like in figure 2.9 a ratio of $n_{\mathrm{d}}/n_{\mathrm{e}} = 0.024$ corresponds to the case of $P = 1$. This means, that at an electron density of $n_{\mathrm{e}} = 4 \cdot 10^{15}\,\mathrm{m}^{-3}$ a dust density of $n_{\mathrm{d}} = 9.5 \cdot 10^{13}\,\mathrm{m}^{-3}$ marks the threshold for an undisturbed plasma. For bigger radii an even smaller dust density is required to cause significant electron depletion in the plasma.
The above described dust charging model does not account for all effects, moreover it was assumed, that the electron energy is distributed maxwellian, which may not be correct, especially in RF-plasmas, as calculated by Denisenko *et al.* [123]. However, for the sake of simplicity of the calculations it shall be applied here, and, in fact, the orbital motion limited theory provides fast and valuable answers.
If the reader is interested, of course, many more models exist to describe the dust charging with more advanced assumptions. The above given theory fails, when the sheath around each particle is not collision-less, more than one ion species is involved or other charging mechanisms like secondary emission have to be considered. Solutions are given in [33, 120, 124], for example. One probably important effect the standard OML model does not account for is the heating of very small dust particles. Due to the energy flux in form of energetic molecules and atoms and exothermal reactions at the particle surface in combination with the little mass of the nanometre sized dust, the nanoparticles can heat up significantly. This may enhance the desorption I_{de} of electrons, that is a function of the adsorption energy E_{s} of electrons at their surface and the particle temperature T_{d}:

$$I_{\mathrm{de}} = Q_{\mathrm{d}} \frac{k_{\mathrm{B}} T_{\mathrm{d}}}{h} \exp\left(-\frac{E_{\mathrm{s}}}{k_{\mathrm{B}} T_{\mathrm{d}}}\right), \tag{2.62}$$

where h is the Planck constant.
Bronold *et al.* [33, 124], therefore, proposed to add the desorption current I_{de} to the current balance in 2.51 onto the particles:

$$0 = I_{\mathrm{i}}(\Phi_{\mathrm{fl}}) + I_{\mathrm{de}}(\Phi_{\mathrm{fl}}) + I_{\mathrm{e}}(\Phi_{\mathrm{fl}}), \tag{2.63}$$

which then leads to a reduction of the particle charge. Hinz proposed in his thesis [87], that this effect may be amplified by the Schottky effect, that occurs at high field strengths at the particle surface and reduces the adsorption energy E_{s} of the electrons even further.

2.3.2 Charge fluctuations on small particles

The above introduced orbital motion limited theory for the charging of spheres in a plasma is not only disturbed by secondary electron emission but also by the finite elementary charge

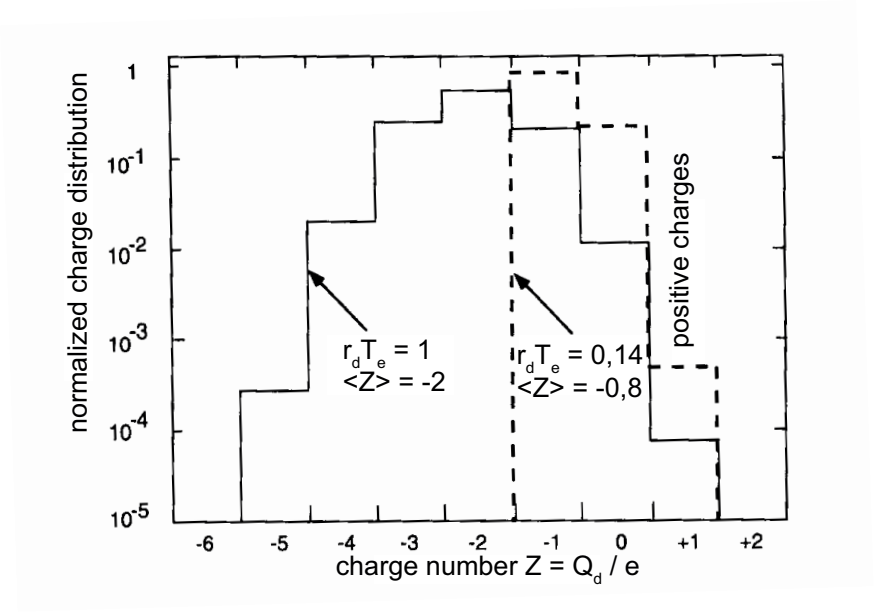

Figure 2.10: On small particles charge fluctuations in the order of their total charge can occur, generating even positively charged dust. Here r_d and T_e are taken in units of nm and eV, respectively. After [125];

of the impinging electrons and ions. As shown in equation 2.57 a very small dust particle carries only a very few elementary charges on average. Because it is on floating potential the ion and electron currents cancel each other out on average, but at a short time scale the exact equilibrium may not be given. This leads to charge fluctuations as demonstrated by Cui and Goree [125] for example. The amplitude of the charge fluctuations ΔQ around the equilibrium charge $\langle Q \rangle = \langle Z \rangle e$ can be estimated to be

$$\frac{\Delta Q}{\langle Q \rangle} = 0.5 \left| \langle Z \rangle \right|^{-1/2} . \tag{2.64}$$

On very small particles, that carry only a few elementary charges, this can even lead to positive charges.
Taking a particle diameter of 0.76 nm as an example the particle charge distribution as calculated by Cui and Goree is shown in figure 2.10 for two different products of the radius with the electron temperature $r_\mathrm{d}/[\mathrm{nm}] \cdot T_\mathrm{e}/[\mathrm{eV}]$. Resuming the graph, particles in a 2.6 eV hot plasma carry an average charge of $\langle Z \rangle = -2$ but round about 1 % of them is not charged at all and 0.01 % are even charged positively. The dashed line accounts for even smaller grains and illustrates, that positive and negative charges can be almost evenly distributed among tiny grains.
Because positive and negative particles are attracted once they are in the vicinity of one Debye sphere to each other, the charge fluctuations can play a crucial role in the beginning of the dust growth process as will be discussed in the following section 3.3. Particles of a few nanometres in size or more, on the contrary, always experience repulsive forces between

each other.

2.3.3 Forces on dust particles

Particles inside a plasma charge up as described in section 2.3.1. Thus not only the gravitational force is acting on them but also an electrical force depending on the background potential. Electric forces repel the particles from each other leading to extensive three dimensional dust clouds. If other forces become dominant, however, the cloud may shrink down to a mono layer in front of the powered electrode for example. Therefore it is necessary to develop an understanding of the forces in order to predict the dust distribution inside a plasma vessel.

Electrical forces In a general form any charged and floating object of charge Q is accelerated by the force

$$\vec{F}_{\mathrm{el}} = -Q\nabla\Phi(x,y,z) \tag{2.65}$$

in a given potential profile $\Phi(x,y,z)$. The potential profile usually exhibits a very strong decrease in the sheath region but is relatively flat elsewhere, as already introduced in figure 2.6. So the electric force resulting from the background potential is most dominant in the sheath, where the potential is only dependent on the distance from the electrode or wall, chosen to be in z-direction here. The electrical field $E(z)$ decreases with increasing distance to the boundary and for a negatively charged particle the resulting force [126]

$$\vec{F}_{\mathrm{sh}} = Q_{\mathrm{d}}\left(1 + \frac{(r_{\mathrm{d}}/\lambda_{\mathrm{D}})^2}{3(1+r_{\mathrm{d}}/\lambda_{\mathrm{D}})}\right)\vec{E}(z). \tag{2.66}$$

acts inwards into the plasma. The factor in the brackets pays attention to the non-uniform polarization of the plasma bulk as response to the emerged particle. For very small particles it is essentially equal to one, but for bigger particles it enlarges the electric field force. It is the main force, that confines the particles in the plasma at any place and it is especially strong in front of the powered electrode, where there is the largest potential drop. This confining force increases with particle radius, because $F_{\mathrm{sh}} \propto Q_{\mathrm{d}} \propto r_{\mathrm{d}}$.
The potential shape can be strongly influenced by the presence of inhomogeneously distributed negative particles. Another way to account for the force produced by a modified potential is to treat the particle interaction directly. Each particle at a distance $d > r_{\mathrm{d}}$, can be treated as a source of the Yukawa potential or Debye-Hückel potential, see equation 2.6. It produces a force acting onto a neighbouring particle of the same charge Q_{d} in the distance $d > 2r_{\mathrm{d}}$ along the direction of their connecting axis $\vec{e}_{\mathrm{d}}$ of the shape [127]:

$$\vec{F}_{\mathrm{Yuk}} = -\frac{Q_{\mathrm{d}}^2}{4\pi\varepsilon_0 d}\left(\frac{1}{d}+\frac{1}{\lambda_{\mathrm{D}}}\right)\exp\left(-\frac{d}{\lambda_{\mathrm{D}}}\right)\cdot\vec{e}_{\mathrm{d}}. \tag{2.67}$$

The repulsive particle interaction counter acts against the confinement, when the dust particle amount reaches a critical value, where the cloud fills the entire plasma bulk and, thus, starts to push out the outer particles. The Yukawa force scales with the square of the dust

radius, because $Q_\mathrm{d}^2 \propto r_\mathrm{d}^2$.

Gravitational force Because the powered electrode is at the bottom in the here used set-up, gravitation pushes the dust onto it. It is calculated by the mass of the dust particle m_d and the standard gravity $g_0 \approx 9,81\,\mathrm{ms}^{-2}$:

$$\vec{F}_\mathrm{g} = -m_\mathrm{d} g \vec{e}_z. \tag{2.68}$$

For a known mass density ρ_d it can be rewritten to

$$\vec{F}_\mathrm{g} = -\frac{4}{3}\pi r_\mathrm{d}^3 \rho_\mathrm{d} g \vec{e}_z. \tag{2.69}$$

However, usually the chemical composition and especially the porosity is not well known, making it difficult to determine the particle mass and, thus, the gravitational force. For an overview over the density range of crystalline poly-acetylenes the reader may refer to [128], however the chemical composition of the produced nano-particles may differ.
The gravitational force scales with r_d^3. It is the reason, that micro particles align in a two dimensional layer or multi layer above the lower electrode, where it is compensated by the electrical force from the sheath [129]. For nano-particles it is very small and much less dominant. Therefore, they can levitate easily by the combination of the residual forces.

Thermophoresis Because the powered electrode is shielded by a ceramic in the used set-up and only connected to the wire delivering the rf-power, it cannot get rid of its heat by conduction. Convection occurs only at higher pressures, so the only cooling comes by radiation, which is relatively little. Moreover, the ion energy is greatly enhanced by the strong voltage drop over the electrode sheath. Therefore the powered electrode can heat up significantly compared to the surrounding.
The resulting temperature gradient ∇T_n in the neutral gas is directed towards the hot electrode. Considering gas kinetics, like done by Rothermel *et al.* [130] following Talbot *et al.* [131], a counter acting force F_th must push any particle away from the electrode:

$$\vec{F}_\mathrm{th} = -\beta \frac{k_\mathrm{B} r_\mathrm{d}^2}{\sigma_\mathrm{n}} \vec{\nabla} T_\mathrm{n}. \tag{2.70}$$

The dimensionless factor β is in the range between 2.66 and 5.66 [127] depending on the model. Furthermore, σ_n stands for the cross section of neutrals with neutrals, which is said to be $42\,\mathrm{Å}^2$ big [119]. An estimation of all the forces introduced is done in figure 2.14 in dependence of the dust radius. For the thermophoretic force it was assumed, that the electrode is 10 K hotter than its surrounding and the chamber height was averaged to be 30 cm, thus, resulting in a temperature gradient of 33.3 K/m. The value β was chosen to be 3.33, like done by Rothermel *et al.* for argon in the pressure range from 14 . . . 46 Pa. As can be seen, under the given conditions, the thermophoretic force dominates the gravitational force for particles smaller than 90 nm, resulting in easily levitating dust clouds or even pushing

particles to the top.
The thermophoretic force may be one reason besides soiling of the reactor, why experiments can be hardly reproducible. After having run an experiment for some hours, the powered electrode can have heated up significantly, especially under high powers.
It is not well understood, how big dust quantities may effect the thermophoretic force. It is expected to saturate far away from the heat source due to cooling effects closer situated particles. Therefore, particles close to the heat source may feel a stronger gradient than those in the shadow of the dust cloud. A detailed model for a silane containing plasma is given in [132].

Ion wind force During the stable plasma process charge carriers are constantly absorbed by its surrounding surfaces. Electrons are driven out of the discharge by their thermal velocity and ions are pushed out towards the lower wall potential. Consequently, in order to achieve an equilibrium state, the amount of ions lost to the wall, described by the rate R_{wall}, needs to be compensated by ionization processes R_{ion} in the plasma volume. Moreover, recombination processes, R_{rec}, in the volume also need to be compensated and in case of a dusty plasma with a high quantity of grains, the ions recombine with the electrons at their surface too, described by R_{dust}. Overall a balance between production and losses of ions must apply, given as

$$R_{\mathrm{ion}} = R_{\mathrm{wall}} + R_{\mathrm{rec}} + R_{\mathrm{dust}} \tag{2.71}$$

on the left hand side and right hand side, respectively. If the rate for wall losses is defined as the amount of ions crossing the sheath edge in front of the walls, ionization processes inside the sheath do not need to be considered, because those ions cannot reach the plasma volume.
All in all, the production of ions in the plasma and their losses to the walls cause a net ion current from the centre of the discharge outwards. Therefore ions don't move randomly by thermal motion but they experience a superimposed motion out of the discharge. The outward motion is a drift through the plasma, in which there are the nano-particles incorporated. As the velocity of the ions is bigger than that of the dust, the situation can be regarded as particles exposed to an ion stream of the velocity [90]

$$v_{\mathrm{s}}^2 = v_{\mathrm{d}}^2 + \frac{8k_{\mathrm{B}}T_{\mathrm{i}}}{\pi m_{\mathrm{i}}}, \tag{2.72}$$

which simply describes the average velocity of a shifted Maxwellian ion-distribution. It consists of the ion drift velocity v_{d} superimposed to the average thermal velocity. For small temperatures T_{i} the drift velocity becomes dominant and vice versa.
The fast ions can either be collected by the particle or only scattered, if they pass close by but do not hit its surface. Ions coming in on a cross section of $\sigma_{\mathrm{c}} = \pi {b_{\mathrm{c}}}^2$ will hit the surface, those further outward will change momentum during the passage through the dust particle field, see figure 2.11. In both cases momentum is transferred to the particle, so the overall ion wind force can be divided into those two components

$$\vec{F_{\mathrm{i}}} = \vec{F_{\mathrm{c}}} + \vec{F_{\mathrm{o}}} \tag{2.73}$$

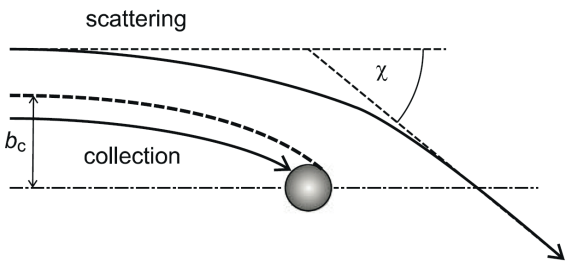

Figure 2.11: The ion wind force is divided into two components: momentum transfer by scattering of ions in the particle field and by collection of ions on its surface. From [90];

respectively. Assuming mono-energetic ions, upon collection they transfer their entire momentum $m_i v$ to the particle and the rate at which this happens can be determined by the ion flux density $n_i v$ times the effective collection cross section $\pi {b_c}^2$, so the overall collection force results in:

$$F_c = n_i m_i v^2 \pi {b_c}^2. \tag{2.74}$$

Because the dust collection radius b_c is effectively enlarged by the attractive force between ions and negatively charged dust particle, it is given as [90]

$$b_c = r_d \sqrt{1 - \frac{2e\Phi_d}{m_i v^2}}. \tag{2.75}$$

Additionally using the average velocity v_s, the average collection force can finally be rewritten as [133]:

$$\langle F_c \rangle = n_i m_i v_s v_d \pi {r_d}^2 \left(1 - \frac{2e\Phi_d}{m_i {v_s}^2}\right). \tag{2.76}$$

It increases proportionally to ${r_d}^2$, and therefore, big particles tend to be pushed out of the discharge, so that a *void* is formed in its center [134, 135], whereas new and very small particles can form inside the void and stay there for a while. The presence of a void has also been found in earlier works on the same reactor as used in this study [136].
The other part of the ion wind force comes from ions deflected by the angle χ as given in figure 2.11, so that they transfer the momentum

$$\Delta p = p\,(1 - \cos\chi) \tag{2.77}$$

to the dust particle.
In order to move forward in the orbital motion theory some assumptions have to be checked: First of all the shielding length λ_s needs to be thought over. For micro-meter sized particles extensive research on their charging and the ion motion in their close vicinity has been done, a good review can be found in [137]. It is shown, that the dust potential is not strictly of Debye-Hückel kind for high ion stream velocities due to wake effects. Here, however, we want to concentrate on dust immersed in the plasma bulk, where the ion drift velocity is relatively small, more precisely, smaller than the thermal ion velocity. This is valid in

the central region, but can be violated in the outer regions of the plasma bulk, where ions are more and more accelerated towards the sheath edge, where they finally reach Bohm velocity. However, here we only want to get a feeling of the order of magnitude in order to compare the ion drag to other forces. Therefore, we assume, that $v_\mathrm{d} \ll v_\mathrm{th,i}$ and, hence, that the shielding can be expressed by the linearized Debye length $\lambda_\mathrm{s} = \lambda_\mathrm{D}$. In experimental investigations from Hebner [138], chlorine metastable and ion drift velocities of 600 to 800 m/s were reported. In [139] the influence of the gas composition, in particular of heavy ions in a light background gas, was investigated and it was demonstrated, that the ion drift velocity can easily overcome the thermal velocity. However, for pure argon in a parallel plate RF discharge, the ion drift velocity was found to be relatively small at 160 m/s, which is round about half of the thermal speed. So the above taken assumption can be doubted, here however, we want to concentrate on a qualitative picture to achieve a simple understanding of the particle forces.
Secondly, Daugherty *et al.* conclude in their work [126] small size of nano-particles validates the assumption, that $r_\mathrm{d} \ll \lambda_\mathrm{s}$, in order for the Debye-Hückel potential to apply. Here the dust radius varies between a few nano-metres and a few hundreds of nano-metres, whereas the shielding length, assumed to be the linearized Debye length, was calculated in 2.3.1 to be $\lambda_\mathrm{s} \approx 20\mu\mathrm{m}$.
Having those two points checked, the standard point-charge treatment with its roots in Chandrasekhar's calculations [140] can be used, where only scattering angles $\chi = 0 \ldots 90°$ are considered. The according impact parameter for a stationary dust particle is then derived to be:

$$b_{90} = \frac{eQ_\mathrm{d}}{4\pi\varepsilon_0 m_\mathrm{r} {v_\mathrm{s}}^2} \tag{2.78}$$

with $m_\mathrm{r} = m_\mathrm{i} m_\mathrm{d}/(m_\mathrm{i} + m_\mathrm{d})$, the reduced mass. The resulting ion scattering force is [133]

$$F_\mathrm{s} = n_\mathrm{i} v_\mathrm{s} m_\mathrm{i} v_\mathrm{d} 4\pi {b_{90}}^2 \Gamma, \tag{2.79}$$

making use of the Coulomb logarithm

$$\Gamma = \frac{1}{2} \ln\left(\frac{{\lambda_\mathrm{D}}^2 + {b_{90}}^2}{{b_\mathrm{c}}^2 + {b_{90}}^2}\right). \tag{2.80}$$

Comparing the contribution to the ion wind force, the scattering force dominates for very small particles. The bigger the particle becomes, however, the more ions will collide with its surface and contribute to the collection force. Finally, when the collection radius reaches $b_\mathrm{c} \approx \lambda_\mathrm{D}$, the above given theory isn't applicable any longer, but the scattering force decreases to an irrelevant level anyway. The overall ion wind force is depicted in figure 2.14, where this transition can clearly be seen.
Taking $r_\mathrm{d} = 10\,\mathrm{nm}$ as example again, the ion wind force dependence on the ion drift velocity v_d has been calculated. When the drift velocity becomes high, the stiffness of the ion trajectories starts to reduce the transferred momentum due to less deflection in the particle field. Therefore, the overall ion wind force exhibits a local minimum for high ion speeds, which in this case can be found at round about $3v_\mathrm{B}$. Hence, for nano-particles smaller than

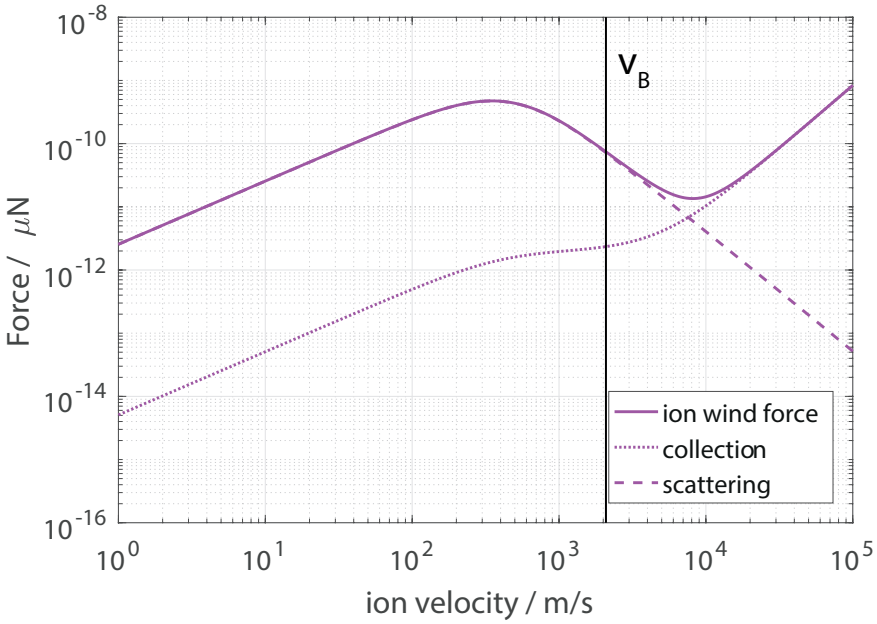

Figure 2.12: The ion wind force, here calculated for $r_\mathrm{d} = 10\,\mathrm{nm}$, exhibits a local minimum at high ion velocities due to stiffer ion trajectories at high speed, and thus, a decrease of the contribution by deflecting ions. In the bulk plasma, however, it is mainly the scattering force, that contributes, because the collection force becomes dominant only for $v_\mathrm{d} \gg v_\mathrm{B}$.

10 nm, the collisional term becomes only relevant in the sheath but not in the bulk. As the local maximum of the ion wind force lies at $300 \ldots 400\,\mathrm{m/s}$, particles close to the sheath edge, where ions have already picked up a considerable amount of speed, should be exposed to smaller drag forces than a little bit further in the bulk.
More advanced calculations have been done by Khrapak *et al.* [141] and Hutchinson [137] for example. A detailed model on the spatial nano-particle distribution in silane plasmas due to the acting forces was developed by De Bleecker *et al.* [142].

Neutral drag force In contrary to the above mentioned forces, the frictional neutral drag force only occurs in a dynamic system, where the dust is moving through the background gas or vice versa. The resulting friction has to be divided into two regimes, distinguishable by the Knudsen number $\mathrm{Kn} = \lambda_\mathrm{mfp}/r_\mathrm{d}$, where λ_mfp is the molecule mean free path in the neutral gas. For $\mathrm{Kn} \gg 1$ the gas flow has to be described by gas-kinetic theory, because the molecules move almost freely in space. It is the so called free-molecule region. For $\mathrm{Kn} \ll 1$, in the so called continuum regime, the flow is laminar and the problem has to be treated like a fluid as firstly done in 1851 by Stokes [143]:

$$\vec{F}_0 = -6\pi\mu r_\mathrm{d}\vec{v}_\mathrm{rel}. \tag{2.81}$$

Important is the relative velocity between the dust particles and the neutral background gas $\vec{v}_\mathrm{rel} = \vec{v}_\mathrm{d} - \vec{v}_\mathrm{n}$. The equation makes use of the viscosity μ, that later was related to the

Figure 2.13: Often carbonaceous nano-particles grown in discharges have a cauliflower-like surface indicating a porous structure. From [29];

Brownian diffusion coefficient D

$$D = \frac{k_\mathrm{B} T_\mathrm{n}}{6\pi\mu r_\mathrm{d}} \tag{2.82}$$

by Einstein [144]. Translating the mean free path through gas-kinetic theory into

$$\lambda_\mathrm{mfp} = \frac{k_\mathrm{B} T_\mathrm{n}}{\sqrt{2}\pi d^2 p} \tag{2.83}$$

with $d = 0.106\,\mathrm{nm}$ for the covalent radius of argon and a gas pressure of $6\,\mathrm{Pa}$ the Knudsen number can be calculated to $\mathrm{Kn} = 1.4{\cdot}10^5$ for nano-particles of size $r_\mathrm{d} = 100\,\mathrm{nm}$. So the dust motion in the here described case clearly has to be described in the free-molecule regime. This was first completely done by Epstein [145] in 1924, who used the famous oil-drop experiments from Millikan [146] to verify his results. The momentum transfer between the dust grain and neutral gas is dependent on the kind of reflection on its surface. If a neutral particle undergoes specular reflection, it can transfer up to two times its initial momentum, whereas in diffuse reflection the lower limit is only one time the initial momentum. Therefore, in his model Epstein introduced the accommodation coefficient δ, which is

$$\delta = \begin{cases} 1 & : \text{specular reflection} \\ 1.44 & : \text{perfectly diffuse reflection} \end{cases} \tag{2.84}$$

for spherical particles. His model can be adapted in plasmas and, thus, the neutral drag force is given as

$$\vec{F}_n = -\delta\frac{4}{3}\pi r_\mathrm{d}^2 m_\mathrm{n} n_\mathrm{n} \bar{v}_\mathrm{th,n} \vec{v}_\mathrm{rel}, \tag{2.85}$$

where $\vec{v}_{\mathrm{rel}}$ is the same as in equation 2.81 and the thermal gas velocity can be expressed as $\bar{v}^2_{\mathrm{th,n}} = (8k_{\mathrm{B}}T_{\mathrm{n}})/(\pi m_{\mathrm{n}})$. Unlike as in the fluid system, where the relation is linear, the neutral drag force increases with r_{d}^2. The reflection of the neutral gas at the surface and consequently the accommodation coefficient must differ for a smooth or a rough surface. Because nano-particles grown in acetylene containing plasmas are known to have a cauliflower-like morphology, see figure 2.13, a coefficient of $\delta = 1.44$ seems to be suitable. However, very small particles often seem to exhibit smooth surfaces, and thus, the coefficient may differ slightly.
In order to get a feeling for the order of magnitude of this force one can calculate the gas flow velocity through 3/8-inch swagelok tubing system at 1 sccm flow rate. Making use of the ideal gas law the gas volume for experimental conditions corresponding to 1sccm at standard conditions is:

$$V_{6\mathrm{Pa}} = \frac{1013\,\mathrm{hPa}}{6\,\mathrm{Pa}} \cdot \frac{300\,\mathrm{K}}{273\,\mathrm{K}} \cdot 1\,\mathrm{cm}^3 = 1.86 \cdot 10^4\,\mathrm{cm}^3, \tag{2.86}$$

so that the minute-wise processed gas column in the tube has a height of 838 m. Consequently the gas flow velocity must be 838/60 m/s. Assuming, that the gas velocity at the exit of the tube, which is in the reactor, is the same as inside the tube, and that the dust particles are at rest, the relative velocity is found to be $v_{\mathrm{rel}} \approx 13\,\mathrm{m/s}$. The resulting force is plotted in figure 2.14. As can be seen there, the neutral drag force can play an important role on the shape of the cloud as it is one of the strongest forces in case of such high relative velocities.
In real experiments the coupling between the discharge parameters and the dust modifies the plasma at the dust position and vice versa. Therefore, a precise calculation of the forces requires a detailed model, that accounts for the effects of high density particle clouds on the plasma, like for example in [147]. Here, a self-consistent model beginning with the coagulation of particles, then describing the charging processes and finally calculating the transport mechanisms by evaluating the forces has been developed.

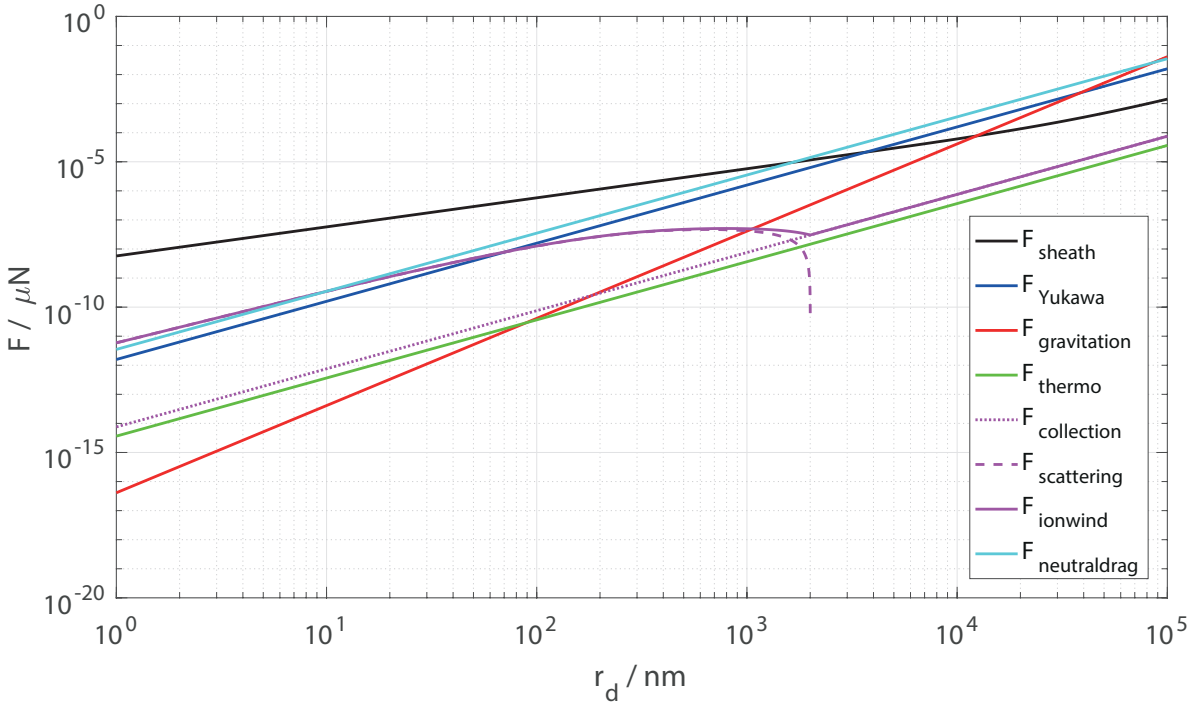

Figure 2.14: An estimation of the forces acting on nano-particles in dependence of their size r_d; Obviously very small particles experience the best ratio of confinement by the electric force from the sheath potential F_sheath to the other forces. Especially the particle-particle interaction F_Yukawa and the ion wind force F_ionwind always act outward of the discharge against confinement. The neutral drag force $F_\mathrm{neutraldrag}$ exerted by a moving background gas, here estimated for a gas velocity of $v_\mathrm{rel} = 13\,\mathrm{m/s}$ for resting particles, acts in direction of the gas flow and, therefore, depends strongly on the gas injection and pumping method. The thermophoretic force F_thermo acts only upward (here estimated for powered electrode temperature elevated by 10 K) and the gravitational force always acts downward (estimated for mass density of particles of $1000\,\mathrm{kg\,m^{-3}}$). Interestingly, the ion wind force does not change much for particles in the size range from 100 to 1000 nm, because that is the transition region, where the scattering force becomes less relevant and the collection force starts to dominate.

Chapter 3

Reactive plasmas

Many different techniques have been developed to deploy thin layers to any given kind of substrate. Among the working horses in industry, which are the physical and chemical vapour deposition (PVD and CVD respectively), also plasma based processes have become increasingly important due to their unique and qualitative deposits. Here again a huge variety of different principles and set-ups can be found. This chapter is only dedicated to the plasma enhanced chemical vapour deposition (PECVD), because it is the kind of reactive plasma used during this thesis.
The PECVD set-up is very similar to the classic CVD. The main difference is, that instead of using heat, the chemicals are activated and transformed by the means of hot electrons from a plasma source, whereas in a CVD this is done by a simple heat source. Therefore, even if in some processes the substrate needs to be heated to elevated temperatures, the process temperature can be lower in PECVD reactors. A good example is the deposition of SiO_2 layers. In a classic approach 650 to 850° C are necessary to convert the precursor into the desired product. In a PECVD reaction, however, it is sufficient to heat the substrate to only 300 to 350° C [102]. This obviously has the advantage, that these thin layers can be applied to more sensitive substrate materials, like SiO_x as a non-permeable gas barrier to the inside of PET bottles [148]. Moreover, lower temperatures are interesting for economical and environmental reasons and, not less important, the coatings often exhibit a higher quality, e.g. better uniformity and better adhesion [149].
Another example for the use of the PECVD is the deposition of diamond like carbon, DLC. It is a very tough layer, used for example on machine tools or in car industry in order to improve wear resistance, tribological properties and hardness. The mostly black thin coatings can be produced by a mixture of gases, containing a carbon rich precursor, added to a halogen plasma [150]. The necessary, diamond specific formation of sp^3-bonds is initiated by an ion bombardment with energies greater 100 eV [101].
Because in most cases the electrons are assumed to be Maxwell-distributed, a small but significant amount of them is highly energetic in the range of several electron-Volts. During elastic and non-elastic collisions they can transfer energy to the participating molecule. This leads not only to indirect heating of the gas but also to excitation, ionization and dissociation. This in turn initiates a huge variety of chemical reactions in the gas phase and at surfaces,

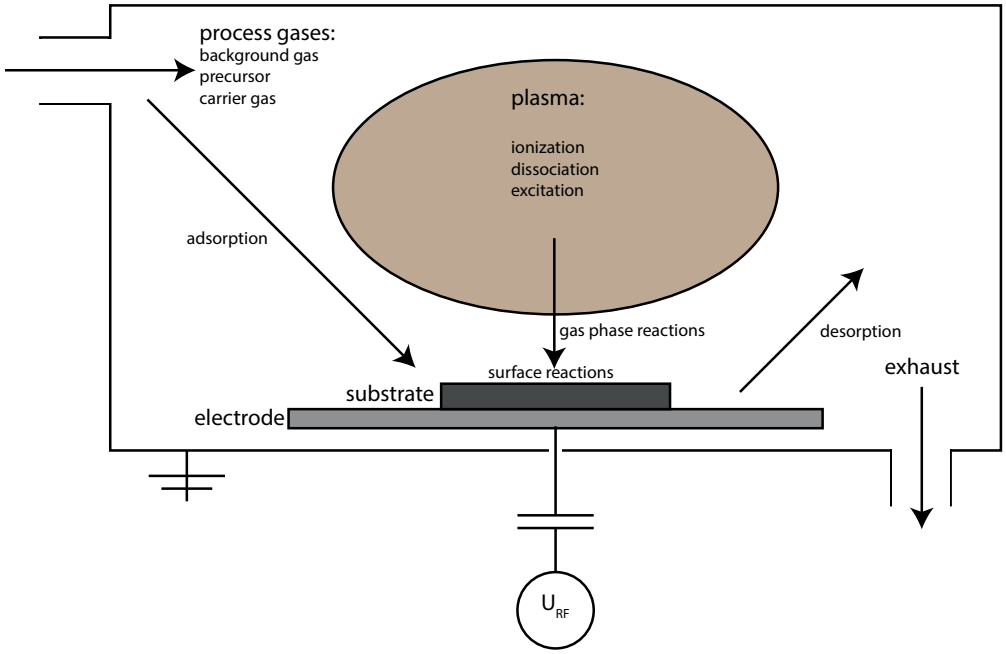

Figure 3.1: The principle of a PECVD process in a RF-reactor; Prior to surface reactions the reactive species need to be formed by the means of plasma reactions and then have to be adsorbed on the substrate. Once on the surface they can desorb again or participate in the growth of thin films. In this kind of set-up vacuum pumps are necessary, which can deal with reactive exhaust gas. After [151];

which challenges researchers to identify the main reactions in a process and to control the chemical outcome of it. A good introduction into this kind of plasmas can be found in [15] and [101].
In this chapter the zoo of different species for the so far known reactions in an argon-acetylene discharge shall be discussed. Furthermore, the reader will be introduced into the growth of nano-particles by the above given plasma, which can be divided into three consecutive steps: nucleation, coagulation and accretion.

3.1 PECVD

Basis of any PECVD process is an essential admixture of a chemically reactive gas to the chemically inert background gas. Whereas the reactive component does most of the chemistry, the background gas is mainly responsible for the physical properties of the discharge. This way, at least in parts, the plasma properties can be decoupled from the chemical reactions, which gives more freedom in the set of adjustable parameters. A very common background gas is argon thanks to its relative low costs and also relatively low ionization energy with 15.76 eV compared to 24.59 and 21.56 eV for helium and neon respectively.
The reactive elements can be brought into the chamber directly as a gas, but sometimes it

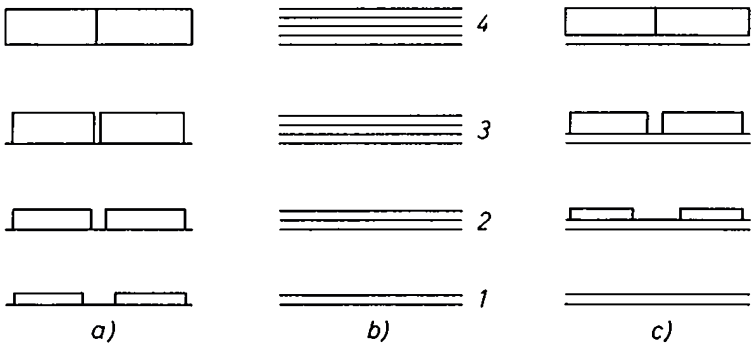

Figure 3.2: For crystalline and polycrystalline films three different growth mechanisms can be identified: a) the Volmer-Weber-, b) the Frank-van-der-Merwe- and c) the Stranski-Krastanov-mechanism. Graphic taken from [152];

is necessary to first evaporate or even sublimate the chemical. Once in the gas phase, those molecules are called *precursor*, because they are the initial building blocks for any reaction in the gas phase or on surfaces. If the evaporation process needs to be enhanced without further heating, the partial vapour pressure can be lowered by transporting the vapour away from the solid or liquid precursor. This is done by a carrier gas, which typically is the same as the background gas. In this work the precursor C_2H_2 is already available in the gas phase, which simplifies its flow controlling. In some cases it can be useful to introduce a third gas like hydrogen in order to steer the chemistry into a certain direction.
The necessary chemical steps for thin film formation can happen in the gas phase or on the surface. It depends on the discharge conditions and the kind of precursor. For thin films with good adhesion, the chemicals need to bond to the surface, which means, that the reactants, which may appear as radicals, ions or neutral molecules, need to only be formed in the gas phase but then to diffuse onto the surface, where they adsorb. On the surface the reactants can further diffuse until they finally find vacant sites to bond covalently to. A principal sketch of a PECVD process with its reactions is shown in figure 3.1.
On the way towards a covalent bond different loss processes counteract against thin film formation. Firstly, during the diffusion towards the surface, the reactants can further dissociate or in a collision combine to a bigger molecule. In the extreme case the combination occurs mainly in the volume, leading to dust formation. They also may charge up negatively, and thus, get trapped in the discharge or simply be pumped out through the exhaust pipes. Secondly, once adsorbed on the surface, the molecules may also desorb again, upon which they can come back again, decompose or also be pumped out. Etching of the surface, actually used for semiconductor industry, can occur chemically or for plasma facing surfaces also physically by energetic ion bombardment. If the time for diffusion on the surface is too short, because the flow of precursor is very high, not all vacant sites will be saturated and the films tend to be porous or to grow in a columnar structure.
In crystalline films the system tends to minimize the surface energy of the substrate, so instead of looking for vacant sites, the ad-atoms tend to attach to atomic steps, which does not further increase the surface area. Here three growth modes, see figure 3.2 are known,

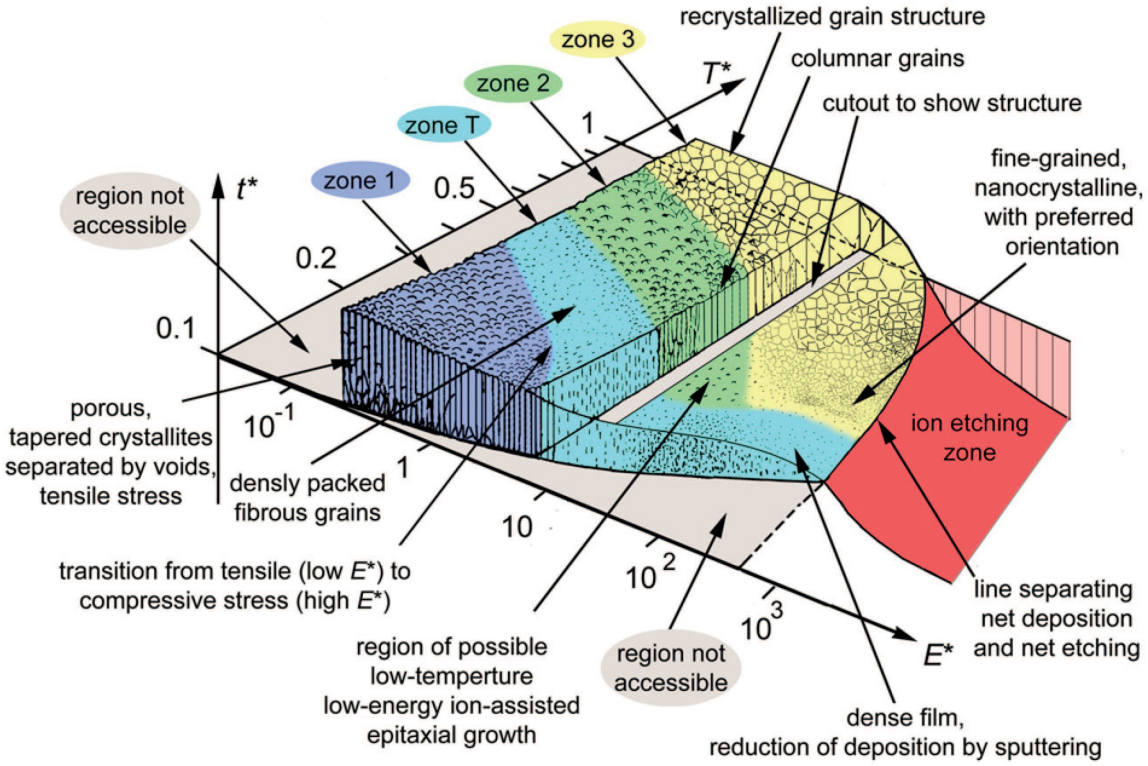

Figure 3.3: The structure zone diagram resumes the influence of effective energy of the impinging species and substrate temperature on the structure of plasma based deposited thin films. Figure from [153]; Here E^*, T^* and t^* stand for the effective energy, normalized substrate temperature and deposition thickness, respectively.

the Volmer-Weber mode, which is a layer by layer growth, the Frank-van der Merwe mode, which desribes the incomplete coverage of the substrate material by formation of clusters on the surface and the Stranski-Krastanov mode, which is an intermediate [152].
Of particular interest for plasma based deposition techniques is the influence of the process parameters on the microscopic structure and quality of the deposited films. It is common, especially for sputter deposition processes, to identify two main factors: the substrate temperature and the energy of impinging ions and atoms. For the illustration of those two parameters Thornton developed the famous structure zone diagram [154] by describing the energy of incoming particles with the process pressure. This has been modified by Anders [153], who rather uses an effective energy E^*, also accounting for energetic ions. In the resulting diagram, see figure 3.3, the deposited film varies in thickness t^* mainly due to the energy flux.
PECVD reactors can be realized in different set-ups. Ranging from DC plasma jets [155] and electron cyclotron resonance ion sources [156] to RF discharges, many industrial processes for different films exist, each with a unique set of parameters. Consequently each set-up and chemical process require other dissociation, recombination, reaction and diffusion rates. The set-up used for this work is presented in chapter 4.

3.1.1 Film growth kinetics

Often for economical reasons the growth rate is one of the most important properties of a process. For comprehensive purposes, the growth kinetics shall be introduced here for the most simple case: species A becomes adsorbed with rate K_a on a surface S, from where it can desorb at rate K_d or form a permanent bond A-S with the surface at the reaction rate K_r. The prior synthesis of the reactant species A by means of dissociation at rate constant K_diss is regarded to occur only in the discharge centre and loss processes, like pumping or recombination, shall not be discussed here.
For an extensive overview over surface growth mechanisms and models the reader may refer to [15, 157], that were mainly used to derive the following paragraphs. For a complete understanding the specific chemical steps and each of the rates need to be considered. This has been intensively studied for example for the growth of silicon from silane during the 80's and 90's. A brief overview over that topic can be found in [158].
To begin with, the species A first needs to reach the surface. Because the neutral density is several orders of magnitude higher than the ion density in the plasma, the neutrals are mainly contributing to most of the film growth. Therefore, the transport of A towards the surface needs to be based on diffusion.

Gas kinetics Considering, that most of the neutrals are represented by the background gas B, the species A must diffuse through it, so that the process can be described by the diffusion constant via

$$D_{AB} = \frac{k_\mathrm{B}T}{M_\mathrm{R}\nu_{AB}}. \tag{3.1}$$

Here the relative mass $M_\mathrm{R} = m_A m_B/(m_A{+}m_B)$ and the collision frequency $\nu_{AB} = n_B\sigma_{AB}\bar{v}_{AB}$ with the mean relative speed $\bar{v}_{AB} = (8k_\mathrm{B}T/\pi M_\mathrm{R})^{1/2}$ have to be used. Doing so

$$D_{AB} = \frac{\pi}{8}\frac{1}{n_B\sigma_{AB}}\bar{v}_{AB} = \frac{\pi}{8}\lambda_{AB}\bar{v}_{AB} \tag{3.2}$$

follows, where σ_{AB} stands for the collision cross section, which typically is in the range of 2-6·$10^{-15}\,\mathrm{cm}^2$, and where $\lambda_{AB} = 1/n_B\sigma_{AB}$ represents the respective mean free path.
When applying $n_B = p_B/k_\mathrm{B}T$ by the use of the ideal gas law, and further assuming the partial pressure of the reactant negligible $p_A \ll p_B$, so that $p_B \approx p_\mathrm{tot}$, the following dependence can be established:

$$D_{AB} \propto \frac{T^{3/2}}{p_\mathrm{tot}}. \tag{3.3}$$

So, increasing the pressure slows the diffusion down, whereas increasing the temperature leads to a better transport of reactants from the center to the surfaces.
Considering the case of a one dimensional reactor with dimension l, so that at $x = \pm l/2$ are the surfaces, Fick's second law can be applied:

$$\frac{\partial n}{\partial t} = D\frac{\partial^2 n}{\partial x^2}. \tag{3.4}$$

Knowing, that in a steady state, the diffusion to the walls must be balanced by the production of species A through the dissociation at the rate R_{diss} of the precursor P of density n_{P} in the chamber volume, where $n_{\mathrm{e}}(0) = n_{\mathrm{e0}}$

$$R_{\mathrm{diss}} = K_{\mathrm{diss}} n_{\mathrm{P}} n_{\mathrm{e0}}, \tag{3.5}$$

one can find

$$\frac{\partial n_A}{\partial t} = D_{AB} \frac{\partial^2 n_A}{\partial x^2} + R_{\mathrm{diss}} = 0. \tag{3.6}$$

Thus, equation 3.6 can be rewritten to

$$- D_{AB} \frac{\partial^2 n_A}{\partial x^2} = K_{\mathrm{diss}} n_{\mathrm{P}} n_{\mathrm{e0}} \tag{3.7}$$

by the help of equation 3.5. Considering $\Gamma_A(0) = -D_{AB} \partial n_A / \partial x|_0 = 0$, it has the solution

$$n_A(x) = \frac{R_{\mathrm{diss}} l^2}{8 D_{AB}} \left(1 - \frac{4x^2}{l^2} \right) + n_{A\mathrm{S}} \tag{3.8}$$

for the density profile of the reactant, with $n_{A\mathrm{S}}$ being its density at the surface. Following Fick's first law and using an expression derived by Chantry [159] the flux of reactants close to the surface must then be

$$\Gamma_A(l/2) = -D_{AB} \left. \frac{\partial n_A}{\partial x} \right|_{l/2} = R_{diss} \frac{l}{2} = \frac{\gamma}{2(2-\gamma)} n_{A\mathrm{S}} \bar{v}_{AB}, \tag{3.9}$$

where the surface loss probability γ was used instead of the reflection coefficient $R = 1 - \gamma$ like in [159]. It varies from 0 to 1 for an absorbing surface but becomes negative in case of a source of reactants. Making use of the ideal gas law again and inserting the mean relative speed shows the pressure and temperature dependence of the reactant flux close to the surface:

$$\Gamma_A(l/2) \propto \frac{p_{A\mathrm{S}}}{T^{1/2}}. \tag{3.10}$$

Solving 3.9 for $n_{A\mathrm{S}}$ yields the reactant concentration at the surface

$$n_{A\mathrm{S}} = \frac{2(2-\gamma)}{\gamma} \frac{R_{\mathrm{diss}}}{\bar{v}_{AB}} \frac{l}{2} = \frac{2(2-\gamma)}{\gamma} \frac{K_{\mathrm{diss}} n_{\mathrm{P}} n_{\mathrm{e0}}}{\sqrt{8 k_{\mathrm{B}} T / \pi M_{\mathrm{R}}}} \frac{l}{2} \propto p_{\mathrm{P}} K_{\mathrm{diss}} n_{\mathrm{e0}} \cdot T^{-3/2}. \tag{3.11}$$

So the reactant concentration $n_A(x)$ now is expressed as a function of the dissociation rate in the discharge center and the surface sticking probability, R_{diss} and γ respectively, for given values of n_{e0}, T, p_{tot} and partial precursor pressure p_{P}. Exemplary the result is plotted in figure 3.4 for three different pressures at a fixed ratio of precursor to argon as background gas. As can be seen, the overall concentration of reactant A increases with increasing pressure, which is due to the overall increase of precursor flow and due to a slow down of its transport towards the surface at $x = l/2$.

The problem changes completely, when nanodust is present in the discharge. The reactant

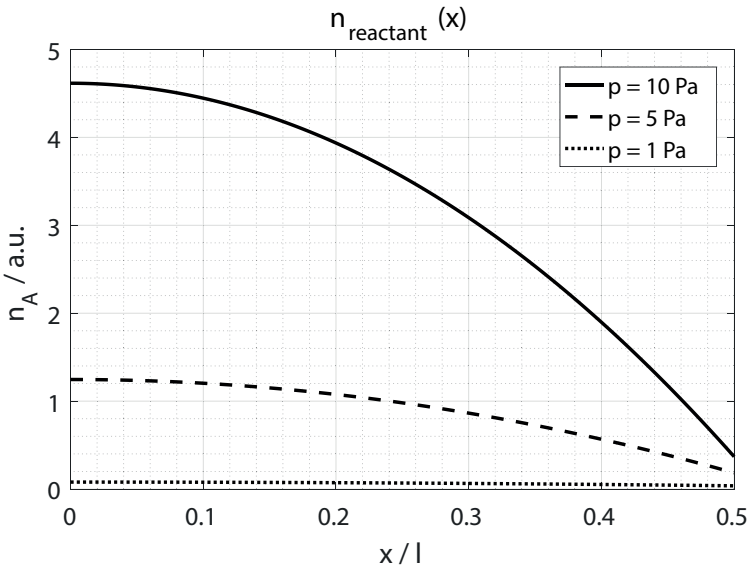

Figure 3.4: With increasing pressure the reactant transport is slowed down, so it can accumulate in the discharge center at $x = 0$. Also at a fixed ratio of precursor to background gas the total concentration of precursor increases with pressure, and thus, the dissociation rate producing the reactant is enhanced.

faces a much bigger effective surface area than in a clean plasma, because each dust grain behaves like a small floating surface, that is not far away from the source of reactive molecules but actually right in the center of the discharge. Therefore, diffusion will not be the main process determining the flux of reactants onto the particle surface. Instead the flux can be simply described by the thermal motion of the reactive molecules [157], when neglecting a back-flow due to a sticking coefficient smaller than one:

$$\Gamma_A = \frac{p_A}{(2\pi m_A k_\mathrm{B} T)^{1/2}} \propto \frac{p_A}{T^{1/2}}. \tag{3.12}$$

Thus, the same dependence on temperature and pressure as in the diffusion case 3.10 can be found, which explains, why the diffusion model also is applicable in non-diffusive cases like in very low pressure [15].
In the above case no volume losses for the reactive species were considered, which can be a good approximation for low pressure reactive plasmas, where the reactant mainly collides with inert argon atoms on the way to the reactor walls. Also, in order to have inelastic collisions, which may result in reactant losses, the molecules must be able to release energy. Therefore, volume reactions often take place through three-body-collisions, which are rare in low pressure. However, if dense nanodust clouds are present in the discharge, the losses onto the particles may be big, and thus, a second case accounting for volume losses $R_\mathrm{loss} = K_\mathrm{loss} n_\mathrm{d} n_A$ shall be derived in the following.
Basis of the reaction-diffusion equation needed is the same formula as in 3.6 but with a second linear term, that describes the losses onto the nanoparticles of density n_d with the

intrinsic reaction rate K_{loss}, that in more detail is a complex function of the surface sticking coefficient, surface reactions and dust radius:

$$\frac{\partial n_A}{\partial t} = D_{AB}\frac{\partial^2 n_A}{\partial x^2} + R_{\text{diss}} - R_{\text{loss}} = 0. \tag{3.13}$$

Hence, one can reformulate equation 3.7 to an inhomogeneous linear differential equation:

$$-D_{AB}\frac{\partial^2 n_A}{\partial x^2} + K_{\text{loss}} n_{\text{d}} n_A = K_{\text{diss}} n_{\text{P}} n_{\text{e0}}. \tag{3.14}$$

Because $-K_{\text{loss}} n_{\text{d}}/D_{AB} < 0$ an exponential ansatz has to be made with the boundary condititons

$$\Gamma_A(0) = -D_{AB}\left.\frac{\partial n_A(x)}{\partial x}\right|_0 = 0, \tag{3.15}$$

$$\Gamma_A(l/2) = -D_{AB}\left.\frac{\partial n_A(x)}{\partial x}\right|_{l/2} = \frac{\gamma}{2(2-\gamma)} n_{AS}\bar{v}_{AB}, \tag{3.16}$$

leading to a solution of the form

$$n_A(x) = C\left(\cosh\left(\sqrt{\frac{K_{\text{loss}} n_{\text{d}}}{D_{AB}}}\cdot\frac{l}{2}\right) - \cosh\left(\sqrt{\frac{K_{\text{loss}} n_{\text{d}}}{D_{AB}}}\cdot x\right)\right) + n_{AS}. \tag{3.17}$$

with the constants n_{AS} and C being lengthy expressions:

$$C = \frac{\gamma}{2(2-\gamma)}\frac{n_{AS}\bar{v}_{AB}}{\sqrt{D_{AB}K_{\text{loss}} n_{\text{d}}}\sinh\left(\sqrt{K_{\text{loss}} n_{\text{d}}/D_{AB}}\cdot l/2\right)} > 0 \tag{3.18}$$

$$n_{AS} = \frac{K_{\text{diss}} n_{\text{P}} n_{\text{e0}}}{K_{\text{loss}} n_{\text{d}}}\left(1 + \frac{\gamma}{2(2-\gamma)}\frac{\bar{v}_{AB}}{\sqrt{D_{AB}K_{\text{loss}} n_{\text{d}}}}\cdot\coth\left(\sqrt{K_{\text{loss}} n_{\text{d}}/D_{AB}}\cdot l/2\right)\right)^{-1}. \tag{3.19}$$

In order to demonstrate the correctness of this solution 3.17, it shall be shown here, that it converges to the simple case 3.8 in the limit $K_{\text{loss}} n_{\text{d}} \to 0$ of no losses to particles.
Because the cosh-expression goes to 0, but C goes to ∞, their first derivatives need to be taken in order to determine if the product converges. The first derivative $\mathrm{d}/\mathrm{d}(K_{\text{loss}} n_{\text{d}})$ of the cosh-expression goes to

$$\begin{aligned}\lim_{K_{\text{loss}} n_{\text{d}}\to 0}\ \frac{\mathrm{d}}{\mathrm{d}(K_{\text{loss}} n_{\text{d}})}&\left(\cosh\left(\sqrt{\frac{K_{\text{loss}} n_{\text{d}}}{D_{AB}}}\cdot\frac{l}{2}\right) - \cosh\left(\sqrt{\frac{K_{\text{loss}} n_{\text{d}}}{D_{AB}}}\cdot x\right)\right)\\ &= \frac{l^2}{8D_{AB}}\left(1 - \frac{4x^2}{l^2}\right),\end{aligned} \tag{3.20}$$

whereas the derivative of the constant C goes to

$$\lim_{K_{\text{loss}} n_{\text{d}}\to 0}\ \frac{\mathrm{d}C}{\mathrm{d}(K_{\text{loss}} n_{\text{d}})} = \frac{\gamma}{(2-\gamma)}\frac{n_{AS}\bar{v}_{AB}}{l} = R_{\text{diss}}, \tag{3.21}$$

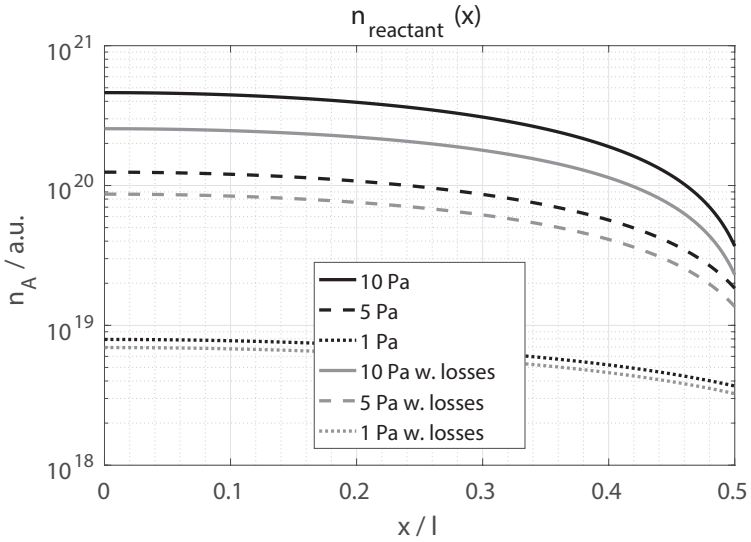

Figure 3.5: When losses are included, the reactant density decreases. Here arbitrary values were chosen for the loss term and the same conditions as in figure 3.4 are plotted.

where in the last step it was used that

$$\lim_{K_{\text{loss}} n_{\text{d}} \to 0} n_{AS} = \frac{2(2-\gamma)}{\gamma} \frac{K_{\text{diss}} n_{\text{P}} n_{\text{e0}}}{\bar{v}_{AB}} \frac{l}{2} = \frac{2-\gamma}{\gamma} \frac{R_{\text{diss}}}{\bar{v}_{AB}} l. \tag{3.22}$$

Hence, one obtains the same equation as in 3.8, if there are no losses either due to a very low nanodust density n_{d} or due to a low constant K_{loss}, which can be the case for very small dust grains. The resulting profile for an arbitrary chosen value of $\sqrt{K_{\text{loss}} n_{\text{d}} / D_{AB}} \cdot l/2$ is compared to the case without losses in figure 3.5.

Anyhow, it can be concluded for the opposite case of high losses $K_{\text{loss}} n_{\text{d}} \to \infty$, that in a simple 1-D model the reactant density n_{AS} close to the surface depends on gas temperature T and partial pressure p_{P} by

$$\lim_{K_{\text{loss}} n_{\text{d}} \to \infty} n_{AS} = \frac{2(2-\gamma)}{\gamma} \frac{K_{\text{diss}} n_{\text{P}} n_{\text{e0}}}{\bar{v}_{AB}} \sqrt{\frac{D_{AB}}{K_{\text{loss}} n_{\text{d}}}} \propto \frac{p_{\text{P}} K_{\text{diss}} n_{\text{e0}}}{\sqrt{p_{\text{tot}} K_{\text{loss}} n_{\text{d}}}} \cdot \sqrt{T^{-3/2}}, \tag{3.23}$$

where relation 3.3 was made use of. Thus, the dependence on the temperature is strongly reduced compared to the case without losses. For the flux to the walls, however, it can easily be calculated, that the relation 3.10 still holds true.
It is important to notice here, that the reactant density at the chamber walls is always lower than in the discharge centre. This is also correct, when including significant losses onto particles. Hence, by measuring the reactant flux onto the chamber walls, which is proportional to the density close to those, the neutral reactant density in the discharge volume is underestimated in both situations. However, if the losses are great, more precisely if the argument in the cosh becomes $\sqrt{K_{\text{loss}} n_{\text{d}} / D_{AB}} l/2 \gg 1$, the ratio between reactant

density in the centre and at $x = l/2$ becomes:

$$\frac{n_A(0)}{n_A(l/2)} \approx \frac{\gamma}{2(2-\gamma)} \frac{l\bar{v}_{AB}}{4D_{AB}} \cdot \frac{2}{1 + \sqrt{K_{\text{loss}} n_{\text{d}} / D_{AB}}\, l/2} + 1, \tag{3.24}$$

which approaches asymptotically

$$\lim_{K_{\text{loss}} n_{\text{d}} \to \infty} \frac{n_A(0)}{n_A(l/2)} = 1. \tag{3.25}$$

So in this case, the density at the walls approaches the density in the centre. On the other hand side, if no losses are assumed, meaning $\sqrt{K_{\text{loss}} n_{\text{d}} / D_{AB}}\, l/2 = 0$ the ratio goes to

$$\lim_{K_{\text{loss}} n_{\text{d}} \to 0} \frac{n_A(0)}{n_A(l/2)} = \frac{\gamma}{2(2-\gamma)} \frac{l\bar{v}_{AB}}{4D_{AB}} + 1 > 1. \tag{3.26}$$

Apart from the sticking coefficient γ the thermal velocity $\bar{v}_{AB}$ and diffusion constant D_{AB} are functions of the ambient temperature. Its ratio determines, how much the reactant density decreases towards the chamber walls by

$$\frac{l\bar{v}_{AB}}{4D_{AB}} \propto \frac{p_{\text{tot}}}{T}. \tag{3.27}$$

Hence, for high temperatures the profile $n_A(x)$ becomes flat regardless the sticking coefficient, but for high pressures the density decreases stronger towards the chamber walls. This knowledge is quiet crucial in order to understand mass spectrometric measurements, that can only capture a local species density, if no scan over the axis x is done.
Furthermore, the above described loss case can also be applied for the precursor gas, index P with the exact same mathematical description. Assuming, that dissociation and losses to the walls are the only sinks for the precursor, then the loss term has to be substituted by the already described dissociation rate and the gain term needs to be substituted by the precursor gas flow rate into the chamber R_{P}, so that equations 3.17 and following can be applied with the following substitutions:

$$\begin{aligned} n_A &\mapsto n_{\text{P}}, \\ K_{\text{loss}} n_{\text{d}} &\mapsto K_{\text{diss}} n_{\text{e0}}, \\ K_{\text{diss}} n_{\text{p}} n_{\text{e0}} &\mapsto R_{\text{P}} \\ D_{AB} &\mapsto D_{\text{P}B}. \end{aligned} \tag{3.28}$$

Also, another sticking coefficient γ needs to be considered, of course.

Surface kinetics Once the species A has reached the surface it can then after being adsorbed react with the surface at the vacant sites of density n_0. In a growth process the amount of vacant sites can be assumed to be constant, because each chemisorbed species later can also provide a vacant site. So the rate of chemisorption must be proportional to

the density of vacant sites, the density of physisorbed reactants, expressed by the surface coverage θ, and to the reaction constant K_r [15]:

$$R_{A\mathrm{S}} = K_\mathrm{r} n_0 \theta. \tag{3.29}$$

Because in the concentration of physisorbed reactants A:S must be constant in a steady state growth process, a link between the surface coverage and the reaction rate constants for adsorption K_a, desorption K_d and chemisorption K_r can be made by

$$\begin{aligned} \frac{\mathrm{d}n_{A:\mathrm{S}}}{\mathrm{d}t} &= K_\mathrm{a} n_{A\mathrm{S}} n_0 (1-\theta) - K_\mathrm{d} n_0 \theta - K_\mathrm{r} n_0 \theta = 0 \\ \Rightarrow \qquad \theta &= \frac{1}{1 + (K_\mathrm{d} + K_\mathrm{r})/K_\mathrm{a} n_{A\mathrm{S}}}, \end{aligned} \tag{3.30}$$

where the right hand side terms describe adsorption, desorption and reactions with the surface respectively. For very fast surface reactions, meaning $K_\mathrm{d} + K_\mathrm{r} \gg K_\mathrm{a} n_{A\mathrm{S}}$ the surface coverage becomes very small $\theta \ll 1$. This is typical for low pressure plasmas, where the initial density of reactant is relatively low and it is also referred to as mass transport limited film growth. The opposite, $\theta \approx 1$, holds true for the case of fast transport towards the surface but low reactivity of chemisorption, which can usually be found at atmospheric pressures. Here the film growth is limited by the surface reactivity.
Inserting equation 3.30 into 3.29 these two cases can also be distinguished for the surface reaction rate, which is just another expression of the film growth rate:

$$R_{A\mathrm{S}} = \frac{K_\mathrm{r} n_0}{1 + (K_\mathrm{d} + K_\mathrm{r})/K_\mathrm{a} n_{A\mathrm{S}}} = \begin{cases} K_\mathrm{r} n_0 & K_\mathrm{a} n_{A\mathrm{S}} \gg K_\mathrm{d} + K_\mathrm{r} \quad \text{surface reaction limited} \\ \frac{K_\mathrm{r} K_\mathrm{a} n_0 n_{A\mathrm{S}}}{K_\mathrm{d} + K_\mathrm{r}} & K_\mathrm{a} n_{A\mathrm{S}} \ll K_\mathrm{d} + K_\mathrm{r} \quad \text{mass transport limited} \end{cases}$$

Therefore, in the surface reaction limited case, the growth rate depends linearly on the reaction rate K_r, which in turn typically scales with the respective activation energy E_a and surface temperature T_S to $K_\mathrm{r} \propto \exp(-E_\mathrm{a}/k_\mathrm{B} T_\mathrm{S})$. However, it is completely independent from the gas kinetics, and thus, from the diffusion and dissociation processes. On the contrary, in the mass transport limited case, the growth rate increases linearly with the reactant concentration close to the surface, which by equation 3.11 scales with the precursor pressure and gas temperature to $n_{A\mathrm{S}} \propto p_\mathrm{P} T^{-3/2}$. Thus, in this case, the process time relies on fast gas kinetics, which not only depend on temperature but also on pressure.
In thin film technology the uniformity is one of the important characteristics of any deposition. So if a process runs in the transport limited regime, the gas supply and flow has to be thought through very carefully in order to guarantee the same amount of reactant at any place of the substrate. Therefore it may be favourable to work in the surface reaction limited regime.
In the case of a nanodusty plasma, where each particle is a deposition surface, the length scale l between the surfaces is very small, in the order of some micrometres. Therefore, after equation 3.11, the density of reactant A close to the particle surface is very low and consequently $K_\mathrm{a} n_{A\mathrm{S}} \ll K_\mathrm{d} + K_\mathrm{r}$ expected. Thus, the process is probably mass transport limited, so that the growth rate should mainly depend on the precursor supply. At a fixed

temperature T the dependence is simply expected to be linear with the partial precursor pressure p_P according to equations 3.1.1 and 3.11. Also, as the relatively fast surface reactions consume the reactant immediately, it is expected, that the partial pressure p_P in the dust cloud is relatively low.

3.1.2 Influence of pressure and power

As demonstrated in the section above, the transport of reactive neutrals depends strongly on the temperatures of the gas and substrate, T and T_S respectively, and also on the total pressure and partial pressure of the precursor, p_{tot} and p_P respectively. But the neutral transport additionally depends on the dissociation rate R_{diss}, that is influenced by the plasma through the electron temperature and density, T_e and n_e. These in turn can mainly be adjusted by the pressure and power of the discharge. Moreover, they affect strongly the ion formation and transport, that also participates in the particle growth. Therefore, the effect of pressure and power shall be described in the following subsection.
During this thesis a capacitively coupled RF reactor named *ATILA* was used for the nanoparticle formation. It is explained in detail in chapter 4, but here it shall already be mentioned, that it is a highly asymmetric plasma, as already introduced and specified in section 2.2.3. The in this section presented measurements concerning the discharge power and pressure have been done in ATILA in the frame of the master's thesis of Nils Lukat [160].
Increasing the power, more of it is delivered to the gas volume and, thus, the overall excitation and ionization rate increases too. However, it does not strictly implicate, that the electron density or the electron temperature in the discharge changes. In a rather large chamber the overall amount of free electrons N_e can also increase by an increase of the effective plasma size V_{pl}. A good method to study this, is to monitor the self-bias voltage when the plasma potential is changing. According to equation 2.39 their relation is strongly linear in case of a fixed symmetry factor B/A between the grounded suface area B and the powered electrode A. However, already by naked eye it can be seen, that for low power or high pressure the intense glow region of the discharges becomes very localized towards the powered electrode.
Therefore, the pressure and power have been varied in the here used set-up, while the plasma potential has been monitored by the means of the ion energy via a mass spectrometer and the self-bias voltage by the means of electrical measurements in the frame of a master thesis [160]. Subsequently one map for each of the two signals has been made for powers from 10 to 90 W versus pressures from 2 to 33 Pa. For measuring the ion energy, the impurity H_3O^+ was taken, because its low collision cross section made it possible to measure up to 34 Pa and it was confirmed, that the energy yielded the same plasma potential as the argon ion energy.
As can be seen from figure 3.6 instead of a linear dependence between V_{bias} and Φ_{pl} an almost inverse behaviour can be observed: With increasing pressure the plasma potential rises, whereas the self-bias voltage drops down. The same holds true for decreasing power. This behaviour is rather unintuitive, because in a rough approximation the plasma potential

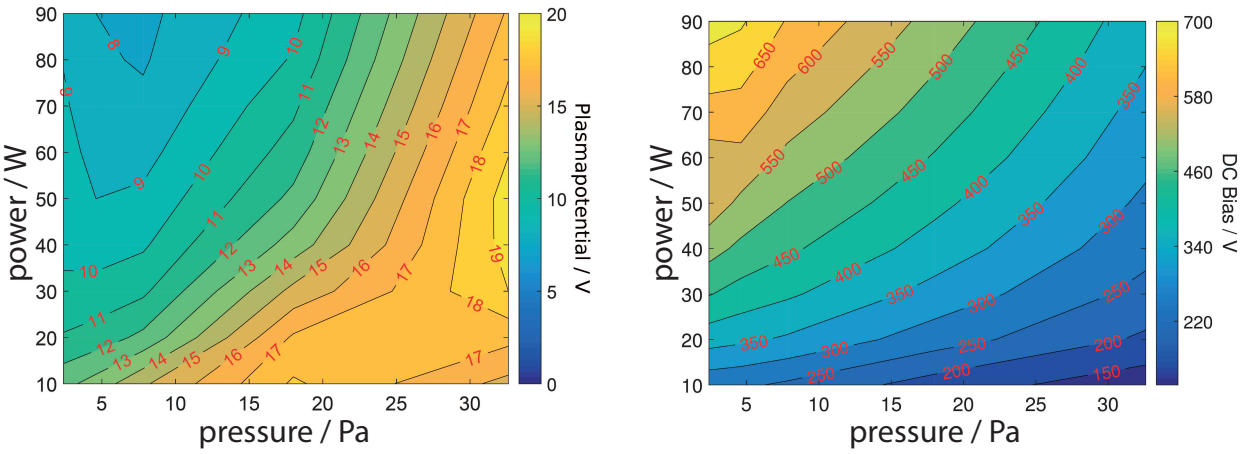

Figure 3.6: The plasma potential is a function of electron temperature and density as well as the plasma size. Measurements in an argon discharge have been done in ATILA by a mass spectrometer at the impurity of mass $m/z = 19$ (left). Also the absolute value of the selfbias voltage (right) is sensitive to the upper mentioned parameters and behaves somewhat inversely to the ion energy. Taken from [160] and modified to english;

can be assumed to follow the electron temperature linearly [90]:

$$\Phi_{\mathrm{pl}} = \Phi_{\mathrm{fl}} - \frac{k_{\mathrm{B}} T_{\mathrm{e}}}{e} \ln\left(0.61\sqrt{\frac{2\pi m_{\mathrm{e}}}{m_{\mathrm{i}}}}\right) \tag{3.31}$$

with the last term contributing positively due to a negative logarithm. So the decrease in Φ_{pl} with rising RF power must be either due to a lowered electron temperature or due to a smaller floating potential Φ_{fl}. However, the floating potential should always be close to zero, because no net DC current is running through the capacitively coupled powered electrode. This means, if the plasma is stable and does not accumulate further charges, no DC current can run through the grounded electrode neither. Thus, the grounded electrode fulfils the definition of being at floating potential with $I_{\mathrm{e}} = I_{\mathrm{i}}$ and consequently the floating potential must be $\Phi_{\mathrm{fl}} \approx 0$. However, in reality measurements usually reveal a significantly positive floating potential. One explanation might be the building up of stronger ion currents onto edges than in front of a plane surface due to an enhanced collection area, that is defined by the sheath edge in front of the wall, not by the wall surface area. Also, the measurement of the floating potential may be slightly too positive due to the geometrical factor, when using a cylindrical probe, see chapter 7.1.
Because in ATILA the grounded electrode is made by the entire rest of the chamber its geometry is rather complex having those edges and plane surfaces and even gaps. Therefore the overall net current through the walls may be zero but locally a positive current will be drawn through edges and a negative one through the plane surfaces, cancelling out in total. However, in that case the definition of the floating potential is not fulfilled locally.
Another explanation for a floating potential not equal to zero may be a bad coupling of the plasma to the grounded electrode, which means, that most of the charges are lost in collisions

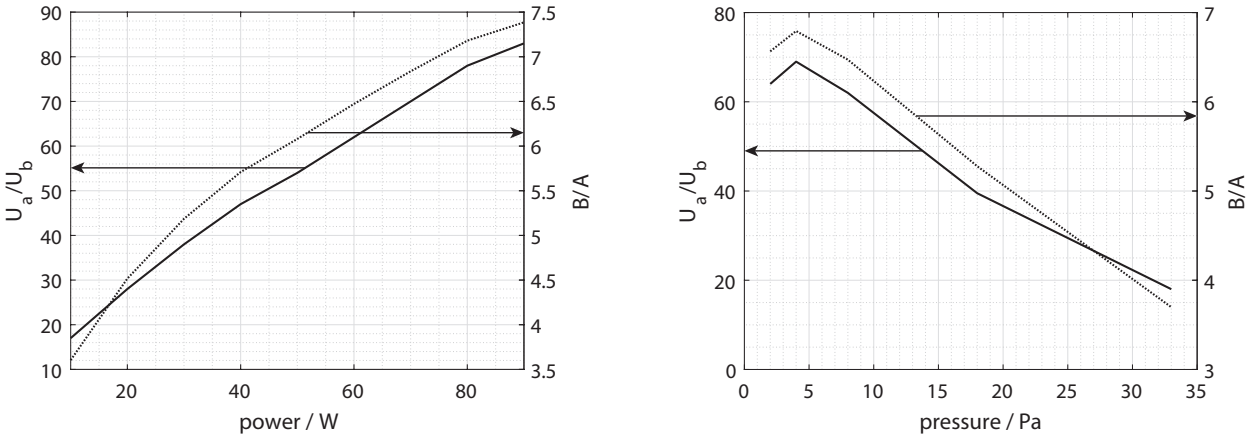

Figure 3.7: The ratio of the powered electrode facing surface A to the grounded electrode facing surface B varies as function of the discharge power (left) and the discharge pressure (right). It is related to a change in the plasma volume, inducing a change in B, whereas the powered electrode surface A remains constant. After [160];

before they can enter the walls. This can happen at high pressures or at low powers, where the plasma is located close to the powered electrode and charge carriers have to travel a long way towards the walls. Not reaching the walls any more, the effective wall is located much closer to the discharge, where the potential is not zero but slightly positive and, thus, the reference potential is not clearly defined.
Recalling section 2.2.3, especially equation 2.36

$$\frac{\bar{U}_\mathrm{a}}{\bar{U}_\mathrm{b}} = \left(\frac{B}{A}\right)^q,$$

a way to quantify the volume change of the plasma is to access the factor B/A via $\bar{U}_\mathrm{a} = \Phi_\mathrm{pl} - V_\mathrm{bias}$ and $\bar{U}_\mathrm{b} = \Phi_\mathrm{pl}$, where A remains constant throughout any parameter variation. So the plasma surface in contact with B can directly be taken from

$$B = A\left(\frac{\bar{U}_\mathrm{a}}{\bar{U}_\mathrm{b}}\right)^{1/q}, \tag{3.32}$$

if the exponent $1/q$ is known. Taking $q = 2.21$ as introduced in chapter 2.2.3, this was applied on the data in figure 3.6, obtained in ATILA [160] for a power variation at 4.6 Pa and a pressure variation at 20 W. The result is presented in figure 3.7.
In this parameter range B/A varies from 3.5 to 7.5. Assuming the plasma to be sphere shaped, for a rough estimation, with a fixed surface area contribution from A this variation would correspond to a volume change of $V_1/V_2 \approx (r_1/r_2)^3 = (8.5A/4.5A)^{3/2} = 2.6$. With an increase in the discharge power P of one order of magnitude but a change in volume V in the order of 2.6 the power density P/V should increase roughly by four times.
So, a change in the plasma volume, as demonstrated above, could explain, that the self-bias voltage and the measured plasma potential behave inversely and that in Langmuir probe

measurements [161] the electron density and temperature increase with power at a fixed pressure due to an increased power density.
In case of the pressure variation a strong reduction of the plasma volume with increasing pressure is observed. Because the power is fixed in this case, the power density should be enhanced, too. Another evidence for that is the increase in the plasma potential, that after equation 3.31 may indicate an elevated electron temperature T_e.
The changes in electron temperature and density also affect a PECVD process. Higher electron temperatures lead to the dissociation of chemical bonds with higher dissociation energies and also to stronger ionization, especially of species with high ionization energy. Resuming a high electron temperature can initiate chemical reactions with high activation energy, whereas low electron temperatures allow a "'softer"' treatment, where mainly easily initiated reactions occur. The electron density actually scales linearly with all the rates associated with electron impact reactions and is therefore mostly desired to be as high as possible.
Independent of the discussion above the pressure also plays an important role regarding the mean free path of reactive, excited and ionized species. When important steps towards a film deposition need to happen in the gas phase a high pressure should be favourable. However, in some cases the collisions in the gas phase become so frequent, that dust particle growth is initiated [162], which usually is undesired. Also at elevated pressures three-body-collisions can happen and open new possible reaction paths.

3.2 Main reactions in acetylene discharges

After having build up a comprehensive picture of gas and surface kinetics the main reactions in acetylene/argon discharges shall be discussed including essential steps for nano-particle formation.
Acetylene, also known as ethyne, ethine, narcylen or vinylene, is a hydrocarbon consisting of two carbon and two hydrogen atoms in a linear structure due to the triple bond between the two carbon atoms:

$$\mathrm{H{-}C{\equiv}C{-}H}$$

It has a mass of 26.04 u and the ionization energy for the direct electron impact ionization to $C_2H_2^+$ is 11.41 eV [163], which is below the one of argon.
Several reaction mechanisms in acetylene containing plasmas are already known. Experimental works [67, 72, 74, 164–167] try to identify not only the main reactions starting from the dissociation of acetylene but also to find the precursors for nano-particle growth ending in hydrocarbons with several carbon atoms. A nice review including gas phase and surface reactions has been written in 2010 by Benedikt [168].

3.2.1 Reactions involving acetylene and acetylene ions

In a first step acetylene needs to be dissociated. This may happen upon electron impact but also de-excitation of argon Ar* during inelastic collisions with acetylene. Especially

reaction type	reaction	rate const. /(cm^3/s)	reference
e^- impact dissociation	$e^- + C_2H_2 \rightarrow C_2H + H + e^-$		[169]
	$e^- + C_2H_2 \rightarrow C_2 + 2H + e^-$		[169]
	$e^- + C_2H_2 \rightarrow C_2 + H_2 + e^-$		[169]
dissociative ionization	$e^- + C_2H_2 \rightarrow C_2H^+ + H + 2e^-$		[169]
	$e^- + C_2H_2 \rightarrow C_2H + H^+ + 2e^-$		[169]
	$e^- + C_2H_2 \rightarrow C_2^+ + H_2 + 2e^-$		[169]
dissociative e^- attachement	$e^- + C_2H_2 \rightarrow C_2H^- + H$		[170]
dissociative collisions	$H^+ + C_2H_2 \rightarrow C_2H^+ + H_2$	$4.3 \cdot 10^{-9}$	[171]
	$C_2H_3^+ + C_2H_2 \rightarrow C_4H_3^+ + H_2$	$2.4 \cdot 10^{-10}$	[171]
	$C_2H_2^+ + C_2H_2 \rightarrow C_4H_2^+ + H_2$	$0.43 \cdot 10^{-9}$	[172]
	$C_2H_2^+ + H_2 \rightarrow C_2H_3^+ + H$	$0.48 \cdot 10^{-9}$	[173]
	$C_6H_2^+ + C_2H_2 \rightarrow C_8H_2^+ + H_2$	$0.17 \cdot 10^{-9}$	[173]
	$Ar^* + C_2H_2 \rightarrow C_2H + Ar + H$	$3.5 \cdot 10^{-10}$	
	$C_2H^- + C_2H_2 \rightarrow C_4H^- + H_2$	$1.0 \cdot 10^{-12}$	[171]
dissociative recombination	$C_2H_2^+ + e^- \rightarrow C_2H + H$	$5.0 \cdot 10^{-8}$	[168, 174]
	$C_2H_2^+ + e^- \rightarrow C_2 + H + H$	$3.0 \cdot 10^{-8}$	[168, 174]
	$C_2H_2^+ + e^- \rightarrow CH + CH$	$1.3 \cdot 10^{-8}$	[168, 174]
	$C_2H_2^+ + e^- \rightarrow CH_2 + C$	$5.0 \cdot 10^{-9}$	[168, 174]
	$C_2H_2^+ + e^- \rightarrow C_2 + H_2$	$2.0 \cdot 10^{-9}$	[168, 174]

Table 3.1: Various dissociation processes for C_2H_2 in low temperature argon plasmas

important for those collision processes are argon metastables Ar^m as their life time is long enough to account for a considerable amount of collisions. Another process are dissociative collisions with a variaty of ions, where the ions possess enough intrinsic energy to initiate a break up of the bonds inside the acetylene molecule.
The dissociation processes of neutral acetylene and its ionized form are summarized in table 3.1. A very important reaction in C_2H_2 plasmas is the dissociative electron attachement to the acetylene molecule, where after it breaks into a C_2H radical and one hydrogen atom. The splitting of hydrogen is easier (threshold energy of 7.5 eV) than the breaking of the triple bond between the carbon atoms (threshold energy of 10 eV), so it is the preferred reaction. Dissociative recombination reactions are more pronounced in plasmas of very low electron temperature and the given rate constants actually apply for ETP plasmas.
Not only do $C_2H_2^+$ ions get lost by dissociation but also they tend to attach to other molecules. Therefore this channel also accounts for losses of acetylene from the discharge via precedent ionization. The ionization can happen by direct electron ionization [169]

$$e^- + C_2H_2 \rightarrow C_2H_2^+ + 2e^- \tag{3.33}$$

or by collision with argon ions [175, 176]

$$Ar^+ + C_2H_2 \rightarrow C_2H_2^+ + Ar \tag{3.34}$$

attachement of	reaction	rate constant /(cm^3/s)	reference
$C_2H_2^+$	$C_2H_2^+ + C_2H_2 \rightarrow C_4H_2^+ + H_2$	$0.43 \cdot 10^{-9}$	[172]
	$C_2H_2^+ + C_2H \rightarrow C_4H_2^+ + H$	$1.4 \cdot 10^{-9}$	
	$C_2H_2^+ + H_2 \rightarrow C_2H_3^+ + H$	$1.0 \cdot 10^{-11}$	[171]
	$C_2H_2^+ + C_4H_2 \rightarrow C_4H_2^+ + C_2H_2$	$0.9 \cdot 10^{-9}$	[173]
	$C_2H_2^+ + C_2H_2 \rightarrow C_4H_2^+ + H_2$	$0.43 \cdot 10^{-9}$	[172]
C_2H_2	$C_2H_2^+ + C_2H_2 \rightarrow C_4H_2^+ + H_2$	$0.43 \cdot 10^{-9}$	[172]
	$C_2H_3^+ + C_2H_2 \rightarrow C_4H_3^+ + H_2$	$2.4 \cdot 10^{-9}$	[171]
	$C_2H_2^+ + 2H_2 \rightarrow C_2H_3^+ + H$	$0.48 \cdot 10^{-9}$	[173]
	$C_4H_2^+ + C_2H_2 \rightarrow C_6H_4^+$	$2.0 \cdot 10^{-10}$	[172, 178]
	$C_6H_2^+ + C_2H_2 \rightarrow C_8H_4^+ + H_2$	$1.2 \cdot 10^{-9}$	[173]
	$C_4H_3^+ + C_2H_2 \rightarrow C_6H_5^+$	$2.2 \cdot 10^{-10}$	[173]
	$C_6H_4^+ + C_2H_2 \rightarrow C_8H_6^+$	$7.0 \cdot 10^{-11}$	[172]
	$C_2H + C_2H_2 \rightarrow C_4H_2 + H$	$1.3 \cdot 10^{-10}$	[171]
	$H + C_2H_2 \rightarrow C_2H_3$		[171]
	$C_2H^- + C_2H_2 \rightarrow C_4H^- + H_2$	$1.0 \cdot 10^{-12}$	[171]

Table 3.2: Various attachement processes for $C_2H_2^+$ and C_2H_2 in low temperature argon plasmas

and hydrated argon ions

$$ArH^+ + C_2H_2 \rightarrow C_2H_2^+ + H + Ar, \tag{3.35}$$

as well as in collisions with excited argon atoms

$$Ar^* + C_2H_2 \rightarrow C_2H_2^+ + Ar + e^-. \tag{3.36}$$

Apart from that, acetylene ions are formed during the following reactions [173, 177]:

$$C_2H_3^+ + H \rightarrow C_2H_2^+ + H_2 \tag{3.37}$$
$$C_2H_3^+ + C_2H \rightarrow C_2H_2^+ + C_2H_2 \tag{3.38}$$
$$H^+ + C_2H_2 \rightarrow C_2H_2^+ + H \tag{3.39}$$
$$H_2^+ + C_2H_2 \rightarrow C_2H_2^+ + H_2 \tag{3.40}$$

Another contribution to the losses of acetylene is its participation in neutral form in a variety of reactions in which it is not dissociated but attached, resulting in bigger molecules. The attachement reactions for ions and neutrals are summarized in table 3.2.
Counteracting against the loss processes is the gas inlet of acetylene. Besides of that, several

other production channels exist, given in the following reactions [171, 173, 179, 180]:

$$C_2H_2^+ + e^- \rightarrow C_2H_2 \tag{3.41}$$
$$C_2H_2^+ + C_4H_2 \rightarrow C_4H_2^+ + C_2H_2 \tag{3.42}$$
$$C_2H_3^+ + C_2H \rightarrow C_2H_2^+ + C_2H_2 \tag{3.43}$$
$$C_4H_2^+ + C_4H_2 \rightarrow C_6H_3^+ + C_2H_2 \tag{3.44}$$
$$C_4H_3^+ + C_4H_2 \rightarrow C_6H_2^+ + C_2H_2 \tag{3.45}$$
$$H + C_2H \rightarrow C_2H_2 \tag{3.46}$$
$$H_2 + C_2H \rightarrow C_2H_2 + H \tag{3.47}$$
$$C_2H^- + H \rightarrow C_2H_2 + e^- \tag{3.48}$$
$$C_2H^- + C_2H_2^+ \rightarrow C_2H + C_2H_2 \tag{3.49}$$

Special attention has to be payed to the vinylidene ion

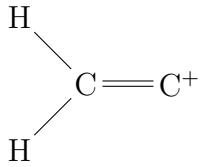

(3.50)

which is an isomer of the acetylene ion. It has the same mass and chemical composition as $C_2H_2^+$ and yet it yields other reactions. It is probably formed in the ionization of acetylene by argon ions 3.35, where the charge transfer unleashes the energy difference of their ionization energies $E_{res} = E_{ion,Ar} - E_{ion,C2H2} = 4.4\,eV$ [168]. The consequence becomes obvious when looking at the dissociative recombination of this molecule, which preferably results in $CH_2 + C$ and subsequent $C_2 + H + H$ instead of $CH + CH$ and $C_2H + H$ as it is preferred for the decomposition of $C_2H_2^+$. Therefore, the rate constants for dissociative recombinations, described in table 3.1, may need to be adjusted depending on the discharge conditions.
Summarizing, a huge bunch of basic reactions already has to be considered only accounting for first order reactions with acetylene or acetylene ions. In order to fully identify the most important reaction paths the products of the above given reactions also need to be analysed concerning their losses and gains while respecting all the reaction constants. Therefore, a simulation, that models the chemical dynamics is inevitable. Theoretical works dealing with hydrocarbon plasmas for thin film deposition but also for particle growth include [68, 171, 175, 179, 181–184].

3.2.2 Reaction paths towards nano-particle nucleation

In the following section the most important reaction pathways for the formation of big molecules shall be discussed. They can be separated into three categories: reactions with negative ions, positive ions and neutral molecules. Because during the process all possible intermediate products are present the challenge of experimental works, like mass spectrometric investigations, is to identify the important pathways out of hundreds of possibilities

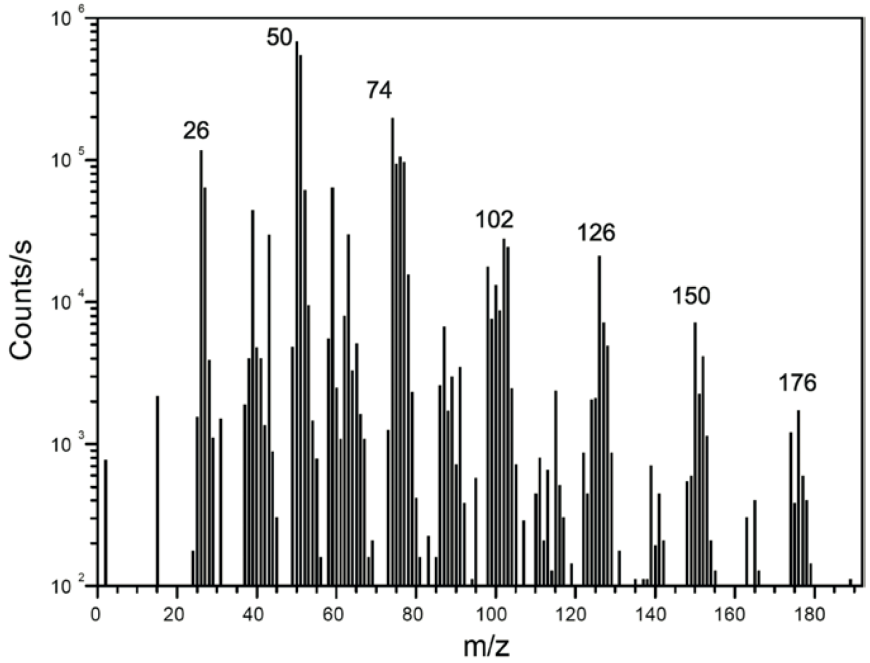

Figure 3.8: Typical positive ion spectrum of an acetylene discharge at low pressure as obtained by [67] and reproduced by [168];

leading to the intermediate compound.
One very specific feature of C_2H_2 plasmas is the dominance of molecules with an even number of carbon atoms in all mass spectra, for negative and positive ions as well as for neutral spectra [168]. This strongly indicates, that the triple bonding between the two carbon atoms in acetylene stays intact during plasma treatment. In fact it was shown by IR absorption spectroscopy, that even the less abundant odd-carbon-atom molecules still preserve the triple bond [67].

Positive ions A typical positive ion mass spectrum of low temperature acetylene plasmas, as obtained by [67] is shown in figure 3.8. It is dominated by $C_2H_2^+$, $C_4H_2^+$, $C_4H_3^+$ and $C_6H_2^+$ ions indicating a reaction path with stepwise addition of C_2H_2:

$$\begin{aligned} & & \rightarrow C_{2n+2}H_4^+ \\ C_2H_2^{(+)} + C_{2n}H_2^{(+)} \rightarrow & (C_{2n+2}H_4^+)^* & \rightarrow C_{2n+2}H_3^+ + H \\ & & \rightarrow C_{2n+2}H_2^+ + H_2 \end{aligned} \tag{3.51}$$

Here the $^{(+)}$ indicates, that either one of the reaction partners on the left side is an ion. It was observed, that varying the discharge pressure from low to high, the dominant positive ion shifted from low carbon number $C_2H_2^+$ to longer molecules of higher carbon number $C_6H_2^+$ at 200 to 6700 Pa [185]. So for low pressures on the left hand side of reaction 3.51 may be written as $C_2H_2^+ + C_{2n}H_2$. The intermediate product is annotated with a star, that stands for excitation. The de-excitation provides then enough energy to split of an hydrogen

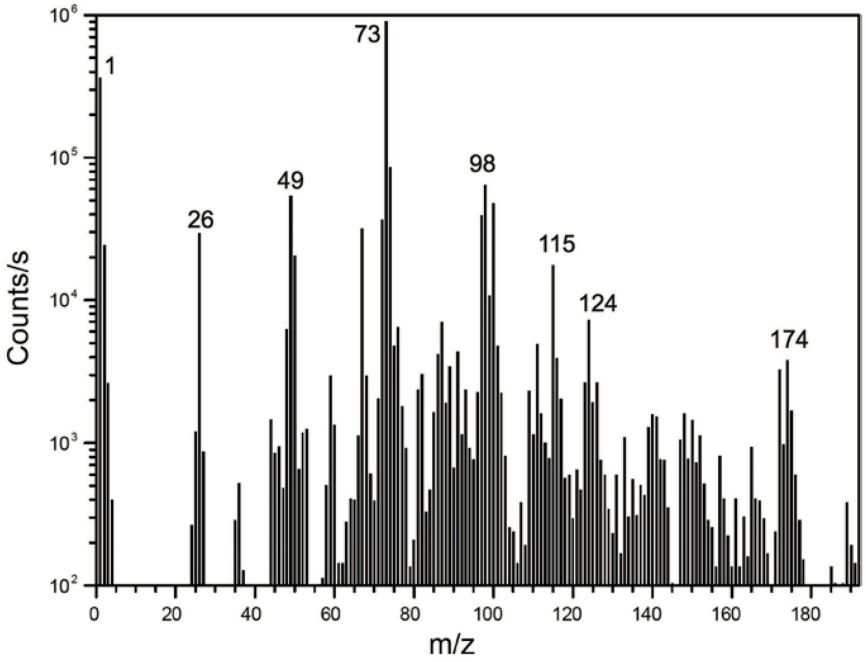

Figure 3.9: Typical negative ion spectrum of an acetylene discharge at low pressure as obtained by [67] and reproduced by [168];

atom or molecule.
Because nano-particles immersed in a plasma are charged negatively from a certain size on, these ions are expected to strongly participate in their growth by contributing to the enhanced ion current and subsequent sticking to the surface. This happens during the last phase of particle genesis, as described in the section 3.3 In the earliest stage of particle synthesis, the seed formation, however, the negative ions are thought to play a crucial role.

Negative ions Negative ions are of special interest in acetylene plasmas, not only because they modify the quasi-neutrality equation by a reduction of n_e but also because they are confined in the plasma due to its positive potential. Therefore, they stay in the discharge as long as their lifetime τ. From the negative ion mass spectrum 3.9, again obtained by [67], can be seen, that the highest intensity was measured at $m/z = 73$, which corresponds to C_6H^-. It is followed by $C_6H_2^-$, $C_8H_2^-$ and C_4H^- in descending order. The peak at $m/z = 26$ probably corresponds to the vinylidene anion

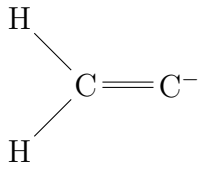

because the acetylene anion is not very stable [168]. The long residence time of anions leaves them enough time to collide often enough to form very heavy molecules, finally ending in a

small seed, and thus, initiating the nano-particle growth [186]. This corresponds well with the observation, that anions are especially easily formed in acetylene plasmas [187].
The reaction mechanisms leading to those anions, however, is not well understood. In [168] it is proposed, that like in the case for positive ions, based on reflections on the respective collision cross-sections, the negative ions grow in a sequential addition of C_2H_2 of this form, also known as the *Winchester mechanism*:

$$C_{2n}H^- + C_2H_2 \rightarrow C_{2n+2}H^- + H_2. \tag{3.52}$$

Also, the direct electron attachement to bigger molecules is more effective than to C_2H_2 [171]. Meantime, the pathway towards $H_2C{=}C^-$, which supposedly is the first building block (n=1) in the chain reaction 3.52 according to [179], remains unclear and the additional question arises, how it can result in alternating triple and single bonds between the carbon atoms when in the vinylidene anion the carbon atoms share a double bond.

Neutrals Neutral molecules are by far the most abundant species in low pressure discharges, because the ionization degree typically is less than 1 %. Therefore, their reactions determine essentially the outcome of any PECVD process including nano-particle synthesis and surface growth on nano-particles.
As can be seen from table 3.2 various reactions can lead to the attachment of C_2H_2 in order to form bigger molecules of even carbon amount, which are also dominant in the neutral spectrum 3.10. The only neutral-neutral reaction, however, is the reaction with C_2H. Therefore, it is believed [168, 179] to be the main precursor for poly-acetylene via

$$C_{2n}H_2 + C_2H \rightarrow C_{2n+2}H_2 + H. \tag{3.53}$$

Another possible mechanism may be the electron-induced C-H bond breakage of large poly-acetylenes and subsequent C_2H_2 attachment:

$$C_{2n}H + C_2H_2 \rightarrow C_{2n+2}H_2 + H. \tag{3.54}$$

However, De Bleecker and Bogaerts [179] leave open for discussion, how the possible reaction

$$C_{2n}H_2 + H \rightarrow C_{2n}H_3 \tag{3.55}$$

due to the relatively high hydrogen content in the discharge contributes to film growth. This idea was expressed by Doyle in [74], where he proposes C_2H, C_4H_3 and C_6H_3 as main precursors for thin film growth without further reactions in the discharge volume.

It should be noted here, that due to the conservation of the triple bonding, the resulting long molecules exhibit alternating triple and single bonds, and thus, poly-acetylene is the suitable term for the molecule of the sort

$$H\text{—}\left(\text{—}C\equiv C\text{—}\right)_n\text{—}H,$$

which is formed in the anionic as well as in the cationic and neutral reactions. Furthermore Consoli *et al.* explain in [188] the existence of hydrogen-richer hydrocarbons. They argue,

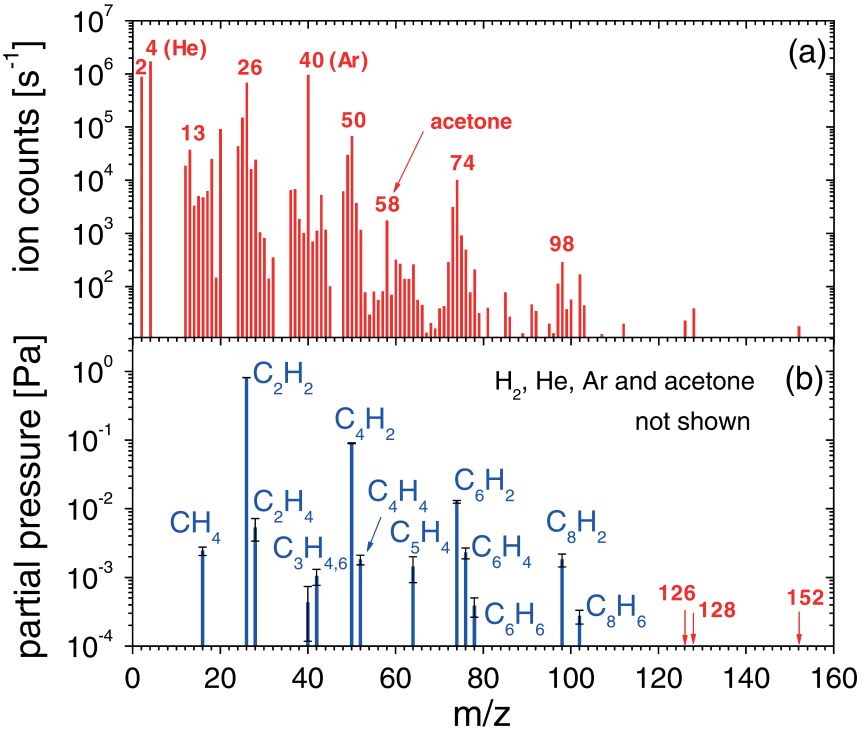

Figure 3.10: The neutral molecule spectrum of an Ar/He/C_2H_2 discharge (a) at low pressure as obtained by [76] has been transformed into partial pressures (b) via Bayes analysis. It clearly shows the dominance of evenly numbered hydrocarbons. Taken from [76];

that C_2H_4 is the precursor for a number of parallel reactions not interfering much with the above discussed pathways, because they observed an augmentation of dependend species, namely CH_4, C_3H_4, C_5H_4, C_6H_4, C_6H_6 and larger molecules of sort $C_{2n}H_4$. They determined the origin of C_2H_4 being an impurity in the acetylene bottle but more importantly also being a sputtered species from carbonaceous surfaces during the plasma process.

Aromatic compounds In a mass spectrum the peak at $m/z = 78\,\mathrm{u}$ can be attributed to a linear chain of carbon atoms consisting mainly of double bonds or more probable of alternating triple and single bonds with termination on CH_3:

$$H_3C-C\equiv C-C\equiv C-CH_3.$$

Another possibility is the existence of benzene, the aromatic representation of C_6H_6

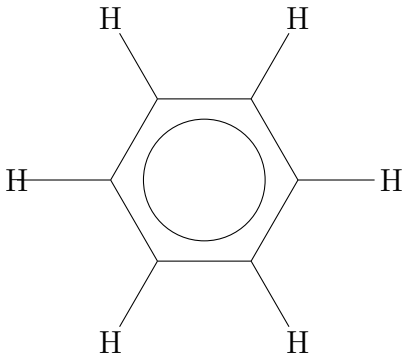

and in fact they have presumably been found by Stefanović *et al.* inside nano-particles [189]. Because benzene is a very stable compound it is also likely to be formed from an energetic point of view. Its synthesis may proceed through acetylene addition to C_4H_5

$$C_4H_5 + C_2H_2 \rightarrow C_6H_6 + H \tag{3.56}$$

and through the cyclization of C_6H_4 and C_6H_6 [190]. Consoli *et al.* [188] propose a fourth pathway towards benzene by the reaction

$$C_4H_4 + C_2H_3 \rightarrow C_6H_6 + H \tag{3.57}$$

based on their observations regarding the influence of C_2H_4 on the acetylene chemistry.
The existence of aromatic rings may be crucial for the nucleation of dust particles. Their stability, and thus longevity, enables the stepwise addition of acetylene to them, which is followed by hydrogen abstraction and finally, by ring closure, resulting in naphtalene:

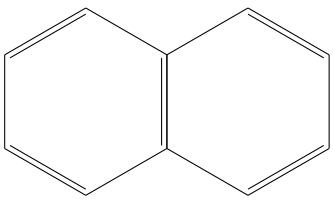

This way even bigger aromatic compounds can form and may also contribute to seed formation in low pressure acetylene plasmas [190].

3.3 Particle growth in three steps

As already mentioned polymerisation does not only occur on surfaces but can also proceed in the gas phase, if the respective precursor concentration is high enough. The subsequent seed formation then finally leads to small particles, the nanodust. In 1993 firstly suggested by Bouchoule *et al.* [191] for silane plasmas SiH_4, it is now widely excepted, that the growth of polymer particles takes place in three distinct steps [27,192,193]. Of course, the chemistry behind silane plasmas is totally different from acetylene chemistry and yet most people have

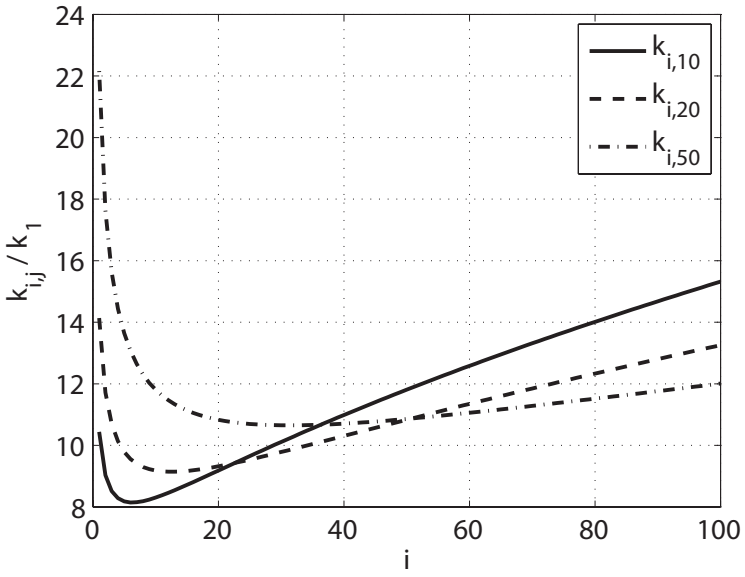

Figure 3.11: The collision rate coefficient $k_{i,j}$ is a function of the size of the participating bodies in terms of mass and cross section. The bigger the size difference the more frequent are the collision events. After [25];

adopted the three step model for the growth of carbonaceous particles. The basis for a transfer from silane to acetylene is the purely physical description of the seed formation and the following steps.
Growth phenomena in acetylene often are governed by a cyclic response of the discharge properties, which can be linked to successive generations of dust particles [166, 168, 194]. So in many experiments the three steps cannot take place at the same time.
In the following section those steps towards nano-particles shall be introduced.

3.3.1 Nucleation phase

The first phase of particle growth is called nucleation phase. Besides its purely physical description it is marked by plasma chemistry, namely the ability of the precursor to form long living radicals and negative ions. The role of negative ions and formation of large molecules has intensively been discussed in section 3.2.
Those large molecules consisting of i elementary units, for acetylene the elementary unit would be either two C-atoms or one benzene, shall be named A_i. On their diffusive way through the discharge chamber they collide with other molecules of size j. With a certain chance those two clusters can attach to each other and form an even bigger molecule consisting of $i + j$ monomers:

$$A_i^{(\pm)} + A_j \longrightarrow A_{(i+j)}^{(\pm)}. \tag{3.58}$$

Because the relative thermal velocity between A_i and A_j, as already used in equation 3.2, scales with their relative mass M_R like $M_\mathrm{R}^{-1/2}$ and inserting $M_\mathrm{R} \propto ij/(i+j)$, the collision

rate coefficient must obey [25]

$$k_{i,j} = k_1 \sqrt{\frac{1}{i} + \frac{1}{j}} \cdot \left(i^{1/3} + j^{1/3}\right)^2 , \tag{3.59}$$

where it was also used that the collision cross section is proportional to the area given by the sum of each individual cluster radius $\propto i^{1/3}$. Besides the fact, that the absolute collision rate also depends on the densities n_i and n_j

$$R_{i,j} = n_i n_j k_{i,j} \tag{3.60}$$

the coefficient $k_{i,j}$ exhibits a minimum for $i = j$ for any size of the cluster A_i, illustrated in figure 3.11. The most effective combination for collisions, therefore is the collision between large i and small j and vice versa. It is the reason, why the large molecules collect reactive monomer on their way through the discharge. In [25] a critical size of $i = 10 \ldots 100$ monomers is given, from which on the collecting speeds up significantly, without any chemical considerations.
Not only can small clusters grow, but they also can get lost. Large molecules can break apart again, they can evaporate and they can get lost to the walls or electrode by diffusion and convection. External forces can drive the molecules out of the discharge, like a high pump rate or a high gas throughput. From a certain cluster size on a hot electrode might exert a thermophoretic force pushing the clusters towards the chamber walls.
As long as the loss terms outweigh the production of clusters, the nucleation stops before the critical cluster size is reached. Only, if the lifetime of large molecules is long enough and collisions occur sufficiently frequent, then nucleation is efficient enough to initiate particle growth. Because of the drastic change in collection efficiency once the critical nuclei size has been reached, the discharge behaviour is expected to also change drastically and suddenly with only a slight concentration increase around the according critical precursor concentration.
Impurities in the discharge can ultimately change the ability of a discharge to form particles. If for example an impurity reacts with the end-group of a large molecule, no further monomer can attach, and thus, chain reactions like 3.53 are terminated before reaching the critical cluster size. From above considerations it also becomes clear, that the chamber volume or more precisely the chamber volume in relation to the discharge pressure is a crucial parameter. In large volumes the residence time of reactants can be large at a given pressure and consequently more collisions can occur for a molecule before being lost to the walls by diffusion. Thus, the larger the chamber, the higher the risk to deal with particle formation even at lower pressures.
Another crucial point during the nucleation phase is the role of negative ions. As they are trapped in the positive plasma potential due to their low energy at room temperature, their residence time in the reactor is determined by their lifetime but not additionally shortened by diffusion to the walls. When bonding to a neutral molecule it may keep its charge like in the chain reaction 3.52 and then still be trapped. Growing bigger, the above given argument of enhanced collision probability for larger molecules now makes even more sense. Their participation in nucleation reactions, therefore, may be strongly enhanced.

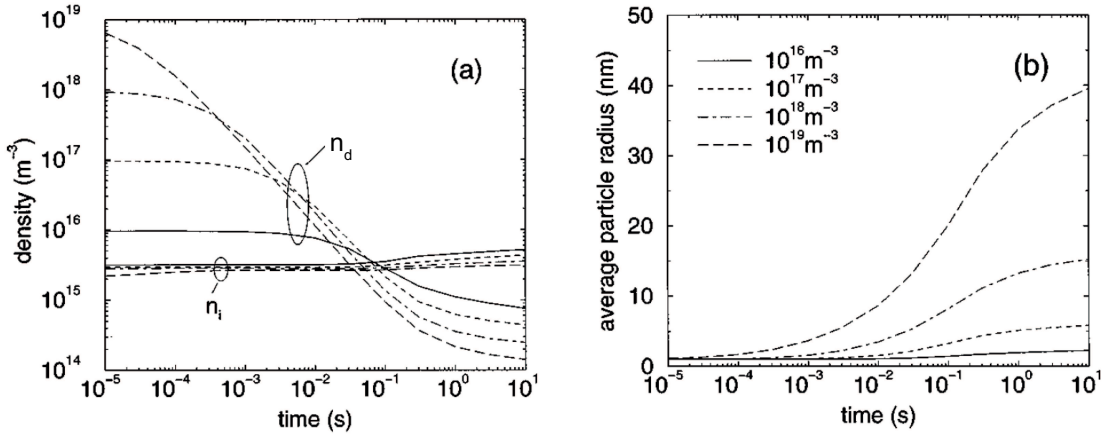

Figure 3.12: Different initial values of the cluster density n_d result in different evolutions and final densities. In (a) the density evolution is plotted, whereas in (b) the respective particle growth in terms of particle or cluster radius is shown. Also the ion density n_i is modified as a consequence of the permanent charge of particles after the coagulation event. From [195];

3.3.2 Coagulation phase

During this step the charge fluctuations as described in section 2.3.2 are of importance.
At certain cluster size, their collision with electrons is not that much determined by the wave functions of the molecule outer electrons, but can be stochastically described like collisions with hard micro-spheres. This size in the order of $r_d \approx 1\,\text{nm}$, which corresponds to a volume of $\approx 1000\,\text{Å}^3$ or in other words round about 1000 atoms, that is, in case of acetylene, 500 monomer units. The charge fluctuations produce negative clusters as well as positive ones and, hence, provoke a mutual attraction between the small clusters.
This has been described in more detail for low pressure plasmas for example by Kortshagen and Bhandarkar [195], who developed a model, which explains the coagulation of aerosols in a discharge. They don't only take the electron and ion currents into consideration but also the emission of electrons due to photoelectron and secondary electron emission. Therefore, the charge distribution on the clusters is shifted towards more positive values.
The mutual attraction leads to coagulation, which can happen on a very short time scale in the order of one second, as demonstrated in figure 3.12. It terminates, when all the positive charged nuclei have vanished by forming bigger particles. Those bigger particles then are permanently charged negatively and, therefore, repel each other. Here, a basic principle of particle formation is already imposed upon this model: As soon as the coagulation takes place, no significant amount of new nuclei is formed in the discharge any longer. Otherwise, after coagulation, there would still be a certain amount of positively charged clusters and coagulation does not stop.
The termination of nuclei formation may be explained by the high density of newly formed nano-particles, and hence, the big surface area, that suddenly appears in the centre of the discharge. It collects many of the reactive molecules, before they can collide with other precursor molecules in the volume, suppressing any kind of chain reaction. As can be seen

from figure 3.12, a high initial nuclei density leads to a small final particle density and a low initial nuclei density to the opposite, because then the resulting particle radius after coagulation is much bigger.
According to the model of Kortshagen and Bhandakar [195] the particle density n_d evolves with $t^{-6/5}$ during the coagulation phase. Therefore, the particle radius must increase with an inverse behaviour $r_\mathrm{d} \propto t^{2/5}$, because of the preservation of total particle mass:

$$n_\mathrm{d}(t) r_\mathrm{d}^3(t) = \text{const.} \tag{3.61}$$

For low discharge powers the model predicts strong decreases in the particle density during coagulation, and thus, large particles, when it is finished. The reason is the little charging of particles due to low plasma densities. As a rule of thumb the authors state, that the coagulation terminates, when the particle density has roughly reached the ion density $n_\mathrm{d} \approx n_\mathrm{i}$.
Whereas the ion density changes only slightly, the electron density is massively reduced after the coagulation due to the collection of electrons by the bigger nano-particles. In order to keep the discharge alive, more energy is transferred to the residual electrons on average. This is plausible in a global sense, as the power density delivered by the generator does not change. The sudden increase in average electron energy often is referred to as the α-γ'-transition [27, 196]. Fridman *et al.* [27] demonstrated in a model, that the transition is caused by a change of the electron loss mechanism. Whereas in the α-mode most of the electrons are lost to the reactor walls due to ambipolar diffusion, the majority is lost to the dust particles in the γ'-mode. In other words, the increase of electron losses provokes a rise in electron temperature. Consequently, they calculated, that the electron temperature can rise up to three times of the initial value.
In the α-mode electrons are heated through the small RF fluctuations in the bulk plasma, called ohmic heating. Usually in RF-discharges electrons can also be heated by the strong electric fields in the sheath region above the powered electrode. Here, the cyclic sheath collapse and expansion can kick electrons into the bulk plasma with high velocities. The latter heating mechanism is called stochastic heating and dominant in the γ-mode, which should not be confused with the γ'-mode. The γ'-mode simply serves as an analogy to the above described distinction of the heating mechanisms, which often exhibit an abrupt transition. During particle growth the α-γ'-transition also is very sudden. Furthermore, discharges in the α-regime are marked by a more resistive phase angle ϕ between current and voltage, than in the γ-mode, where the discharge becomes highly capacitive. For the α-γ'-transition, however, it appears, that the γ'-mode is more resistive due to high losses of electrons onto the particle surfaces.

3.3.3 Accretion phase

At the end of the coagulation phase the particle size is in the range of a few tens of nanometres. Hence, they behave like solid bodies in the plasma and charge up to the floating potential, forming a sheath around them. In this dusty plasma, as qualitatively described

in chapter 2.3, the further growth process can be described like thin film growth on a substrate.
The peculiarity of nano-dusty plasmas is the high surface area, that is provide by dense particle clouds. Additionally this surface is situated directly in the plasma volume, where dissociated reactive species originate from. Thus, the reactive molecules, like radicals and positive ions, are almost instantly consumed by the particle surface. Several measurements show, that the dust radius increases linear in time during this last growth stage [84,197,198]. Only when the dust density in the volume has decreased significantly is the precursor consumption not focussed on the particle surface any longer. Then new seed formation can happen as a result of increasing precursor concentration. This way a cyclic synthesis of nano-particles can be observed in many discharges.
Often, the old dust generation doesn't need to disappear completely from the discharge, before a new generation is born. If a void of sufficient size is formed, so that diffusion in it is slow enough to cause a sufficient amount of collisions between reactive molecules before reaching the dust cloud, a new generation can be born inside the void. This growth regime shall further be referred to as *multiple generation growth*, whereas in the *single generation growth* the seed formation can only proceed after complete vanishing of the former generation. A crucial parameter to switch between the two regimes is the discharge pressure, that mainly influences the diffusion length for reactive molecules.

Chapter 4

The plasma chamber ATILA

The main work of this thesis has been done on the PECVD reactor ATILA. Breaking down its complex geometry, its size can be estimated by a vertically aligned cylindrical tube of height 32 cm and a diameter of 44 cm. The entire chamber walls are grounded and therefore form the counter part of the powered electrode at the chamber bottom. The latter is embedded in a ceramic for insulation and of 12 cm in diameter. All the plasma facing components are built of stainless steel, except for small contributions from insulators and for the chamber windows, that are made of acrylic glass or conventional quartz glass.
The power is supplied via a matching network from Advanced Energy™, that is fed by the Cesar® Power Generator equally from Advanced Energy, which delivers up to 100 W at 13.56 MHz to the discharge. Because the electrode is capacitively coupled to the generator, it can charge up, which is monitored in the matching network and then passed to the generator via a RS232 interface. The generator then picks up the selfbias-voltage, forward power P_{fwd} and reflected power P_{refl} and transmits them to a LabVIEW program on the computer. Here the matching network can be chosen to either match manually or automatically. For particle growth experiments the matching network was always used in the automatic mode in order to keep the forward power stable, and thus, the power in the discharge.
At the same time an additional detector of the applied voltage and current is available in order to detect the phase angle between those two directly at the electrode. The instrument from Advanced Energy is called Z-Scan and is mounted between the matching network and the electrode, measuring in-situ and non-invasive. The phase angle can be capacitive (-90°), resistive (0°) or inductive (+90°). In this particular set-up it is mostly capacitive in the range of -80°.
The data obtained by the Z-Scan and the self-bias voltage, the electrical measurements, serve as process monitor as they are sensitive to any change in the reactor. Variations in pressure, power and gas mixture as well as the growth of nano-particles lead instantly to changes in the electrical characteristic of the discharge.
The vacuum in the reactor is obtained by a two stage pump system consisting of a dry scroll pump, which is an Edwards nXDSi pump compatible for reactive gases, and of a turbo molecular pump from Varian, which is fitted with magnetic bearings, running at a frequency of 200 Hz. The turbo molecular pump can be tuned up to 800 Hz of turning speed, but in

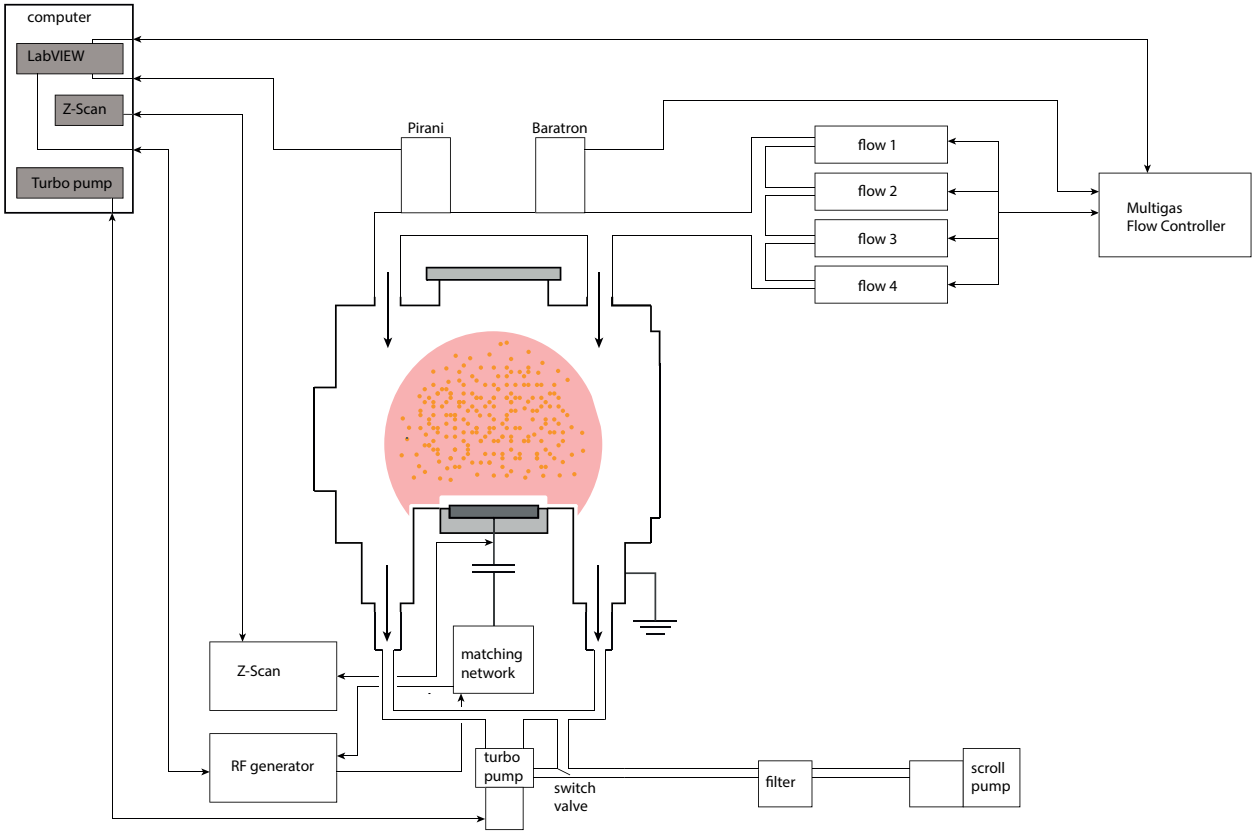

Figure 4.1: The experiment is mainly computer controlled and monitored by three different programs. Whereas the software for the Z-Scan and the turbo molecular pump are commercial, the LabVIEW software was developed in the workgroup plasma technology at the University of Kiel.

order to keep the gas fluxes low, 200 Hz was found to be a good value, resulting in round about 10^{-2} Pa base pressure.
After each experiment, the vacuum chamber is flooded several times with air and evacuated through a bypass, that connects the chamber directly to the scroll pump in order to avoid the turbo from getting filthy as good as possible. Furthermore, this way residual nano-particles are washed out of the chamber volume, minimizing health risk when opening the reactor besides wearing protective clothing and masks. After being flushed through the bypass the particles are collected in an additional filter in front of the scroll pump, because the carbon rich dust wears of the pump tip seal quickly and in order to reduce the dust load of the exhaust gas. Additionally a bypass in the scroll pump is used to dilute the process gases, which also is supposed to protect the seal from wearing of. Using the filter and the pump bypass the minimum intermediate stage pressure comes to round about 10 Pa, which is sufficient for operating the turbo molecular pump.
A MKS dual pressure gauge consisting of a Pirani and a Penning sensor covers the entire pressure range from 10^{-6} to 10^{5} Pa. Additionally for better sensitivity in the process pressure

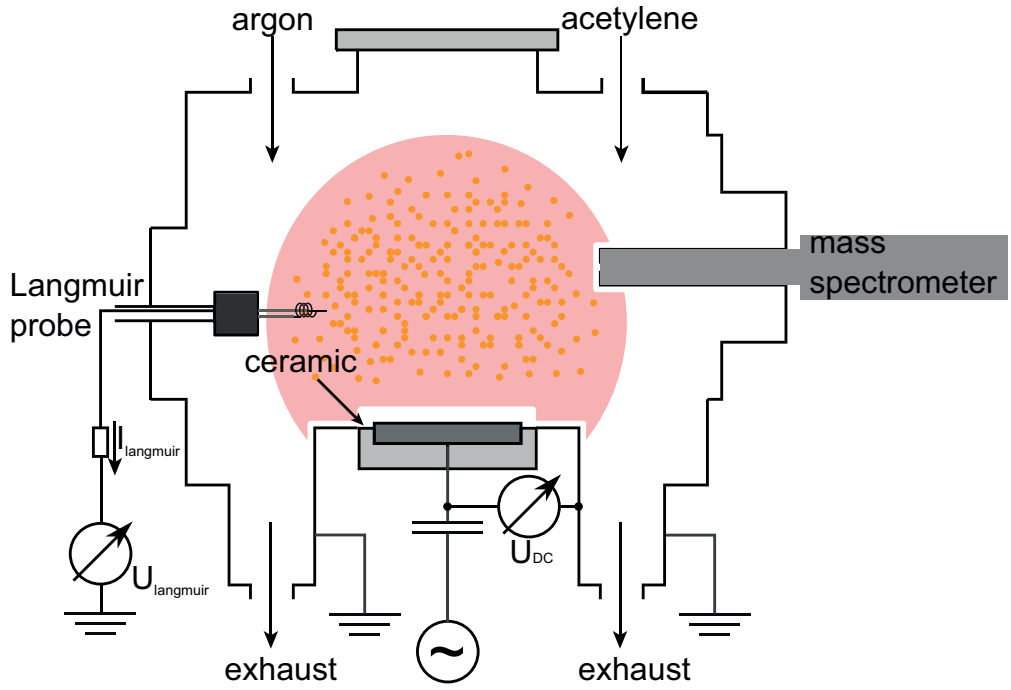

Figure 4.2: The principle setup of ATILA: While the nano-particle growth is monitored by the self-bias voltage measurement, here U_{DC}, different diagnostics can be applied through various flanges. Exemplary shown here are the simultaneous measurements with a Langmuir probe and a mass spectrometer.

range from 10^{-2} to 10^{2} Pa a MKS baratron measures independent of the gas type.
As the turbo molecular pump rotates continuously at 200 Hz the pressure needs to be controlled via the gas flow. Therefore, four MKS gas flow controllers of size 100, 50, 20 and 10 sccm can simultaneously be used for four different gases, respectively. With the help of LabVIEW™ they are computer controlled via the MKS Multigas Flow Controller, which also transduces the baratron signal. A controlling scheme is shown in figure 4.1.
A number of different flanges are available for conducting various measurements as demonstrated in figure 4.2. During this work flanges have been modified in order to mount a Langmuir probe, windows for phase resolved camera measurements and laser light scattering diagnostics, a mass spectrometer, a quartz crystal microbalance for monitoring deposition rates and movable substrate holders for the collection of particles. Those measurements will be presented separately in the following chapters including a theoretical overview for the comprehension of each technique.

4.1 Particle growth regimes

Depending on the collision rate $R_{i,j}$ between the reactive precursor dissociation products i and j in the discharge volume, different particle growth regimes can be realized in ATILA. Recalling equation 3.60, that describes the amount of reactions per volume and time, we can find the total amount of collisions per time $C_{i,j}$ between those two species by multiplying with the reactor volume V:

$$C_{\mathrm{i,j}} = n_i n_j k_{i,j} V. \tag{4.1}$$

Assuming, that the densities n_i and n_j are each directly proportional to the partial pressure of the precursor p_{p},

$$C_{\mathrm{i,j}} \propto p_{\mathrm{p}}^2 V \tag{4.2}$$

can be concluded. Thus, a big reactor is suitable for many collisions and with a given reactor size the only way to change the amount of collision events per second between reactive radicals, is to adapt the precursor flux, and thereby, changing the partial precursor pressure.

Thin film deposition regime If almost no collisions occur, the molecules can not attach to each other in the gas volume, but they deposit on the reactor walls and electrodes. Therefore, at very low precursor concentrations, no nano-particles are formed. Instead the conditions are suitable for thin film deposition. Using acetylene, in ATILA the thin film deposition regime can be achieved at precursor flow rates of $\Gamma_{\mathrm{C2H2}} \lesssim 1\,\mathrm{sccm}$.

Single generation particle growth At intermediate precursor concentrations, sufficient collisions on the molecules way towards the walls occur, so that nano-particles are formed before the reactive molecule is lost from the gas volume.
As already described in chapter 3.3, the dust particles, once having reached a critical size, repel each other and grow further by surface deposition of radicals. During the surface deposition phase, the precursor is almost completely consumed, so that its partial pressure p_{p} decreases strongly, and thus, no further nucleation can occur. In other words, the process switches into the thin film deposition regime, but with the already existing particles immersed in the plasma. It is only when the particles reach a size, that they are pushed out of the discharge, that the precursor concentration can recover and new nuclei can be formed. Because this only one generation of particles grows together at a time, we call this growth regime *single generation particle growth.*
It requires flow rates of round about $1\,\mathrm{sccm} \lesssim \Gamma_{\mathrm{C2H2}} \lesssim 2\,\mathrm{sccm}$.

Multiple generation particle growth Special attention needs to be paid to the void, that can be formed in the discharge center. Here, precursor consuming particles are absent. Therefore, its concentration can be locally higher than in the dust cloud. If the void volume V_{void} overcomes a critical size, one can again apply equation 4.2, but by replacing the reactor volume V with V_{void}. It becomes obvious, that the free void space may provide a cell for particle nucleation inside another dust particle generation, if the precursor concentration is sufficiently high.

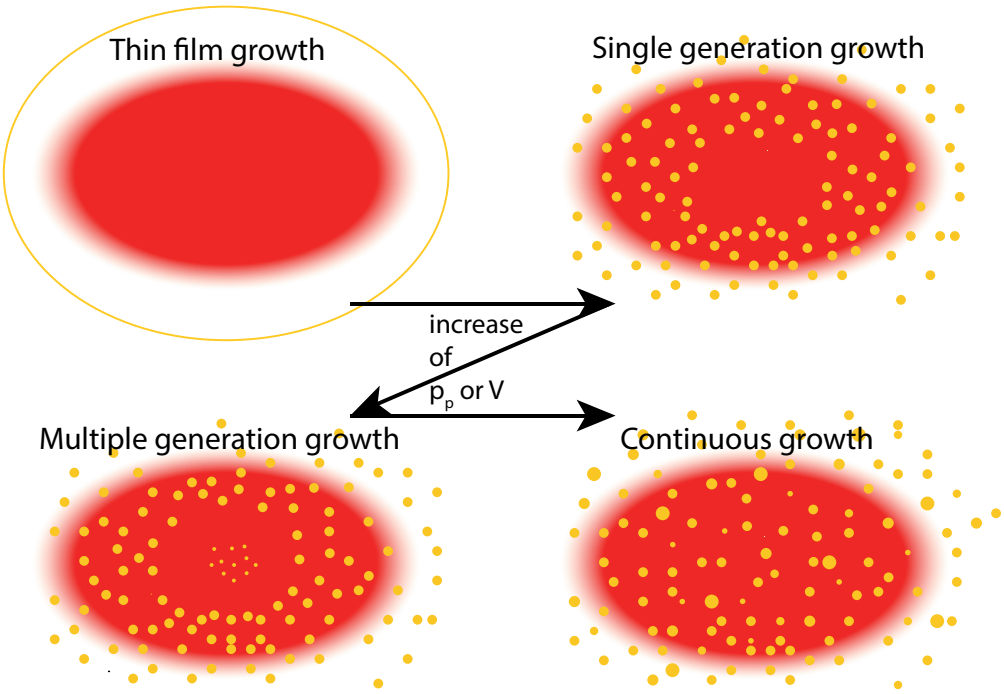

Figure 4.3: Four principally different growth regimes can be achieved by varying the precursor flow Γ_{C2H2} and thereby changing the partial precursor pressure p_p in the reaction chamber. Also the choice of the chamber size V plays a role.

Because the new nuclei then also grow together like the first generation, but the generations do not intermix with each other, and thereby form a seperate dust generation, we call this regime the *multiple generation particle growth*. In ATILA it can be obtained at values of $\Gamma_{C2H2} \gtrsim 2\,\text{sccm}$. However, as the void shape and size also depend on other discharge parameters like the total pressure and discharge power, it may vary slightly.
The multiple generation particle growth can include two or more generations at a time, because a new void can also form inside the dust cloud in the void. Using laser light scattering systems, as will be described later in chapter 6, onion-like structures can be observed in this case.

Continuous particle growth For very high precursor concentrations, the growth slowly moves into the *continuous particle growth regime*, where even small dust-free spaces fulfil the condition for nucleation. Then new nuclei are constantly being formed, and thus, the generations cannot be seperated from each other. This regime produces a huge quantity of dust in a short time, but it is much less controllable than growing particles in successive generations. The required precursor flow rate is rather large $\Gamma_{C2H2} \gg 2\,\text{sccm}$.
A principle sketch of the four different growth regime is depicted in figure 4.3. During this study, the single generation regime was chosen. It has the advantage, that any experiment is correlated to only one particle size of the actual single generation, that is present.

Chapter 5

Electrical measurements and particle size correlation

Throughout the thesis all measurements have been time-correlated to the simultaneously obtained self-bias voltage signal and it is therefore the basis of the experimental work. The self-bias voltage is part of the electrical measurements, which also include the phase shift between voltage and current at the powered electrode, as well as the forward and reflected power of the discharge.
Because the growth of nano-particles causes very distinct patterns in the electrical measurements, they can be utilized to estimate the progress of the actual particle generation or to identify the growth regime, e.g. they allow to distinguish between multiple and single generation particle growth, which have been desribed earlier in chapter 4.1. Deriving quantitative results for plasma properties from these measurements, however, is a more challenging task and requires the use of additional diagnostics.
As already mentioned, this thesis concentrates uniquely on the single generation growth regime. It's cyclic behaviour allows to compare different measurements over several growth cycles, because of the process stability. The process can run for several tens of minutes before switching to an other growth regime or before other significant changes can be observed. Typically, the deposition of dust and thin films on the chamber walls and electrode leads to an increase of precursor material in the gas volume by sputtering with ions. Therefore, after a rather long time, the process tends to shorter cycle durations and in extrem cases can switch to the multiple particle generation growth regime.
Furthermore, the conditions, at which single generations can be achieved, are relatively tight set in terms of the freedom in pressure, power and gas mixture. Therefore, already the evidence of working in the single generation particle growth mode ensures similar discharge conditions, and hence, good comparability between measurements of different experimental runs.
When starting a new process, however, a certain conditioning of the reactor can be observed, which mainly is the deposition of a thin film on the cleaned chamber walls and electrode. Therefore, in most experiments the first growth cycle differs from the following ones, and thus, often is not used in the diagnostic procedure.

5.1 Self-bias voltage and power

In figure 5.1 the principal shape of the the self-bias voltage in the single generation particle growth regime is shown together with the measurement of the reflected power in front of the RF generator. The yellow spheres sketch the growing particles, as confirmed by ex-situ SEM measurements, obtained in co-work with A. M. Hinz [84], where an average cycle duration of $T = 166 \pm 20\,\mathrm{s}$ was determined. The evolution of the voltage can be divided into three separate phases as also depicted. The choice of the distinction was purely made upon the signal shape. Whereas the self-bias voltage during phase I is stable and close to the the value of a pure argon discharge, it then rapidly increases during phase two, towards more positive values. Note, that the absolute value of the voltage decreases due to its negative polarity. The slight decrease at the beginning of phase I can be attributed to a small pressure increase, as will be presented in chapter 9.

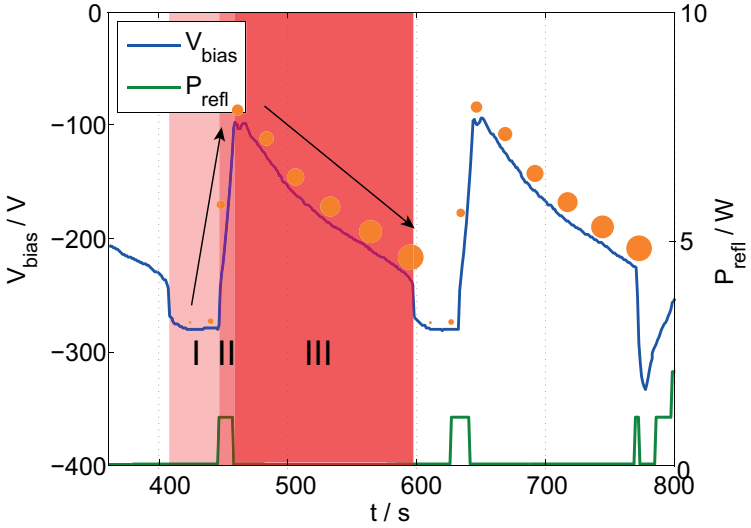

Figure 5.1: The self-bias voltage cycle can be divided into three distinct phases. In phase I particles start to form and the voltage is relatively stable, during phase II a rapid increase towards to smaller absolute values takes place and in the last phase, III, the signal slowly recovers towards its initial value. During the rapid change in the discharge characteristic at the end of phase I, the automatic matchbox reacts too slow to match the discharge to zero reflected power.

Depending on the discharge conditions, the voltage change during phase II is immense, in the here given example a drop from roughly -280 to $-100\,\mathrm{V}$, in fact it is too strong to originate from an effective discharge power or pressure change, see figure 3.6 in chapter 3.1.2. Therefore, a drastic change in the discharge characteristic needs to be considered at the end of phase I. Recalling equation 2.39 any decrease in the self-bias voltage can be linked to a decrease of the plasma potential or a decrease of the symmetry factor B/A of the plasma facing electrodes. Whereas the first is not trivial to obtain, the latter can be attributed to a change of the plasma size during particle growth, as already quantitatively

described in chapter 3.1.2. Indeed it can be seen easily by naked eye, that the intense plasma glow approaches the electrode and is actually the closest, when the self-bias voltage is at its maximum, further confirmed in chapter 8.
The sudden transition from a stable plasma in phase I to the fast changing electric signals may be related to the permanent negative charging of the nano-particles. The permanent charging is the outcome of the coagulation phase as described in chapter 3.3.2, which is an event on a short time scale in the order of one second. So it is quiet consistent with the fast transition of an undisturbed plasma in phase I to a disturbed one in phase II. Furthermore, as also discussed in chapter 3.3.2 the end of the coagulation phase is associated with the transition of the α- to the γ'-mode. This in turn is caused by a change of the electron loss mechanism, which again might be linked to the loss of electrons onto the particle surfaces.
Another feature displayed in figure 5.1 is the small reflected power at the transition from phase I to II. It is probably related to the inertia of the automatic matching unit. In fact the change of the plasma happens to be so drastic, that the electric motors adjusting the capacitors in the match box can not react quickly enough. However, the percentage of reflected power is in the range of 10 % of the forward power and therefore sufficiently small to be insignificant in the overall process. Nevertheless, it demonstrates the rapid modification of the plasma by particles, that pass a critical size.

5.2 Phase angle

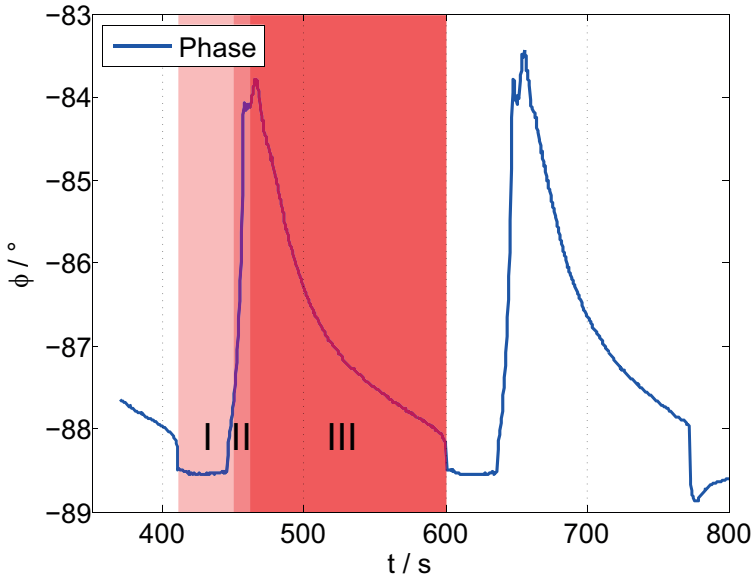

Figure 5.2: The phase angle ϕ resembles much the qualitative evolution of the self-bias voltage. Being relatively stable at an almost purely capacitive value of $-89\,^\circ$ during phase I it changes rapidly in phase II towards a slightly more resistive value of $-84\,^\circ$. It then slowly recovers to the initial value during phase III.

Another measurement indicating the α-γ'-transition is the phase angle ϕ between the applied voltage and current. As presented in figure 5.2 it qualitatively resembles the evolution of the self-bias voltage. In detail the phase angle is also stable during phase I, increases drastically in phase II and recovers slowly during the last phase. Also the small jumps at the beginning and end of phase I are visible.
The phase angle is the result of a complex plasma resistivity linking the applied voltage and current:

$$\underline{U}(t) = \underline{Z} \cdot \underline{I}(t). \tag{5.1}$$

The real part of $\underline{Z}$

$$\underline{Z} = R + jX \tag{5.2}$$

is the ohmic resistance R, produced by the limited drift velocity of the charge carriers in the bulk plasma. The imaginary part X consists of a capacitive, C, and an inductive, L, component:

$$X = -\frac{1}{\omega C} + \omega L. \tag{5.3}$$

The inductive component originates from the charge carriers inertia upon the time varying external field, whereas the capacitive part is mostly determined by the sheath. Here the charge of the electrodes faces the plasma potential in a distance of the sheath thickness, like two charged parallel plates separated by a certain distance in a capacitor.
Consequently, a by 90 ° negative angle indicates a perfectly capacitive discharge with a low resistivity in the plasma bulk. Two possibilities are favoured to explain the transition towards a more resistive discharge in phase II: Either the bulk plasma becomes more resistive or the sheath capacitive impedance decreases. Both explanations have the same idea in common: The power is less dissipated in the sheath and more in the bulk, in other terms the electron losses become more important in the bulk.
It is obvious, that the sheath capacitance must change, because the self-bias voltage also changes, and thus, the sheath voltage: $U \approx V_{\text{bias}}$. Taking Child Langmuir's law 2.24 we can see, that

$$U^{3/2} \propto j_{\text{i}} \cdot d^2 \tag{5.4}$$

this needs to induce a change in the sheath thickness, if the current density doesn't adjust in exactly the same way as the tension. So in general a lower absolute value of the self-bias voltage induces a smaller sheath in front of the powered electrode, and therefore, the capacitive impedance must decrease, too.
Furthermore, also an increase in the plasma resistivity is plausible as the nano-particles, once charged, act as an additional sink for ions and electrons. In other words the electron density n_{e} decreases. What's more, the electron-neutral collision frequency ν_{ne} may increase due to more energetic electrons in the dusty plasma [84]. Both parameters influence directly the plasma conductivity [15]

$$\sigma_{\text{e}} = \frac{n_{\text{e}} e^2}{m_{\text{e}} \nu_{ne}} \tag{5.5}$$

towards smaller values, and hence, a higher ohmic resistivity.

5.3 Particle size measurement

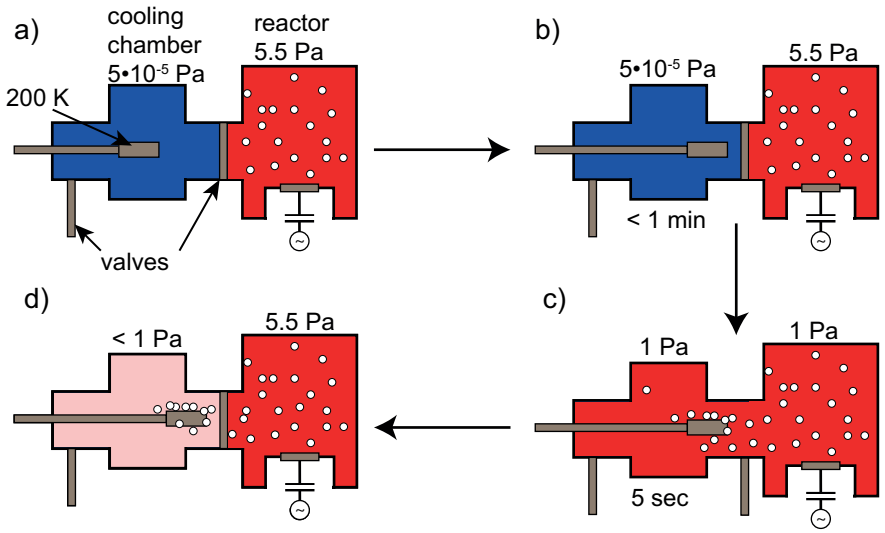

Figure 5.3: The sampling of nano-particles was done by the aid of a second chamber at lower pressure (a). By opening the valve in between the reactor and the cooling chamber a neutral gas flow transported the particles out of the reactor and onto a cooled sample (c). Taken from [161] and modified to English;

In order to determine more precisely at which critical size the transition between phase I and II occurs, a collection experiment in co-work with A. M. Hinz was conducted. The technical details are described in [84] and shall not be discussed here. In short, the following collection concept was applied: A second chamber was installed next to the reactor, containing a cooled sample holder, where two silicon wafer pieces were mounted, one with its surface normal pointing towards the reactor, the other one with the surface normal perpendicular to it.
Because the pressure in the cooling chamber was kept five orders of magnitude below the one in the reactor, a significant gas drag acted on the particles upon opening of the intermediate pneumatic valve. The nano-particles were then pushed onto the substrates. A schematic drawing of the sampling method is shown in figure 5.3. The substrates were cooled down to 200 K in order to enhance the sticking of the dust.
The rapid pressure decrease when opening the valve left traces in the electrical measurements, which allowed for determining the exact point of time of the collection t_{coll}. This point of time was then correlated to the precedent growth cycle, so that the reduced time t_{red} within the period of one growth cycle T could be calculated:

$$t_{\mathrm{red}} = \frac{t_{\mathrm{coll}}}{T}. \tag{5.6}$$

The ex-situ analysis of the samples by SEM measurements then allowed to derive the exact size distribution of the particles at different reduced collection times within the growth cycles. The resuming result is presented in figure 5.4. Some experiments were done without

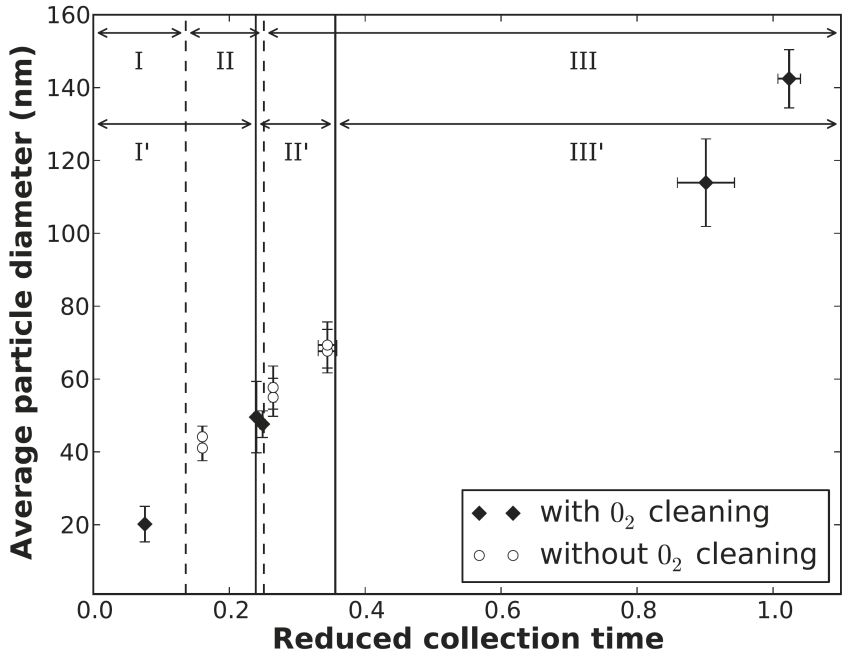

Figure 5.4: The particles grow almost linear in diameter, when plotted versus the reduced collection time. The full check sign data stand for particle growth experiments after having the reactor cleaned with an oxygen plasma, the empty circles represent experiments without having the reactor cleaned before. The corresponding phases within the growth cycle are denoted with I',II',III' and I,II,III, respectively. Taken from [84];

having the reactor cleaned before and for others an oxygen plasma was used to clean the electrode and chamber walls. This resulted in different cycle durations, especially phase I was much longer for the latter case, as also shown in the above mentioned figure.
This result can be explained in two ways. The oxygen plasma basically burns all the surfaces it is in touch with, which means it can act on molecules by splitting them into small pieces and oxidizing them, in this case to either CO_2 or H_2O in principal. Because the plasma also is in the volume in may additionally remove any residual seeds from the gas phase, like big molecules, that by hazard have not been pumped out. These seeds may speed up the first phase of nano-particle formation and therefore lead to shorter cycle times.
The other possibility is, that the removal of relatively volatile products from the chamber walls and electrode reduce the amount of sputtered reactive species during the particle growth process. In fact, it was observed, that after long process times the plasma is able to generate stable growth cycles without any addition of acetylene, only by sputtering. Because the reactive species concentration is especially crucial during the first phase of particle formation, clean reactor walls may also lead to longer growth cycles.
However, both conditions lead to similar results, that can be summarized as follows: During phase I particles start to form, the exact onset of particle production cannot be determined by the electrical measurements, but no small particles were found in the end of phase III, so

they need to start growing some-when in phase I. The smallest detected size in this set of experiments was 20 nm in diameter, however, smaller ones down to 10 nm have already been found.
During phase II they grow from round about 40 nm to 50 nm in diameter. Therefore, it can be concluded, that the critical size at which the particles start to influence the discharge is shortly below 40 nm. It is a relatively large size at which, taking classic considerations 2.57, the particles should already carry around 70 elementary charges.
In phase III the particles grow steadily up to round about 150 nm. Here the growth mechanism is clear, it corresponds to the accretion phase dominated by the deposition of radicals and ions on the particle surface. Nevertheless it is unclear, why the self-bias voltage slowly recovers in this phase, whereas the particles still grow, and thus, attract more and more electrons. This question and also the jump of the voltage at the end of phase III will partly be answered in chapter 6.
One very critical problem arises from the particle size measurements, which questions, that the particles undergo the coagulation phase as described in chapter 3.3.2. From a simultaneous coagulation for all particles one would not expect any effect on the discharge before the coagulation but due to the permanent charge a significant influence afterwards. That would correspond to the transition from phase I to II. However, it then cannot be explained how relatively large particles of 20 nm can even be found before the transition, because they are too big to be considered as primary cluster in the nucleation phase.
In order to resolve the paradox more precise information about the dust density and distribution and also about the plasma parameters, e.g. the electron and ion densities, n_e and n_i, respectively, as well as the electron temperature T_e and the plasma potential Φ_{pl}, are required. The following chapters present some measurements with exactly this aim in mind.

Chapter 6

Laser light scattering at dense particle clouds

Apart from the induced changes, which may result in a stronger light emission or a change in the plasma sheath thickness, nano-particles are not visible for the human eye. Therefore, a laser beam or laser sheet is commonly used in scattering (LLS) experiments. The typical set-up consists of the laser, in some cases some optics, and a camera, that detects the scattering signal. Often a filter in front of the camera is used in order to suppress the background from the luminous plasma. For very small particles the scattering needs to be described by Rayleigh scattering, when the particle size is in the order of the light wavelength Mie theory needs to be applied [65, 198, 200–202] and for big particles the scattering becomes a subject of geometric optics.
The laser light scattering experiments have been performed in 2017 together with Zahra Marvi during her stay as a guest scientist at the Institute of Experimental and Applied Physics of the Kiel University.
LLS experiments can be done in transmission mode, where the extinction of a laser is measured or in scattering mode. The first is much easier to set-up by simply using a laser and a light detection instrument [203] and it has already been done in former works [55]. However, it can not resolve spatially as it remains a line-integrated method. Hence, here the scattered laser light, coming back from the nanoparticles, was recorded with a camera in a 90° angle. Because no information on the polarization state and no angular variation has been performed but only the green part of light has been recorded, the measurements can be resumed to be of photometric nature. For an extensive overview over photometry the interested reader may refer to the handbook of optics from Bass *et al.* [204].

Rayleigh scattering Rayleigh scattering is based on the electric dipole moment $\vec{p}$ of the scattering particles. If the wavelength of the light $\lambda = 2\pi c/\omega > 10 r_\mathrm{d}$ is greater than the dimension of the particle, its dipole moment is excited in the passing electromagnetic field of the light, absorbing it partly and emitting the same wavelength with an intensity distribution and polarization according to the emission from a dipole antenna. Therefore, the scattering intensity in direction of the incident light ($\theta = 0$) is maximal, whereas half of that intensity

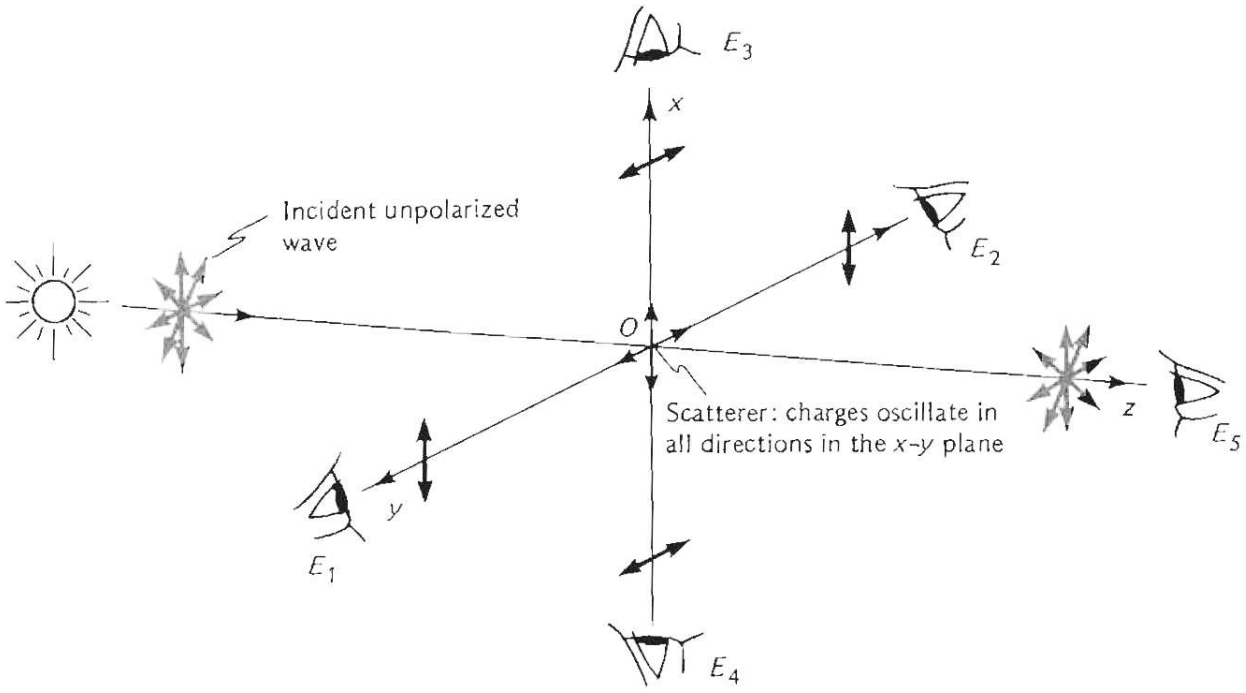

Figure 6.1: Due to the induced directional charge fluctuations inside the nano-particle, the Rayleigh-scattered light is linearly polarized for a 90° scattering angle. From [199]

can be found orthogonal, $\theta = \pi/2$, to it:

$$I(\theta, r) = \frac{\omega^4 |\vec{p}|^2}{32\pi^2 \varepsilon_0 c^3 r^2} \left(1 + \cos^2\theta\right) \tag{6.1}$$

Here ε_0 denotes the absolute permittivity in vacuum, c the according speed of light and r is the distance to the scattering particle. The term in the brackets consists of share of light with polarization perpendicular to the scattering plane (1) and parallel to it ($\cos^2\theta$). For practical reasons and a good signal to noise ratio, the camera usually is mounted in a 90° angle to the optical laser axis and a laser of high frequency ω is of advantage. Then the scattered light is exclusively linearly polarized perpendicular to the axis of the incident laser beam, as depicted in figure 6.1.
Often, an already polarized light source, e.g. a laser is used. Also in this case, only the perpendicular component is scattered, so that, for a high scattering intensity, the polarization direction of the light source needs to be chosen correctly.
Following [205, 206], equation 6.1 can be rewritten by the use of the scattering cross sections for perpendicular and parallel to the scattering plane polarized light, $\sigma_{\mathrm{s,o}}$ and $\sigma_{\mathrm{s,p}}$ respectively:

$$\begin{aligned} \sigma_{\mathrm{s,o}} &= \frac{\lambda^2}{4\pi^2} \alpha^6 \left| \frac{\bar{m}^2 - 1}{\bar{m}^2 + 2} \right|^2 \propto \frac{r_{\mathrm{d}}^6}{\lambda^4} \\ \sigma_{\mathrm{s,p}} &= \sigma_{\mathrm{p,o}} \cos^2\theta \propto \frac{r_{\mathrm{d}}^6}{\lambda^4}, \end{aligned} \tag{6.2}$$

where the coefficient α is the often used size parameter

$$\alpha = \frac{2\pi r_\mathrm{d}}{\lambda} \tag{6.3}$$

and m is the complex refractive index of the dust material:

$$m = n - \mathrm{i}k. \tag{6.4}$$

The use of an average complex refractive index $\bar{m}$ in equation 6.2 simply accounts for the possibility of different sphere materials, like N_2 and O_2 for the scattering of sunlight in the atmosphere. Here, the value used in publications of Greiner *et al.* [66, 198] of

$$m = 1.54 + 0.02\mathrm{i} \tag{6.5}$$

can be applied for carbonaceous nano-particles grown from acetylene.
The scattered intensities can then be related to the cross sections as a function of the incoming laser beam intensity I_0 as

$$\begin{aligned} I_\mathrm{s,o} &= I_0 \frac{1}{r^2} \sigma_\mathrm{s,o} \\ I_\mathrm{s,p} &= I_0 \frac{1}{r^2} \sigma_\mathrm{s,p} \end{aligned} \tag{6.6}$$

Consequently, as follows from equation 6.2 the scattered intensity is dependent on the particle size to the power of six. Therefore, Rayleigh scattering is difficult to observe for very small dust grains.
For extinction measurements it is useful to know the extinction cross section σ_ext. All light, that is either scattered or absorbed, gets extinct in forward direction, so it must be

$$\sigma_\mathrm{ext} = \sigma_\mathrm{sca} + \sigma_\mathrm{abs}, \tag{6.7}$$

where σ_sca and σ_abs stand for the total cross sections of absorption and scattering, with the latter being the integral of $\sigma_\mathrm{s,o} + \sigma_\mathrm{s,p}$ over all possible scattering angles θ:

$$\begin{aligned} \sigma_\mathrm{sca} &= \frac{2\lambda^2}{3\pi} \alpha^6 \left| \frac{\bar{m}^2 - 1}{\bar{m}^2 + 2} \right|^2 \\ \sigma_\mathrm{abs} &= \frac{-\lambda^2}{\pi} \alpha^3 \cdot \mathrm{Im} \left[\frac{\bar{m}^2 - 1}{\bar{m}^2 + 2} \right]. \end{aligned} \tag{6.8}$$

As long as the imaginary part k of the refractive index m is not negligible, the extinction is strongly dominated by the absorption at particles due to the α^3 dependence versus α^6 in the case for scattering, keeping in mind, that $\alpha \ll 1$ for Rayleigh scattering. Here, however, the particles are almost perfectly dielectric and therefore have a very small imaginary part in the refractive index as given in 6.5, thus they are not absorbing. Then the extinction is defined by the scattering of light:

$$\sigma_\mathrm{ext} \approx \sigma_\mathrm{sca} \propto \frac{r_\mathrm{d}^6}{\lambda^4}. \tag{6.9}$$

That's why in dust clouds from acetylene, extinction measurements are equally sensitive to the dust radius as scattering measurements, and hence, also difficult to measure for very small dust grains. Another obstacle in dusty plasmas may be multiple scattering, which depolarizes the scattered light and also leads to a more isotropic intensity distribution.
If the beam passes through a particle cloud, the scattering of multiple spheres needs to be summed up. Assuming a dust density distribution $n_\mathrm{d}(z)$ across the beam path l through the dust cloud, the detectable transmitted intensity I_tra of a laser beam passing through the dielectric cloud is given by the Lambert-Beer law to

$$I_\mathrm{tra} = I_0 \exp\left(-\sigma_\mathrm{ext} \int_0^l n_\mathrm{d}(z)\mathrm{d}z\right) \tag{6.10}$$

or

$$I_\mathrm{tra} = I_0 \exp\left(-2\sigma_\mathrm{ext} \int_0^R n_\mathrm{d}(r)\mathrm{d}r\right) \tag{6.11}$$

for a radially symmetric cloud shape $n_\mathrm{d}(r)$ with $r = 0$ for the discharge centre and $r = R$ for the outer cloud boundary.
From above given considerations about the polarization state of scattered light, it becomes obvious, that care needs to be taken of linearly polarized incident light, as it often is the case for LLS experiments. When setting the polarization parallel to the scattering plane, ideally no intensity will be scattered sidewards in a 90° angle. In the opposite case of perpendicular polarization the forward and sidewards scattered intensities are equal in the scattering plane.

Mie Scattering When the dust size reaches the same order of magnitude as the laser wavelength $0.1\lambda < r_\mathrm{d} < 20\lambda$, the scattering becomes more complex. Hence, using a green laser, typically at a wavelength of 532 nm, the Mie scattering slowly starts at a particle size of $r_\mathrm{d} \approx 50$ nm or a diameter of ≈ 100 nm already. Because here the polarization and intensity distribution $I(\theta)$ are strongly dependent on the particle size, it can be utilized for in-situ particle size and density detection [63, 66, 198]. However, multiple scattering for the case of optical dense clouds challenges the precision of this technique [66, 207] and makes it necessary to develop new models. It shall be mentioned here, that the scattering of light at nano-particle clouds is not only a laboratory problem, but also of strong interest in astrophysics. Therefore, existing models describing transmission through and scattering at interstellar dust clouds can be adopted here [207] to the usually even simpler laboratory dusty plasmas. In low temperature plasmas the particles can mostly be assumed to be spherical, the incident light can be chosen to be monochromatic and all scattering angles can be observed.
In this study, the maximum size of grown particles was found to be ∼150 nm in diameter, which is roughly 0.25λ for the wavelength 532 nm of a green laser. Up to this ratio, the Mie theory results in similar intensities as the Rayleigh theory and the more handy expressions of the latter can be applied. Therefore, the Mie theory shall not be discussed in detail here.

Geometric optics In the geometric limit $r_\mathrm{d} > 20\lambda$ the scattered light becomes a complex function of the dust size and the refractive index of the scatter medium, which is of interfer-

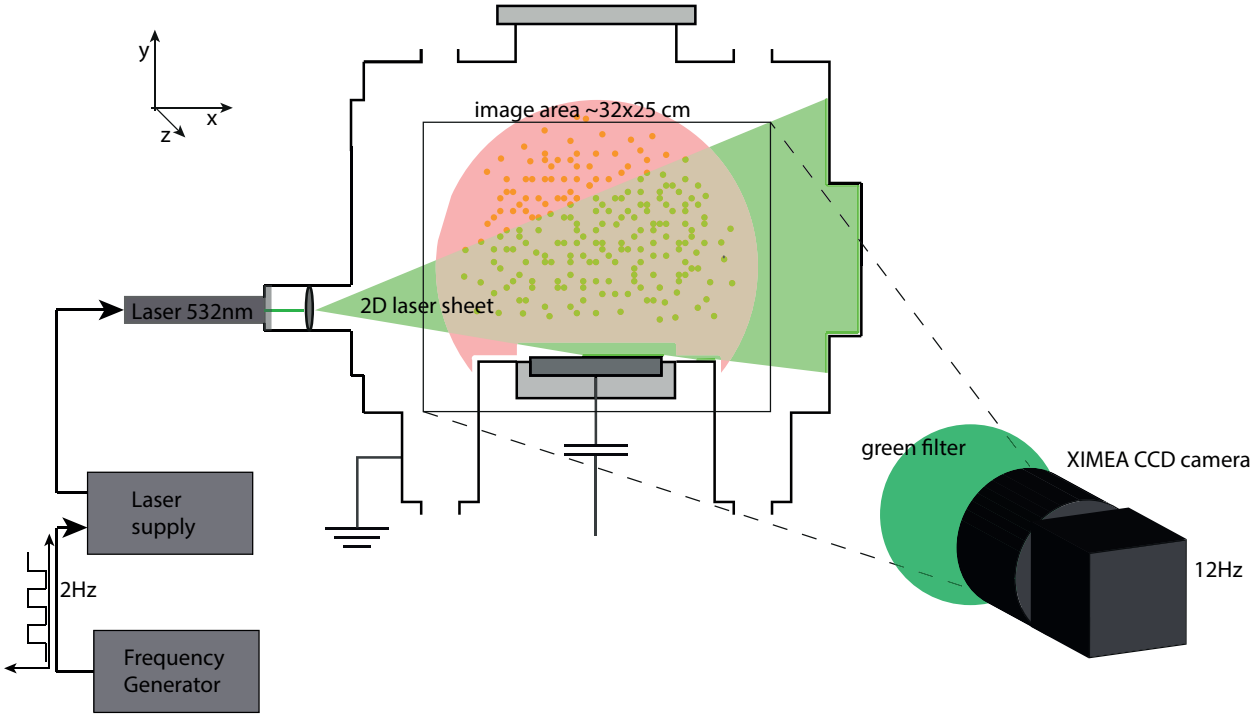

Figure 6.2: A laser beam is widened to a 2D-sheet illuminating a central cut through the nano-particle cloud. A CCD camera is mounted in a 90° angle, here in z-direction in order to have the image plane in x-y orientation with focal point in the 2D-sheet. The image area is 32x25 cm^2. A bandpass filter blocks most of the discharge emission but transmits the laser reflection to the camera.

ence nature. A popular example for this case is the diffraction of sunlight in water droplets, leading to rainbows. In the case of the particle sizes produced during this work, however, the geometric limit is not of interest and shall not be further discussed.

6.1 Setup

The setup for LLS measurements consists of a 350 mW strong green laser at 532 nm wavelength coupled into the reactor by a quartz window. The beam shape optics for generating a two dimensional beam in the x-y-plane of 30° opening angle are mounted right behind. Perpendicular to the laser sheet, in z-direction, a high resolution CCD camera from XIMEA can record at a frame rate of up to 12 frames per second at the given light intensities. For better signal to noise ratio a bandpath filter is mounted in front of the camera optics, transmitting green light.
The laser is supplied by a proper power supply, designed for fast laser on and off switching rates, which in turn is controlled by a square wave voltage from a frequency generator. The square wave delivers +5 V for the laser to be switched on an 0 V for it to be switched off at a rate of 2 Hz. Therefore, running the camera at its highest frame rate, three frames can be

taken during each laser on and laser off time, which is necessary for the post processing of the videos.
In order to minimize the noise by diffuse reflections of the laser light at the chamber walls, carbon fiber velvet, a vacuum compatible tape consisting of carpet like micro carbon fibres, was installed at the exposed spots. It almost completely absorbs the incident laser light. The XIMEA camera with a CCD chip of 2048x2048 pixels resolution is mounted in front of a quartz window with a zoom objective focussed onto the electrode centre. For laser safety the beam path is completely enclosed in metal housings and the camera window and optics are installed inside an impermeable textile shielding, so that no laser light can leave the setup. The videos are recorded in uncompressed RGB colour format, using a *LabVIEW™* program after setting the camera parameters adequately in the National Instruments Measurement & Automation Explorer. For good light sensitivity a maximum frame rate of 12 Hz corresponding to an exposure time of 80 ms was chosen.

6.2 Post processing of the laser light scattering videos

In order to subtract the background originating from plasma emission and from laser reflections at the chamber walls, the raw video data need to be processed. A *MATLAB™* routine is developed, that half-automatically detects the laser off and on times, does an averaging of the frames within those times and produces a black and white video of 2 Hz frame rate corresponding to the laser on times. Finally the collected data can be correlated to the electric signal of the self-bias voltage. In the following section the processing method and its difficulties shall be introduced and discussed briefly.
At first the LLS video needs to be read in into Matlab as well as the corresponding self-bias voltage signal together with the respective times and dates. A synchronization makes sure, that the time axis of the electrical measurements fits to the frame times of the movie file. The movie file is then converted into a black-and-white video by picking the green pictures out of the three RGB pictures per frame. This minimizes the calculation time for processing the data.
In the next step a region of interest (ROI), defined by two x-y coordinates, is chosen manually by clicking into an exemplary frame of the movie, in which a strong laser reflection at the electrode can be seen. The ROI needs to contain a region of strong reflections in order to serve for the detection of the laser on and laser off frames in the next step, as indicated in figure 6.3
The detection of the laser period is done by averaging the intensity of the ROI and plotting it against the frame number. The signal clearly fluctuates at the frequency of 2 Hz, which corresponds to 6 frames. A threshold intensity is defined, below which a frame is sorted to the laser off time, represented by the black stars in figure 6.4. All the other frames are considered as taken during the laser was switched on (red stars). This way frames, that are taken when the laser switches on or off and therefore are not illuminated throughout the entire exposure time, are considered as laser on frame. As a smoothing of those data (solid red line) reveals, this turns out to result in a more stable intensity than using a threshold

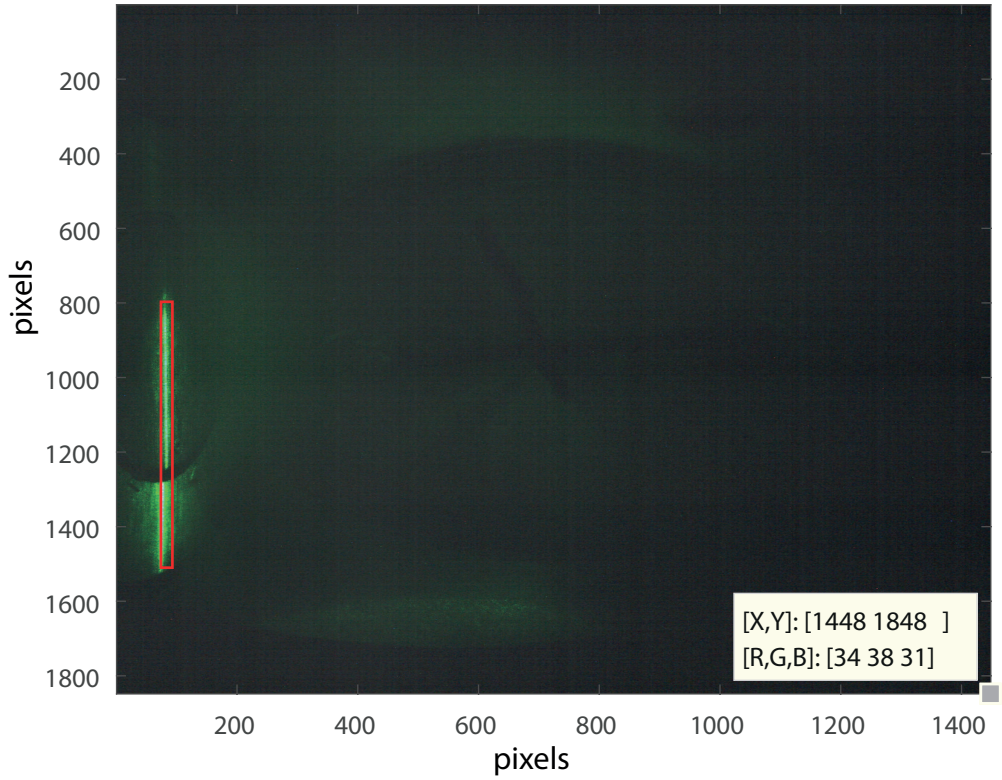

Figure 6.3: The laser beam is strongly reflected on blank surfaces. This is used to determine the frames taken during laser on and laser off period from a region of interest, here marked in red. From the 2048x2048 available pixels only 1848x1448 pixels are used in order to increase the frame rate and to minimize storage usage.

for the laser on frames as well (solid green line).
The upper step is one of the most critical and difficult during the post processing of the raw image data. Because the laser off frames are used for background subtraction it is necessary to sort them correctly. As the background intensity varies in time due to a constantly changing plasma emission, the threshold for detecting those frames has to be changed accordingly. Therefore, the threshold is redefined every 12 frames using a percentage (for example 110 %) of the minimum intensity within those 12 pictures. Another difficulty, as can be seen in figure 6.4, is the strong instability of the laser. It is not clear, where the instability originates from, but it may be the power supply from the 220 V power grid, which already supplies the discharge. Using all residual frames, which have not been sorted to the laser off times, and averaging over all frames within one laser on period (red solid line), results in an intensity evolution with the less fluctuations due to rather good stochastic. However a slight flickering still remains after this treatment.
Having all frames during each laser on and laser off period averaged, the data are now ready for subtracting the background. The laser off pictures directly yield a video of the plasma emission, that passes through the filter in front of the camera at a frame rate of 2 Hz. The laser on frames, however, contain not only the LLS signal but also the plasma emission.

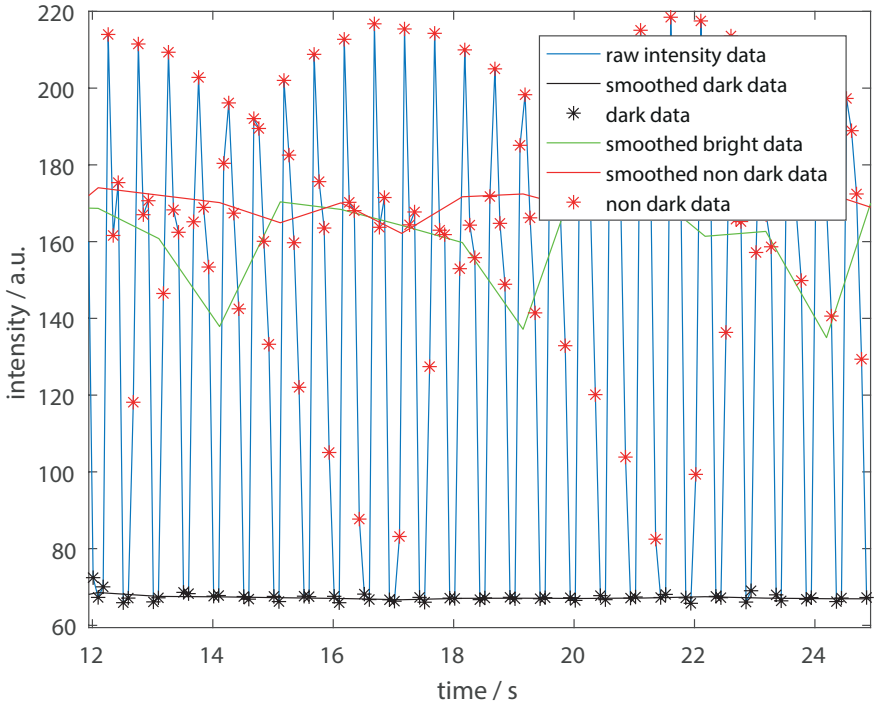

Figure 6.4: During laser off times, the background intensity is given by the plasma emission (black stars). When the laser is switched on, the intensity is much less stable due to laser instabilities. Therefore an averaging of all frames within each laser on period (red stars) has to be done (solid red line). If a threshold is used for detecting the laser on times, the smoothed signal (green solid line) fluctuations are higher than if all frames, that don't correspond to laser off, are considered as laser on (solid red line).

Thus, each laser off picture P_{bckg} is subtracted from the following laser on frame P_{on} and, hence, the LLS signal is extracted, resulting again in a video with frame rate 2 Hz.
This is where the calibration file comes into play. Because the LLS signal still contains noise from reflections of the surrounding walls and the electrode, a single picture P_{cal} is obtained by averaging the laser signal in the same way but having the plasma shut off. It is then subtracted from the LLS signal, so that the resulting video frames $P(t)$ can be summarized by:

$$P_{\mathrm{LLS}}(t) = P_{\mathrm{on}}(t) - P_{\mathrm{bckg}}(t) - P_{\mathrm{cal}}. \tag{6.12}$$

In a final step the videos can not only be synchronized with the self-bias voltage but also with the other electrical measurements. In this chapter slight changes in the gas pressure shall also be presented.

6.3 Experimental results

Several LLS measurements for different pressures, flow ratios of argon to acetylene and powers have been done. For the scope of this work, it is sufficient to present only one measurement

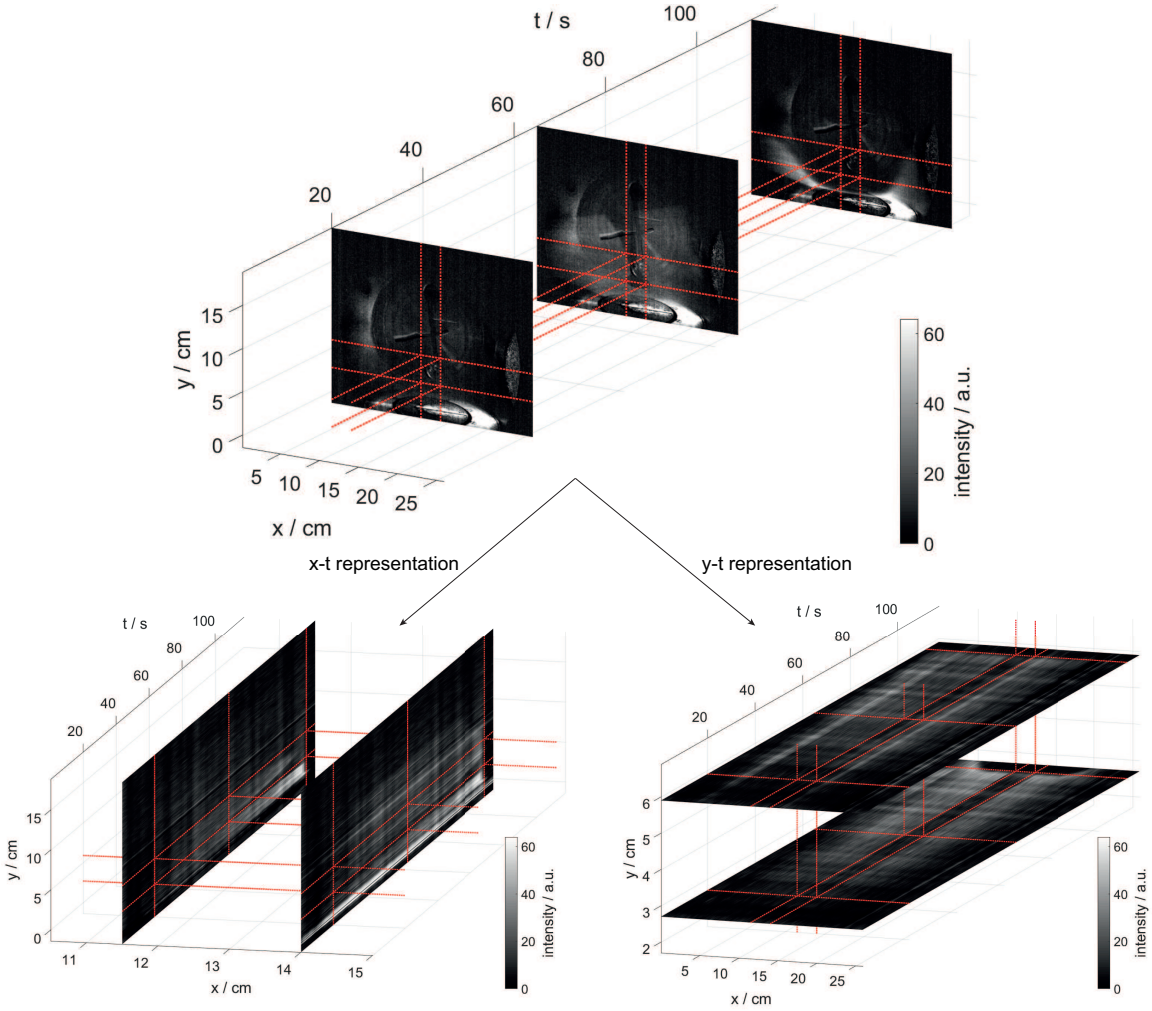

Figure 6.5: The three dimensional data (x-y image plane and time t) can be presented in three different manners. Whereas the upper plot delivers precise information about the spatial distribution, the two lower plots allow a more precise analysis of the temporal evolution along one spatial dimension.

and to further discuss the principal influence of the above given parameters.
Here, LLS signals for argon and acetylene flow rates of 10 and 1.3 sccm respectively, resulting in 4 Pa gas pressure and for a discharge power of 10 W shall be presented. At the given conditions growth cycles of an average period of 115 ± 6 seconds have been established during the measurement. Hence, a time resolution of 2 Hz is easily sufficient to resolve the particle cloud evolution.
The 3-dimensional data, x, y and time, can be presented by slices along each of these dimensions. For comprehension a scheme of that is shown in figure 6.5. Here three slices along the x-y-plane and two slices each along the y-t- and x-t-plane are depicted.

For a better resolution along the dimension of interest, eight slices of each dimension are then assembled to a bigger picture as given in figures 6.6, 6.7 and 6.8, which is sufficient to get an overview of the dust cloud evolution. Additionally all the slices are correlated in time to the self-bias voltage, which allows for a rough size estimation of the particles at any given time, following chapter 5.

6.3.1 Dust distribution

Under all the tested different discharge conditions the same general behaviour of the particle cloud has been found. A new generation of dust starts with a relatively low plasma glow that increases sharply after some tens of seconds and decreases in volume at the same time by approaching the powered electrode. At this point of time the self-bias voltage increases drastically and a very small increase of diffuse scattering in the entire chamber can be observed, as well evidenced in figures 6.7 and 6.8. Because the scattering signal to the background noise ratio is so tiny it is difficult to use the signal as evidence for early particles. However, it doesn't take long for a small void in the lower centre of the discharge to appear. It can already be seen, when carefully studied in the upper right picture in figure 6.6 at 25 seconds, which corresponds to a particle size of 40 to 50 nm at the end of phase II, see chapter 5.
As the void provides a sharp boundary between a volume without particles and a region with particles, it is a useful tool to improve the visibility of the dust cloud.
Later on in the growth cycle a dust free channel starts to appear ranging from the top of the discharge out of the laser sheet down to the void. It is slightly asymmetric shifted to the left side of the reactor from the camera perspective. From this series of measurements it cannot be seen, where the channel ends towards the top, because the laser sheet does not range high enough. Then both, the channel and the void slowly grow in size, with the channel taking form of a v-shape towards the end of the cycle, well depicted in figure 6.6.
Finally a kind of explosion takes place, where the void opens up very radically in the matter of one frame, corresponding to a time scale of half a second. After this event the upper region of the discharge seems to be free of particles and the residual dust can be found in the lower outer region of the plasma and within a thin layer of dust above the electrode. Slowly the residual dust is pushed further and further outside and depending on the conditions it can completely vanish from the illuminated region.
The correlation with the self-bias voltage now shows the reason for the voltage drop at the end of phase III. It falls at the same time as the void explosion takes place. So the effect of the dust on the discharge diminishes in a sudden event and therefore leaves a drastic footprint in the electrical signals. In the here shown series the time resolution of the electrical measurements is not very good, in fact it is only 0.2 Hz, because the computer was not capable to process the video data and the electrical measurements quicker. Therefore, the voltage drop does not seem as drastic as presented in chapter 5, although it actually is.
Before getting into the details of the obtained data one last issue shall be discussed. An intensity drop can be expected due to the opening angle of the laser sheet, reducing the laser intensity towards the right. This can lead to the impression of an asymmetric dust cloud

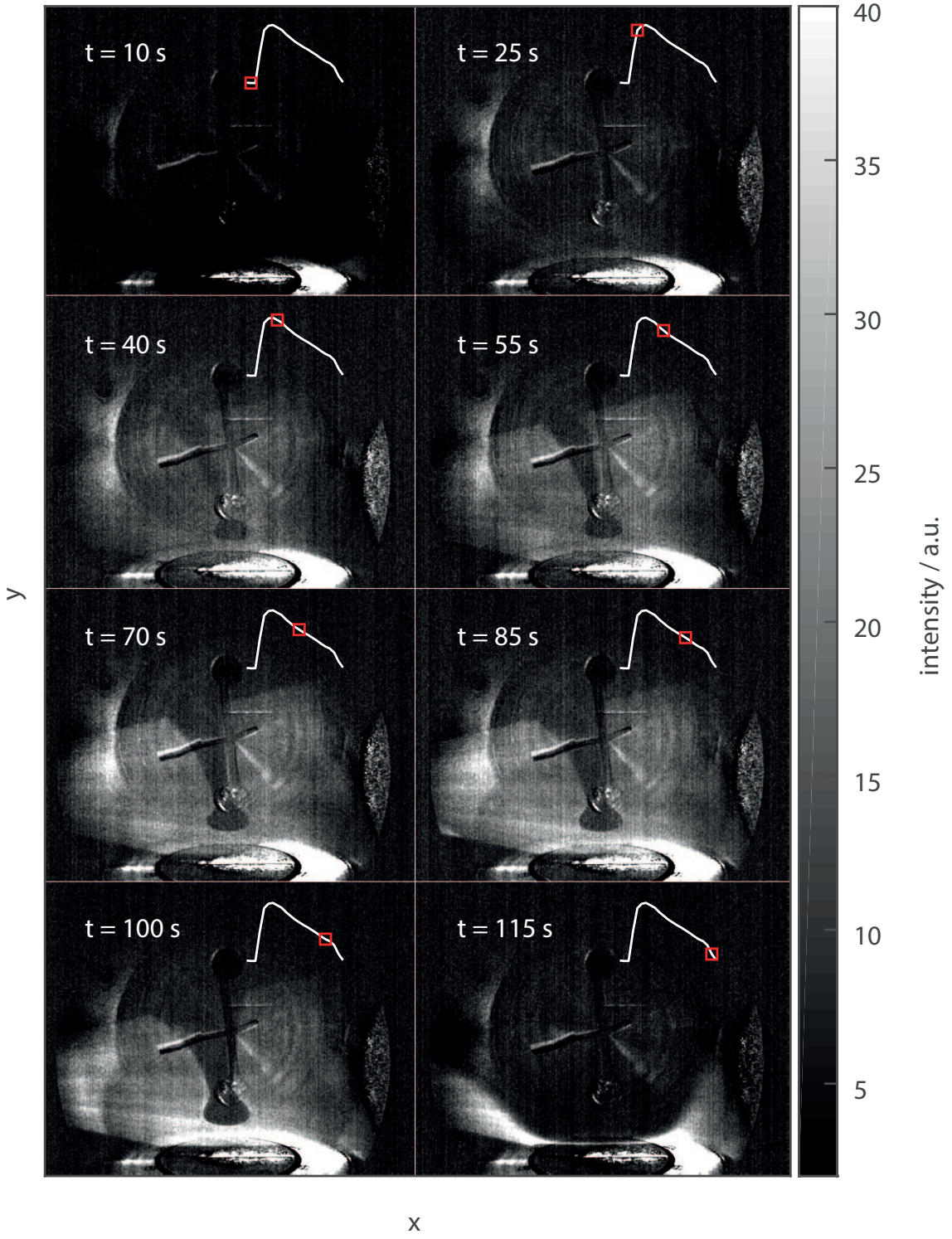

Figure 6.6: The evolution of the particle cloud throughout one growth cycle, as seen after the image processing; For according plasma emission, see figure 6.14;

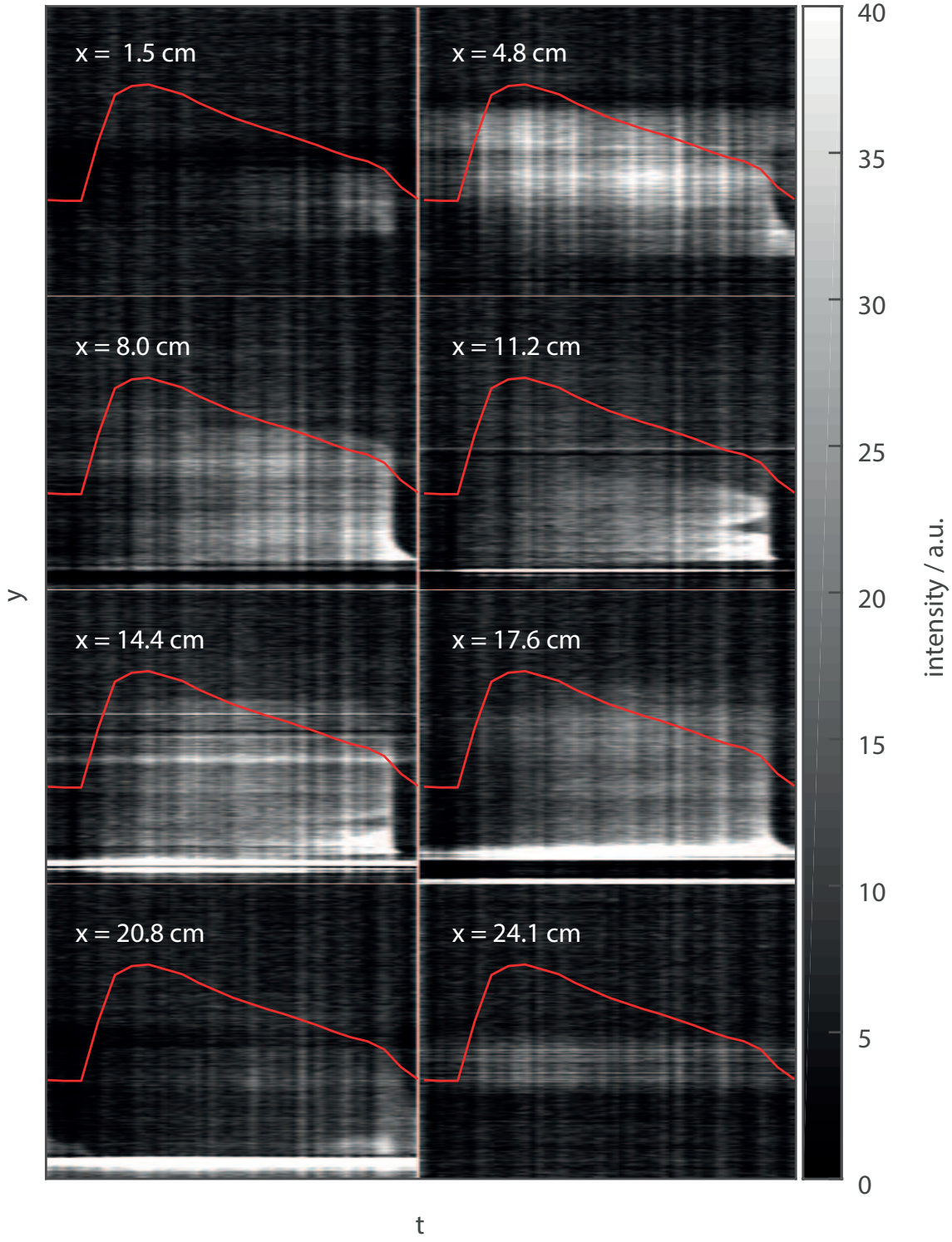

Figure 6.7: The evolution of the particle cloud throughout one growth cycle, as seen for different positions of x; For according plasma emission, see figure 6.15;

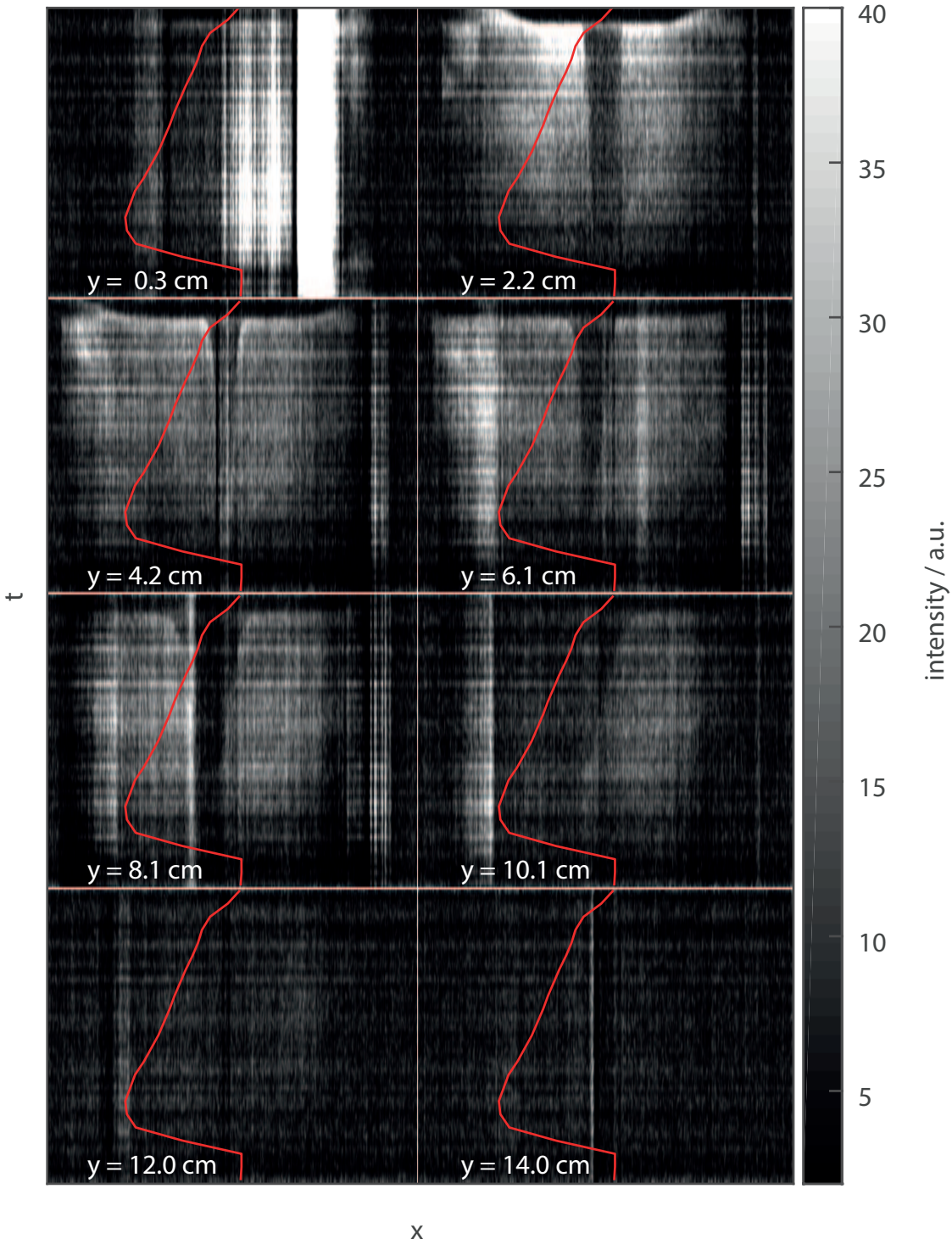

Figure 6.8: The evolution of the particle cloud throughout one growth cycle, as seen for different positions of y; For according plasma emission, see figure 6.16;

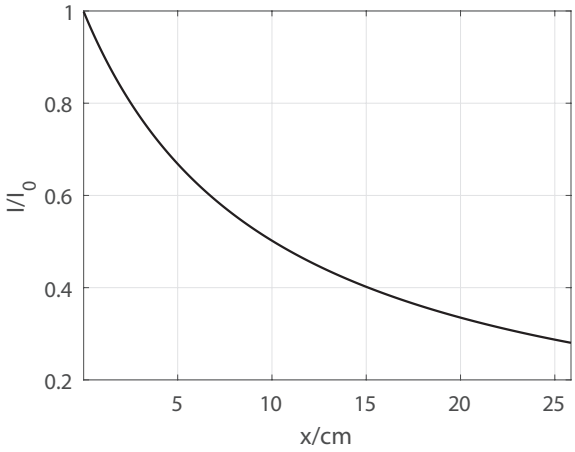

Figure 6.9: Theoretically, the incident beam looses intensity towards the right side of each frame due to the 30 ° dispersion in y-direction. The scattered light then obeys the same loss in intensity, as it is proportional to the incident beam intensity.

shape. Having a 30 ° opening angle of the laser in one dimension (y-direction), assuming no dispersion in the second dimension and measuring the height of the laser sheet to be 5.4 cm at the entrance of the image plane ($I(x = 0) = I_0$), the intensity decrease can be estimated to be:

$$I(x) = I_0 \frac{2.7}{2.7 + x/[\mathrm{cm}] \cdot \tan(15\,^\circ)}. \tag{6.13}$$

This results from trigonometric calculations and is depicted qualitatively in figure 6.9. Therefore, the incoming laser intensity is reduced by a factor of almost 4 from the right to the left in the image plane. Due to an unknown offset however, no corrections to the scattering signal have been done.
The sheath thickness in front of the powered electrode changes throughout the growth cycle. As the particles are strongly repelled by the electric field within it, they accumulate at the sheath edge and above, but they do not enter the sheath, phenomenon well known from dusty plasmas with microscopic particles. Thus, the absence of dust can be interpreted as sheath region. Taking the series of pictures in figure 6.7, the image at $x = 11.2\,\mathrm{cm}$ shows the development of the sheath thickness, however, it is difficult to see clearly due to the reflection of the laser on the electrode. Therefore, another slice has been made and a close-up of the sheath development and the plasma particles above has been performed as depicted in figure 6.10.
Marked in green is the zero level along the y-axis, which corresponds to the electrode surface. Also plotted alongside is the self-bias voltage evolution in red for orientation. During the first half of the cycle the sheath is not clearly visible, because the laser scattering at the particles is too small to give a good contrast. From second 60 on, however, it seems, that the sheath expands linearly in time until there are no particles left anymore.
In numbers the sheath thickness can be measured to 6 mm at $t = 60\,\mathrm{s}$ and then increases with a speed of $0.05\,\mathrm{mm/s}$ to 8 mm at the end of phase III. Another feature, that can be

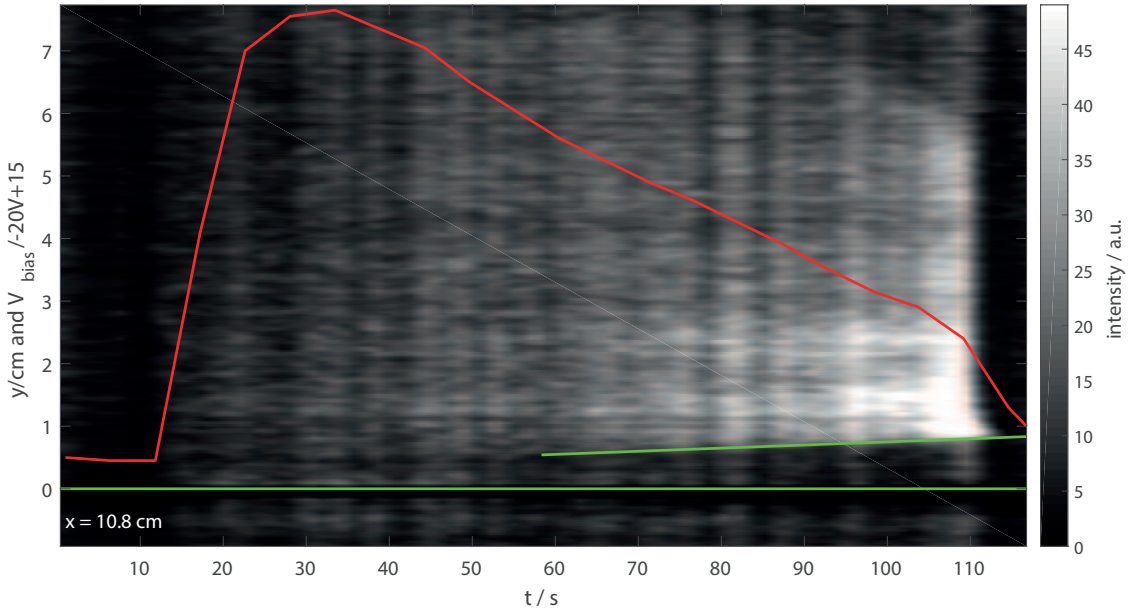

Figure 6.10: The sheath tickness in front of the electrode increases linearly in time throughout the second half of the growth cycle, as marked in green. The horizontal green line marks the electrode level. Shown in red is the time correlated evolution of the self-bias voltage.

seen very well in this close-up is the increase in brightness at the beginning of phase II and the exact accordance of the void explosion with the drop of the voltage at the end of phase III. The increase of brightness may partly be due to an imperfect subtraction of background noise, but also to the first glimpse of the growing particles, where they are still in the range of less than 40 nm in diameter.

Last but not least, apart from the channel, that slowly moves into the slice in the upper right part of the figure, it seems, that the intensity evolution is not the same in the lower region of the discharge, than in the upper one. Towards the end of phase II the brightness in the lower part is much stronger than in the upper region, whereas it was almost the same in the beginning. That's why the intensity evolution at different heights in the discharge is compared in figure 6.11.

Together with the evolution at different heights at the right hand side of the void, the intensity evolution inside the void is plotted in blue. This serves as a reference, if one assumes, that the void is completely dust free. One can see, that inside the void the intensity does not vary greatly throughout the cycle, except for the end of phase III. Here, probably the subtraction of the background was not performed perfectly due to the difficulties described in section 6.2.

Whereas all the regions outside of the void evolve similarly in quality and quantity for the first 60 seconds, they seperate in the second half of the growth cycle. Interestingly, the time at which the curves start to separate coincides with a very slight change in the slope of the self-bias voltage during phase III. This change of the self-bias voltage can sometimes be seen much stronger, especially for low pressures.

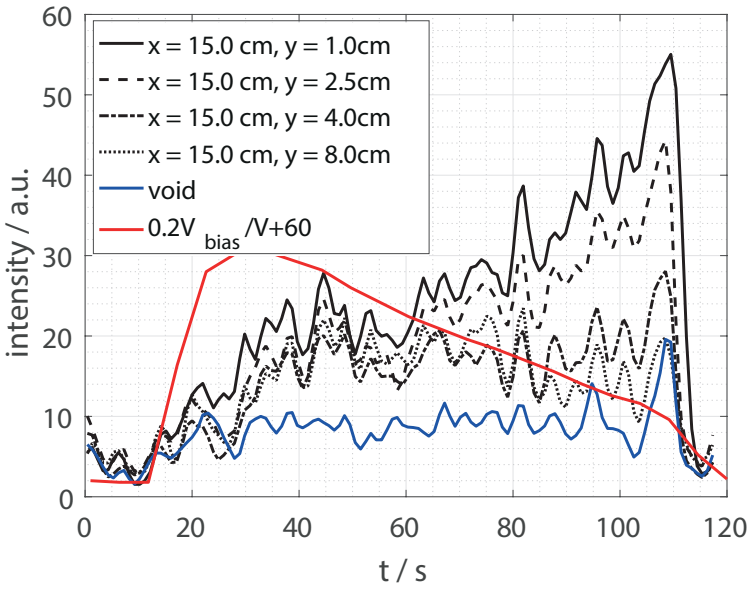

Figure 6.11: The measured light intensity is evolving differently at different heights above the powered electrode (y-values) outside the void. As a reference, where there are no particles, the intensity inside the void can be taken (blue line). In general the high regions loose intensity after half of the cycle duration, whereas shortly above the electrode the intensity increases up to the end of phase III.

Then in the second half the upper regions loose in intensity and the lower ones still gain. In fact, the lowest depicted point at 1 cm of height, which is just above the sheath (see figure 6.10) continues from the onset of phase II until the end of phase III to increase almost linearly in luminosity. With the void explosion all observed points turn dark, but the lowest one at last, because some particles are still trapped shortly above the electrode as can also be seen in figure 6.6 in the last frame at $t = 115\,\mathrm{s}$.

6.3.2 Particles from former cycles

In the very outer region of the discharge there is a small dust cloud, that never vanishes. It can still be seen during phase I. It is located very low, next to the grounded part, that is enclosing the powered electrode. The same series of snapshots as in figure 6.6 is given for a close-up in figure 6.12. The fact, that the dust remains in a very low position and that it always scatters more light than the rest of the cloud leads to the conclusion, that it is a group of relatively big particles. Gravity lets them sediment downwards and the scattering signal is stronger for big particles.
Evidence for a small amount of particles, that does not fall out of the discharge during phase I has already been found in [84], where usually besides the dominant actual generation another population of dust has been collected in little quantity. The size of the second population corresponds well the extrapolated size according to scheme 5.4 from the precedent growth cycle. An example of such a particle is given in the SEM picture in figure 6.13.

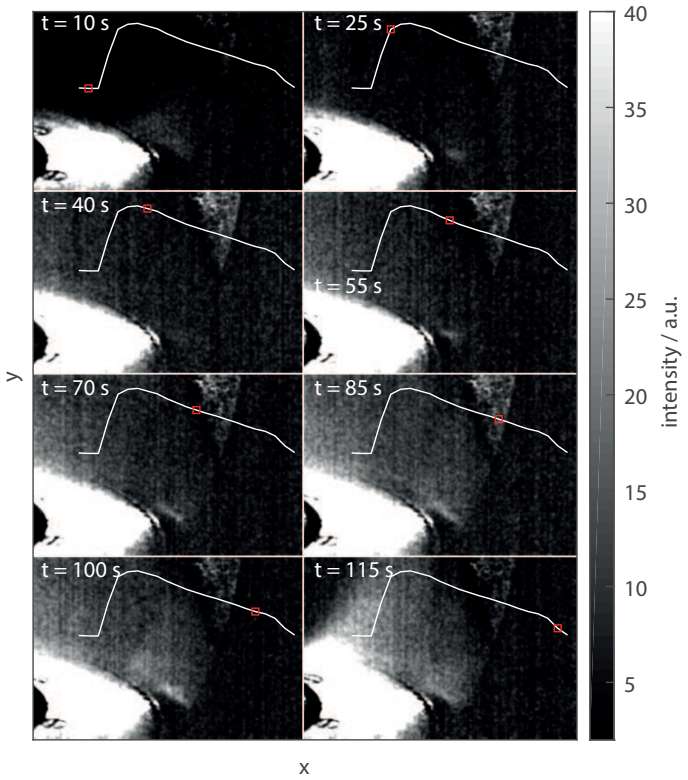

Figure 6.12: To the right next to the grounded electrode a small group of particles does not retreat throughout the entire growth cycle. The relatively bright scattering signal it emits, speaks for a group of relatively large particles.

However, it seems that the quantity is small enough to not affect the plasma significantly. No footprint of this dust can be identified in the characteristics of the electrical measurements. Normally the quantity of these large particles collected is exceeded by some orders of magnitude by the quantity of smaller primary particles. Nevertheless, the term *single generation particle growth* does not seem to be absolutely correct.

6.3.3 Plasma emission

The emission of light from a plasma is strongly related to the density of excited atoms and molecules. When de-exciting they can release a photon of a specific energy. Therefore, the wavelength provides information on the excitation levels and the intensity on the amount of excited species. This can be used to study the electron density and energy, as often the electrons are the main responsible species for the excitation processes. With a known electron energy distribution function, e.g. maxwellian, and an elaborated energy-dependent excitation cross-section, those two parameters can principally be calculated.
However, three-body collisions and excitation through other channels like collisions with metastables complicate the matter. Therefore, it is difficult to obtaine quantitative results by this method and advanced models have been developed. Among those techniques are

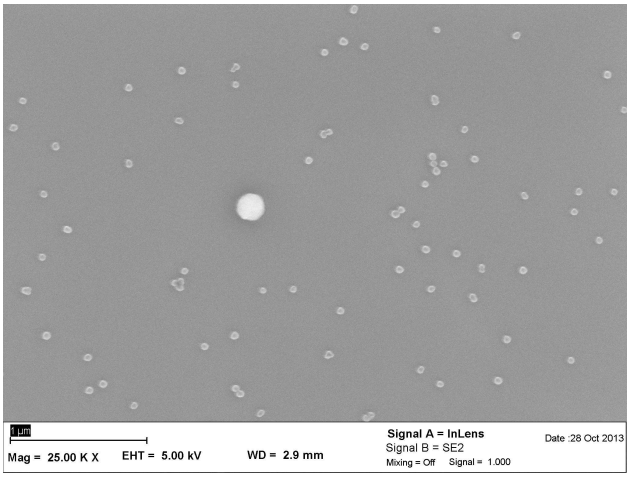

Figure 6.13: Usually in collection experiments besides the generation from the actual growth cycle a few particles from the former cycle can be found, here the big particle among the small ones.

the collisional-radiative model, that already has been applied in argon plasmas, for example in [208–213], and the line ratio method [214–216]. Whereas the first requires sophisticated calculations, the latter lacks accuracy, when inelastic collisions, recombination and diffusion are not negligible for radiative processes. Therefore, in this chapter, the plasma emissivity shall only be regarded as an indicator, where a high luminosity stands for either high electron densities and/or high electron temperatures.
Although a green filter was used in order to minimize the detection of plasma emission by the camera, it was not possible to remove it completely. Therefore, a lavish subtraction method by chopping the incident laser beam was applied as explained in detail in section 6.2. A beneficial side product of this method, however, is the detection of the plasma emission at the wavelengths, that can pass the optical filter. Here, a filter with a bandwidth (FWHM) of 20 nm around the laser wavelength of 532 nm was applied. Even if the region around 532 nm provides a good window, where argon only emits weakly, several Ar I and Ar II emission lines are located around there. Although the intensities are not very high, a plasma emission stronger than the scattering signal was observed. Those lines are resumed in table 6.1.

intensity	wavelength / nm	type	intensity	wavelength / nm	type
100	514.18	II	20	521.68	II
70	514.53	II	7	522.13	I
5	515.14	I	5	542.14	I
15	516.23	I	10	545.17	I
25	516.58	II	25	549.59	I
20	518.77	I	5	550.61	I

Table 6.1: Argon lines passing through the green filter, taken from [217];

For consistency the same series of images as for the dust cloud in section 6.3.1 was produced for the plasma emission, yielding figures 6.14, 6.15 and 6.16. Remarkably, as a general observation it can be stated, that the plasma luminosity correlates quiet well with the evolution of the self-bias voltage. At the transition from phase I to II it becomes suddenly very bright and inversely it becomes darker at the end of phase III. So only by watching the plasma emission, the effect of particles is noticeable.
Another observation, that can be made, is the descending of the bright plasma region above the powered electrode. First of all it seems more localized, apart from also being much brighter (650 a.u. instead of 350), but also it approaches the electrode. That means, that in the discharge centre the bright glow descends, which can be well seen in figure 6.15 at the distances $x = 8\,\mathrm{cm}$ to $x = 17.6\,\mathrm{cm}$.
Therefore the same plot as in figure 6.10 but for the plasma light emission has been repeated in figure 6.17(a), where the green lines still correspond to the sheath thickness determined by the dust cloud presence. As can be seen better in the close-up 6.17(b) of the distance between the electrode and the point of highest emission intensity $I_{\max}$, the point of highest plasma luminosity $y(I_{\max})$ is roughly two times higher than the sheath edge, and thus:

$$y(I_{\max}) \gtrapprox 2 \cdot d, \tag{6.14}$$

where d denotes the sheath thickness. In more detail, the plasma descends in phase II, is the closest at the transition from II to III and then rises slowly up to the end of phase III. Here, it reaches its maximum height, even higher than during phase I, when it obtains a shortly stable medium distance to the electrode.
However, attention has to be paid to the position of the camera, that is some tens of centimetres above the electrode level. Therefore, in contrast to the laser light scattering measurements, the camera now images a line of sight, and thus the intensity observed is an accumulation of the intensities along this line of sight. Because the camera is elevated it is looking down at an angle, the observed maximum of intensity is slightly closer to the electrode than in reality. Nevertheless it is the closest to the electrode, when the self-bias voltage is at its maximum and vice versa, indicating, that the sheath thickness behaves similarly.
For completeness the intensity evolution has again been plotted for the same coordinates as used in section 6.3.1 in figure 6.18. Here the similarity, or in other words the correlation, between the time evolution of the self-bias voltage and the intensity of the light emission can clearly be seen. Also, the void region does not show any anomalous behaviour and again the general trend, the lower the brighter, can be observed.
The void, in contrary to some other experiments like in [218], does not emit more light than the rest of the plasma. Therefore, one can assume, that the electron density and temperature, which essentially affect the excitation rates, do not differ significantly inside the void from the surrounding dusty plasma. However, in this set-up only a small spectral range of the emission is recorded. Because the excitation channels for the different argon lines are not fully accessible, no conclusions on other argon lines can be drawn from these results. And thus, a complete overview over the plasma emissivity is missing, that is necessary to determine the electron temperature and density by optical means.
A more extensive chapter on the plasma emission will follow in 8, which is entirely based

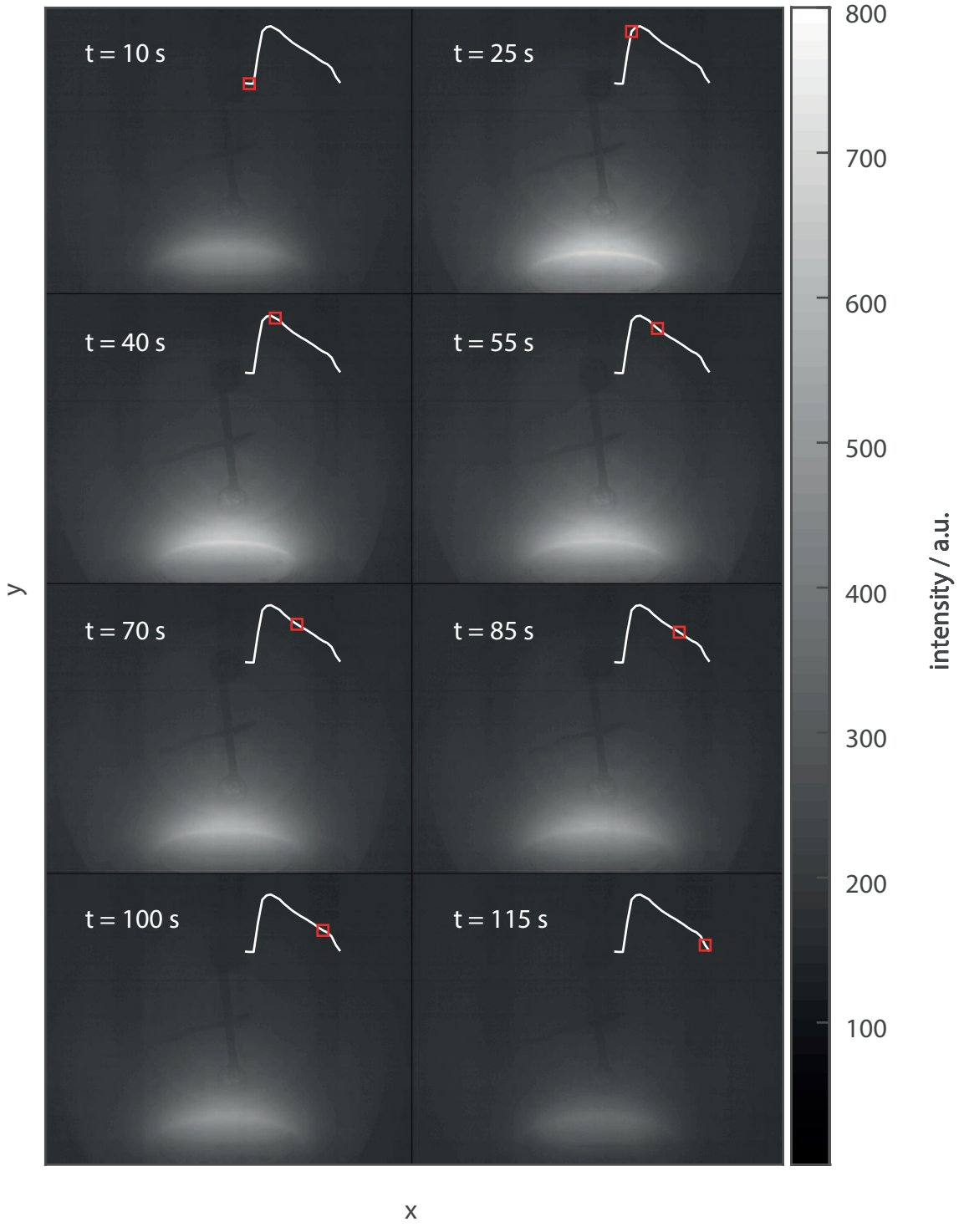

Figure 6.14: The evolution of the plasma emission throughout one growth cycle, as seen after the image processing; For according dust cloud, see figure 6.6;

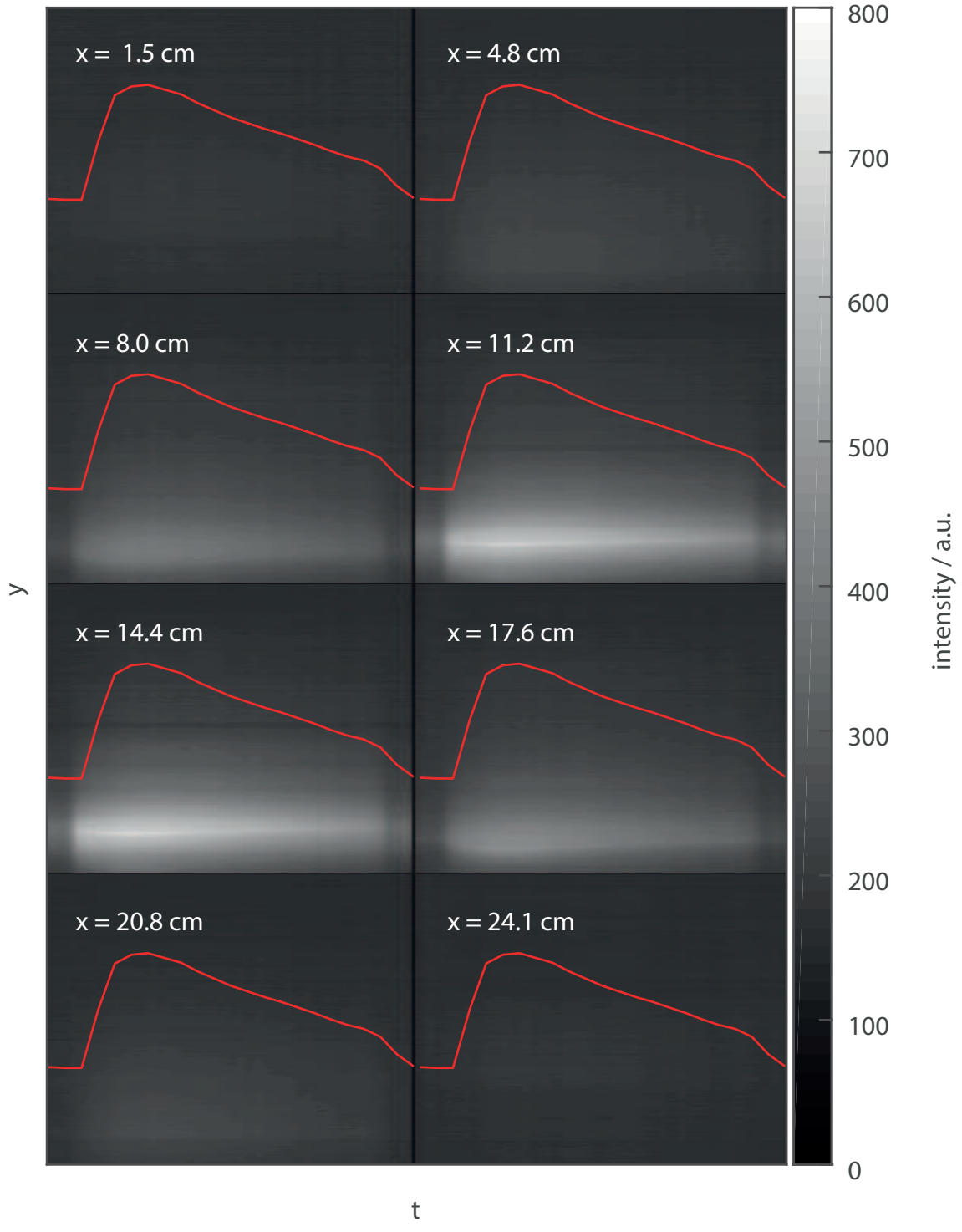

Figure 6.15: The evolution of the plasma emission throughout one growth cycle, as seen for different positions of x; For according dust cloud, see figure 6.7;

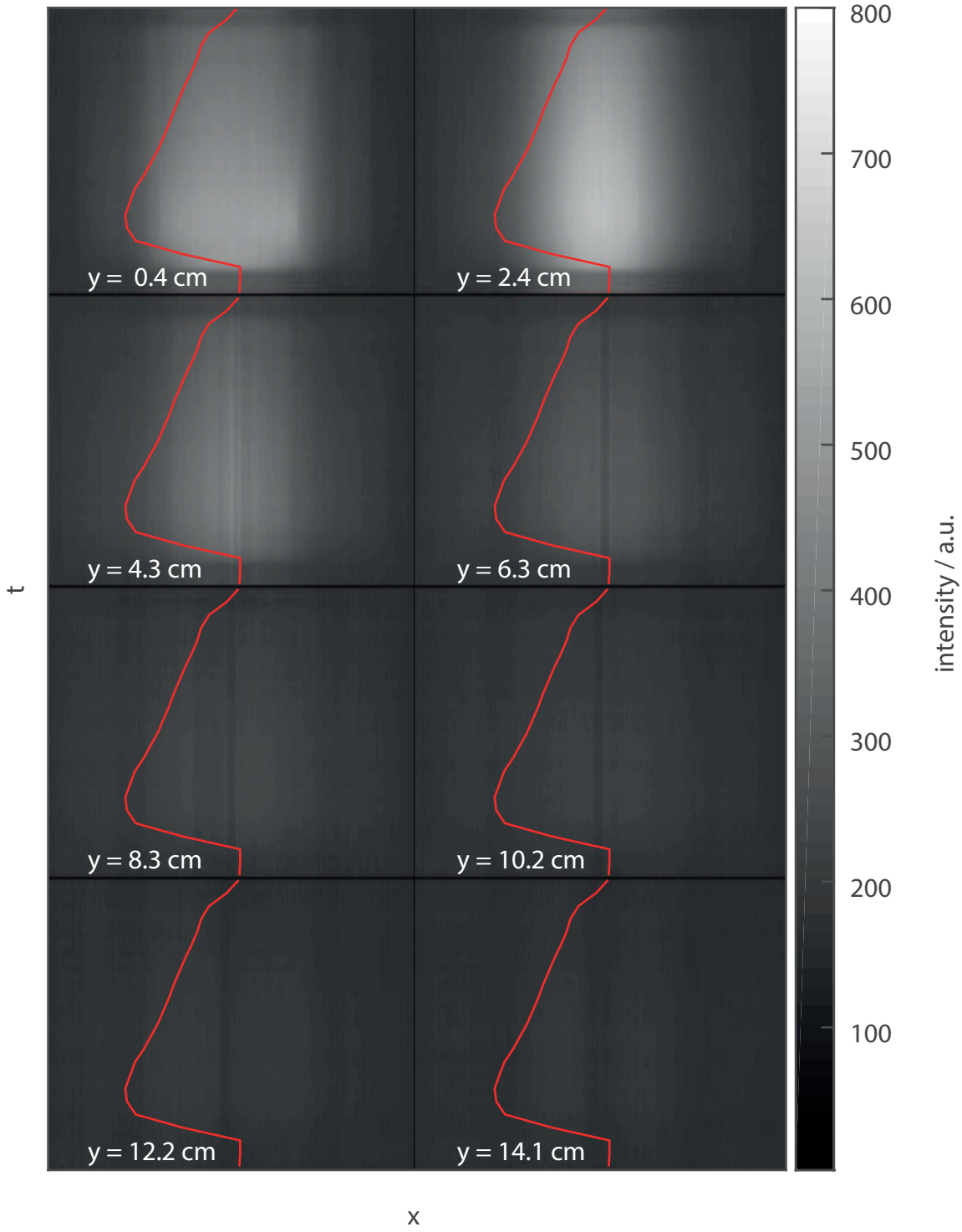

Figure 6.16: The evolution of the plasma emission throughout one growth cycle, as seen for different positions of y; For according dust cloud, see figure 6.8;

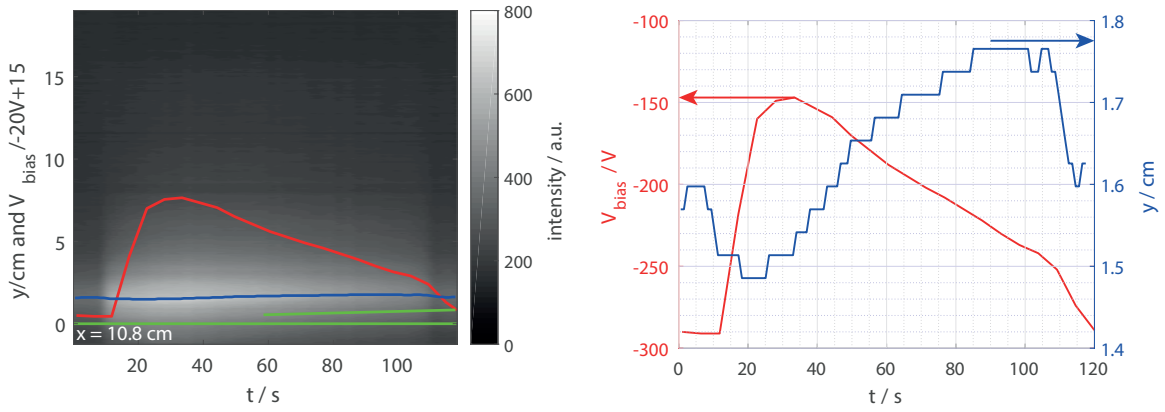

(a) (b)

Figure 6.17: (a) The green lines mark the sheath thickness above the powered electdrode as a function of time determined by the dust cloud shape in section 6.3.1. The background image depicts the plasma emission through the green filter at $x = 10.8\,\mathrm{cm}$. The emission intensity increases sharply with the onset of phase II and decreases again at the end of phase III. Additionally the intensity maximum (blue line) is the brightest but positioned the lowest when the self-bias voltage is at its maximum. (b) A close-up of the distance between the region of maximum brightness and the powered electrod $y(I_{\max})$ (blue line) together with the self-bias voltage (red line);

on the plasma emission and where the camera is mounted on the electrode level in order to minimize the projection error of the line of sight.

6.4 Discussion of the results

Resuming the precedent section 6.3.1 a comprehensive picture of the dust cloud evolution as a function of the particle size can be drawn.

Phase I During the first phase of the growth cycle the plasma emission is low and no particles can be detected by laser light scattering. However, collection experiments and SEM measurements revealed the presence of small, $r_\mathrm{d} < 40\,\mathrm{nm}$, dust particles. Because the self-bias voltage is in a plateau during this phase, one must consider the influence of the particles on the discharge as negligible. Hence, either the particle charge or the particle density is too low to modify the quasi neutrality 2.43 significantly. In other words, the overall particle surface does not yet act as an effective electron sink and the plasma loss mechanisms stay almost unchanged compared to a dust free plasma.
From particle collection experiments it follows, that the nucleation occurs in this phase. However, it remains unclear, if the coagulation also takes place. The linear growth already within this phase suggests, that the coagulation event already finishes some when during phase I. Thus, it is not detectable neither by laser light scattering nor by the electrical

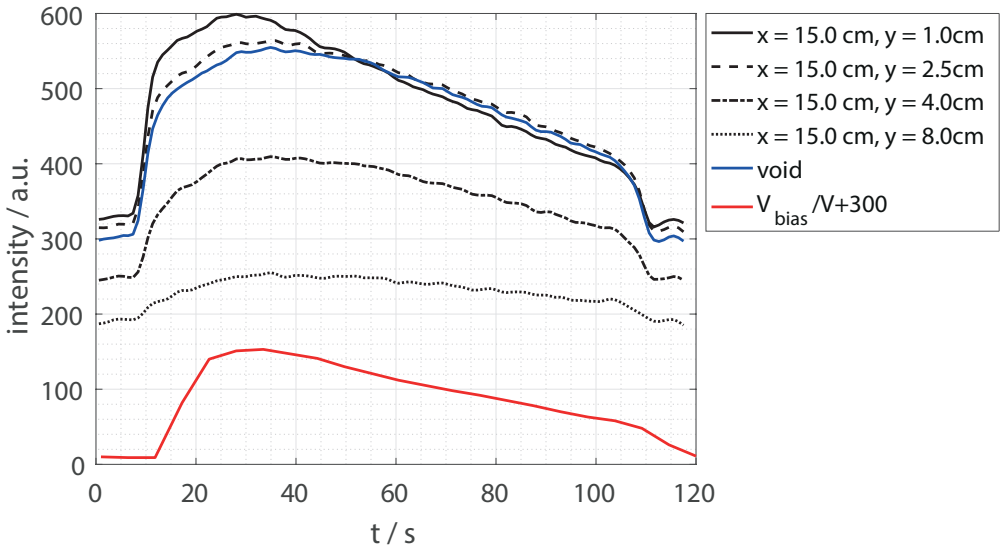

Figure 6.18: The measured light intensity is evolving similarly at different heights above the powered electrode (y-values). The higher, the darker is the plasma though. Also inside the void (blue line) there is no noticeable difference. The shape of the curves resembles very much the shape of the self-bias voltage (red line).

measurements. However, it is puzzling, why the plasma undergoes such a drastic transition from phase I to II, where the electrical signals change as well as the plasma emission and where the particle cloud starts to appear in the LLS signal.
The following suggestion shall be made to resolve the question: nucleation can occur as long as the precursor concentration is high. At this point it can only be assumed, that the precursor concentration does not reduce until the end of phase I. Detailed observations by mass spectrometric means will follow in chapter 9. Thus, the nucleation could happen throughout the entire phase I. If also the coagulation happens throughout the entire phase I, then it is not such a particular event as described by theory in chapter 3.3.2 and consequently particles continue to accumulate in phase I. Taking this picture this phase is marked by a considerable increase of particle density. A dust grain, that is formed early will then continue to grow due to surface deposition until the end of phase I, whereas a particle formed by a coagulation event at the end of phase I enters phase II without further surface deposition.
Assuming, that any particle leaves the coagulation event with the same size r_0 and then grows further with a constant deposition rate R_{surf} until the end of phase I, it obtains the size

$$r_{\mathrm{d1}} = r_0 + R_{\mathrm{surf}} \cdot \Delta t \tag{6.15}$$

during the residual duration Δt of phase I. Therefore, the size difference

$$\Delta r_{\mathrm{d}} = r_{\mathrm{d1}} - r_{\mathrm{d2}} \tag{6.16}$$

between the first particle r_{d1}, that leaves the coagulation and the last r_{d2}, just before phase II, must be

$$\Delta r_{\mathrm{d}} = R_{\mathrm{surf}} \Delta t = R_{\mathrm{surf}} (T_{\mathrm{I}} - t_0), \tag{6.17}$$

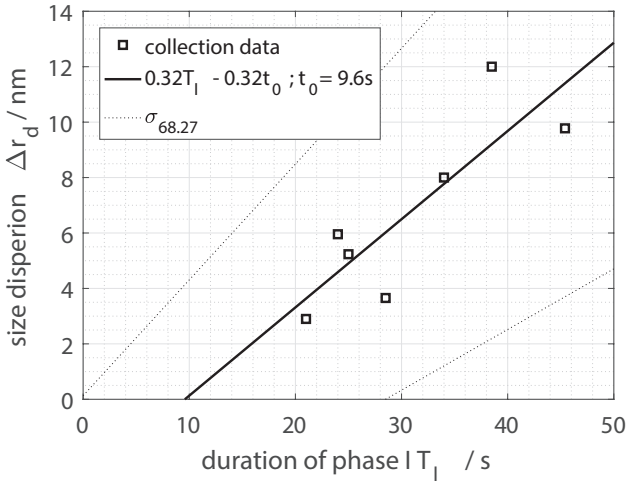

Figure 6.19: Plotting the duration of phase I versus the size dispersion of the particles results in a linear dependence. The dotted lines denote the goodness of the fit (solid line) in means of the standard deviation, which is equal to a confidence interval of 68.27%.

where T_I denotes the duration of phase I and t_0 the point of time, when the first particle appears during phase I. Assuming, that t_0 is a value, that depends on the discharge parameter, but is the same in each experiment, the size dispersion Δr_d of the dust at the end of phase I can be linked linearly to the duration of phase I:

$$\Delta r_\mathrm{d} = R_\mathrm{surf} T_\mathrm{I} - R_\mathrm{surf} t_0 \tag{6.18}$$

If the surface deposition rate is the same for the entire dust population in the following growth phases, there should be no correlation to the duration T_II and T_III of the other phases.
This hypothesis has been applied to the collected particles already described in chapter 5. The standard deviation σ_r size distribution of the collected samples, which was already determined in a previous work [161], can be connected to the size dispersion by

$$\Delta r_\mathrm{d} = 2\sigma_\mathrm{r} \tag{6.19}$$

and then be plotted against the time duration of each of the three phases, for I depicted in figure 6.19, for II and III in figures 6.20(a) and 6.20(b), respectively.
Indeed a dependence can be found, yielding a deposition rate of $R_\mathrm{surf} = 0.32\,\mathrm{nm/s}$ and a x-intercept of $t_0 = 9.6\,\mathrm{s}$, which corresponds to the point of time, when the first particle comes out of the coagulation event, because here the size dispersion must be $\Delta r_\mathrm{d} = 0$.
Plotting the dust particle size evolution once again against the time of collection, but this in time in absolute time units, allows to find the particle size at time $t_0 = 9.6\,\mathrm{s}$. The linear behaviour can be seen even better than in the plot with reduced collection times, see figure 5.4, and the linear fit matches well the experimental findings within a 68.27 % confidence, as presented in 6.21. The fit yields a growth rate of $R_\mathrm{surf} = 0.39\,\mathrm{nm/s}$, which is satisfyingly consistent with the growth rate obtained from the size dispersion above. Assuming a constant

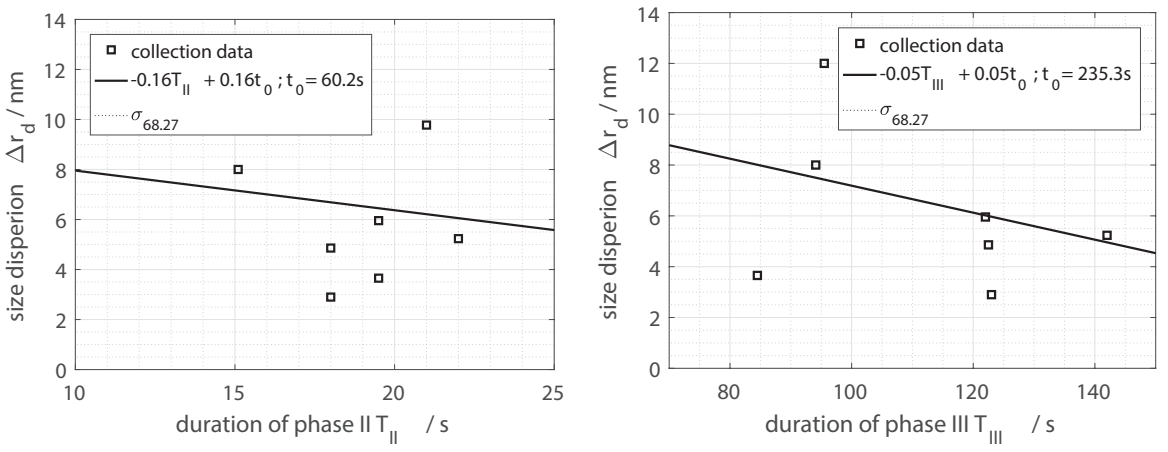

(a) (b)

Figure 6.20: In 6.20(a) no significant correlation between the duration of phase II and the size distribution of collected particles can be found. The same holds true for phase III in 6.20(b). In fact the standard deviation is too big to even fit into the chosen axis.

growth rate as soon as the particles leave the coagulation, the time $t_0 = 9.6\,\mathrm{s}$ in the fit of 6.21 then gives an initial particle radius of $r_{\mathrm{d}0} = 12.6\,\mathrm{nm}$.
Although the standard deviation of the linear fit, marked by the dotted lines in 6.19, is rather big due to bad stochastics, and thus, a precise determination of t_0 is not possible, a linear trend can clearly be seen. Nevertheless, the fit seems to be sufficiently precise to obtain a similar value for the surface growth rate as when plotting the averaged dust particle radius r_{d} against the absolute growth cycle time. For the other two phases, however, the correlation is not evident as expected. Thus, the here presented theory of simultaneous nucleation, coagulation and accretion during phase I is strongly supported by the findings. Furthermore, if the theory holds true, major questions can be answered by this method:

1. The particle size $r_{\mathrm{d}0}$ after the coagulation event can be estimated to be round about 13 nm in radius, which is rather big, but in the range of the expected. Convincingly, it represents round about the size of the smallest collected dust population ($r_{\mathrm{d}} = 10\,\mathrm{nm}$). However, smaller particles have been found in the SEM, that may be either attributed to particles being in the process of coagulation or to the insufficient precision of t_0, and thus, a possibly lower value for $r_{\mathrm{d}0}$. Nevertheless, it possibly does not

2. The coagulation event does not happen only during a very short time, but as long as the precursor concentration is sufficiently high, which is during the second half of phase I, as will be discussed in chapter 9.

3. The plasma starts to be influenced not directly after the coagulation event, but later, when the accumulated dust charges start to reduce the electron density significantly.

The here suggested picture of parallel nucleation, agglomeration and accretion can be better

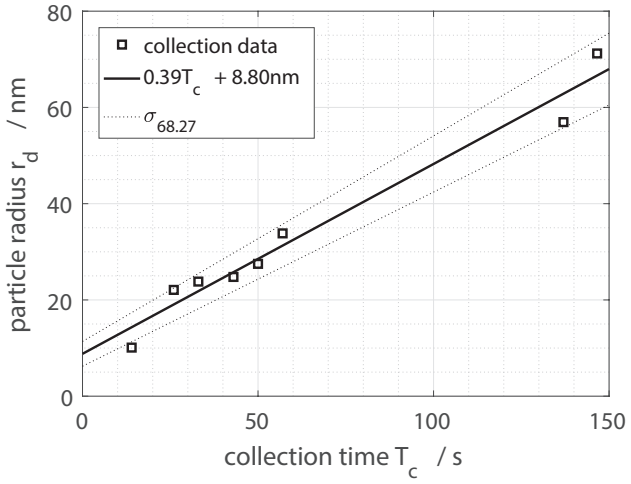

Figure 6.21: Plotting the duration of phase I versus the size dispersion of the particles results in a linear dependence. The dotted lines denote the goodness of the fit (solid line) in means of the standard deviation, which is equal to a confidence interval of 68.27%.

understood, when taking spatially different processes into account. When the first nanoparticles reach a size big enough to carry a permanent negative charge, they move towards an energetically favourable position, towards high plasma potentials. Hence, the dust position and origin must not strictly be the same. Further formed particles then add up to the early dust, so that a permanently charged dust cloud may grow in size close to the discharge center.
However, possibly in the outer regions of the discharge nucleation and coagulation still can take place due to a sufficient distance to the bigger particles, that consume most of the reactive ions, molecules and small clusters in their close vicinity. The nucleation and coagulation then stops, when either the permanently negative dust cloud has grown to an extinct, that no space for it is left, or when the discharge switches into another mode, e.g. from the α- into the γ'-mode.

Phase II Immediately at the onset of phase II the self-bias voltage, phase angle plasma emission and also the position of the maximum in the plasma emission change radically. Hence, the nanodust all the sudden influences the discharge. Regarding the continous particle growth as presented in chapter 5.3 it is mysterious, that the transition happens so quickly and that the induced changes are so big. Also the above presented theory on simultaneous coagulation and accretion does not give any answer on this question. The only prediction, that this theory can make, is that the dust density should constantly increase throughout phase I.
Thus, it shall be proposed, that the transition from I to II, or in other terms the α-γ'-transition, does not coincide with the coagulation of the dust, but rather with a critical combination of dust density and size. The suddenness of the event still remains surprising, however it is also well known for the α-γ-transition, that it happens discontinuously with

sudden jumps in the discharge characteristics [219]. Here, the critical factor is the sheath voltage, that responds like a dc-breakdown if a certain voltage is exceeded. Then, in the γ regime, the discharge is driven by the fast electrons in the sheath, which substantially are secondary electrons.
Something similar may happen during the α-γ'-transition. According to Fridman *et al.* [27] the bulk electrons are consumed by the particles, so that the α process is no longer the dominant ionization process, or it is also possible, that the increasing particle charge and consequently increasing energy of impinging ions produces a significant amount of secondary hot electrons.
In order to get a better insight into the heating mechanism of the discharge phase resolved camera measurements were done, presented in chapter 8.
At the end of phase II a first glimpse of dust can be taken, as the second picture in 6.6 shows. The void can already be seen from this first moment on, so it remains unknown to which point of time it is formed. It is possible, especially regarding the second picture in 6.8, that the void is intrinsic and the very centre of the discharge always is dust free. Anyhow, the entire rest of the discharge volume experiences an increase in the scattering signal, indicating, that the dust cloud is well distributed in the entire chamber.

Phase III The third phase is the longest one and follows the point of maximal dust influence at the transition between phase II and III. In the LLS signal a channel can be noticed ranging from the top of the chamber into the void. It is hard to see, when the channel forms, but it might well be at the beginning of phase III, following picture number four in 6.8.
The channel structure is a result of the incoming gas stream, which is supplied from the top of the reactor. In order to test this hypothesis, the gas supply has been moved in a series of experiments. The results shall not be presented here, but the channel position followed very consistently the nozzle of the gas supply. Therefore, the neutral drag force along the channel must point out- and downward, which is very plausible. Additionally the force must be considerably high in order to gain the upper hand against all the other forces. Indeed the rough estimations from chapter 2.3.3 reveal, that it may be necessary to also consider the neutral drag force as dominant one.
The values used to estimate this force are actually based on the supply tube diameter and the flow rate. What is quiet special in this set-up, is the fact, that the neutral drag force even has to be applied to resting particles and is not dependent on the dust velocity but on the gas stream velocity. This particular result may motivate industry to use neutral drag techniques to remove unwanted dust from the discharge.
In the course of phase III it can then be seen, that the channel structure and the void widen up. Two mechanisms may drive this evolution, based on the growth of the dust. First of all the continous growing results in heavier particles, and hence, the gravitation becomes more and more important. It results in a sedimentation-like behaviour, where the LLS signal becomes lighter in the upper region of the discharge, see figure 6.11, but a continuous increase in the lower parts.
Because the particle collection experiments revealed a continuous growth of the particles, an intensity decrease can only be explained by a reduction of the local dust density. This

may then lead to a reduction of the Yukawa repulsion between particles making it easier for the neutral drag force to push the dust aside. Additionally the drag force increases with the dust radius.
Another mechanism is the growth of the dust charge. With increasing charge, the electrostatic force between the particles must also increase, which at some point may overcome the trapping potential. As the plasma density is expectedly lower in the upper part, the trapping is not as good as in the near electrode region. Consequently the upper part looses more particles then in front of the electrode, where additionally the strong sheath potential ensures a good trapping.
The void obviously needs to grow in size, as the dust does so. Because the void edge is defined by an equilibrium between the electric force originating from the plasma potential profile and the ionwind force, the edge needs to move, when one of the forces is changing. As the ionwind increases up to a particle radius of several hundred nanometres, given in calculations in chapter 2.3.3, the dust is pushed further outside. This void enlargement and even successive voids, that one by one enlarge in time is well known from other experiments as well [220–222]
Taking a closer look at the intensity development $P_{\mathrm{LLS}}(t)$ in the lower discharge regions, it can be noticed, that it inreases rather linearly in time. Taking equation 6.2 and because the dust radius also increases roughly linearly in time t, it is possible to write:

$$t \propto P_{\mathrm{LLS}} \propto n_{\mathrm{d}} r_{\mathrm{d}}^6 \propto n_{\mathrm{d}} t^6 \tag{6.20}$$

and consequently

$$n_{\mathrm{d}} \propto t^{-5}. \tag{6.21}$$

In order for that to hold true it must be assumed, that the CCD chip of the camera has an output linear to the incoming intensity. The dust density reduction in time, is surprisingly high, and thus, a significant deposition of dust on surfaces inserted into the discharge is expected. In order to investigate this deposition rate measurements have been done, presented in chapter 10. This result is in contradiction to earlier works from Beckers and Kroesen, who measured a constant particle density during a certain growth phase in their experiments [223] by the exact same method. It shall be noted here, that the LLS-signal is relatively noisy. Therefore, expression 6.21 should be considered with caution.
At the end of phase III the void explosion takes place, leaving a trace in the electric signals and in the plasma emission intensity. It then is followed by the vanishing of the residual particles, except for an insignificant quantity in the very outer discharge regions. The void explosion is as abrupt as the transition from phase I to II, and therefore, it should be considered, that here the inverse γ'-α-transition occurs.
With the void explosion the dust free space, where α-ionization occurs, suddenly opens up. Consequently, the discharge should run into the α-regime. The stronger α-ionization then may induce an increase in the ionwind force, which accelerates the event. As a consequence it is a self-amplifying process and no surprise, that it happens abruptly.

Electrode current density In figure 6.10 an enlargement of the sheath thickness in front of the powered electrode during the second half of phase III was observed. It is the result of

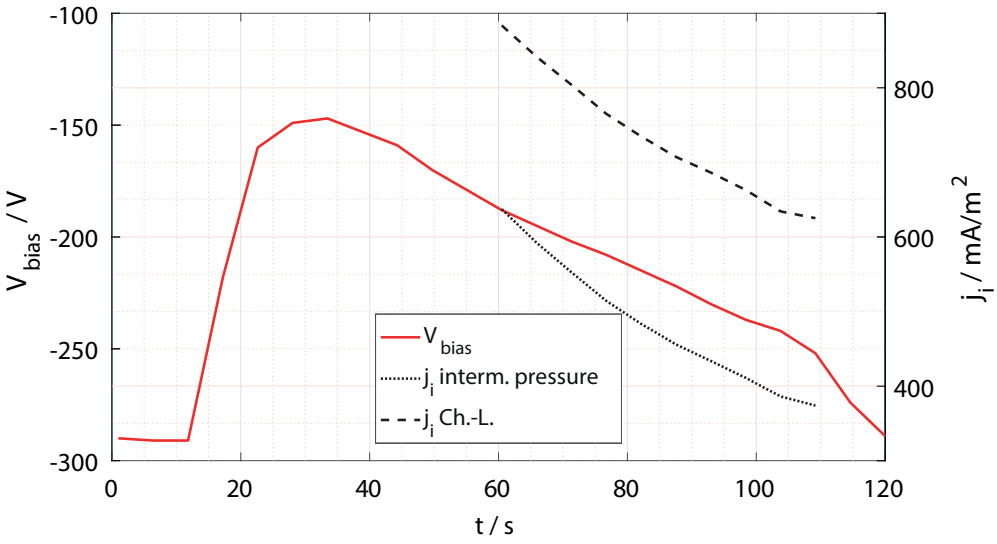

Figure 6.22: According to the Child-Langmuir law, the ion current density j_i can be calculated from the sheath potential $U = \Phi_\mathrm{pl} + V_\mathrm{bias}$ and the sheath thickness d. Presented are the solutions by using the sheath thickness, obtained from the LLS measurements as given in figure 6.10, and the simultaneously registered self-bias voltage, according to the low pressure case (dashed line) and the intermediate pressure case (dotted line), from equations 2.24 and 2.26 respectively.

the sheath potential $U = \Phi_\mathrm{pl} - V_\mathrm{bias}$ increase, which follows directly from the Child-Langmuir law, as introduced in chapter 2.2.1.
Estimating the plasma potential to be at around $\Phi_\mathrm{pl} \approx 20\,\mathrm{V}$, which is almost negligible compared to the self-bias voltage, and taking the pressure to be $p = 3.9\,\mathrm{Pa}$, as measured with the Baratron when the image in figure 6.10 was taken, the ion current density j_i can be calculated. The results for the low pressure formula 2.24 and the intermediate pressure 2.26 have been calculated comparatively as a function of the self-bias voltage V_bias, depicted in figure 6.22. For both solutions the ion current density decreases through the last half of phase III, however, the relative reduction is bigger for the intermediate pressure case due to the ratio of the exponents for U and d.
A decrease of the ion current density may be attributed to the change in two parameters, the ion density and the electron temperature, because those are the only two variables regarding the ion flux density at the sheath edge (index s):

$$j_\mathrm{i} = e n_\mathrm{i,s} v_\mathrm{B} = 0.61 e n_\mathrm{i0} \sqrt{\frac{k_\mathrm{B} T_\mathrm{e}}{m_\mathrm{i}}}, \tag{6.22}$$

see sections 2.2.1 and 2.2.2. So, during the last half of phase III either the electron temperature decreases or the ion density. In order to find out, which of those two plays the more important role, more diagnostics need to be applied. Especially Langmuir probe measurements, which will be treated in chapter 7, allow to determine all the necessary basic plasma parameters.

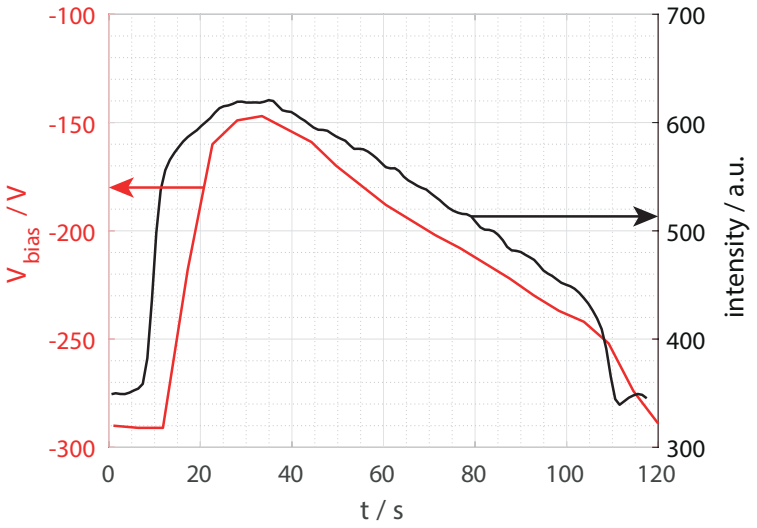

Figure 6.23: The point of highest intensity is not only changing its distance to the electrode, as demonstrated in figure 6.17(b), but also its luminosity at $\lambda = 532\,\text{nm}$. The change of a factor of roughly 2 is correlates very well to the self-bias voltage evolution. The change of the plasma brightness is caused by a change in the plasma temperature. With particles being present, the discharge is more luminous, which indicates an elevated electron temperature in this experiment.

Emission intensity As already described in section 6.3.3 the plasma emission intensity can be used as an indicator for electron density and temperature. Because in general one can assume the electron density to decrease with the presence of nanoparticles, a higher plasma emission intensity indicates an increase in the high energy tail of the electron energy distribution (EEDF). This can be related to a change of the EEDF but also to an overall more excited electron population, thus, a higher electron temperature.
Obtaining quantitative results from the emission intensity though is much more complicated, because metastables can also excite the argon atoms and stepwise excitation cannot be excluded neither. Furthermore, a low spectral resolution may make it impossible to separate argon lines from molecular lines of reactive species. Those, however, are additionally dependent on their species densities.
With the green filter mounted in front of the camera lenses, argon lines around 532 nm, as described in table 6.1, can be observed. Figure 6.23 shows that the maximum intensity of the discharge varies by a factor of round about 2 throughout the growth cycles as a function of the particle influence. It correlates perfectly with the self-bias voltage, any deviation may be attributed to the poor time resolution of the self-bias voltage measurement. Thus, a significant electron temperature increase needs to be considered. However, in other yet similar works [224] even an increase by a factor of ten has been observed for the 750 nm argon emission line. Hence, the temperature change can not be registered by only one emission line, but for addressing the problem appropriately, advanced emission spectra techniques need to be applied, as mentioned in section 6.3.3.

Chapter 7

Langmuir probe measurements

What is useful for various applications on one side, is causing dramatic changes in the plasma on the other side: the accumulated particle surface strongly modifies the loss channels for electrons, ions, radicals and even photons. To get a grip of the magnitude of this additional surface, one only needs the dust density n_d and the dust radius r_d giving the single particle surface area A_d:

$$A_\mathrm{d} = 4\pi r_\mathrm{d}^2. \tag{7.1}$$

The accumulated dust surface of all particles together in the entire discharge volume V_reactor then needs to be

$$A_\mathrm{total} = n_\mathrm{d} V_\mathrm{reactor} A_\mathrm{d}. \tag{7.2}$$

This surface area can be compared to the reactor wall surface area, which may be approximated by a cylindrical chamber of 32.4 cm of height and 22 cm in radius: $A_\mathrm{wall} = 7520\,\mathrm{cm}^2$. Although the nanodust cloud provides its surface directly inside the plasma, and thus, can have an even bigger impact on the plasma itself and the chemistry, the ratio Θ of the wall surface to the one of the dust can give a first impression on the importance of the dust:

$$\Theta = \frac{A_\mathrm{total}}{A_\mathrm{wall}}. \tag{7.3}$$

Taking various values from [63, 147, 225, 226] in different plasmas for different dust sizes a range of $n_\mathrm{d} = 0.2 \ldots 1500 \cdot 10^9\,\mathrm{cm}^{-3}$ can be evaluated. The closest match in terms of conditions may be the experimental observations by Tadsen *et al.* [63], who observed dust of 196 nm radius at a density of $4.6 \cdot 10^7\,\mathrm{cm}^{-3}$ grown by a radio frequency acetylene discharge, which ultimately yields a surface factor $\Theta = 1.48$. Hence, the particles provide a surface area roughly the same size as the chamber walls and, enlarging the impact even more, this surface is situated directly inside the plasma.
In order to quantify this impact, a fundamental question is the change in the electron temperature and density. Several techniques can be applied to access those values among which are microwave interferometry, absorption and emission spectroscopy. However, probe measurements are able to fully capture the entire electron characteristics with a rather simple set-up. Here Langmuir probes [80–83] and multipole resonance probes [227, 228] are the best

known methods, whereas Langmuir probe measurements are one of the oldest, and therefore very well established, technique to obtain extensive data. Besides the electron temperature and density, the ion current density, the plasma and floating potential as well as the electron energy distribution can be measured.
The high output of information but also the relatively simple set-up of Langmuir probes are the reason, why it was utilized in this work. However, many approximations and simplifications have to be made for it to be applicable and the set-up needs to be adapted to rf-discharges as well as to the reactive, dielectric depositing plasma environment. Therefore, a fundamental understanding of the probe theory is inevitable. It shall be discussed in the following section together with all the assumptions, that need to be made, and the difficulties, that have to be overcome.
Later the used set-up will be presented and also the results obtained before a discussion closes this chapter. The Langmuir probe measurements were performed in collaboration with Yerbolat Ussenov from the Al-Farabi Kazakh National University in Kazakhstan in the frame of a 3 month stay at the lab facilities in Kiel Germany.

7.1 Langmuir probe theory

Since its first description by Irving Langmuir and Mott-Smith in 1926 [114], different theories around the small electrical probes, inserted into a plasma, have been developed in order to account for different probe geometries and various sorts of plasmas. Reviews and extensive descriptions can be found elsewhere [90, 150, 229–232], here some fundamentals shall be discussed in order to understand the challenges when applying electric probes to a nano-dusty reactive RF plasma.
Three basic single probe designs exist, planar, cylindrical and spherical probes, see in figure 7.1 (a), (b) and (c), respectively. Inserting them into a plasma, they pick-up the ions and electrons from the discharge. In other words, a current $I_{\mathrm{probe}}(U_{\mathrm{probe}}) = I_{\mathrm{i}}(U_{\mathrm{probe}}) + I_{\mathrm{e}}(U_{\mathrm{probe}})$ in dependence of its potential $U_{\mathrm{probe}} = \Phi_{\mathrm{probe}} - \Phi_{\mathrm{pl}}$ can be measured. Doing a voltage sweep for U_{probe} from negative to positive values three different regions can be attributed to the resulting current curve: For strongly negative values ions are attracted but electrons repelled. This is called the *ion saturation regime*, see region I in figure 7.2.
Increasing the voltage, more and more of the hot electrons can reach the probe. All electrons at energies below $k_{\mathrm{B}}T_{\mathrm{e}} = eU_{\mathrm{probe}}$, however, are still repelled. It is therefore called the *electron retardation regime*. The floating potential Φ_{fl} falls within this regime and is defined by equal ion and electron currents $I_{\mathrm{i}} = -I_{\mathrm{e}}$, and thus, $I_{\mathrm{probe}} = 0$. From this point on the electron current dominates for further potential increases.
The last region is called the *electron saturation regime*, which starts at $\Phi_{\mathrm{probe}} = \Phi_{\mathrm{pl}}$, and thus, $U_{\mathrm{probe}} = 0$. Having a positive potential against the plasma, the cold and low energetic ions cannot reach the probe any longer but the electron current saturates. For positive potentials the different probe shapes make the current response differ strongly. Whereas planar probes exhibit a plateau-like electron saturation, cylindrical probes are marked by a further steady increase in the current for this region. And for spherical probes, the bend at

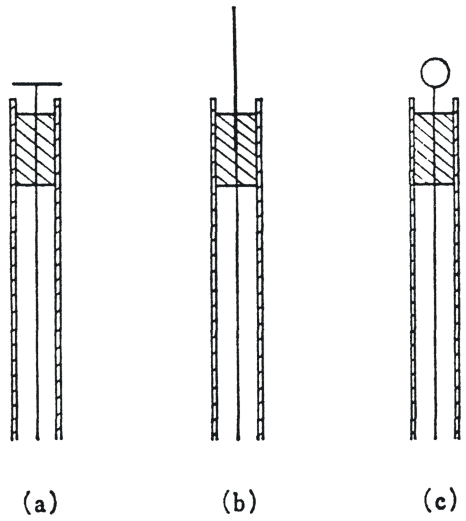

Figure 7.1: Three basic probe shapes are utilized for Langmuir probe measurements, planar, cylindrical and spherical, (a), (b) and (c) respectively. The conducting metal wire is shielded by an insulating tube. Taken from [150];

the plasma potential can't be seen any more.
The three different regimes shall be discussed and quantified in more detail in the following subsections. All calculations presented relate to the most simple case, which is a collision-free case with only one sort of single positively charged ions and with a maxwellian electron energy distribution. Trying to provide more exact solutions can quickly extend the calculations to a degree, that does not fit into the frame of this work any more, and thus, shall not be done here.

7.1.1 The ion saturation regime

The ion saturation current simply depends on the amount $n_{\mathrm{i,s}}A$ of ions, that cross the sheath edge in front of the probe surface A, and their velocity, which must be the Bohm velocity at that point. It therefore can easily be determined to be

$$I_{\mathrm{i,sat}} = n_{\mathrm{i,s}} e v_{\mathrm{B}} A \approx 0.61\, n_{\mathrm{i0}} e \cdot \sqrt{\frac{k_{\mathrm{B}} T_{\mathrm{e}}}{m_{\mathrm{i}}}} A, \tag{7.4}$$

where the approximation from equation 2.35 was used. However, attention must be paid to the surface A. Whereas for a planar Langmuir probe the area of the sheath edge A_{s} equals the probe surface, this does not hold true for cylindrical and spherical probes. As the ion current is dependent on A_{s} rather than A, consequently a correction factor needs to be introduced for the two latter designs.
In order to understand the ion motion around and towards a cylindrical or spherical probe the *Orbital Motion Limit* (OML) model can be applied very similar to what has already been introduced for the particle charging in section 2.3.1. Therefore, we will make use of

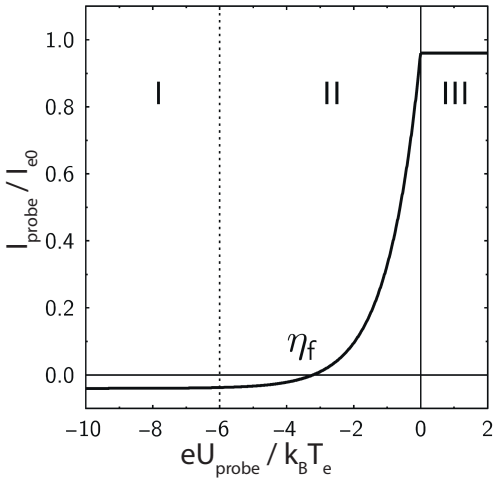

Figure 7.2: The I-V-curve, here for a planar probe, can be divided into three regions: I for small potentials, here represented as to $k_\mathrm{B}T_\mathrm{e}$ normalized energy eU_probe, II for intermediate potentials and III for positive values. At the floating potential, here represented by its energy equivalent η_f, the ion and electron current contribute to equal parts, and thus, cancel each other out. Taken from [90] and nomenclature modified;

equation 2.47 directly, which describes the effective cross section for the collection of ions by a dust particle in terms of the effective collection radius b_c. Although equation 2.47 treats a sphere, one can use the same relation between the radius r of a cylindrical object and its effective collection radius b_c. Taking the square root of that equation yields:

$$b_\mathrm{c} = r_\mathrm{d}\left(1 - \frac{2q\Phi_\mathrm{d}}{mv^2}\right)^{1/2}. \tag{7.5}$$

Now, replacing the initial ion energy with $\frac{1}{2}mv^2 = k_\mathrm{B}T_\mathrm{i}$ and using the probe potential $\Phi_\mathrm{probe} - \Phi_\mathrm{pl}$, referenced to the plasma potential Φ_pl, and radius a rather than the dust potential Φ_d and r_d, respectively, one obtains the real collection radius, see figure 7.3:

$$b_\mathrm{c} = a\left(1 - \frac{e(\Phi_\mathrm{probe} - \Phi_\mathrm{pl})}{k_\mathrm{B}T_\mathrm{i}}\right)^{1/2} = a\left(1 - \frac{eU_\mathrm{probe}}{k_\mathrm{B}T_\mathrm{i}}\right)^{1/2}. \tag{7.6}$$

Because the potential drop towards the probe $U_\mathrm{probe} = \Phi_\mathrm{probe} - \Phi_\mathrm{pl}$ yields a negative value, the effective collection radius is enlarged for ions. Hence, for cylindrical probes the probe surface area needs to be replaced with $A_\mathrm{c} = 2\pi b_\mathrm{c} l$, where l denotes the probe tip length. Consequently, the ion saturation current is no longer independent of the probe potential:

$$\begin{aligned} I_\mathrm{i,sat,cyl} &= 0.61\, n_\mathrm{i0} e \cdot \sqrt{\frac{k_\mathrm{B}T_\mathrm{e}}{m_\mathrm{i}}} \cdot 2\pi a l \sqrt{1 - \frac{eU_\mathrm{probe}}{k_\mathrm{B}T_\mathrm{i}}} \\ &= 3.83\, a l n_\mathrm{i0} e \sqrt{\frac{k_\mathrm{B}T_\mathrm{e}}{m_\mathrm{i}}} \cdot \sqrt{1 - \frac{eU_\mathrm{probe}}{k_\mathrm{B}T_\mathrm{i}}}. \end{aligned} \tag{7.7}$$

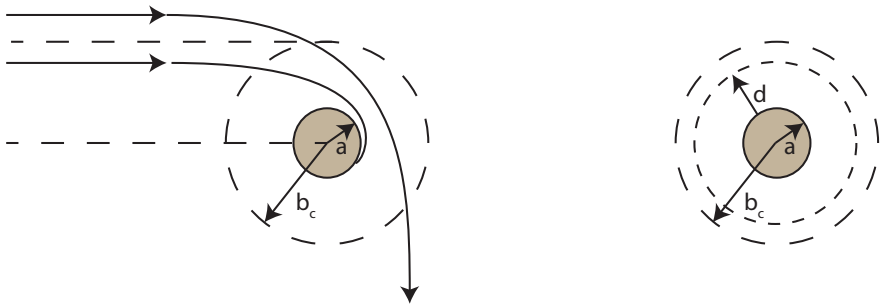

Figure 7.3: Cross-sectional view of the Langmuir probe of radius a: The collection radius b_d according to OML theory describes the collection cross section as seen from far away of the particle, see left side of figure. The OML theory looses its validity, if the collection radius is outside of the plasma sheath of thickness d, as depicted on the right side. This may happen for big probe radii, for example.

In order for this equation to hold true for all values $U_\mathrm{probe} < 0$, the effective collection radius should not exceed the sheath edge radius much $b_\mathrm{c} \lessapprox a + d$, where $a + d$ is the probe radius plus the sheath width d, see figure 7.3. If it exceeds the sheath edge radius by far, shielding from the plasma needs to be taken into account and the effective collection radius would need to be smaller. The sheath width can be expressed by the Child-Langmuir law for the current between two coaxial cylinders [98, 103] of radius a and r_0:

$$i_\mathrm{i} = \frac{8\pi\sqrt{2}}{9}\varepsilon_0\sqrt{\frac{e}{m_\mathrm{i}}}\cdot\frac{U_\mathrm{probe}^{3/2}}{a\beta^2} \tag{7.8}$$

with the dimensionless parameter

$$\beta^2 = 4.6712\frac{r_0}{a}\left(\log\frac{r_0}{a} - \log\sqrt{2}\right)^{3/2}, \qquad \text{for } r_0/a > 10. \tag{7.9}$$

The radius r_0 stands for the sheath edge radius, thus, $r_0 = a + d$. If the sheath thickness is smaller than $d < 9a$ the equation becomes less precise, meaning an error greater than 1 %. Here, the values provided by Langmuir and Blodgett [103], given in table 7.1 at the end of this chapter, need to be applied. The unit of the current density i_i is [A/m], which corresponds to a current per length along the cylinder axis.
Because the ion current density $j_\mathrm{i} = i_\mathrm{i}/(2\pi r_0)$ at the sheath edge is plasma dependent rather than dependent on the probe potential, it can be assumed to be constant for constant plasma conditions, and hence, the value β^2 needs to adjust to a varying probe potential U_probe. So the sheath thickness changes as a function of the probe potential. Now, in order to validate, that $b_\mathrm{c} < a + d = r_0$, b_c/a and r_0/a, obtained from β^2, are plotted together in graph 7.4. To do that, the ion mass was set to be the one of argon, the probe radius was set to $a = 50\,\mu$m and the ion current density at the sheath edge is found to be $j_\mathrm{i} = 0.61\,n_\mathrm{i0}ev_\mathrm{B}$. Combining with equation 7.8

$$\text{const} = j_\mathrm{i} = 0.61\,n_\mathrm{i0}ev_\mathrm{B} = \frac{4}{9}\varepsilon_0\sqrt{\frac{2e}{m_\mathrm{i}}}\cdot\frac{U_\mathrm{probe}^{3/2}}{a^2}\cdot\left(\frac{r_0}{a}\beta^2\right)^{-1}, \tag{7.10}$$

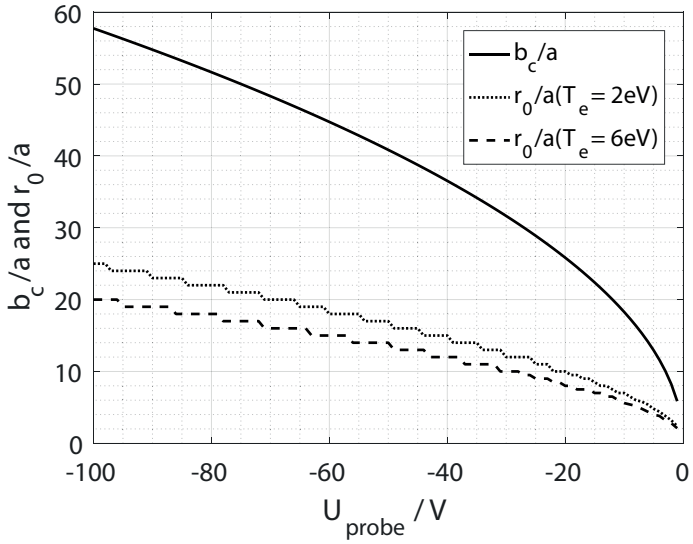

Figure 7.4: Numerical solutions for the sheath width, represented by r_0/a are obtained for two different electron temperatures $T_\mathrm{e} = 2\,\mathrm{eV}$ and $6\,\mathrm{eV}$ according to the Child-Langmuir law, described in [103]. It is compared to the effective probe collection radius b_c, also normalized to the probe radius a, as calculated from the OML theory. The collection radius exceeds the sheath edge radius by a factor of more than 2 for any probe voltage U_probe.

which can be solved numerically for r_0/a as function of the probe voltage U_probe for different $T_\mathrm{e} = 2\,\mathrm{eV}$ and $6\,\mathrm{eV}$ but a fixed ion temperature of $T_\mathrm{i} = 0.03\,\mathrm{eV}$. Together with $n_\mathrm{i0} = 4 \cdot 10^{15}$ it reproduces the values used in chapter 2 and can then be compared to b_c/a obtained by using the same values in equation 7.6.
As can be seen from figure 7.4, the collision radius from the OML theory as given by Piel [90] exceeds the sheath width by a factor of more than 2 for any given probe potential. Therefore, the OML theory may be erroneous, when applied to cylindrical probes with big diameter (here $100\,\mu\mathrm{m}$). An overestimation of the collection radius leads to an underestimation in the ion density in the plasma bulk. What's more, it does not take collisions into account, that may decrease the real ion current, which would lead to a further underestimation of the ion density. The discrepancy between the b_c and r_0 becomes worse with increasing ion density and increasing electron temperature and vice versa.
Therefore, another expression, derived by Mott-Smith and Langmuir [114], and summarized by Chen [233] shall be used instead. It actually is the same expression as equation 7.7, when replacing those parts coming from the sheath condition, e.g. using the bulk density n_i0 instead of the sheath edge density $0.61 n_\mathrm{i0}$ and the thermal ion speed $(k_\mathrm{B} T_\mathrm{i}/2\pi m_\mathrm{i})^{1/2}$) instead of the bohm velocity v_B. It is valid for small ion temperatures $T_\mathrm{i} \ll T_\mathrm{e}$ and $U_\mathrm{probe} < 0$ and takes the compact form of:

$$I_\mathrm{i,sat,cyl} = 2\sqrt{2} a l n_\mathrm{i0} e \sqrt{\frac{k_\mathrm{B} T_\mathrm{i}}{m_\mathrm{i}} - \frac{e U_\mathrm{probe}}{m_\mathrm{i}}} \approx 2\sqrt{2} a l n_\mathrm{i0} e \sqrt{-\frac{e U_\mathrm{probe}}{m_\mathrm{i}}} \tag{7.11}$$

This equation shall be used to fit the ion current in this work. However, although it gives a reasonable fit, that is more precise than a simple linear fit through the ion saturation region, the absolute values of n_{i0} turn out to be too high. This is due to the fact, that this formular also relies on a collection of ions, that originate from a region beyond the sheath edge, where shielding would need to be accounted for.
Therefore, under the assumption that the non-radial velocity component is negligible, the ion density needs to be found from equation 7.10 after having determined r_0. This can be done by setting the fitted ion current to the probe $I_{\mathrm{ion,Chen}}$ equal to the total current crossing the sheath edge according to

$$I_{\mathrm{ion,Chen}}(U_{\mathrm{probe}}) = 2\pi r_0 l \cdot j_{\mathrm{i}}(U_{\mathrm{probe}}, r_0) \tag{7.12}$$

for all negative probe potentials U_{probe}. It needs to be solved numerically and yields the sheath radius in dependence of the potential $r_0(U_{\mathrm{probe}})$, as well as the ion current density at the sheath edge in dependence of the potential $j_{\mathrm{i}}(U_{\mathrm{probe}})$. Ideally, the latter should be a constant, which turns out to be not exactly the case. However, as has been compared during this thesis, it yields a more constant ion density j_{i} than the collisionless planar probe sheath theory 2.24, the intermediate pressure sheath theory 2.26 or the collisional Mott-Gourney law 2.27.
This confirms, that the here chosen cylindrical sheath approach may be the most accurate solution for the determination of the ion density. Nevertheless, the obtained ion current density at the sheath edge is not perfectly constant, so its mean value in the measurement range is taken for the determination of the ion density:

$$n_{i0} = \frac{\bar{j_{\mathrm{i}}}}{0.61 e v_{\mathrm{B}}}. \tag{7.13}$$

But first, the electron temperature needs to be obtained in order to fill in the correct Bohm velocity v_{B}.

7.1.2 The electron saturation regime

In the electron saturation regime the probe is biased positively against the plasma potential. Therefore, all ions, which are little energetic, are repelled but all electrons attracted. Thus, the measured current equals the electron saturation current. For a planar probe the electrons contribute solely with the velocity component $v_\perp = v_{\mathrm{e}} \sin\theta$, where θ describes the inclination angle between the probe surface normal and the electron trajectory. After proper integration over a halfspace and all velocities in the maxwellian distribution one obtains [90]:

$$I_{\mathrm{e,sat}} = -\frac{1}{4} A e n_{\mathrm{e0}} \bar{v}_{\mathrm{th,e}} = -\frac{1}{4} A e n_{\mathrm{e0}} \sqrt{\frac{8}{\pi} \frac{k_{\mathrm{B}} T_{\mathrm{e}}}{m_{\mathrm{e}}}}, \tag{7.14}$$

where $\bar{v}_{\mathrm{th,e}}$ stands for the mean thermal velocity of the electrons and A again is the plane probe surface area.
However, as for this work a cylindrical probe was used, the electron saturation current also

needs to be discussed for this case. Here, the electrons can orbit around the probe, so the OML theory needs to be applied exactly in the same way as for the ion saturation current. One only needs to replace the thermal ion energy $k_\mathrm{B}T_\mathrm{i}$ with electron energy $k_\mathrm{B}T_\mathrm{e}$ in the collision radius in order to account for a bigger effective probe area:

$$b_\mathrm{c} = a\left(1 + \frac{eU_\mathrm{probe}}{k_\mathrm{B}T_\mathrm{e}}\right)^{1/2}. \tag{7.15}$$

Now, of course, U_probe is positive, so again the effective collection radius is enlarged. Because the electrons are much more energetic than the ions, their trajectories are stiffer, and hence, they are not that easily collected. Therefore, the collection radius is much smaller than for ions and shielding by the plasma like for the ions does not need to be accounted for.
However, for a probe potential $\Phi_\mathrm{probe} = \Phi_\mathrm{pl}$ there is neither attraction nor repulsion, so no orbiting takes place. Thus, the electron saturation current equals equation 7.14 with setting $A = A_\mathrm{cyl} = 2\pi al$. For higher probe potentials the radius a is enlarged and the electron saturation current for a cylindrical probe of length l can completely be described by

$$I_\mathrm{e,sat,cyl} = -\frac{2\pi}{4} a l e n_\mathrm{e0} \sqrt{\frac{8}{\pi}\frac{k_\mathrm{B}T_\mathrm{e}}{m_\mathrm{e}}} \cdot \left(1 + \frac{eU_\mathrm{probe}}{k_\mathrm{B}T_\mathrm{e}}\right)^{1/2}. \tag{7.16}$$

The easiest way to find the electron density from Langmuir probe measurements therefore is, to find the deflection point in the curve, that marks the plasma potential. Then the electron current $I_\mathrm{e}(U_\mathrm{probe} = 0)$, that almost equals the total current $I_\mathrm{probe} = I_\mathrm{e} + I_\mathrm{i}$ at this point, because the ion contribution shrinks to almost zero, gives the electron density according to equation 7.16 for $U_\mathrm{probe} = 0$.
In real measurements, however, it can be quiet challenging to measure the plasma potential Φ_pl, because the deflection point may be hard to read for cylindrical probes. Also, when a huge quantity of electrons is drained from the discharge by collecting them onto the probe, it can affect and modify the discharge. In order to reduce the invasive effects to a minimum, the probe should not be biased strongly positive but only far enough to clearly see the deflection point. Additionally, the tip length can be reduced to a minimum, which reduces the surface area and therefore limits the currents, but kept long enough to have significant currents for negative probe potentials, that can further be read out by the electronics. The probe tip length becomes the more relevant the lower the plasma density is, because in this case the currents are already low, which requires a long tip in order to have a good signal, but the plasma also is more sensitive to the drainage of electrons as it already only possesses a few.
Because different probe designs draw different saturation currents, the Langmuir curves look different, too. A comparison of planar (P), cylindrical (C) and spherical (S) probes is resumed in figure 7.5.

7.1.3 The electron retardation regime

The electron retardation regime lies in between the two saturation regimes. It is when only energetic electrons can reach the probe due to its repelling potential. The ion contribution

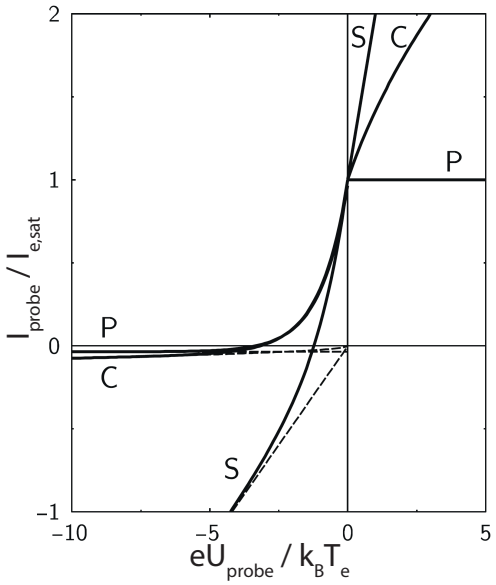

Figure 7.5: The shape of the Langmuir curve varies from one probe design to another, according to the OML theory. Demonstrated here are the mathematical solutions for spherical (S), cylindrical (C) and planar (P) probes at $T_\mathrm{e}/T_\mathrm{i} = 100$. Taken from [90] and nomenclature modified;

for this region has already been defined in section 7.1.1, so for understanding the total current $I_\mathrm{probe} = I_\mathrm{e} + I_\mathrm{i}$ only the electron current still needs to be developed.
Assuming a maxwellian electron energy distribution, with negative probe potential the amount of electrons, that can reach the probe potential, must be shrinked to the amount of electrons, that have exactly this energy or greater. Therefore, the electron current simply is the saturation current reduced by the Boltzmann factor from the energy distribution:

$$I_\mathrm{e}(U_\mathrm{probe}) = I_\mathrm{e,sat}(U_\mathrm{probe} = 0) \cdot \exp\left(\frac{eU_\mathrm{probe}}{k_\mathrm{B}T_\mathrm{e}}\right). \tag{7.17}$$

Taking the natural logarithm a linear dependence on the probe voltage can be deduced:

$$\ln \frac{I_\mathrm{e}(U_\mathrm{probe})}{I_\mathrm{e,sat}(0V)} = \frac{e}{k_\mathrm{B}T_\mathrm{e}} \cdot U_\mathrm{probe}. \tag{7.18}$$

This can be utilized to find the electron temperature. As can be seen from equation 7.18, the inverse slope of a semi-logarithmic plot of the electron current relates to it by being proportional to $k_\mathrm{B}T_\mathrm{e}/e$.
In many cases, however, the relation between the logarithmic electron current and the probe voltage does not appear perfectly linear. It is an indicator for a non-maxwellian electron population. Then the entire probe theory as developed is not reliable and the errors of the measurement may be rather high.
To get an insight into the electron energy distribution function (EEDF) the well-known

Druyvesteyn method can be applied. It makes use of the second derivative of the measured current $\mathrm{d}^2 I_{\mathrm{probe}}/\mathrm{d}U_{\mathrm{probe}}$, that can be obtained numerically from the taken data. However, for calculating the second derivative numerically requires very good data with little noise, because the noise becomes enhanced. As for this work the data are not clear enough, the Druyvesteyn method was not used and shall not be discussed in further detail. The work presented in the following sections is restricted to the above explained theory due to the poor signal to noise ratio. Consequently, the error bars can be expected to be rather large.
Another method to roughly determine the electron temperature is to measure the floating and the plasma potential, Φ_{fl} and Φ_{pl} respectively. The floating voltage is very easy to obtain as it simply reads as the probe potential at zero current $I_{\mathrm{probe}}(U_{\mathrm{fl}} = \Phi_{\mathrm{fl}} - \Phi_{\mathrm{pl}}) = 0$, because the ion and electron current cancel each other out

$$\begin{aligned} I_{\mathrm{i}}(U_{\mathrm{fl}}) &= -I_{\mathrm{e}}(U_{\mathrm{fl}}) \\ \Rightarrow 2\pi r_0(U_{\mathrm{fl}}) l \cdot j_{\mathrm{i}}(U_{\mathrm{fl}}) &= \frac{A_{\mathrm{probe}}}{4} n_{\mathrm{e}0} e \sqrt{\frac{8}{\pi}\frac{k_{\mathrm{B}}T_{\mathrm{e}}}{m_{\mathrm{e}}}} \cdot \exp\left(\frac{eU_{\mathrm{fl}}}{k_{\mathrm{B}}T_{\mathrm{e}}}\right) \\ \Rightarrow 0.61 A_{\mathrm{probe}} \frac{r_0(U_{\mathrm{fl}})}{a} n_{\mathrm{i}0} e \sqrt{\frac{k_{\mathrm{B}}T_{\mathrm{e}}}{m_{\mathrm{i}}}} &= \frac{A_{\mathrm{probe}}}{4} n_{\mathrm{e}0} e \sqrt{\frac{8}{\pi}\frac{k_{\mathrm{B}}T_{\mathrm{e}}}{m_{\mathrm{e}}}} \cdot \exp\left(\frac{eU_{\mathrm{fl}}}{k_{\mathrm{B}}T_{\mathrm{e}}}\right), \end{aligned} \tag{7.19}$$

where equations 7.10 and 7.17 for cylindrical probes were used and r_0 can be determined experimentally from equation 7.12. Because the electron temperature in the square root cancels out, this can be simplified to:

$$k_{\mathrm{B}}T_{\mathrm{e}} = \frac{eU_{\mathrm{fl}}}{\ln\left(0.61 \frac{r_0(U_{\mathrm{fl}})}{a} \sqrt{2\pi} \frac{n_{\mathrm{i}}}{n_{\mathrm{e}}} \sqrt{\frac{m_{\mathrm{e}}}{m_{\mathrm{i}}}}\right)}. \tag{7.20}$$

It is the same expression as derived for plane probes in [90], but the additional r_0/a term in the denominator corrects for a cylindrical probe according to the the cylindrical Child Langmuir law.
Additionally in some cases the ion density does not equal the electron density. This may occur in strongly electro negative or in dusty plasmas. Therefore, the coefficient $n_{\mathrm{i}0}/n_{\mathrm{e}0}$ needs to be defined properly, which can be done by reading the saturation currents and using equations 7.16 and 7.7. Because this involves the electron temperature $k_{\mathrm{B}}T_{\mathrm{e}}$ again, according to equation 7.13, the upper expression cannot solely be applied for the determination of the electron temperature. However, it is a great comparison to the slope method 7.18, which may be used to check the consistency between the obtained plasma potential $\Phi_{\mathrm{pl}} = \Phi_{\mathrm{fl}} - U_{\mathrm{fl}}$ and the electron temperature T_{e}. If the plasma potential has been analysed correctly in a previous step and the ion density is correctly obtained as well, the electron temperatures found by the slope method and equation 7.20 should be equal.
Often, quasineutrality, $n_{\mathrm{i}0}/n_{\mathrm{e}0} = 1$, in the bulk plasma can be assumed, so that for a planar probe, where $r_0/a \to 1$, the expression simplifies even further to [90]:

$$k_{\mathrm{B}}T_{\mathrm{e}} = \frac{eU_{\mathrm{fl}}}{\ln\left(1.53 \sqrt{\frac{m_{\mathrm{e}}}{m_{\mathrm{i}}}}\right)}. \tag{7.21}$$

Often, this equation is applied for cylindrical probes, too. However, in contrary to expression 7.20 it is wrong, as also described by Chen and Arnush in [234], for example.

7.2 Setup

The principal set-up of a Langmuir probe consists of a metal wire, which is exposed to the plasma, and a current and voltage measurement unit. The exposed tip of the wire is 12 mm long in this experiment and its location is centered at 24 ± 1 mm above the powered electrode. A principle scheme is shown in figure 4.2 in chapter 4.
The tip length has been chosen to be of this length in order to draw significant currents from the discharge but to keep the currents as small as possible at the same time, so that the plasma is disturbed as little as possible. The height above the electrode matches well to be inside the bulk plasma and inside the dust cloud below the void, as can be compared to chapter 6. Therefore the probe measures inside the plasma during phase I as well as during phases II and III. However, during phase II and III the probe tip is exposed to the nanodusty plasma.
Anyway, these are not the only aspects, that need to be considered when doing Langmuir probe measurements. What's more, different probe designs require different mathematical descriptions and the probes need to be adapted to specific plasmas. As in ATILA the plasma is generated by an RF-source, the plasma potential varies slightly in the plasma bulk according to the RF frequency, see section 2.2:

$$\Phi_{\mathrm{pl}} \rightarrow \Phi_{\mathrm{pl}}(t) = \bar{\Phi}_{\mathrm{pl}} + \Delta\Phi_{\mathrm{pl}}(t). \tag{7.22}$$

This is problematic, because usually it is not possible to measure faster than the shifting plasma potential. In the following is presented, how this is resolved technically.

7.2.1 RF compensation

Due to the slow measurement process, a time averaged current is measured, which in other words is the average over many different probe voltages as $\Phi_{\mathrm{pl}}(t) - \Phi_{\mathrm{probe}} = U_{\mathrm{probe}}(t)$ now is a sine wave with unknown amplitude, due to the shifting plasma potential $\Phi_{\mathrm{pl}}(t)$ around its time average $\bar{\Phi}_{\mathrm{pl}}$. Consequently, the measured current is not well defined like depicted in figure 7.6. Sharp features are smeared out, which especially affects the electron retardation *knee*, so that the resulting electron temperature is too high. Additionally the RF can cause the measurement electronics to fail or to be disturbed, so it needs to be kept out of the current signal as well.
In order to get rid of the RF distortion a passive RF compensation can be utilized. It comprises a low-pass filter, that suppresses the RF fluctuations directly behind the probe and an additional *pick-up probe*, that is a floating object in the plasma, which picks-up the RF fluctuations $\Delta\Phi_{\mathrm{pl}}(t)$ and transmits them via a capacitor to the Langmuir probe. The pick-up probe must have a much bigger surface area than the Langmuir probe and the

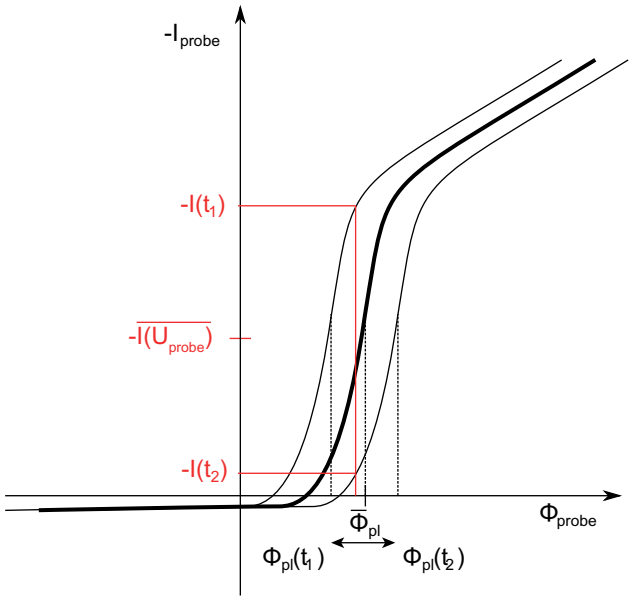

Figure 7.6: A time varying probe potential lets the probe current flucutuate as well $I = I(t)$. Therefore, in RF plasmas the measured current is time averaged if no RF compensation is used.

capacitor size must be chosen according to the plasma generator frequency, so that it acts as a high-pass filter, that cuts-off any DC-current but let's the RF pass through. This way the Langmuir probe is galvanically separated from the pick-up and an external voltage can be supplied to it without transferring it to the pick-up probe.
The use of the pick-up probe is, that it sets the plasma potential fluctuations $\Delta\Phi_{\mathrm{pl}}(t)$ onto the applied probe voltage $\bar{\Phi}_{\mathrm{probe}}$. Then the real probe potential is time dependent and can be written to

$$\Phi_{\mathrm{probe}}(t) = \bar{\Phi}_{\mathrm{probe}} + \Delta\Phi_{\mathrm{pl}}(t). \tag{7.23}$$

This way the probe voltage, referenced to the plasma potential, stays stable throughout the RF cycle:

$$\begin{aligned} U_{\mathrm{probe}} &= \Phi_{\mathrm{probe}}(t) - \Phi_{\mathrm{pl}}(t) = \left(\bar{\Phi}_{\mathrm{probe}} + \Delta\Phi_{\mathrm{pl}}(t)\right) - \left(\bar{\Phi}_{\mathrm{pl}} + \Delta\Phi_{\mathrm{pl}}(t)\right) \\ &= \bar{\Phi}_{\mathrm{probe}} - \bar{\Phi}_{\mathrm{pl}} = \mathrm{const.} \end{aligned} \tag{7.24}$$

In this work the pick-up probe is realized as a second tungsten fiber of same diameter as the Langmuir probe, but of more length. It is winded in spirals around the actual probe tip in order to pick-up the RF in the closest vicinity of the Langmuir probe. However, the spiral diameter is in the order of centimetres, so that it does not have much influence on the plasma condition around the probe tip.
An electrical circuit of the used probe is shown in figure 7.7 together with a schematic overview of the set-up. As can be seen the pick-up probe was equipped with the additional option to be biased with an external DC power supply. This was used to draw high electron currents at a positive potential from time to time. Thereby, the probe starts to glow and

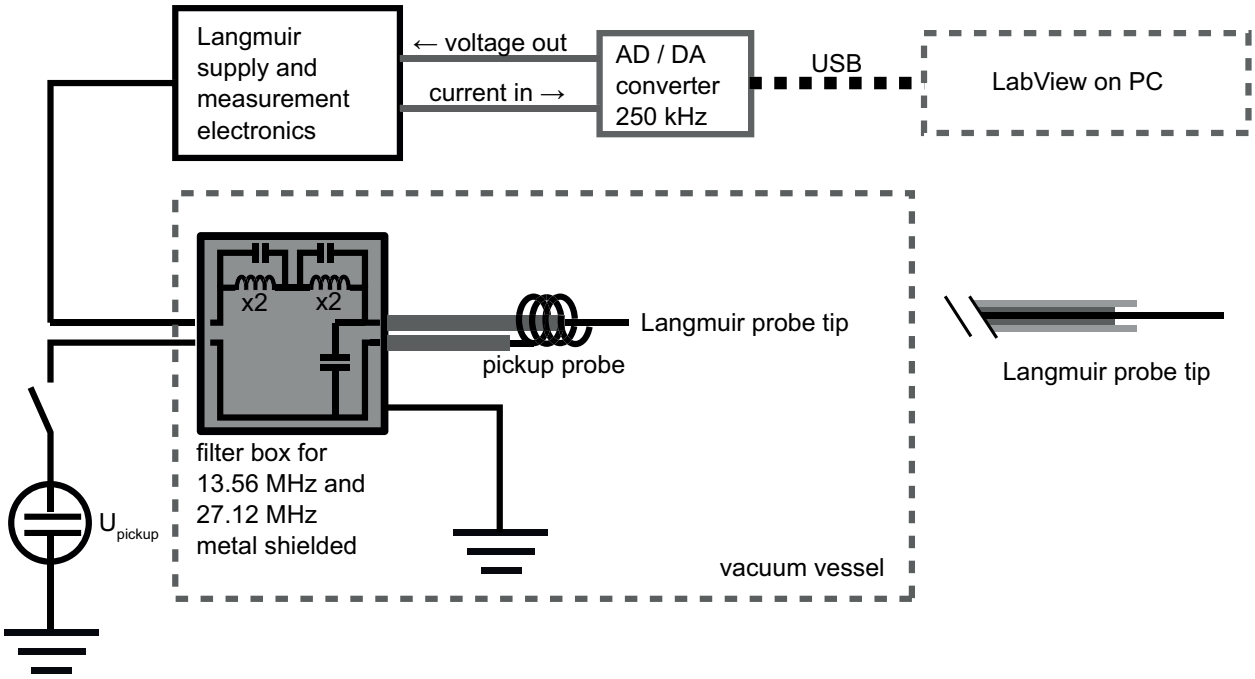

Figure 7.7: The Langmuir probe together with the pick-up probe and the passive RF filters is mounted inside the vacuum vessel. The pick-up probe can be set to an external potential as additional option. The Langmuir probe is controlled via external electronics that are managed with *LabVIEW™* and an AD/DA converter from *NATIONAL INSTRUMENTS™*.

evaporate any dirt from its surface.
However, on the pick-up probe the dielectric depositions don't pose a big problem, because the RF current can still be transferred like through a capacitor. During the measurements, of course, the pick-up probe needs to be floating, hence, it is disconnected from any outer potential. In order to fabricate a much greater collection surface than the Langmuir tip surface, the pick-up probe can be bend to a spiral, and thus, be several centimetres long. The bending of the tungsten fiber to a spiral was achieved by carefully winding it into a screw threat. After releasing the fiber it stays in this shape.
The RF filters are mounted inside a metal housing for proper shielding from the plasma in the vacuum vessel in order to be as close as possible to the probe. There are four filter units, two for the first harmonic at 13.56 MHz and two for the second harmonic at 27.12 MHz of the RF. They have been properly tuned after assembling the Langmuir probe, so that any stray capacities are taken into account. The probe itself consists of a 100 μm diameter tungsten wire, that is shielded with a ceramic tube. An additional inner tube makes sure, that the wire does not come into contact with the exit of the tube, where a conducting deposition could cause a short circuit to ground or enlarge the effective probe surface area.
The measurement electronics, developed at the Institute of Experimental and Applied Physics at the Kiel University, comprises four different current measurement resistances R_{meas} and subsequent amplification electronics. The resistances serve for the probe current measure-

ment and they are chosen to maximize the measured voltage $U_{\mathrm{res}} = R_{\mathrm{meas}} I_{\mathrm{probe}}$ up to 1 V, but not to saturate the amplification electronics. This way the current measurement is as precise as possible but because the resistances are directly set into the circuit between plasma and probe voltage supply, the real probe voltage is calculated from the supplied voltage Φ_{supply} by:

$$I_{\mathrm{probe}} = \frac{U_{\mathrm{res}}}{R_{\mathrm{meas}}} \tag{7.25}$$

$$\bar{\Phi}_{\mathrm{probe}} = \Phi_{\mathrm{supply}} - U_{\mathrm{res}}, \tag{7.26}$$

where $\bar{\Phi}_{\mathrm{probe}}$ is defined as in equations 7.23 and 7.24.
The supply voltage $U_{supply} = \Phi_{\mathrm{supply}} - \Phi_{\mathrm{gnd}} = \Phi_{\mathrm{supply}} - 0$, which is referenced to ground, on the other hand is generated by an amplification of the AD/DA converter signal U_{out} through the measurement electronics. Here, ± 10 V are transformed into ± 150 V for the probe voltage, referenced against ground. By applying the amplification factor G to the analog output of the NI card the applied voltage is then simply obtained as $U_{\mathrm{supply}} = G \cdot U_{\mathrm{out}}$.
The analogue digital converter is controlled by a *LabVIEW™* program on the computer and does not only send the output voltage but also captures the current measurement. The data are correlated and collected by the *LabVIEW™* software and can then be processed by *MATLAB™*.

7.2.2 Process specific challenges

Due to the reactive environment some challenges have to be overcome. One of them is the deposition of dielectric material onto the probe surface during the process. When measuring this cannot be avoided. However, in between each measurement the probe can be biased either strongly negative or positive. Thereby, either an ion or an electron current, respectively, is drawn. Whereas the objective of a strong electron current is to glow the tungsten wire tip thanks to electric heating just like in a light bulb, the objective of a strong ion current is rather sputtering thanks to the energetic ions. The current of the latter method remains relatively low due to the limited saturation current, but the single ion energy increases linearly with the applied probe voltage.
To make sure, that the probe does not get dirty during the measurement process itself, the only optimization possibility is to sweep the voltage as fast as possible and then return into the high current mode quickly. The time resolution of the electronics was tested by wiring the analogue output to the input and checking for a linear response. It was found to deviate from the expected behaviour at a voltage rise of 100 V at a rate of $f_{\mathrm{p}} = 40$ kHz, meaning at a slope of 4000 V/ms. Therefore, any faster voltage scan was avoided. The resulting probe sweep time T_{sweep} then depends on the number of measurement points N per curve and can be calculated to

$$T_{\mathrm{sweep}} = N/f \tag{7.27}$$

and should be kept in the range of a few seconds.
In this particular experiment the nanodust also contributes to a dielectric deposition. In fact,

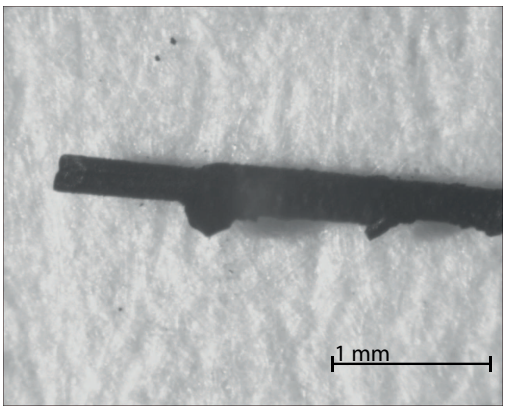

Figure 7.8: In nanodusty plasmas the dust particles can be attracted by the probe. In case of hydro-carbonaceous precursors this leads to a dielectric deposition, that not only hinders the probe currents but also changes the probe geometry in a matter of a few minutes.This picture, taken with an optical microscope shows the effect of an Ar/C_2H_2 plasma in ATILA.

when the nanodust is present it can consume high amounts of precursor, thereby reduce its concentration, and hence, reduce the surface deposition of dielectric material. Thus, in nanodusty experiments, deposition by dust particles is the main contribution. The resulting deposition rate can be as huge, that the probe is completely covered in a thick layer of blackish dielectric material after a few minutes of use, as seen under an optical microscope in figure 7.8.
This does not only change the measured currents due to the insulating deposition, but also due to a strongly modified probe geometry. Last but not least, the probe surface may not be on the set potential due to surface charging. A mono-layer of particles generates a deposition thickness in the order of a few nanometres. From other collection experiments we know, that this can easily be obtained in the matter of a few seconds, when applying a positive bias to the probe.
Therefore, the collection of particles needs to be prevented by all means. A method to keep microparticles from being attracted to the probe, has been tested and applied by Klindworth *et al.* [80]. They applied a negative voltage, to the probe when not measuring and an arbitrary sweep pattern for measuring rather than a linear voltage sweep. This means, that the probe is biased positively only for very short times distributed arbitrarily throughout the measuring time. They proved, that the probe stays clean even after several measurements using this method. The key for this to work is, that the probe is biased positively during a time scale τ_s, which is shorter than the time scale at which the dust particles can react with respect to their inertia. The inertia can be described using the dust plasma frequency from equation 2.15:

$$\tau_s \overset{!}{<} \tau_{pd} = 2\pi \cdot \sqrt{\frac{\varepsilon_0 m_d}{n_d Q_d^2}} \tag{7.28}$$

Whereas in the case of Klindworth *et al.* a time scale of $\tau_s = 40\,\text{ms}$ was sufficient due to the high inertia of big particles, the response time of nano-particles is significantly smaller.

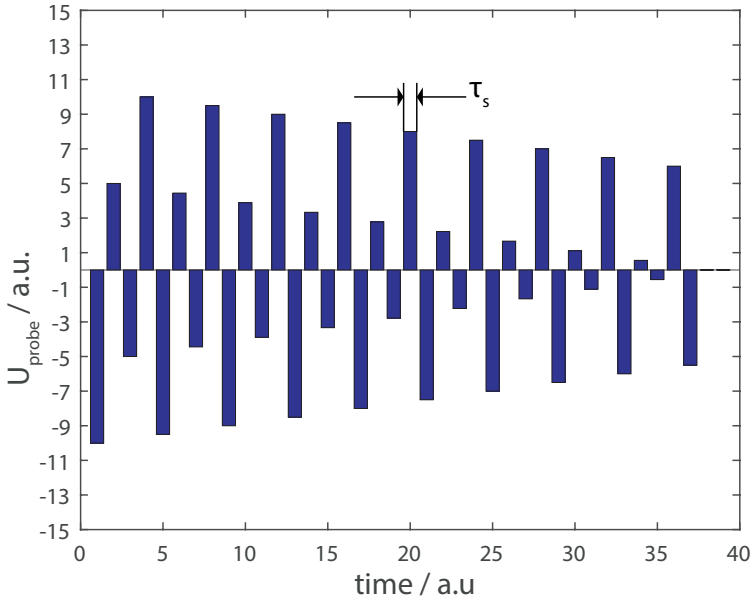

Figure 7.9: The principal sweep pattern of the Langmuir probe is not a linear ramp but a complex pattern, that is at ground potential $\bar{U}_{\mathrm{probe}} = 0\,\mathrm{V} = \Phi_{\mathrm{gnd}}$ on average, which is negative against the plasma potential $\Phi_{\mathrm{pl}} > 0\,\mathrm{V}$ and biased positively only during short intervals $\tau_{\mathrm{s}} < \tau_{\mathrm{pd}}$ (equation 7.28).

This has two reasons: Firstly, the particle density is much greater, decreasing τ_{pd} according to 2.15 and secondly, when applying approximation 2.57 and $m_{\mathrm{d}} = \frac{4}{3}\pi\rho_{\mathrm{d}} r_{\mathrm{d}}^3$, equation 2.15 becomes

$$\tau_{\mathrm{pd}} \approx 2\pi \cdot \sqrt{0.34 \cdot \frac{\varepsilon_0 \rho_{\mathrm{d}} r_{\mathrm{d}}}{e^2 n_{\mathrm{d}}} \cdot [\mathrm{nm}]^2} \propto \sqrt{\frac{r_{\mathrm{d}}}{n_{\mathrm{d}}}}, \tag{7.29}$$

which obviously decreases with smaller dust radius r_{d}. Bilik *et al.* [83] predicted the response time to be of the order of $\tau_{\mathrm{pd}} \approx 0.7\,\mathrm{ms}$, which is two orders of magnitude below the case of Klindworth *et al.*. The challenge in this work therefore is to perform a voltage sweep with an arbitrary voltage pattern, that fulfils the restriction 7.28 for each sample on the sweep curve and to keep the probe clean in between the measurements or even to clean it actively from the deposition caused by radicals and ions from the additionally reactive environment. The sweep pattern used in this experiment is shown in figure 7.9. On average it is on ground potential $\bar{U}_{\mathrm{probe}} = 0\,\mathrm{V} = \Phi_{\mathrm{gnd}}$, which is negative against the plasma potential $\Phi_{\mathrm{gnd}} < \Phi_{\mathrm{pl}}$. This way the dust particles can only feel a repulsive potential exerted by the probe and cannot be extracted onto the probe surface.
Because the nano-dusty plasma possesses only few free electrons, the electron current is not sufficient to heat the probe enough for an effective cleaning. Instead it was found, that a strongly negative probe can be cleaned by sputtering from the fast ions as long as it is not too dirty. Therefore, in this experiment, the following procedure was chosen:

1. ignite argon plasma, probe is biased positively

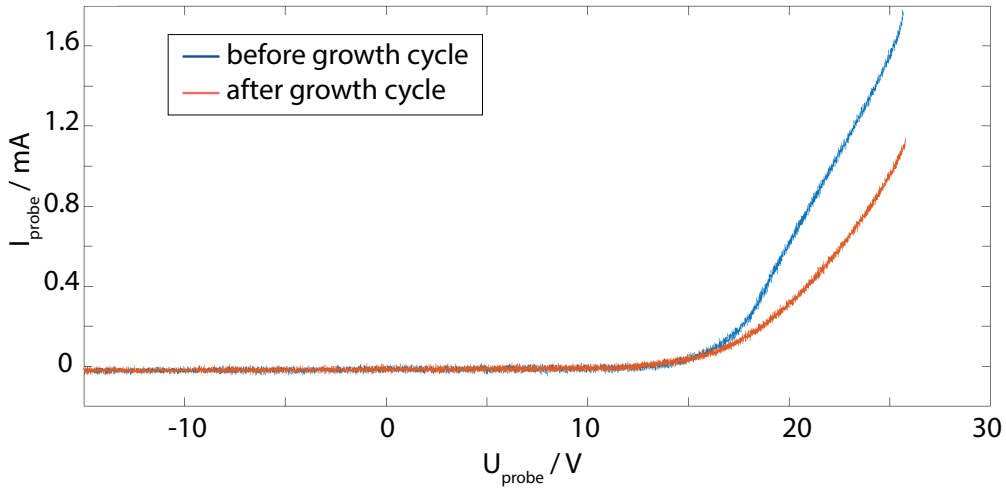

Figure 7.10: Comparing the Langmuir curves before (blue) and after (red) one growth cycle reveals changes in the probe due to deposition of dielectric material. These curves were taken during phase I of two consecutive growth cycles with several measurements in between. Obviously the curve shapes deviate from each other.

2. glowing of probe, to make sure it is clean in the beginnning
3. bias probe strongly negative
4. introduce acetylene to plasma
5. do measurements with the complex sweep pattern throughout one growth cycle
6. keep the probe biased negatively in between the measurements for cleaning by sputtering

A way to test, if this procedure is capable of keeping the probe operational in the difficult environment, is to track changes in the I-V-curve, when keeping the discharge conditions stable. Here, it was done by comparing the Langmuir curve shape during phase I before and after the measurements throughout one growth cycle. The result ideally is the same. A comparison for an unsuccessful procedure, where the two Langmuir curves deviate from each other due to a strong deposition after the growth cycle is shown in figure 7.10.

7.2.3 The dust plasma frequency

As it turned out, a key role for keeping the probe clean is the duration τ_s, at which the probe is biased positively. With increasing measurement rate and thereby decreasing duration τ_s the curves become more and more similar until the curve after one growth cycle falls exactly onto the first one. This is the case, when the measurement rate becomes faster then the dust plasma frequency, or in other words, when $\tau_s < \tau_{pd}$.
Hence, under the assumption that the current to the probe deviates for $\omega_s < \omega_{pd}$ deviates

from the pure ion and electron current, this method provides a possibility to measure the dust plasma frequency $\omega_{\mathrm{pd}} = 2\pi/\tau_{\mathrm{pd}}$, from which plasma properties of high interest might be deduced, at least approximately. For example, taking equation 7.28, one can see, that the dust plasma frequency is related to the particle mass, density and charge, which are three crucial parameters and a hot topic at the moment.
In this discharge, at 9 W of discharge power, a pressure of 5.6 Pa from 7.7 sccm of argon and 0.5 sccm of acetylene flux, we found an agreement of the two Langmuir curves for a duration $\tau_{\mathrm{s}} = 0.\bar{3}\,\mathrm{ms}$. This points to a maximum dust plasma frequency of $\omega_{\mathrm{pd}} \approx 18.8 \cdot 10^3\,\mathrm{s}^{-1}$ under given conditions during particle growth, which is even two times greater than the value given by Bilik *et al.* [83]. Without further measurement, however, it is not sure, when during the growth cycle this value is reached. Possibly, as equation 7.29 suggests, this value is met in the beginning of the cycle, where the particle radius is small but the density high. From equation 7.28 it also becomes clear, that the frequency increases with the dust charge. Therefore, the highest value should be achieved, when

1. the particle density is high
2. the particle size is low
3. the particle charge is high.

Because point 1 and 3 coincide with the prerequisites for a highly affected plasma, it shall be suggested here, that the plasma frequency reaches its highest value, when the self-bias voltage deviates the most from its undisturbed value. That is at the transition from phase II to phase III. At this point of time the particles have reached a size of $r_{\mathrm{d}} \approx 25\,\mathrm{nm}$, according to chapter 5.
Using this size, a roughly estimated mass density of $\rho_{\mathrm{d}} = 1000\,\mathrm{kg/m^3}$ like in section 2.3.3 and using equation 7.29 the dust density can be calculated approximately to

$$n_{\mathrm{d}} \approx 0.34 \cdot \frac{\omega_{\mathrm{pd}}^2 \varepsilon_0 \rho_{\mathrm{d}}}{e^2} \cdot 25 \cdot \left[\mathrm{nm}^3\right] = 1.04 \cdot 10^{12}\,\mathrm{m}^{-3}. \tag{7.30}$$

This is in the low range of what has been observed by Tadsen *et al.* [63] by means of Mie-analysis, and thus, despite the many assumptions and approximations it may be close to reality. However, it is a very vague value. For example an overestimation of the particle charge Q_{d} leads to a strong underestimation of the dust density, because it contributes with the square of its value, see equation 2.15. It may explain, why with above given approximations, the dust density is found to be only in the lower range of what has been observerved by Tadsen *et al.* [63], although in the here presented thesis the particle size is smaller. The dust charge, however, is expected to be much smaller than predicted by the model in equation 2.57 due to the low electron density, as also found experimentally by the above named authors. They concluded, that the dust charge is reduced to 2...8 % of the from equation 2.57 predicted value.
Taking an exemplary charge reduction to 10 % into account would lead to a hundred times higher dust density of

$$n_{\mathrm{d}} \approx 10^{14}\,\mathrm{m}^{-3}. \tag{7.31}$$

7.3 Course of action for data analysis

In the following, it shall be summarized how the values n_e, n_i, T_e, Φ_{pl} and Φ_{fl} have been obtained from the probe measurement data in this work with the help of *MATLAB™*. This way the reader may be guided step by step through the probe analysis, because the order in which parameters are retrieved is non-trivial.

1. In the first step the data are loaded into the matlab environment and an offset scan, that depends on the chosen current measurement resistance is subtracted from the data. The offset is an additional voltage, that is on top of the current measurement. It results from the OP amplifiers in the measurement electronics and can be determined by measuring a voltage sweep without plasma, giving a current value, where it should actually be zero.

2. Then, the plasma potential is determined by building the first derivative of the probe current. In order to do that, the IV-curve needs to be smoothed for noise reduction first. The plasma potential Φ_{pl} is at the voltage, where the current is at its maximum in the first derivative.

3. As next the ion current is fitted according to the expression from equation 7.11. Here, the above obtained plasma potential is used as $U_{probe} = \Phi_{probe} - \Phi_{pl}$. This way it does not need to be fitted as an additional parameter and makes the fit much more reliable. Thus, the only fit parameter is the ion density n_{i0}. Additionally, the ion temperature is set to 0.025 eV. Although the resulting ion density is not reasonable with up to one order of magnitude above the electron density, the fit will serve as physically founded approximation in order to distinguish the electron from the ion current. The ion density will finally be determined differently as follows later.

4. The floating potential Φ_{fl} is found by smoothing the total probe current and reading the potential at the zero crossing. It is actually the simplest parameter to obtain.

5. Now the ion current can be subtracted from the probe current, so that only the electron part remains.

6. Having the pure electron current identified, it can be plotted in a semi logarithmic graph, in which the linear region representing the electron retardation region can be fitted linearly. The inverse of the slope then yields the electron temperature T_e according to equation 7.18. This is the first of two here applied methods to find the electron temperature, and thus, will be referred to as T_{e1} in the following sections.

7. Subsequently the electron density can be calculated according to equation 7.14 by making use of the above obtained electron temperature and by inserting the value of the electron current at the plasma potential $I_e(\Phi_{pl})$:

$$n_{e0} = \frac{4I_e(\Phi_{pl})}{Ae}\sqrt{\frac{\pi}{8}\frac{m_e}{k_B T_e}}. \tag{7.32}$$

A comparison of the real probe data and the sum of the ion current fit and the theoretical electron current (taking the obtained density and temperature values for a maxwellian EEDF) in a plot can now be done. This way the experimentalist can validate the correctness or goodness of the until here obtained values.

8. In order to determine the ion density, the sheath thickness around the probe tip must be known. It depends on the applied voltage and, therefore, it must be calculated for each applied voltage. This is done numerically by finding r_0, so that the theoretical ion current according to Langmuir and Blodgett [103], in particular $I_{\text{theo}} = l \cdot i_{\text{i}}$ with i_{i} from equation 7.10, equals the experimental ion current in the ion fit curve.

9. Once the sheath thickness is known, the ion current density across the sheath edge can be calculated through equation 7.12. Ideally j_{i} should be independent on the probe voltage. This, however, is not the case. A comparison to the earlier described other sheath theories 2.2.1 shows, that this method yields the most constant ion current density with the smallest relative deviations, nevertheless. Hence, it shall be considered to be the most accurate description in the case of this work.

10. From the ion current density across the sheath edge, the ion density can now easily be found according to equation 7.13. A good validation of the ion density can be made by doing a probe measurement in a simple argon plasma, where $n_{\text{e}} = n_{\text{i}}$. If the measured density values agree well, the above described analysis method is accurate. Indeed, it could be verified, that the densities agree within a few percent for a clean and pure argon plasma at different powers in the same pressure range as during the particle growth process. However, an additional parameter may be adjusted in order to bring the two densities into agreement: The factor 0.61 in equation 7.13, which describes the relative plasma density at the sheath edge, may vary for different plasmas. Often it is experimentally found to be 0.5 due to ion losses in collisions in the pre-sheath. Therefore, one may use this factor as margin to adapt this method to a specific plasma.

11. At last another useful test can be done on the obtained parameters. Making use of equation 7.20, which applies r_0, $U_{\text{fl}} = \Phi_{\text{fl}} - \Phi_{\text{pl}}$, $n_{\text{i}} = n_{\text{i0}}$ and n_{e}, the electron temperature T_{e2} can be calculated as a comparative value. Yielding approximately $T_{\text{e1}} \approx T_{\text{e2}}$, it serves as a confirmation for the correctness of all the measured values as an addition to the similarity between the fit curves and the real probe data.

The above described steps have been applied to all the evaluated probe curves. It has been found, that the difference between T_{e1} and T_{e2} never exceeds 10 % of the absolute value, which is rather satisfying.

7.4 Experimental results

This section will present the results of the Langmuir probe measurements. All the measurements have been time correlated with the simultaneously taken self-bias voltage. This way

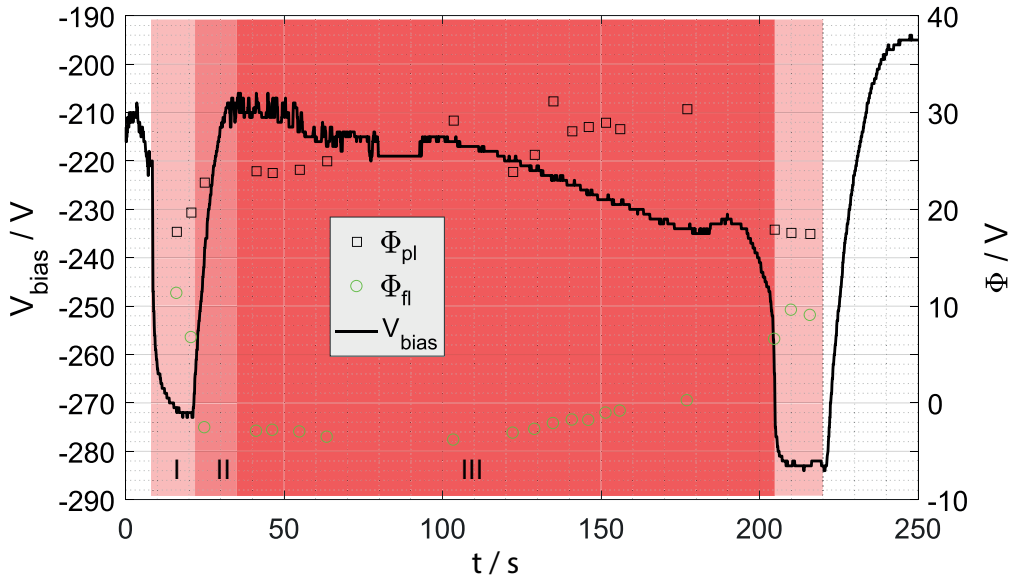

Figure 7.11: The floating potential Φ_{fl} (green circles) decreases drastically to even negative values at the onset of phase II and then recovers slowly during the second half of phase III. The plasma potential Φ_{pl} (black squares), on the contrary, increases at the beginning of phase II and stays on a high level or even increases slightly further until the end of phase III.

the obtained plasma parameters can be put into the context of the particle growth cycles. A general problem has been encountered during the probe measurements: The presence of the Langmuir probe, in particular the additional grounded and floating surfaces as well as the biased probe tip, has an influence on the discharge conditions. The additional surfaces act as electrodes and so any Langmuir probe measurement is always invasive. This is especially critical in this experiment, because the electron density is already drastically reduced due to the collection of electrons on the nanodust. With only a few electrons left, any further electron current drawn from the discharge may effect the plasma even more.
Hence, the self-bias voltage signal does not exactly evolve as usually, when there is no probe in the discharge. Nevertheless, qualitatively the evolution stays the same with its three distinct phases. Only the absolute values seem to be disturbed by the measurement, leading to a less pronounced change in the self-bias voltage. Whereas under standard conditions it usually varies from $\sim -290\,\mathrm{V}$ during phase one to $\sim -100\,\mathrm{V}$ at the transition between phase two and three, it now only reaches up to $\sim -200\,\mathrm{V}$ at the transition. Nevertheless, the self-bias voltage still is useful to identify those different phases and to correlate the Langmuir probe measurements to the growth progress during each nanoparticle cycle. Here, the results for the first growth cycle of an experiment shall be presented.
In a first plot 7.11 the plasma potential Φ_{pl} in black squares and the floating potential Φ_{fl} in green circles are shown. The self-bias voltage V_{bias} is plotted simultaneously for comparison, and hence, the phases I, II and III are marked in bright, medium and darker violet, respectively. During the first phase, which is represented by the first and the three last

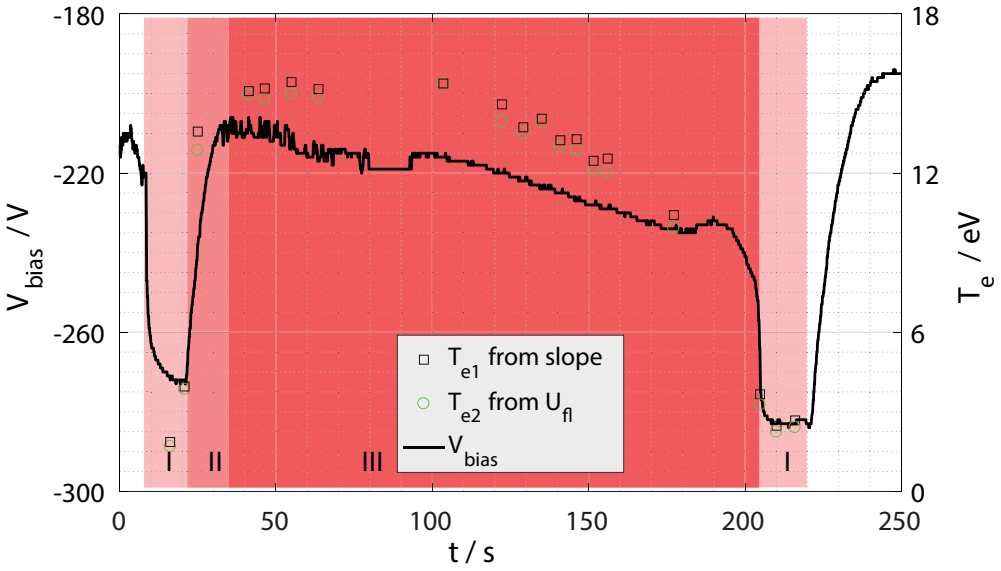

Figure 7.12: The different analysis methods, from the slope of the electron retardation current (red squares) and from the floating voltage (green circles) yield similar results. Whereas the electron temperature is low with 2 . . . 3 eV during phase I, it increases drastically during phase II and has its maximum in the first half of phase III at round about 15 eV. It then slowly reduces and drops significantly at the end of phase III.

measurements, the plasma potential can be localized at $\sim 18\,\mathrm{V}$, while the floating potential is relatively high at $\sim 10\,\mathrm{V}$. This changes abruplty in phase II, where the plasma potential increases and the floating potential decreases rapidly. Already in the very beginning of phase II or at the transition between phase I and II, both values change significantly. Throughout the third phase both potentials remain relatively stable. To be more precise, the floating potential reaches its minimum with $\sim -4\,\mathrm{V}$ roughly in the middle of phase III, whereas the plasma potential exhibits a relatively large fluctuation but seems to grow slowly up to the end of phase III to around $\sim 30\,\mathrm{V}$.
It shall be mentioned here, that the fluctuations of the plasma potential do most probably not represent real changes in the discharge but originate from difficulties to determine the plasma potential properly from the first derivative in case of a dusty plasma. With dust particles present (phase II and III) the maximum in the first derivative of the electron current is smeared out and may therefore have large error bars in the range of $\pm 5\,\mathrm{V}$. However, by plotting the theoretical probe current according to the obtained values, only little deviations between the theoretical curve and the real measurement could be found. Hence, the potential evolution as shown in graph 7.11 shall be assumed to be qualitatively correct.
As next the electron temperature as obtained from the slope in a semi logarithmic plot of the electron current T_{e1} (black squares) is shown together with the temperature T_{e2} obtained from the floating voltage U_{fl} (green circles) and again the self-bias voltage in figure 7.12. It can easily be noticed, that both temperatures yield almost the same values throughout the entire growth cycle. This confirms the consistency in the above discussed theory and the

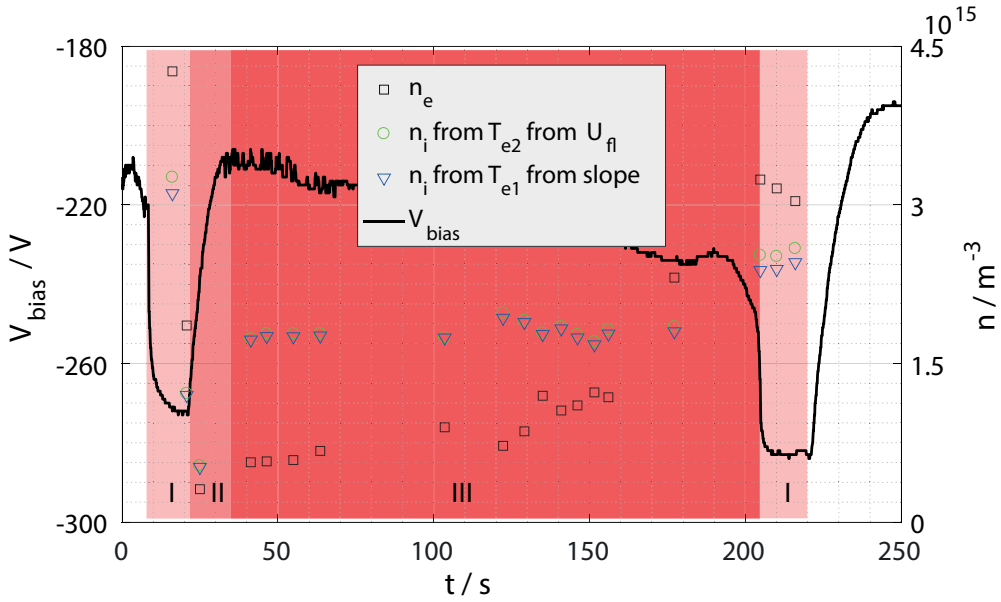

Figure 7.13: The ion density as calculated with the aid of T_{e1} (blue triangles) does not differ significantly from the one determined with help of T_{e2} (green circles). Both decrease significantly at the beginning of phase II to $\sim 5 \cdot 10^{14}\,\mathrm{cm}^{-3}$, then stay relatively stable throughout phase III at $\sim 1.810^{15}\,\mathrm{cm}^{-3}$. The electron density n_e (black squares) is drastically reduced during phases II and III.

measurement.
Moreover, a small difference in the electron temperature can be seen between the very first measurement ($T_e \approx 1.5\,\mathrm{eV}$) and the last two ($T_e \approx 2.5\,\mathrm{eV}$). Hence, a small drift in the measurement or the discharge condition can be found. This may be due to a conditioning process of the discharge, because the presented growth cycle is the first one during this experiment. Thus, at the end of this cycle a few of the particles might reside in the discharge, while a new generation is formed. Hence, the condition in the beginning of the first and the second cycle is not identical, and the slightly elevated temperature in the second phase I indicates a residual influence of some nanodust.
Nevertheless, a principal trend can be resumed as follows: The electron temperature is relatively low during phase I with 1.5 to 3 eV. Then during phase II it shoots up very rapidly to enormous temperatures of more than 10 eV. It reaches its maximum roughly in the middle of phase III with values as high as 15 eV and finally drops down slowly during the rest of phase III in order to recover to the low value of phase I.
The fluctuations in the determined temperatures are fairly small and can be roughly estimated to $\pm 2\,\mathrm{eV}$, which corresponds to $\sim \pm 15\,\%$ at high electron temperatures.
At last, in figure 7.13, the density evolution for the electrons and ions is shown. While, as described above, the electron density is taken from the current at the plasma potential, the ion density has been obtained by equation 7.13. Here a choice for the electron temperature, that is hidden in v_B needs to be made. Therefore, two different ion densities are plotted,

using either T_{e1} or T_{e2}. However, due to the little difference in those two, the ion densities are equally closely matched.
Another feature is striking, though. During phase I the electron density is higher than the ion density, which is unexpected and not reasonable. Only two possible scenarios could explain $n_i < n_e$. One of it may be charge exchange collisions in the sheath around the probe tip, which would reduce the effective ion velocity and thus their current. Another possibility is the presence of high mass ions due to the polymerization to longer hydrocarbon chains. Because argon is difficult to ionize, the presence of other gases may change the ionized species away from argon to easily ionizable trace gases. The dominance of heavy hydrocarbon ions has for example been calculated by Schweigert *et al.* in [175]. Those authors identify $C_6H_4^+$, $C_6H_5^+$ and $C_4H_2^+$ as equally important main ion species in a similar CCRF argon/acetylene discharge, followed by $C_8H_6^+$ and $C_4H_3^+$. Argon ions, however have been calculated to contribute only to less than one percent to the total ion density in the discharge centre.
Taking a mean mass of the tree most important hydrocarbon ions yields an average ion mass of 67.7 amu. Considering the next important ion to be of even greater mass, one can round this value up to 70 amu, which is significantly higher than the argon ion mass, and hence, affects strongly the calculated Bohm velocity, which contributes to the ion density calculation through equation 7.13. Thus, a higher mass yields a smaller Bohm velocity and therefore a higher ion density. Note, that it has no effect on the calculated electron temperature T_{e1} found by method 1 though, which is the inverse of the slope in a semi-logarithmic plot of the probe current, but a slight effect on T_{e2} through m_i in the logarithm of equation 7.20. However, as we do not know the exact ion composition in the probe region, we will keep the ion mass fixed throughout the entire growth cycle to be the mass of argon ions as a classical and conservative estimation. At this place, however, it may probably explain, why the electron density is measured to be higher than the ion density during phase I.

7.5 Discussion

Summarizing, a method to avoid probe contamination was found and successfully applied. Furthermore, as a by-product, the dust particle plasma frequency was determined to be $\omega_{pd} < 18.8\,s^{-1}$ throughout the growth cycle. This limit is two times greater, than the value found by Bilik *et al.* [83], and thus, it is almost in agreement with her work. Using a particle size of $r_d = 25\,nm$ and a mass density of $\rho_d = 1000\,kg/m^3$ the measured dust plasma frequency allows to roughly estimate the dust density to be in the order of $n_d \approx 1 \cdot 10^{12} m^{-3}$, which is lower than the measurement results by Tadsen *et al.* [63]. However, a charge reduction to 10 % due to electron rarefaction would lead to a 100 times higher dust density, and thus, the value of $n_d \approx 1 \cdot 10^{12} m^{-3}$ can be regarded as a lower limit for the real density. It shall also be mentioned here, that the dust plasma frequency measurement is independent of the applied method of evaluating the Langmuir probe characteristics.
In further studies it may even be possible to measure the dust plasma frequency time resolved during the growth cycle. This is particularly interesting, because when both, the dust size and the dust plasma frequency, can be measured time resolved, the dust density can be

determined at each point during the growth cycle. By a spatial scan, this measurement may become a spatio-temporal tool, in order to investigate the dust cloud in great detail. However, it would require the following changes to the here applied method:

1. The probe surface needs to be kept clean passively before and after the experiment. An active cleaning after the experiment would risk to destroy any thin film, that was intentionally deposited in order to measure, that the probe frequency is still below the dust plasma frequency. It could be realised by a moveable shield, that is put in front of the probe before and after each probe measurement.

2. A more advanced method to quantify the deposited particles on the probe surface might be necessary.

One possibility to measure the deposited dust on the probe surface might be electron microscopy, which would have the great advantage, that the size of the dust can be perfectly correlated to the dust plasma frequency measurement. Furthermore, it would allow to distinguish between a thin film formation from vapour deposition and a thin film through dust deposition. Here, it may be interesting, to use a planar probe surface instead of a cylindrical one. However, these investigations are beyond the scope of this thesis and shall only be given as an outlook for further research.
In order to overcome several difficulties in evaluating the Langmuir probe data in this particular plasma and configuration a method was developed, which brings to consistency two different widely used methods to retrieve the electron temperature:
The first method makes use of the inverse of the slope in the semi-logarithmic U-I-plot according to equation 7.18. This method was applied without any changes to the standard theory.
The second method makes use of a dependence of the voltage difference between floating and plasma potential on the electron temperature. Here, the standard theory has been extended and adapted to cylindrical probe designs and to plasmas, where $n_\mathrm{e} \neq n_\mathrm{i}$. For the calculation of $T_{\mathrm{e}2}$ equation 7.20 was applied, which necessitates to know

1. the effective probe collection radius at the floating potential $r_0(U_\mathrm{fl})$,

2. the electron density n_e, which can easily be obtained through standard theory,

3. and the ion density n_i.

The effective collection radius has been calculated numerically according to works from Langmuir [98, 103] on the space charge sheath around coaxial cylinders. The result then permits to retrieve the ion density by comparing the total measured ion current to the sheath edge surface.
The so obtained two electron temperatures $T_{\mathrm{e}1}$ and $T_{\mathrm{e}2}$ are in great agreement throughout the entire growth cycle, as shown in figure 7.12, which is a good indicator for the validity of this model. Nevertheless, with maximum 15 eV the temperature is very high and out of range of simulation results [175, 235]. Furthermore, in a similar experimental work of Bilik *et al.* [83] the obtained electron temperature of $T_\mathrm{e} \approx 4.5\,\mathrm{eV}$ was far lower in the dusty

argon/silane plasma.
Furthermore, the electron density decrease of a factor of round about 10 from phase I to phase II is higher than in above mentioned measurements (factor of 3). However, this is in better agreement with microwave interferometric measurements from Hinz *et al.* [77], where n_e was out of the measurement range during the last two growth phases in a similar reactor and similar conditions, meaning a density reduction of a factor of round about 40. The different reactors and chemistries, therefore, are not necessarily comparable by quantitative means, but it shows, that the here obtained values are in a reasonable range.
From this an important conclusion can be drawn: For the electron density calculations the most critical is to identify the plasma potential correctly, and thus, a correct electron density is a further indicator for the validity of the plasma potential measurement. Consequently, by making use of equation 7.20 to calculate the electron temperature and comparing it to the method making use of the slope in the semi-logarithmic U-I-plot, the obtained values seem very consistent within the obtained data.
The difference between the ion density and the electron density is a measure for the dust charge density according to equation 2.43. This reaches its maximum in the beginning of phase III, where there is also the biggest deviation in the self-bias voltage compared to an undisturbed plasma. Here, the ion density is $n_i \approx 1.7 \cdot 10^{15}\,\mathrm{m}^{-3}$ while the electron density reduces down to $n_e \approx 0.5 \cdot 10^{15}\,\mathrm{m}^{-3}$.
The absolute difference between the two must then be attributed to the dust charge density, being in the order of

$$Zn_d \approx 1.2 \cdot 10^{15}\,\mathrm{m}^{-3}. \tag{7.33}$$

Taking into account the rough estimate $n_d > 1 \cdot 10^{12}\,\mathrm{m}^{-3}$, as obtained from the measured dust plasma frequency ω_{pd}, it can be concluded, that each dust grain accumulates $Z \approx 1200$ elementary charges at that time of the growth cycle. From equation 2.57 on the contrary, a dust charge number of 120 would be expected for isolated particles of size $r_d \approx 35\,\mathrm{nm}$.
This discrepancy may be caused by a wrong dust material density estimation $\rho_d \approx 1000\,\mathrm{kg/m}^3$ or by a charge reduction of the dust charge, which then affects the calculation of the dust density in equation 7.28. Freely assuming a charge reduction to 10 % of the theoretical value as described above, the dust density needs to be 100 times higher. Then, the dust charge number would on the one hand side reduce to $Z \approx 12$ after equation 7.33 but on the other hand it would also meet the condition to be 10 % of the theoretical value after equation 2.57. This is another nice consistency check of the here performed Langmuir probe measurements. Hence, a charge reduction of 90 % to $Q_d \approx -12e$ at the beginning of phase III and a simultaneous dust density of $n_d \approx 10^{14}\,\mathrm{m}^{-3}$ shall be proposed here.
According to equation 2.61 an approximate Havnes value P can be calculated from above estimations for the beginning of phase III. Having $n_d/n_e \approx 0.2$, a dust radius of $r_{d\mu m} \approx 0.035$ and an electron temperature of $T_{eV} \approx 15$ a value of

$$P \approx 73 \tag{7.34}$$

can be determined. Hence, with a of $P \gg 1$, the plasma is strongly affected by the particles in terms of the Havnes parameter, too.

Although these values need to be interpreted as rough estimates, it demonstrates, how powerful the Langmuir probe measurements can be, when combined with the electron microscopy and when time correlated to the self-bias voltage. The reader may note, that a dust charge reduction of 10 % due to the electron rarefaction is still a conservative estimation compared to the values given by Tadsen *et al.*, the Havnes parameter is in the same order of magnitude with a maximum of $P \approx 50$ in their case, though.
If a time resolved dust plasma frequency measurement was available, this way not only plasma potentials, ion and electron densities and electron temperature could be determined, but also the dust density and charge at any time in the growth cycle. Even a spatio-temporal resolution is possible. Therefore, the Langmuir probe can potentially resolve all the basic parameters of a dusty plasma apart from the chemical composition.
Special attention needs to be paid to the fact, that the nanodusty acetylene-argon plasma is more or less electronegative. The negative dust particles as well as negative ions like C_2H^- contribute to an electronegative part of the plasma. This affects the description of the plasma sheath by a modified sheath potential due to a smaller Bohm velocity [236]

$$v_\mathrm{B}^2 = \frac{k_\mathrm{B} T_\mathrm{e}}{m_\mathrm{i}} \cdot \frac{n_{\mathrm{i,s}} T_-}{n_{\mathrm{e,s}} T_- + n_{-,\mathrm{s}} T_\mathrm{e}}, \tag{7.35}$$

where the index s stands for the according values at the sheath edge and the index $-$ for the negative ions.
Various theories for Langmuir probe measurements in electronegative plasmas can for example be found in [236–239]. However, finding the appropriate model, adjusting fit parameters and verifying its validity can be a PhD study for itself, which is why this thesis goes without a more extensive Langmuir probe model and remains rather simple. More general aspects of electronegative discharges can be found in [240].

r_0/a	β^2	r_0/a	β^2	r_0/a	β^2	r_0/a	β^2	r_0/a	β^2
1.00	0.00000	1.4	0.14856	2.4	1.5697	3.8	5.3795	5.8	13.407
1.01	0.00010	1.5	0.2282	2.5	1.7792	4.0	6.0601	6.0	14.343
1.02	0.00040	1.6	0.3233	2.6	1.9995	4.2	6.7705	6.5	16.777
1.04	0.00159	1.7	0.4332	2.7	2.2301	4.4	7.5096	7.0	19.337
1.06	0.00356	1.8	0.5572	2.8	2.4708	4.6	8.2763	7.5	22.015
1.08	0.00630	1.9	0.6974	2.9	2.7214	4.8	9.0696	8.0	24.805
1.10	0.00980	2.0	0.8454	3.0	2.9814	5.0	9.8887	8.5	27.701
1.15	0.02186	2.1	1.0086	3.2	3.5293	5.2	10.733	9.0	30.698
1.2	0.03849	2.2	1.1840	3.4	4.1126	5.4	11.601	9.5	33.791
1.3	0.08504	2.3	1.3712	3.6	4.7298	5.6	12.493	10	36.976

Table 7.1: β^2 as a function of radius, with a probe radius, r_0 sheath edge radius, taken from [103];

Chapter 8

Phase resolved imaging of the electrode sheath

As not only the particles themselves but also the plasma provides indirect valuable information about the growth process of nano dust, it can be useful to broaden the diagnostic methods. Combining different *in situ* as well as *ex situ* methods is one route to investigate growth phenomena [84, 241]. Phase resolving cameras are another very powerful tool to get an insight into spatial and temporal excitation patterns and hence into the excitation and de-excitation mechanisms of an RF plasma. Introduced by de Rosny *et al* [242], they have already been applied in combination with a spectrograph for phase-resolved optical emission spectroscopy (PROES) [243] to investigate electron beams and excitation patterns in RF plasmas [244–247] and to determine quenching coefficients for emitting states of various species [248, 249] or combined with laser Stark spectroscopy for space and time resolved electric field measurements [250]. For an extensive literature overview on PROES in RF plasmas the reader may refer to Schulze *et al* [251].
The principal of phase resolved camera measurements is based on such a high time resolution, that a sufficient amount of photographs can be taken during one RF cycle (13.56 MHz) of duration $\tau_{\mathrm{rf}} = 74\,\mathrm{ns}$. In this work, a fast camera from ANDOR™ Technology was able to resolve this cycle down to gate lengths of 2 ns by the use of an electronic shutter. This way it is possible to visualise emission patterns evolving during the growth of nanoparticles from an argon-acetylene plasma in the sheath region in front of the powered electrode.

8.1 Camera Set-up

Since the latest processes [84] were run at 9 W discharge power and at a total pressure of $p \approx 5 \ldots 5.5\,\mathrm{Pa}$ and an argon-acetylene ratio of 10:1 to 10:2, the same was chosen for this experiment. The principal Setup is also the same as in previous experiments above in chapters 6 and 7. However, in order to avoid a distortion of the plasma, no invasive diagnostic like the Langmuir probe was employed at the same time. Therefore, one has to rely onto the reproducibility of the experiment to make comparisons to the former experimental runs. A small window was mounted at one side of the reactor, in order to get a straight side view

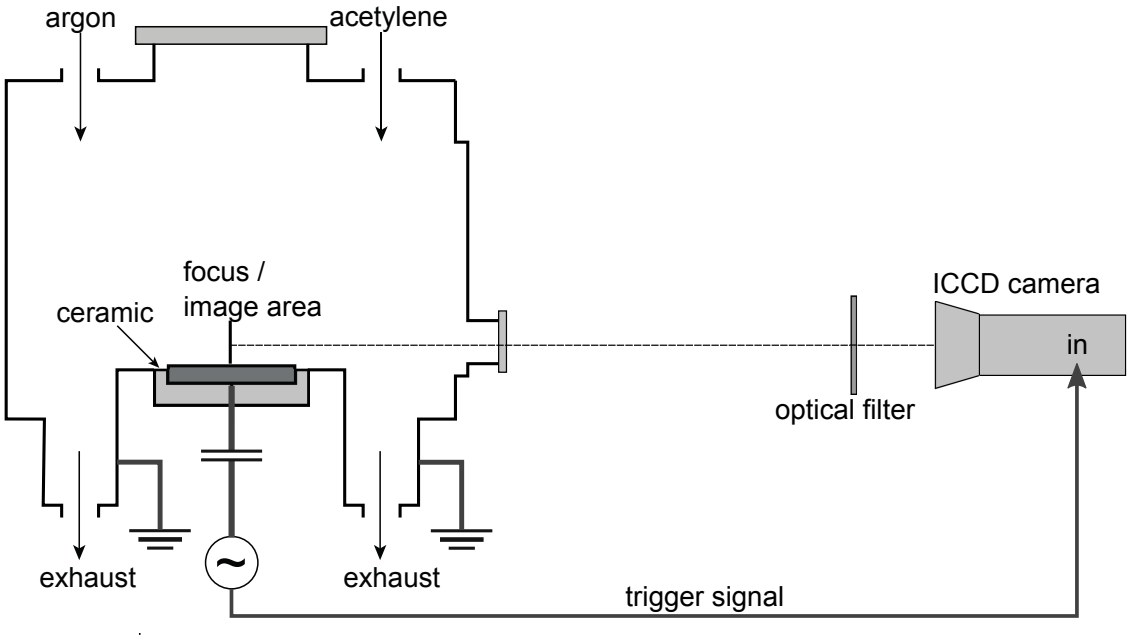

Figure 8.1: Sideview of the setup: The camera is focussed in the center of the discharge and aligned with the height of the electrode.

to the sheath in front of the powered electrode, as shown in figure 8.1
During successive particle growth cycles the plasma sheath was optically recorded with a fast gating camera. The New iStar ICCD (intensified charge-coupled device) camera from ANDOR™ Technology model DH320T-18U-A3 has an image intensifier mounted in front of the common CCD sensor. It consists of a photo cathode, a MCP (micro-channel plate) and phosphor screen. Incoming photons are thereby firstly converted into electrons, which can be multiplied by the micro-channel plate and then back-converted into photons by phosphor-luminescence [252]. The sensitivity or quantum efficiency (QE) of the intensifier tube is dependent on the wavelength of incoming light. Whereas low wavelengths are limited by the transmission properties of the input window, long wavelength light is cut off by the photo cathode. Efficiency curves are plotted in figure 8.2. Here the camera model with a photo cathode of type Gen III - FL (EVS, -A3) was used.
By using the cathode voltage as an electronic shutter, the camera can be fed with the trigger output signal from the RF generator. The gating time τ_{gate} during which the electronic shutter is open can be as small as 2 ns and an internal digital delay generator was used to add an offset to the external trigger signal. The delay time τ_{delay} was increased in either 2 or 1 ns steps. While the photo cathode was triggered with RF frequency, the phosphor screen and CCD accumulate the counts of photons during one exposure time τ_{exp} in the range of seconds. This way one RF cycle of 73.75 ns can sufficiently be time resolved with enough intensity. For simplicity one RF cycle was taken to be 74 ns long, so that 37 images with a delay step of 2 ns or 74 images taken with delay steps of 1 ns represent one entire RF cycle. The camera was focussed on the centre of the electrode in a distance of 1.65 m from the

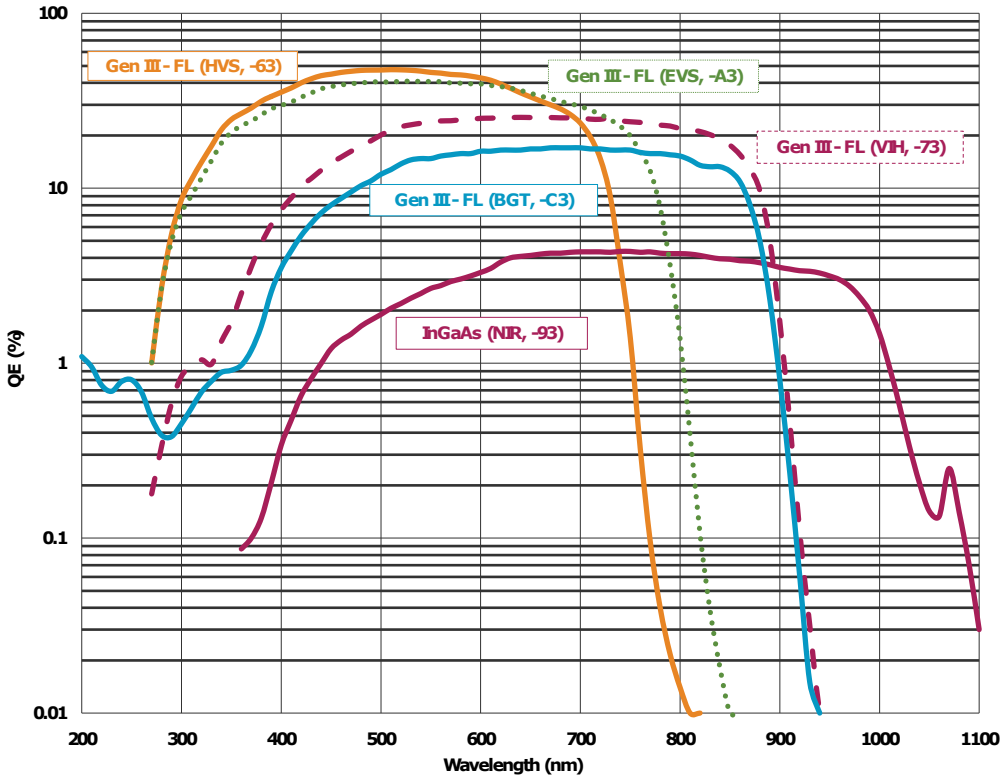

Figure 8.2: Transmittance of intensifying cameras is limited by the sensitivity or rather quantum efficiency (QE) of the intensifier tube. For this research the photo cathode of type Gen III - FL (EVS, -A3) was used.

front plate of the camera and horizontally and vertically aligned in a way, that a perfect side view of the electrode was given. Due to the relatively long distance between camera and plasma the depth of field is good, thus for simplicity we consider to portray a perfect side view projection of the plasma. Using a zoom factor of 300, it was measured with a slide gauge, that 10 mm in vertical direction in the focal plane equal 90 pixels on the camera CCD chip.
Measurements without and with longpass filter in front of the camera have been done. Whereas in the measurements without filter the entire optical emission was recorded only limited by the cameras properties, the filter absorbed light up to 695 nm, so that the strong argon lines, which usually dominate the spectrum, were transmitted. The specific transmittance of the filter (RG695) from SCHOTT is presented in figure 8.3.
Thus, using this set-up either light in the range of 280 to 810 nm or emission in the range of 695 to 810 nm can be recorded. Table 8.1 shows the transmitted lines according to [253] and [254], which are long enough to pass through the filter and small enough to be intensified by the intensifier tube. Except for C_2 all the molecular species are either related to nitrogen or oxygen and thus are only present as small amounts of impurities. Therefore their relative intensity should be rather low in comparison to the strong argon lines. It is unclear if pure carbon is present in the discharge, but if so, there are only two lines originating from singly

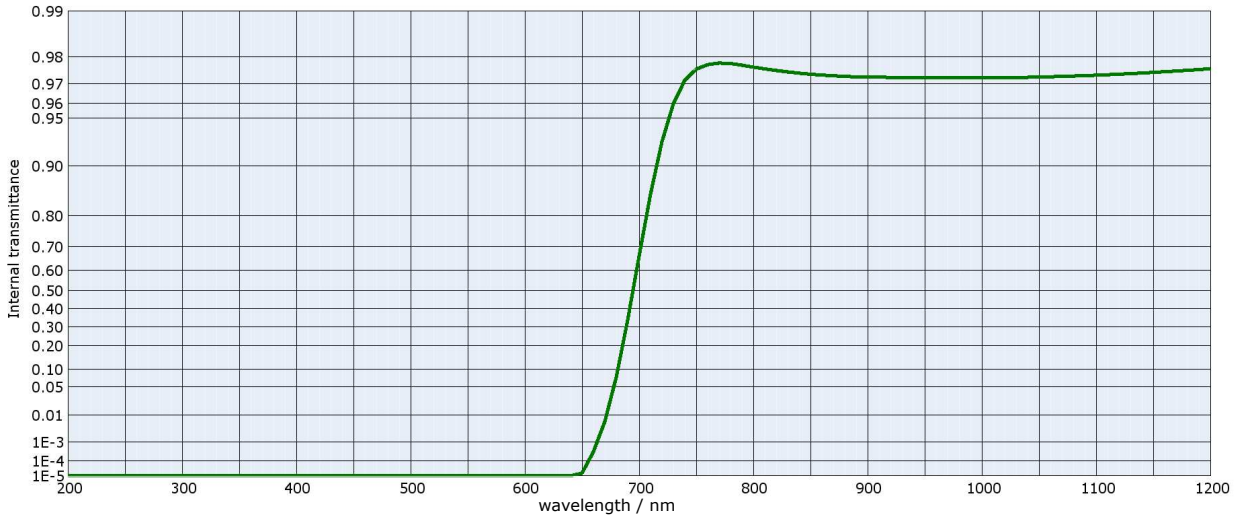

Figure 8.3: The SCHOTT filter absorbs light with low wavelengths and transmitts the ArI lines.

charged carbon between 695 and 810 nm. Also the quantity of C_2 is expected to be low, as mass spectrometric investigations confirm, as will be shown later in chapter 9. Summarizing, the glow observed with filter mounted in front of the camera, is supposed to be dominated by neutral Argon de-excitation.
On the opposite, in the region of 280 to 695 nm a huge number of molecular bands, hydrogen lines and emission from singly charged Argon are expected to occur. Thus the overall emission patterns were compared to those with filter.

8.2 Image Processing

Each photograph taken was turned according to the electrode direction to minimize the tilt of the pictures. As the image width is smaller than the electrode diameter, the plasma sheath is assumed be homogeneous across the width of the photograph. Henche, each picture was horizontally compressed to an intensity profile $I_{\tau_{\text{delay}}}(y)$ along the vertical direction y by taking the horizontal mean as shown in figure 8.4. Thereby the signal to noise ratio was significantly improved.
The internal digital delay generator brings the necessity to calibrate image series. Taking a light bulb as stable light source, the measured overall sum of pixel intensities

$$P_{\tau_{\text{delay}}} = \sum_{y} I_{\tau_{\text{delay}}}(y) \tag{8.1}$$

in one picture is not stable when shifting the delay τ_{delay} to the trigger signal from zero to 80 ns as shown in figure 8.5. At the end of the presented RF cycle a sudden increase in intensity occurs, which can be neglected, as one entire RF cycle contains all information.

emitting molecules	wavelength / nm	emitting atoms	wavelength / nm
H_2O	716.45	C II	723.13
H_2O	722.7	C II	723.64
H_2O	809.7	Ar I	696.54
CO	721.04	Ar I	706.72
CO	783.39	Ar I	714.70
OH	728.42	Ar I	727.29
OH	752.91	Ar I	738.40
OH	775.58	Ar I	750.39
OH	791.85	Ar I	751.47
O_2	759.37	Ar I	763.51
N_2	738.66	Ar I	772.42
N_2	750.39	Ar I	794.82
N_2	759.1	Ar I	800.62
N_2	762.62	Ar I	801.48
N_2	775.32	Ar I	810.37
N_2	778.0		
N_2	805.76		
NH_2	735.0		
NH_3	791.9		
NO	778.76		
NO	786.19		
C_2	785.25		
CN	787.64		
HCN	791.2		

Table 8.1: Strong emission lines in the range of 695 to 810 nm according to [253] and [254].

Fitting the intensity versus delay time with a quadratic polynomial yields

$$\begin{aligned} P(\tau_{\text{delay}}) &= a_0 + a_1\tau_{\text{delay}} + a_2\tau_{\text{delay}}^2 \\ a_0 &= (4237 \pm 7)\,\text{counts}\,/\,\text{s} \\ a_1 &= (1.384 \pm 0.438)\cdot 10^9\,\text{counts}\,/\,\text{s}^2 \\ a_2 &= (-5.971 \pm 6.209)\cdot 10^{15}\,\text{counts}\,/\,\text{s}^3, \end{aligned} \tag{8.2}$$

which is displayed in figure 8.5. The choice to take a polynomial fit is based on its simplicity and yet good fit. Normalizing the function by its mean $\langle P\rangle$, it was then used to calibrate all intensity data $I(\tau_{\text{delay}}, y)$ by the expression

$$I_{\text{cal}}(\tau_{\text{delay}}, y) = \frac{\langle P\rangle}{P(\tau_{\text{delay}})}\cdot I(\tau_{\text{delay}}, y), \tag{8.3}$$

so that in the case of the light bulb, $I_{\text{cal}}(\tau_{\text{delay}}, y_0)$ becomes an almost constant value over τ_{delay}.

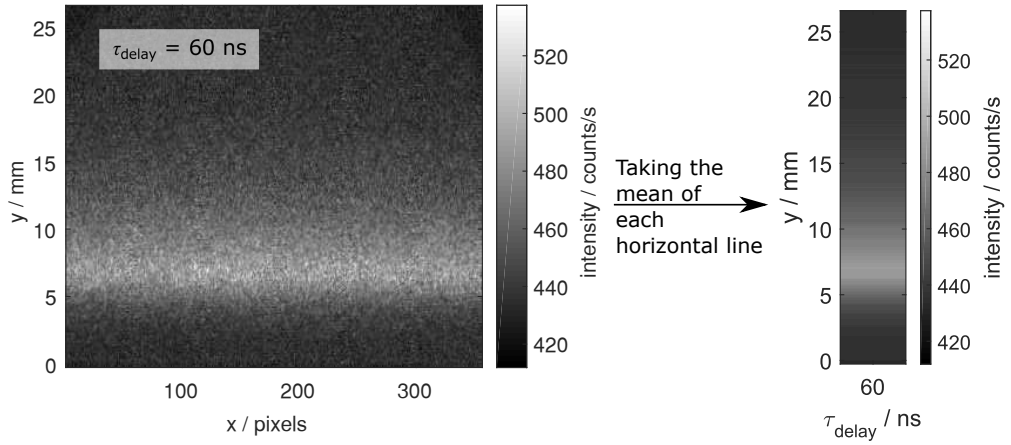

Figure 8.4: By taking the horizontal mean of one picture, it is reduced to a vertical intensity profile at the delay time τ_{delay} it was taken.

All the compressed photographs taken at a consecutive time series τ_{delay} can then be merged to one single picture displaying $I(\tau_{\mathrm{delay}}, y)$ in a two dimensional colour plot. As for some reason in some of the merged pictures a few shots at certain times τ_{delay} are not properly exposed, these shots are sorted out by a matlab routine and replaced by the mean of neighbouring shots. Finally all pictures are duplicated and reunited to cover two entire RF cycles and then are noise reduced by an adaptive Wiener method, where each pixel is compared to 5 neighbouring pixels in direction of the time axis τ_{delay}.
Exposure times of 0.012 s for measurements without and 0.05 s for measurements with filter lead to total acquisition times of 0.7 and 3 s respectively per merged picture. Several of those a few second long measurements can now be done during one growth cycle, tracked through the self-bias voltage recording. Here, only a few chosen measurements shall be presented, marked as a to i in figure 8.6.
As usual, the following typical features of the self-bias voltage can can be observed:

1. The self-bias voltage is the most negative and tends to stay at a fixed value of -300 to -250 V. The particle diameter ranges from 20 to 40 nm.

2. The self-bias voltage increases rapidly up to round about -100 V. The particle diameter increases from 40 up to 50 nm.

3. A slow decrease of the self-bias voltage takes place until it finally drops down rapidly to the value of stage 1. The particles steadily grow to sizes of 140 nm in diameter.

During these experiments the consecutive single generations could be achieved by adjusting the parameters as follows:

- output power at 13.56 MHz of 9 W
- total pressure of 4.9 to 5.1 Pa

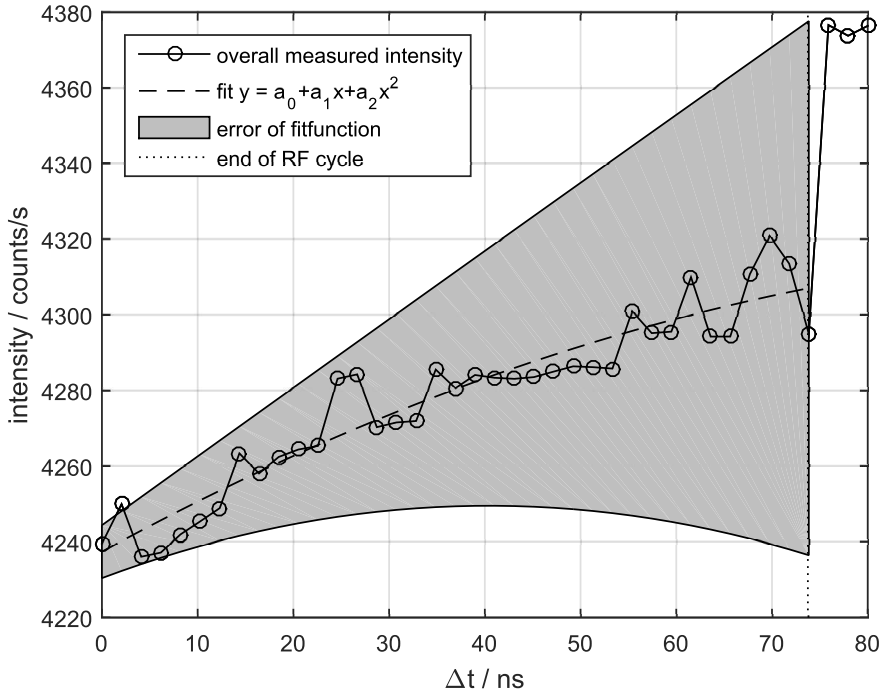

Figure 8.5: The overall measured intensity $P(\tau_{\text{delay}})$ of an image is not independent of the delay to the trigger signal even for a constant light source. A quadratic polynomial suits well to fit the intensity data versus the trigger offset τ_{delay}.

- acetylene admixture of 3.6 to 7.2 % with an argon flow of 14 sccm.

Unfortunately the variation of the self-bias voltage is not always reproducible with the same parameters, because the reactor changes during the process. The chamber walls and electrodes get deposited with dust so that its surface changes. Thus, secondary electron emission, sputtered material composition and surface charges can change from experiment to experiment, so that the acetylene admixture has to be adjusted before each experimental run to achieve single generation particle synthesis. Furthermore, the process may heat the electrode leading to an additional thermophoretic force onto the dust and thereby changing the dust cloud shape and composition. However the acquisitions with and without filter can be compared qualitatively by looking at the emission patterns.

8.3 Measurement results during particle growth

In this section the acquired de-excitation patterns (at points a to i in figure 8.6) will be presented.
As already introduced, PROES in a capacitively coupled pure argon discharge has already been done for example by Nemschokmichal *et al.* [244] or Mahony *et al.* [246, 247]. To characterize the discharge in our reactor, the emission patterns during an argon discharge at similar pressure as for particle synthesis and at same power have been acquired. As the

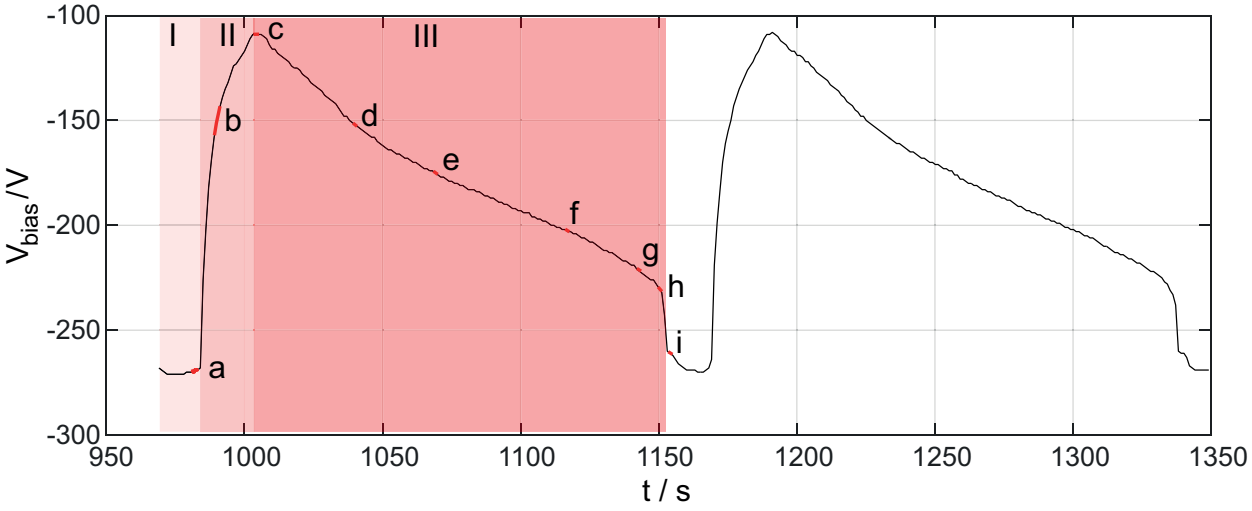

Figure 8.6: The self-bias voltage again shows the distinct phases I to III during particle growth. The red lines marked with a-i represent the acquisition periods of the phase resolving camera, that shall be presented in the following section.

pattern does not differ qualitatively from the one during phase I of the growth cycle, as shown in figure 8.7 (point a), the emission during particle growth shall directly be discussed without showing the pattern of a pure argon discharge.
In an rf discharge an alternating electrical field accelerates free electrons, whereas the ions are only under influence of a time averaged field. The driven electrode is capacitively coupled and due to the high asymmetry of the reactor it charges up to almost half of the applied peak-to-peak voltage in average. Therefore, the ions are constantly attracted by the negatively charged electrode resulting in a constant ion flux towards it. However electrons follow the rapidly changing electric field. So, once per rf cycle the electrode charges up to a voltage positive enough for the hot electrons to overcome the trapping by the plasma potential. This way the overall current crossing the sheath is balanced at exactly the dc-selfbias voltage of the electrode.
In the phase of electrons reaching the electrode the positive space charge in the sheath is disturbed by being flooded with electrons, thus, it is called *sheath collapse*. During sheath expansion, directly after the sheath collapse, residual electrons are accelerated into the volume by the again negatively charged electrode. The electron stream leads to excitation on its pathway. The conclusive de-excitation can then be clearly seen in the measured patterns. A strong glow reaching from close to the electrode at height $y = 5\,\mathrm{mm}$ protruding with time into the plasma can be found at round about 50 ns in figure 8.7. For the rest of the RF-cycle the de-excitation seems to be greater than excitation, so that the glow intensity decreases until the next sheath collapse.
At point a in figure 8.6 particles start to be formed, thus they are small. Once particles are present in the plasma, their size in this growth stage ranges from 20 to 40 nm. The fact, that they do not change the selfbias voltage in comparison to a dustfree plasma, indicates,

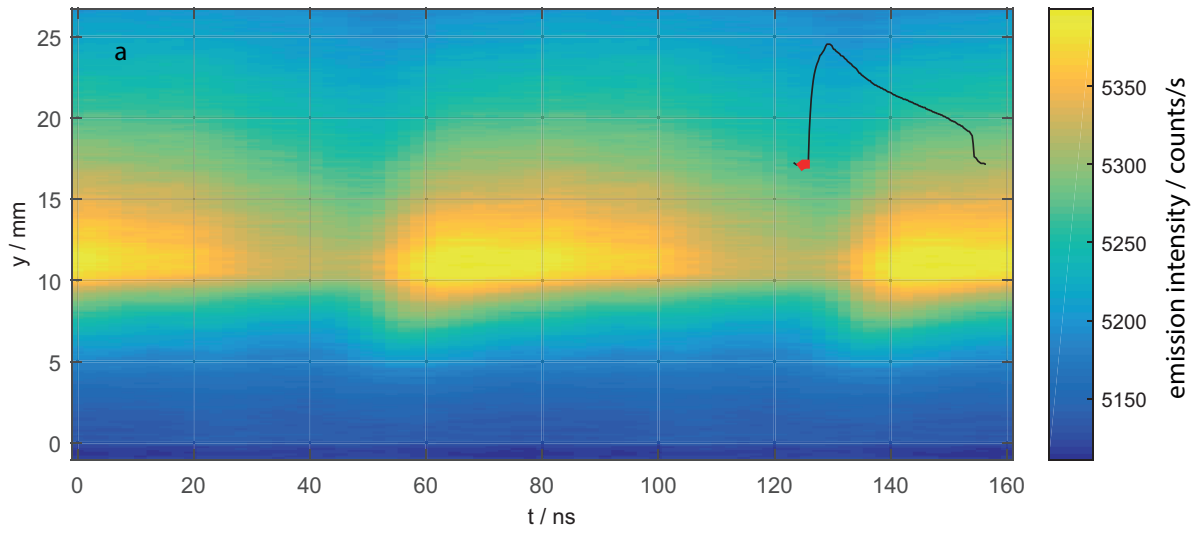

Figure 8.7: During stage one of particle growth (matching mark a in figure 8.6) the emission pattern resembles the pattern in a pure argon discharge. Electrons are accelerated into the volume by an expanding sheath at the trigger offset time of around $\tau_{\text{delay}} = 50\,\text{ns}$.

that the electron density is not much disturbed neither. This assumption is in agreement with the de-excitation pattern, which does not differ qualitatively from a dust free plasma. Electrons close to the electrode do make their way into the plasma without being caught by charging particles.
The second phase of particle is very short and undergoes a huge change in the discharge characteristics. Therefore, with a time resolution in the order of seconds, it is difficult to measure. The time to record the excitation pattern exceeds the time scale during which the selfbias voltage and consequently the plasma is stable. So taking point b in figure 8.6 needed as much time as it took the voltage to increase about 10 V. An increase in the selfbias voltage strongly affects the sheath thickness (and vice versa) and by this leads to a lowering of the location of the glow. Therefore a drift exists in the measurement of the de-excitation pattern. At the end of the rf cycle at $\tau_{\text{delay}} = 73\,\text{ns}$ the intense glowing region is further down to the electrode than in the beginning. As the second cycle is only a double of the first one, the same can be observed from 74 to 150 ns.
Drawing any other conclusion from this image is doubtful because other parameters like intensity do also vary during the acquisition time and are only partly attributed to dependencies on the rf cycle. Nevertheless, the pattern can be regarded as similar to the one at point c in figure 8.6, which is discussed in the following.
At point c the selfbias voltage is at its maximum at round about -110 V. This is well reflected in the position of the glow maximum. With only round about 5 mm above the electrode, see in figure 8.9, it is at the shortest distance during particle growth. Moreover, the emission intensity correlates well to the position of the glow. At point c the intensity is the highest, whereas at point a it is the lowest. Both, the sheath thickness as well as the glow intensity, are dependent on the electron density and temperature as well as on the chemical composi-

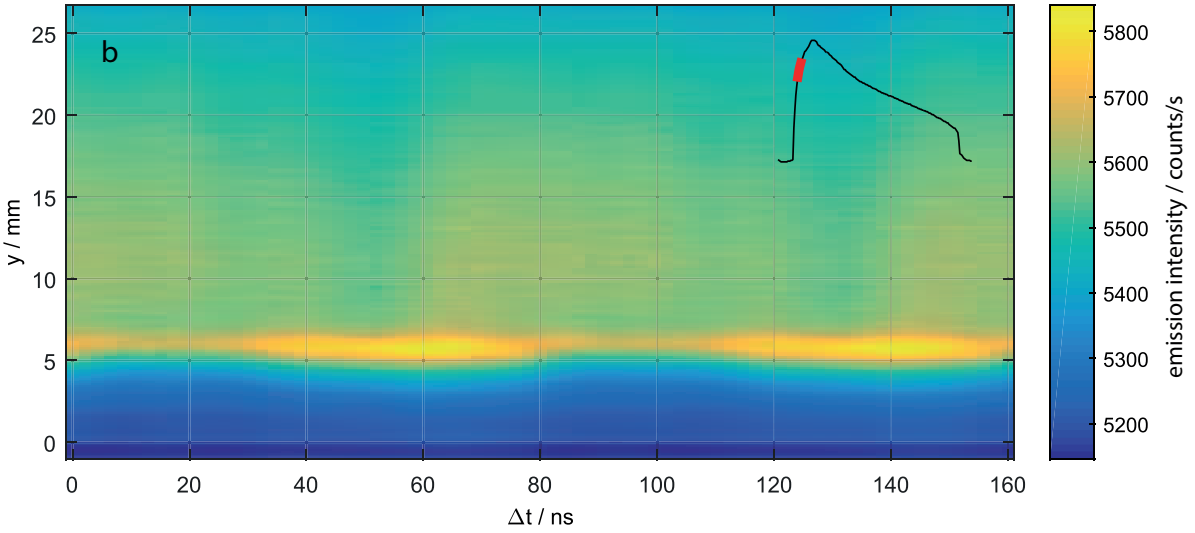

Figure 8.8: During stage two of particle growth (matching mark b in figure 8.6) the plasma environment changes quicker than the time needed to acquire the de-excitation pattern. An increase in the selfbias voltage leads to a descent of the plasma glow towards the electrode. This can be seen as a slight slope downwards from nanosecond 0 to 73. The overlapping of the changing plasma and the specific emission pattern is difficult to interprete.

tion of the gas.
Another observation is a second region of intense glow. Whereas in the volume the glow remains more or less constant in intensity and shape compared to point a, the strong glow close to the electrode has two maxima, which are very close to each other. During the sheath collapse electrons are first accelerated towards the electrode. This leads to a bright region ranging from round about 35 to 45 ns. The second maximum is hard to distinguish from the first one but during sheath expansion electrons are accelerated oppositely resulting in a bright region from round about 50 to 65 ns.
The two maxima cannot be resolved better because the lifetime of excited atoms and molecules can be in the order of tenth of nanoseconds, which is probably longer than the duration of the sheath collapse. Nevertheless, from figure 8.7 one can conclude, that the electron upstream into the plasma has to happen at around 50 ns but the strong glow close to the electrodes brightens already at 35 ns. So it must be related to a downstream of electrons. Hence, the sheath collapse duration is as long as roughly 15 ns. The phase shift between current and voltage is relatively small, in the order of $< 5°$, throughout one growth cycle, see chapter 5, which corresponds to a time shift of < 1.0 ns. Furthermore, the phase shift must completely be determined by the electron current, as the ion current is constant over the entire RF cycle. Therefore, it can be assumed, that the point of time of the sheath collapse in the other emission patterns does not differ significantly.
The downstream might already be present in figure 8.8, which shows very similar features despite a voltage drift. It is also interesting to notice, that in figure 8.9 a relatively dark zone between the intense glow and the plasma glow in the volume exists, separating the two regions.

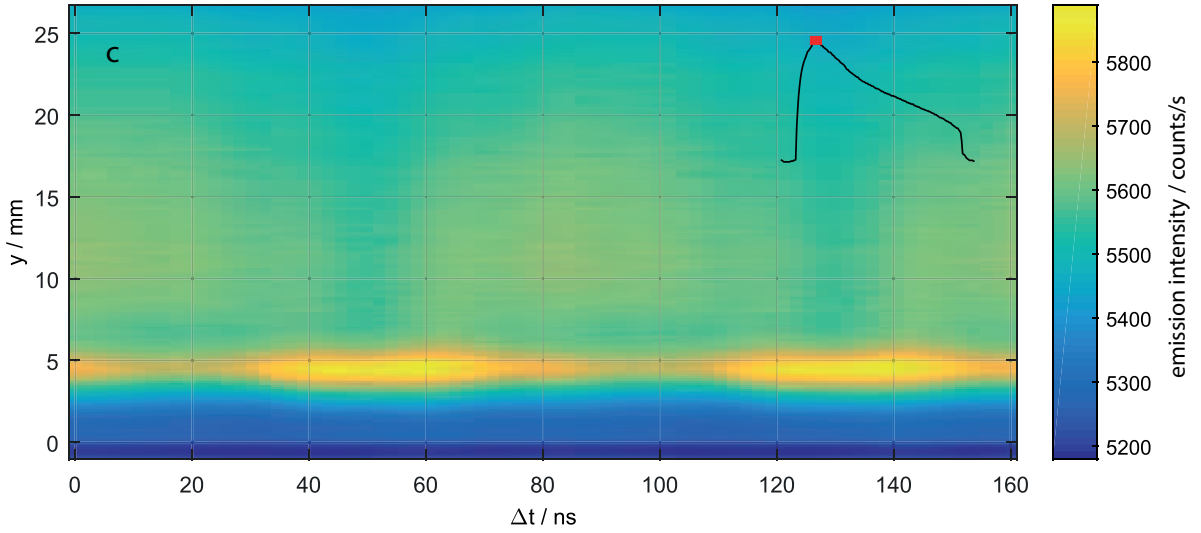

Figure 8.9: Between stage two and three of particle growth (matching mark c in figure 8.6) the plasma glows intense and close to the powered electrode.

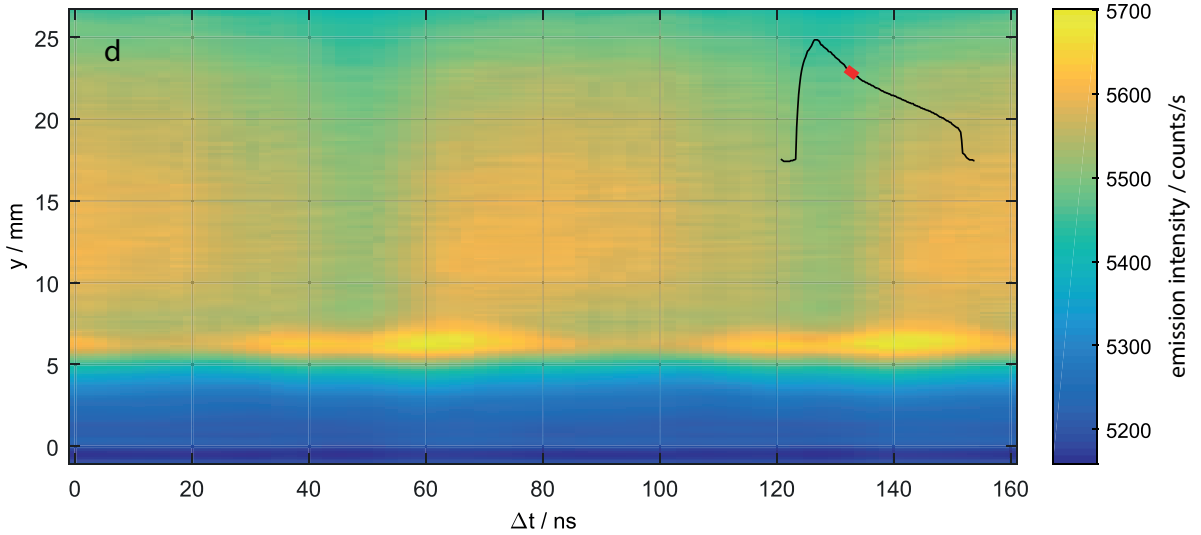

Figure 8.10: Emission pattern in the first half of phase III, corresponding to point d in figure 8.6; The bright localised lower glow region slowly moves upward.

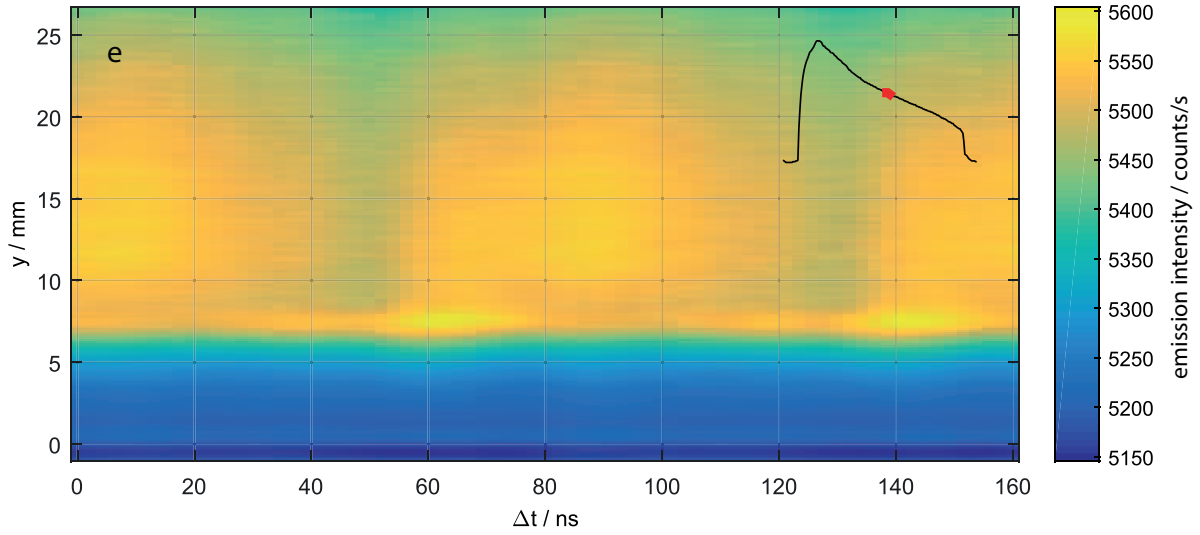

Figure 8.11: In the emission pattern at the middle of phase III, corresponding to point e in figure 8.6, the lower bright glow region attaches to the main plasma glow and looses in intensity.

Moving on in the growth cycle to point d, see figure 8.10, the selfbias voltage drops and with it the bright area close to the electrode lifts up again. Also the brightness is reduced, whereas the glow further in the volume stays approximately at the same level. This trend continues smoothly throughout phase III of the growth cycle, as can be seen in the figure sequence 8.11, 8.12, 8.13 and 8.14.

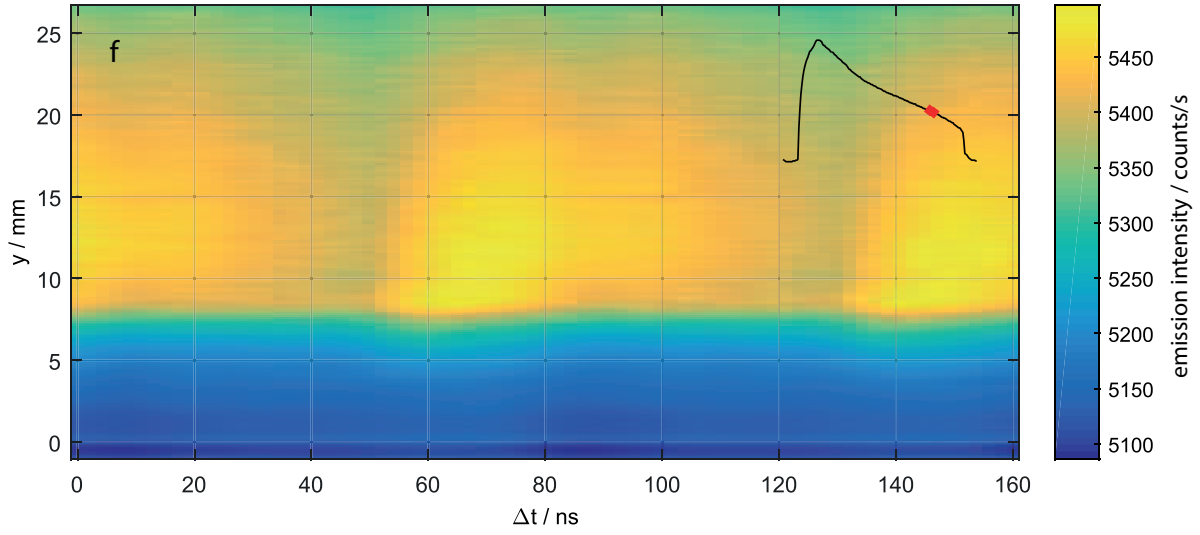

Figure 8.12: Emission pattern towards the end phase III, corresponding to point f in figure 8.6; The lower bright glow has completely integrated into the main glow region.

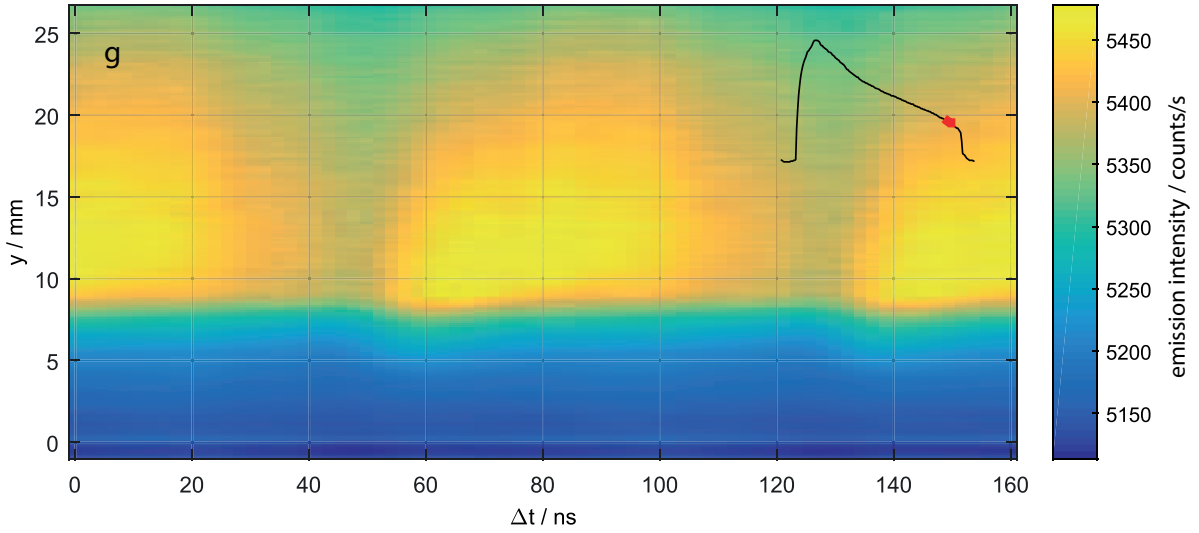

Figure 8.13: Emission pattern at the end of phase III, corresponding to point g in figure 8.6;

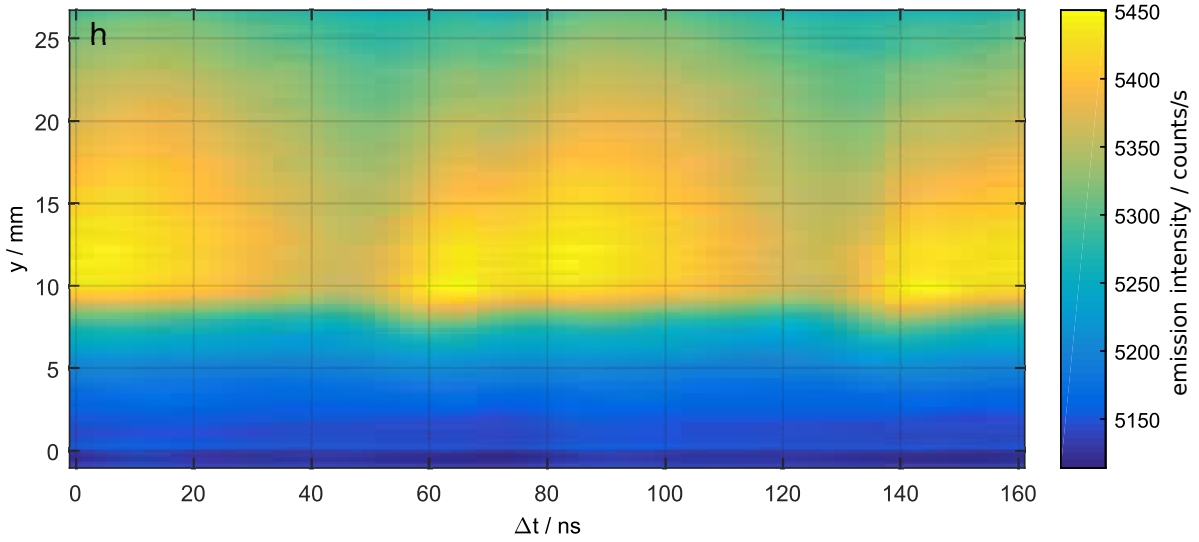

Figure 8.14: Emission pattern at the transition from phase III to phase I, corresponding to point h in figure 8.6; Qualitatively the shape of phase I is already restored, but the glow is more intensive and reaches further up into the plasma.

During phase III the nanoparticles grow from 50 to 140 nm. Meantime, towards the end of phase III the lower intense glow is slowly disappearing by gradually moving upwards into the normal glow and by integrating into it. At point f in figure 8.6, after round about 75 % of phase III, the two glow regions are already hard to distinguish. Interestingly the overall plasma glow already finds back to its initial position and shape before the end of phase III but its brightness is still a little bit higher and it seems to be of a bigger size reaching further into the plasma bulk compared to figure 8.7 from phase I.
Finally during the transition from phase III to phase I, when the majority of the residual particles is expected to leave the plasma, the emission intensity drops back to the same value as in the beginning and also the size of the glow shrinks back to the initial appearance.

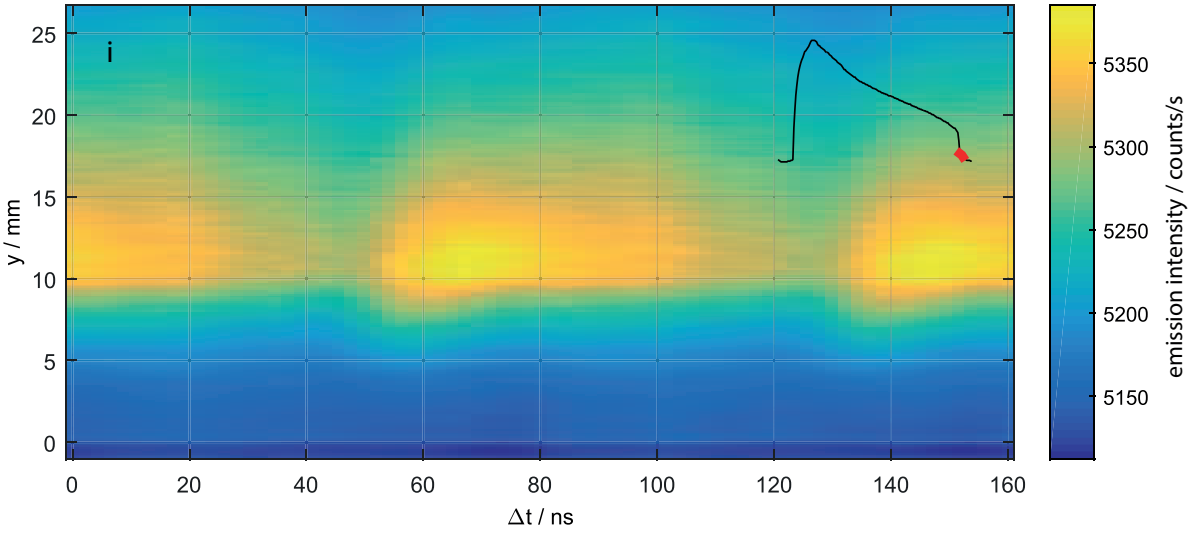

Figure 8.15: The emission pattern, here corresponding to point i in figure 8.6, has recovered to its original shape and low intensity in phase I.

The slight deformation of the shape in figure 8.14 and 8.15, meaning a darker space at time 73 ns, is probably due to the acquisition process. It results from doubling and assembling the picture, which happens to be at 73 ns. Thus, it is an artefact of the image processing and shall not be assumed to be of relevance.

8.4 Discussion

The de-excitation patterns in the sheath region of an CCRF discharge in the course of a dust particle growth cycle have been examined. Not only the intensity but also the shape of de-excitation varies drastically during these cycles. Whereas in phase I of particle formation the pattern matches qualitatively the case in a pure argon discharge, it is strongly affected by particles of sizes greater than 40 nm in diameter, which covers the phases II and III.
Also de-excitation patterns with a filter have been obtained. They are not presented in order to keep the chapter reasonably short and because they do not differ significantly from those without filter. Therefore, it can be concluded, that many of the ArI lines do either behave in the same way as the molecular bands, which can be found at lower wavelengths, or argon is the dominant emitter due to the low concentration of reactive chemicals. If this is the case, a change in luminosity must be caused by a change in the excitation rate, because the concentration of argon can be considered stable. These events are strongly dependent on the quantity of high energetic electrons, which are related to the presence of dust.
It shall be mentioned, that the region of interest in this series of pictures is fairly small and close to the electrode, so that not the entire plasma volume is portrayed. As the plasma is locally influenced by the locally varying dust density, size and charge, the here presented plasma region can be very different from other parts, like the bulk plasma. On bigger length scales concentration gradients of the reactive species need to be taken into account, which

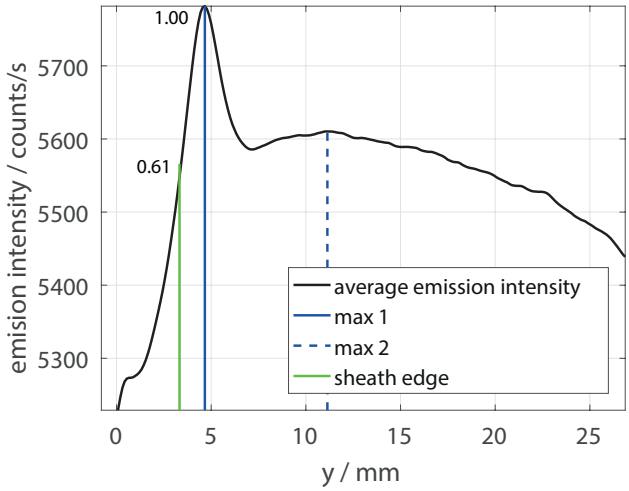

Figure 8.16: Averaging one RF cycle, a vertical light emission profile can be plotted. It clearly shows two different maxima, here marked with max 1 and max 2. The second maximum denotes the usual bulk glow, which is existent throughout the entire particle growth cycle. The green line marks the distance to the electrode, where the emission intensity decreases to 0.61 of its maximum value, which is used as a measure for the sheath edge, inspired by the Bohm criterion.

also may contribute to a variation in the emitted light wavelength and intensity [218].
Trapping a considerable amount of electrons, and thus lowering the electron density, the presence of particles induces a change in the plasma, which occurs as the α-γ'-transition, see section 3.3.2. The transition marks the turning point at which the volume ionization, quantified by the α-ionization, becomes less pronounced than ionization in the sheath region. This is provoked by the consumption of free electrons by the dust surface, as already discussed in 6.4. With the here applied technique it is possible to visualize the α-γ'-transition by the means of the excitation of atoms and molecules.
As already mentioned in the section above, during phase II and III a bright glow close to the electrode is present, which slowly integrates itself into the usual bulk glow during phase III. Using an intensity profile, averaged over one RF cycle along the vertical y-axis of the above presented figures 8.7 to 8.15, this becomes very obvious, shown in figure 8.16. Whereas max 1 denotes the lower intense glow region, max 2 stands for the maximum in the bulk glow. The latter can be seen throughout the entire particle growth cycle and only varies little in intensity and position.
The green line marks the distance to the electrode, where the emission intensity decreases to 0.61 of its maximum value. It is inspired by the Bohm criterion, where the sheath edge is defined as the point, where the electron density has decreased to 0.61 of the bulk value $n_{\mathrm{e,s}} = 0.61 n_{\mathrm{e0}}$, see section 2.2.2. Considering, that it is mainly the electrons who excite, this choice may be very suitable for the sheath edge determination. However, it does not account for a spatial variation in the electron temperature, which also contributes to a spatial variation in the excitation pattern. Nevertheless, a comparison of the so determined sheath edge

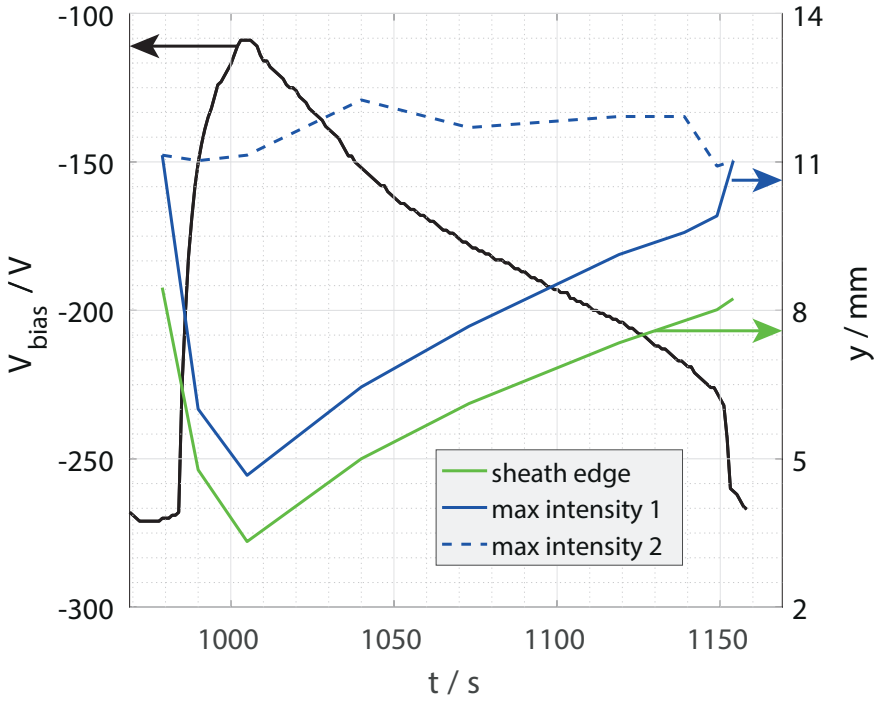

Figure 8.17: Tracking the positions of the two glow maxima from figure 8.16 and of the sheath edge, a correlation to the self-bias voltage (black line) can be made. The agreement to the sheath edge position (green line) determined in the LLS measurements, see figure 6.10, is excellent.

position with the sheath edge position determined by the means of laser light scattering on particles shows an excellent agreement, as can be seen in figure 8.17. As well as in figure 6.10 as in figure 8.17 the sheath edge is localized at 8 mm from the electrode during phase I and at 5 mm in the middle of phase III.
Differently to the LLS measurements, however, it is now possible to track the sheath edge throughout the entire growth cycle, as has been done in figure 8.17. Thus, the sheath edge comes astonishingly close to the electrode at the transition between phase II and III with only 3.3 mm distance. Furthermore, it is nicely displayed, how the sheath width evolves oppositely to the self-bias voltage, which shows the tight correlation between those two parameters.
Concerning the location of the maximum glow intensity, it can be seen, that the main bulk glow (max intensity 2) stays relatively stable, whereas the lower bright glow starts to appear in phase II and then descends drastically, reaching its minimum height of 4.7 mm between phase II and III. During phase III it slowly climbs up again and finally merges with the upper glow region in phase I.
Therefore, it seems to be evident to take the upper glow as the usual plasma glow like in an undisturbed pure argon plasma, while the lower glow must be attributed to the α-γ'-transition. Hence, in an illustrative picture the lower glow may be the visualized γ'-process. It's nature lies in between the surface ionisation, referred to as γ-process, and the ohmic

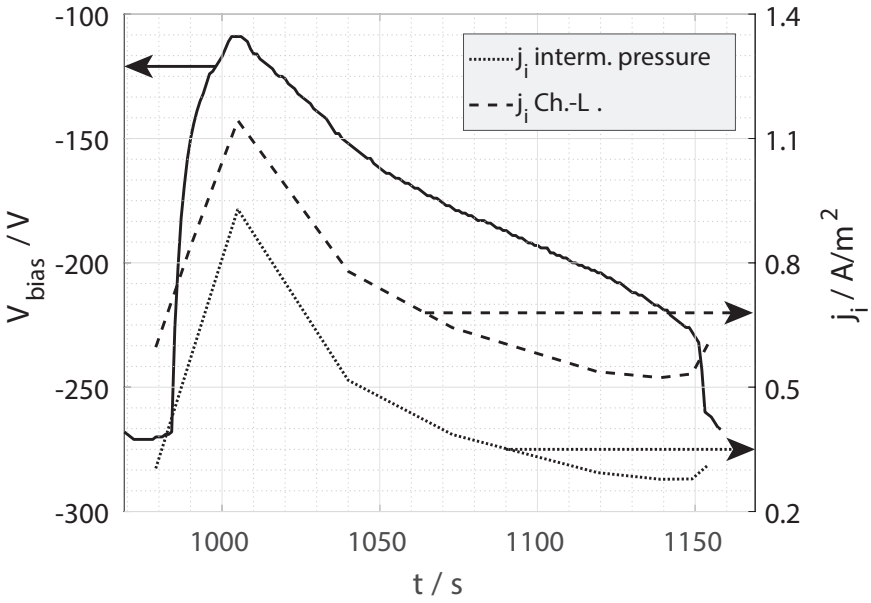

Figure 8.18: From the sheath thickness and the self-bias voltage the ion current density j_i can be calculated according to the intermediate pressure formular 2.24, dotted line, and to the planar Child-Langmuir law 2.26, dashed line.

heating, referred to as α-process. The γ'-process seems to take place in the sheath, leading to a dense and possibly also hot plasma, where there is the plasma sheath in an undisturbed plasma.
The physical mechanism behind the γ'-glow, however, is less obvious. It may be related to a sort of discontinuity at the dust cloud edge, where hot electrons are coming out of the dust cloud, but are no longer consumed by the dust in the same way as they are inside the cloud. This might lead to a region of elevated electron density and / or electron temperature at the edge of the dust cloud. Then, this is possibly amplified by the hot electrons ejected from the sheath at the end of the sheath collapse, indicated by the temporal localisation of this glow around the sheath collapse in the time space diagrams of the excitation patterns (figures 8.8 to 8.14).
Having the sheath width in front of the electrode determined throughout the entire growth cycle, figure 6.22 can now be completed. In that figure the collision free Child-Langmuir-Law and the intermediate pressure law was used to calculate the ion current density onto the electrode as a function of the sheath width and the electrode potential. It has been repeated with the values obtained with the phase resolved camera, shown in figure 8.18. The agreement to chapter 6 is good.
With $1.15\,\mathrm{A/m^2}$ for the collision-less case the ion current is the largest at the transition between phase II and III and decreases similar to the self-bias voltage during phase III. It actually decreases even slightly below the value $0.6\,\mathrm{A/m^2}$ of phase I. This is in contradiction to the Langmuir probe measurements in chapter 7, where a decrease of the ion density was measured during phases II and III. However, one needs to keep in mind, that the increase in

ion current may also be related to an increase in the electron temperature, and thus, an elevated Bohm velocity. What's more, the ion current increase may also be strongly influenced by a local electron and ion population in front of the powered electrode, as it is indicated by the above discussed γ'-glow.
Because in time average no net currents can occur to or from the capacitively coupled powered electrode, the ion current must be balanced by the time averaged electron current $j_\mathrm{i} = \bar{j}_\mathrm{e}$. This means, that the electron rarefaction by the dust surface is actually overcompensated in front of the powered electrode by either a high electron temperature or by a high local electron density. This is probably again attributed to the γ'-glow.
Summarizing this chapter, the evolution of the light emission during one RF-cycle was captured thanks to the camera from ANDOR™ Technology. This was done for several points in one dust growth cycle and correlated to the self-bias voltage. A strongly localised and intense glow close to the powered electrode was found to appear during phases II and III, where the influence of the particles also disturbes the self-bias voltage. The cause of this glow is not completely resolved, but it seems to be related to the mechanism of the α-γ'-transition, picturing a heating mechanism, that originates from the interplay of the sheath collapse and the edge of the dust cloud, that is in close vicinity.
Additionally, the sheath edge was documented by a simple approach, taking the distance to the electrode at which the emission intensity decreases to 0.61 of its maximum value. This approach was verified by the good agreement to the findings in chapter 6. The knowledge of the sheath width finally allowed to determine the ion current density, and consequently, also the time averaged electron current density throughout the dust growth cycle.
In order to investigate more precisely the chemistry and the different excitation channels of argon a future experiment can be the more advanced phase resolved optical emission spectroscopy (PROES). The de-excitation of various chemical species could be traced throughout the entire growth cycle, permitting to detect more precisely the excitation event by knowing the life time of the excited species. This way a more detailed insight into α-γ'-transition might be achieved, determining the velocity of certain electron populations.

Chapter 9

Energy resolved mass spectrometric measurements

As already mentioned in previous chapters, it is useful to combine several different diagnostics in order to better understand the growth mechanisms of nanoparticles. Starting with the electric characteristics of the discharge it was shown, that the formation of nanoparticles in the plasma takes place in a stepwise manner. These steps have also been traced in Langmuir probe measurements and with the phase resolved camera and the spatial dust cloud shape was equally recorded by the means of laser light scattering, showing the changes in it with those three growth phases.
In this chapter, the chemical reactivity during the growth phases shall be revealed by the help of mass spectrometry. It will be shown, that not only the concentration of the precursor, C_2H_2 varies significantly throughout the particle growth cycle, but also all other reactive species. However, as will be discussed, often it is difficult to distinguish between cause and effect.
Another interesting plasma feature, that can be revealed by mass spectrometry, is the ion density. Whereas in the first nucleation phase negative ions, which cannot be measured in this set-up, are expected to play a crucial role, in the last phase of the growth by surface deposition onto the particles radicals and positive ions should be most important. Thus, the evolution of the ion concentration has been measured too, from the beginning of the particle growth cycle until the end. Last but not least the ion measurement contains additional information about the plasma by the energy, with which the ions are ejected from it.
The instrument used during this thesis is the *PSM003* from Hiden Analytical. After a short overview over the principles of mass spectrometry, it will be presented in more detail in this chapter, including a summary of the used voltage values on the numerous electrodes.

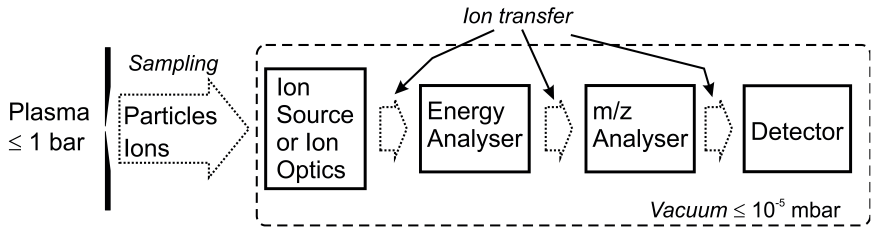

Figure 9.1: Charged and neutral particles can be extracted from the plasma and pass through different stages in the mass spectrometer. This conceptual scheme, describing that process, is taken from [257].

9.1 Principles of quadrupole mass spectrometry in low temperature plasmas

Different mass spectrometers have been developed since their first rudimental introduction in 1897 by Sir J. J. Thomson [255]. They rely on the extraction of the species of interest from the region of interest and subsequent analysis of them by manipulating their trajectories through the instrument. In this section a short overview on the principle of quadrupole mass spectrometers shall be given. For more details the interested reader may refer to specialized literature, like [256–258].

In the case of low temperature plasmas under vacuum this implies a second pumping stage with even lower vacuum on the instrument side in order to actively pump the atoms and molecules out of the discharge chamber. Anyway, very low pressure in the order of $\leq 10^{-3}$ Pa is required in the instrument in order to keep collisions between gas molecules in it down to a minimum. Because the pressure gradient is relatively small, and thus, the instrument pumping stage does not need to be as powerful, vacuum vessels like low temperature discharge chambers are already perfectly suited for mass spectrometry. The even lower vacuum in the mass spectrometer is achieved by installing a small orifice with an opening in the order of 100 μm in between the chamber and the instrument. This way a sufficient vacuum is sustained on the instrument side, the plasma process is only little affected and the atom flow through the orifice is sufficient as well as happening in a well defined place.

Following, two cases must be distinguished. If neutral atoms and molecules shall be analysed (RGA mode), they now need to be ionized in order to enable the manipulation of their trajectories. This happens in the so-called *source* or *ion source* on a well defined potential. Contrarily, if ions are to be measured (+ionSIMS or -ionSIMS mode), they need to be extracted with the help of a potential on the *extractor* directly behind the orifice. However, as they are already ionized, the source remains inactive for these species. From the source on, the measurement of neutrals and ions is the same in principal, because now they both are ions.

With the help of ion transfer optics, which basically consist of hollow electrodes, so-called *electrostatic lenses* through which the ions can pass, the ions are then transferred into first the energy analyser. Those ions with the right energy can pass it and are further transferred

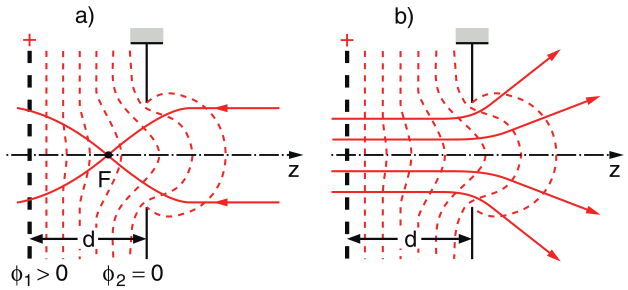

Figure 9.2: With the help of electrostatically charged electrodes ions and electrons can be deflected and, thus, their trajectories manipulated. Here, in (a) electrons coming from the right hand side are focussed into point F, whereas electrons coming from the left hand side (b) are defocussed. Graphic taken from [259];

into the mass analyser, which more precisely is a filter for a certain mass to charge ratio m/z. If they also pass this one, they finally are transported by electrostatic potentials to the detector. In the end, neutrals have been filtered according to their ionisation energy and mass to charge ratio, whereas the ions are filtered according to their incoming kinetic energy and their mass to charge ratio. The detector finally does not only determine if particles of this charge to mass ratio and this energy are present in the plasma, but also how many. The conceptual scheme of a mass spectrometer is shown in figure 9.1.
The ion trajectories are controlled by numerous electrostatic lenses in the mass spectrometer, principally follow the electric field imposed by the potential Φ set to the lenses, see figure 9.2, according to their equation of motion

$$m\frac{\mathrm{d}^2\vec{r}}{\mathrm{d}t^2} = e\vec{\nabla}\Phi\left(\vec{r}\right). \tag{9.1}$$

Similar diffraction equations as for optical lenses can be deduced by the use of the focal length f. However, the exact potential distribution, and hence, the exact focal length need to be calculated by numerical simulation codes.
Nevertheless, the principle of the other five components extraction, source, energy filter, mass filter and detector can be discussed qualitatively. Because it is necessary to know these principles in order to understand the way a mass spectrometer works, and thus, to interprete the results, it shall be done in the following.

9.1.1 Extraction of molecules and ions from the plasma

The first step towards analysing a chemical substance via mass spectrometry is to bring it into the gas phase. Fortunately, this is already inherent in plasmas. As next, two different principal particle types need to be distinguished in low temperature plasmas.
The first type are neutral atoms and molecules. They can be extracted with a pressure gradient out of the plasma volume. This is achieved by the help of an orifice and the additional pumping stage in the instrument. Typically, in low temperature plasmas of several Pascals

of working pressure a 100 μm opening is a good size to do that. Using mass spectrometry in ambient pressure would require an additional pumping stage in order to achieve sufficiently low pressures on the instrument side. The speed of the incoming neutral species in low pressure plasmas is thermal, and thus, negligible in comparison to the few eV, that they will gain once being ionized.
The second type of particles are positive ions. They are mainly formed somewhere in the bulk plasma, and thus, possess an energy of $E_{\mathrm{i,pot}} = q_{\mathrm{i}}\Phi_{\mathrm{pl}}$. When drifting slowly out of the plasma centre towards the plasma sheath edge, they transform a part of this energy into kinetic energy according to the Bohm velocity $E_{\mathrm{i,kin}}(z=0) = 1/2\, m v_{\mathrm{B}}^2$ and then attain their full kinetic energy in front of the grounded orifice of $E_{\mathrm{i,kin}}(z = z_{\mathrm{wall}}) = e\,(\Phi_{\mathrm{pl}} - \Phi_{\mathrm{wall}})$, see also equation 2.17.
Those ions, that pass through the small orifice are extracted by the first ion lens in the system, the *extractor*, and then focussed further into the instrument by the help of a second lens, the *lens*. The extractor voltage basically modifies the acceptance angle for incoming ions. It can also compensate a slight misalignment in the set-up.
The third type of particles are negative ions. Also formed in the plasma bulk, they do not leave the plasma due to trapping by the positive plasma potential. The common way to detect negative ions, therefore, is to shut off the plasma, for example by pulsing it, and to measure in the afterglow. This needs to be timed well and also demands a careful interpretation of the results. In the set-up used here it was not possible to examine negative ions, although it is a very important research to be done on nano-dusty plasmas due to the role of anions during nucleation, see chapter 3.3.
The orifice needs to be replaced from time to time, because it may wear out from the ion bombardment and, thereby, become bigger and also loose its regular round shape. Furthermore, eventual dielectric depositions from a reactive plasma can change its surface potential from ground to floating and, thus, affect the ion trajectories. In that case the orifice needs to be cleaned carefully without damaging the tiny hole or the ion extraction needs to be recalibrated.

9.1.2 Source

Whereas for positive and for negative ions the ion source can be switched off and all parts simply set to a certain potential, neutral atoms and molecules still need to be ionized in the mass spectrometer in order to enable further analytical steps.
Different ionization methods exist, for example electrospray, fast atom bombardement or photo ionization. However, for the analysis of gases electron collision ionization sources are most commonly used. As already indicated by the name, they make use of free electrons, that collide with the gas molecules and either attach at very low energies or ionize at elevated energies. As standard an electron energy of $E_{\mathrm{e}} = 70\,\mathrm{eV}$ is used on databases like NIST, which makes spectra comparable. At this energy the atoms and molecules are ionized according to species dependent cross sections.
Technically it is realized by a hot filament, that emits electrons, which are accelerated vertically to the atom flight direction onto an anode grid as schematically sketched in figure

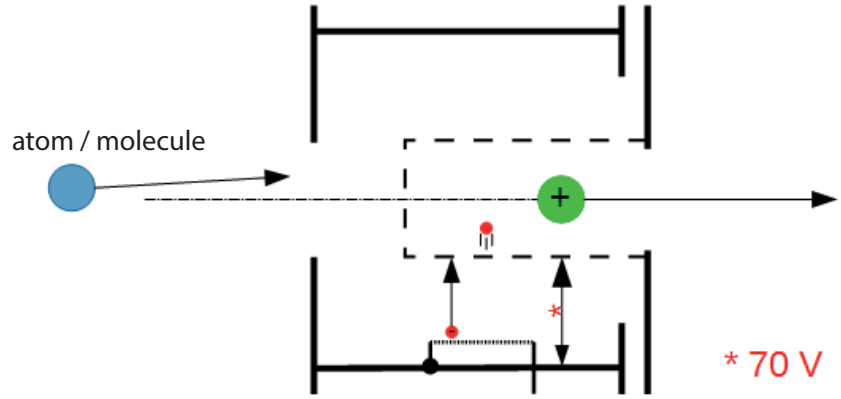

Figure 9.3: In an electron collision ionizer the atoms or molecules are ideally ionized inside the cylindrical grid, where there is a well defined potential and electron energy. Graphic taken from [160] and translated;

9.3. Inside the cylindric anode grid, where the collisions with neutrals take place, the electric field approaches zero. This has two consequences: Firstly the potential, where the ions are created is almost constant over the entire ionization volume and secondly the electron energy remains constant too in this zone. Therefore, it allows to control the collision energy and the ion energy for subsequent analysis steps precisely.
The here used mass spectrometer is equipped with such a source. It allows not only to control the electron energy and ion potential but also the electron current. It is useful in order to adapt the total ionization events and, thus, the consequent ion current through the instrument. This way the amount of ions can be tuned towards a detector signal, that is sufficiently large for a good resolution but not in saturation neither.
One disadvantage of this technique is, that the relatively high electron energy leads to dissociation of molecules in the ion source. Thus, what is further analysed is the convolution of the cracking pattern in the ion source with the the real chemistry in the discharge chamber. Eventually, many radicals from the discharge cannot be detected because they hide behind the much higher peaks from the dissociation in the mass spectrometer.

9.1.3 Energy filter

The principle of any ion energy filter is to force the ions onto bent trajectories in order to pass through it without getting lost on walls or electrodes. Because the trajectory is energy dependent only one selected energy is able to pass through. Different ways to deflect the ions in a magnetic or an electric field can be realized. Very common are electrostatic sector energy analyser and Bessel boxes. The latter is installed in the here used mass spectrometer and, therefore, shall briefly be introduced.
The modified Bessel box basically is a *cylinder* with an electrode at both ends and a centre stop in its middle, as shown in figure 9.4. The opening of the electrodes, the so-called *endcaps*, is centred like the centre stop. Very fast ions do therefore come in straight and collide with the stop, where they loose their charge. Little too energetic ions collide with

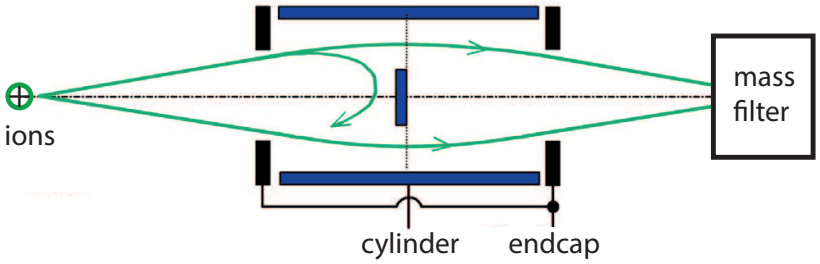

Figure 9.4: Thanks to the cylinder and the endcap potential the Bessel box can be tuned to let pass through only those ions with one specific energy. Shown here is a modified Bessel box as installed in the Hiden Analytical PSM003, which has a so-called centre stop in its middle in order to improve the energy resolution. Graphic from [260] and modified;

the cylinder walls. On the other hand side, ions of very low energy cannot overcome the cylinder potential and are repelled and then lost in a backward movement.
It can be achieved by a slightly repulsive potential, meaning e.g. a slightly higher potential than the plasma potential $\Phi_{\mathrm{cyl}} \geq \Phi_{\mathrm{pl}}$ for positive ions. The endcaps, however, are on a lower potential, typically $\Phi_{\mathrm{endcap}} \approx \Phi_{\mathrm{pl}} - 20\,\mathrm{V}$, in order to shape the electric field inside the Bessel box correctly.
Only ions with the desired energy can pass the Bessel box by describing the in figure 9.4 shown trajectory. Additionally they need to have a small off-centre movements. Ions of sufficient energy, that are perfectly aligned on axis always hit the centre stop. Therefore, the modified Bessel box design has a transmission of only round about 10 %, which is relatively low. Furthermore, its energy resolution of round about 1 eV is not as good as for example for the electrostatic sector energy analyser. However, it allows to build very compact and easy-to-use mass spectrometers and is sufficient for most applications.

9.1.4 Mass filter

Strictly spoken the mass filter does not filter masses but the mass to charge ratio m/z of the incoming particles. Similar to the other parts of the instrument different principles and designs for mass filters exist. Anyhow, a very good vacuum is required for all of them, because any collision disturbs the measurement.
One critical property of the mass filter is its resolution A. A slight error in the mass determination Δm originates from the fact, that the incoming ions do not follow perfectly the optical axis and that their energy is not perfectly unified. At a given mass m the resolution is, therefore, defined as

$$A = \frac{m}{\Delta m}. \tag{9.2}$$

The error Δm is defined as the distance between two distinguishable mass peaks. Commonly two peaks are assumed distinguishable, when the minimum in between is smaller than 10 % of the signal height. Thus, the greater A the better the instrument.
Some of the most precise mass filters are based on the trajectory manipulation in magnetic

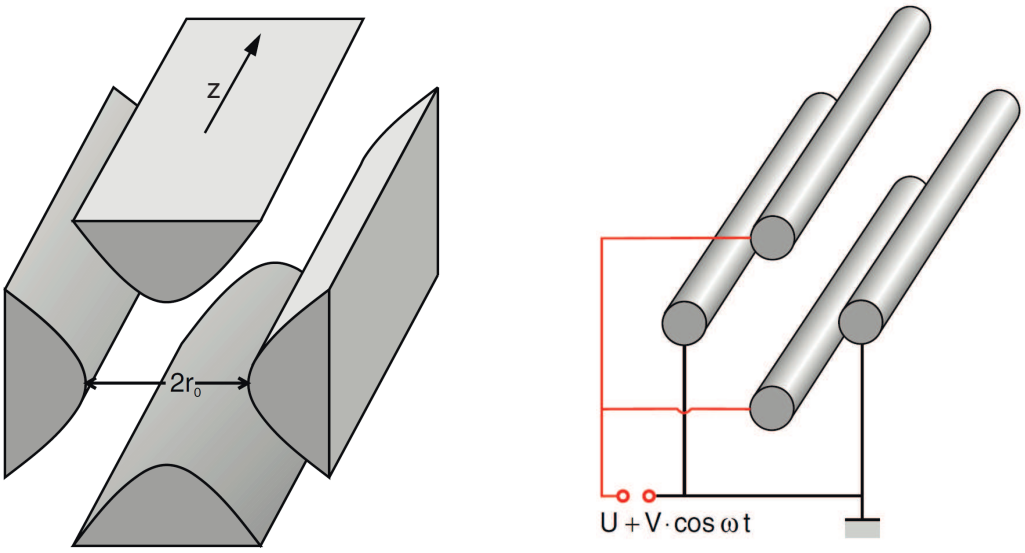

(a) (b)

Figure 9.5: The hyperbolic shaped electrodes 9.5(a) of a quadrupole mass filter are aligned parallel and coupled diagonally with a phase shift of π between the pairs. Usually, simple, round rods 9.5(b) are used instead of the expensive hyperbolic shape. The applied voltage consists of a DC part U and an RF part V. From [259], y-axis changed to z;

fields B, which forces the ions into a circular path of the Larmor radius:

$$r_{\mathrm{L}} = \frac{mv}{zeB} \propto \frac{m}{z}. \tag{9.3}$$

Another design are time-of-flight mass filters. The simple idea is to measure the time it takes for each particle to pass through a certain distance at a given energy. Because the energy is gained through electrostatic acceleration by a certain potential U, it is dependent on the m/z ratio and, thus, the ratio can be calculated with the time t of flight and the distance s:

$$\frac{m}{z} = \frac{2eUt^2}{s^2}. \tag{9.4}$$

These mass filters need to be used in a pulsed mode in order to trigger the incoming events correctly. However, one big advantage is, that in each pulse the entire mass spectrum can be obtained. Another one is the great mass range, that is only limited by the length of the tube and the quality of the vacuum. Hence, these mass filters offer a great time resolution of down to some microseconds with huge spectra in the same time.
In the PSM 003 a quadrupole mass filter is installed. Its theory is more complex, but its compact and affordable design and high transmission make it very popular. Though in this instrument the maximum mass range is limited to 300 amu, quadrupole filters can reach up to 2000 amu [256] with a sufficient mass resolution and satisfying time resolution. In 1989 the noble price in physics was awarded to Wolfgang Paul partly for the invention [261] of

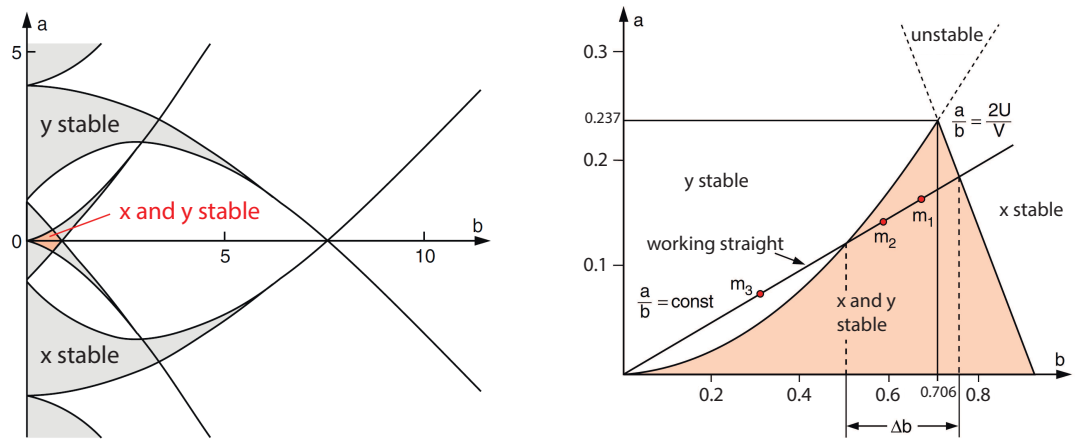

Figure 9.6: In an a-b-diagram, figure 9.6(a), the stable solutions of the Mathieu functions 9.9 can be illustrated, here marked in red. Keeping the ratio U/V constant while varying the frequency ω allows to move back and forth on the working straight in figure 9.6(b). Taken from [259] and translated;

the quadrupole filter.
Basically, a quadrupole filter consists of four long electrodes, which ideally are of hyperbolic shape. However, it is sufficient and much cheaper to use four simple, metallic, round rods assembled parallely. In a cross-section view they need to be arranged quadratically with the same voltage on the diagonally opposing electrodes. An RF voltage V of $\omega \approx 100\,\mathrm{MHz}$ is then applied to the electrodes with a phase shift of π between the two electrode pairs. A scheme of the rod assembly is shown in figure 9.5(a) and 9.5(b). Simultaneously a DC voltage U is added, so that the applied voltage can be written as:

$$\Phi_0(t) = U + V \cdot \cos(\omega t)\,. \tag{9.5}$$

Note, that the DC voltage stabilizes the ions in direction of the repulsively charged rods but destabilizes in the other direction. This is partly compensated by the RF voltage. In the x-y plane a quadrupole field is created of the form

$$\Phi(x, y, t) = \frac{\Phi_0(t)}{2r_0^2}(x^2 - y^2), \tag{9.6}$$

where r_0 stands for the distance between two diagonally facing electrodes. The mass selection is achieved by tuning the frequency ω and the ratio of DC to RF amplitude U/V, as demonstrated in the following.
The equation of motion for the ions can be split up into the x and y direction in the cross-sectional plane

$$\begin{aligned} \ddot{x} + x\frac{q}{mr_0^2}\left(U + V \cdot \cos(\omega t)\right) = 0 \\ \ddot{y} - y\frac{q}{mr_0^2}\left(U + V \cdot \cos(\omega t)\right) = 0 \end{aligned} \tag{9.7}$$

with the ion charge $q = ze$. By introducing the dimensionless parameters

$$a = \frac{4qU}{mr_0^2\omega^2}, \qquad b = \frac{2qV}{mr_0^2\omega^2} \qquad \text{and} \qquad \tau = \frac{1}{2}\omega t \tag{9.8}$$

the equations can be rewritten in form of the Mathieu function:

$$\begin{aligned} \frac{\mathrm{d}^2x}{\mathrm{d}\tau^2} + x\left(a + 2b\cos(2\tau)\right) = 0 \\ \frac{\mathrm{d}^2y}{\mathrm{d}\tau^2} + y\left(a + 2b\cos(2\tau)\right) = 0. \end{aligned} \tag{9.9}$$

These two differential equations have stable and unstable solutions depending on the amplitude of the parameters a and b. In case of stable solutions the ions oscillate with a limited amplitude in x and y direction, so that they do not collide with the electrodes while travelling forward in z direction. For unstable solutions the oscillations increase during the ion flight time through the quadrupole, so that eventually the ion leaves the field or collides with the rods.
In an a-b-diagram the stable regions can be represented like in figure 9.6(a). At a fixed ratio between $2U/V = a/b = \text{const}$ and at a constant frequency ω all masses, that lead to a stable solution of the equations 9.9 need to be on the working straight in the red area in figure 9.6(b), here m_1 and m_2. Tuning a, b, and ω correctly, the working straight cuts the red area just below the tip of the red triangle, so that the mass range Δm, that fits in there, is smaller than 1 amu, and thus, the mass resolution is improved.

9.1.5 Detector

In a last stage those ions, that passed all the previous steps, need to be detected and counted. Again different devices can be used for this purpose. Often Faraday cups and secondary electron multipliers (SEM) are used. In some instruments both of them are installed in order to cover a broad signal intensity range. In this PSM003 only a SEM is available.
When leaving the mass analyser, the ions are strongly accelerated by a negative voltage in the range of -1 to -3 kV. Then they hit onto a first electrode, the so-called *1st-dynode*. Here they release secondary electrons, which are again accelerated with round about 100 V onto the next dynode, where they in turn release several electrons each. Repeating this process several times an electron avalanche is produced, that amplifies the incoming ion current by a factor of up to 10^8.
The SEM version in the PSM003 is a channel electron multiplier (CEM). Here the discrete dynodes are replaced by two curved continuous electrodes as depicted in figure 9.7. The voltage is applied to along the electrode plates, so that the discrete voltage steps from the classic SEM become continuous.
SEMs are very sensitive to arcing, that is why they can only be operated in high vacuum. If the pressure in the instrument becomes too large, it needs to be shut down.

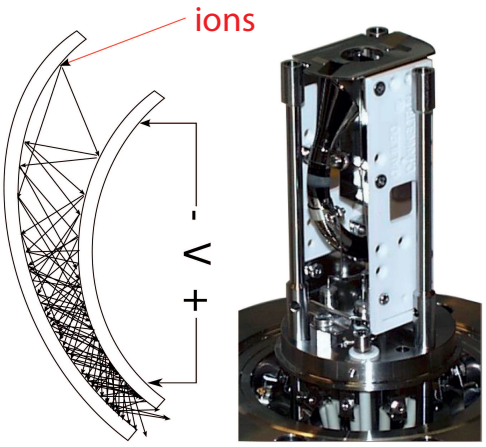

Figure 9.7: In the CEM electrons are multiplied by the secondary electron emission on two curved electrodes, that continuously change the surface voltage along them. The right hand side shows a photograph of the here used CEM in the PSM003. Taken from [160];

9.2 The Hiden PSM003 mass spectrometer

The mass spectrometer PSM003 from Hiden Analytical was introduced into the chamber from the side, as already shown in figure 4.2. The height of the small hole in the orifice above the powered electrode was 10 cm with 6 cm radial offset to the centre of the discharge. So the centre of the powered electrode is at a distance of 11.7 cm to the orifice. This is a compromise between little disturbance of the plasma due to the big grounded trunk of the instrument inside the plasma and a good position for gathering data, that are representative for the main plasma bulk. It should also be noted, that the mass spectrometer head is mounted in between the gas inlets for argon and acetylene and the powered electrode. This may slightly affect the measured intensities due to diffusion gradients of reactive gas densities in the volume.
Whereas the argon flow was fixed at 10 sccm during the measurements, the acetylene flow had to be adjusted between 1 to 2 sccm in order to achieve proper nanoparticle formation. This flow resulted in a pressure of 6 Pa. Nanoparticle formation then occurs as single generation particle growth as it has already been described in chapter 5 and 6.
As particles grew, mass spectrometry was applied. The orifice was chosen to 50 μm through which atoms and molecules from the chamber can enter the mass spectrometer, where the pressure is in the range of 10^{-5} to 10^{-4} Pa in order to prevent collisions between gas molecules. The orifice is at grounded potential like the chamber walls. Thus, negative ions cannot overcome the potential drop across the sheath in front of the mass spectrometer but positive ions and neutrals are able to pass through and to be detected. Consequently two different modes were used in this work, Residual Gas Analysis *RGA* for neutrals and secondary ion mass spectrometry *+ionSIMS*. Latter mode name is confusing because here it was applied to detect primary ions originating directly from the plasma in the reactor.
In RGA mode neutrals are ionized in the ionisation source of the mass spectrometer, whereas

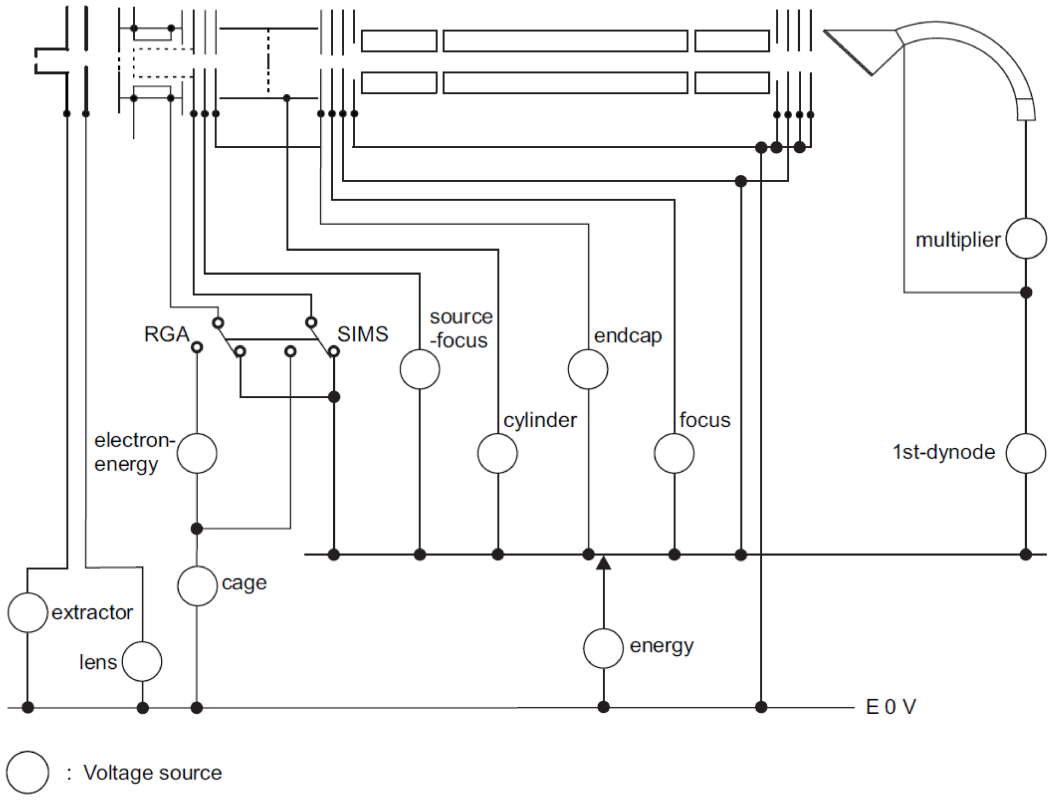

Figure 9.8: Scheme of the Hiden PSM003 mass spectrometer, taken from *PSM003 User's Manual*

in +ionSIMS mode the ionisation source is switched off. A scheme of the lens system with most of the tunable units is shown in figure 9.8. The first two lenses through which ions and neutrals have to pass after the orifice are the *extractor* and the lens. Both are set to 0 V to ground potential respectively in RGA mode in order to block most of the incoming ions but supplied with a negative voltage in +ionSIMS mode for focussing the ion trajectories. Next step is the ionisation chamber consisting of a cage and a filament, which emits electrons at an adjustable electron current. By adjusting the voltage offset *electron-energy* a defined energy is given to the filament. In these experiments an energy of 70 eV was chosen as this value yields high cross-sections for electron impact ionization for most of the chemicals inside the reactor [257]. As most of the ions are then formed close to the grid at potential *cage* by electron detachment in electron neutral collisions the kinetic energy of the produced ions is approximately $e \cdot cage$. In +ionSIMS mode the filament current is set to 0 as well as the filament voltage and thereby it is shut off. The grid voltage, which otherwise is used for extracting electrons at a certain energy, is set to the potential defined by *energy*. The adjustments made to the numereous units in +ionSIMS and in RGA mode for the here presented measurements are listed in table 9.1 with respect to the units' definitions as given in figure 9.8.

	RGA	+ionSIMS
exctractor / V	0	-40
lens / V	0	-154
cage / V	5	not used
electron energy / V	70	not used
energy / V	4	adjusted to the plasma, see section 9.3
source focus / V	-200	-28
cylinder / V	0	0
endcap / V	-5	-18
focus / V	-100	-10
transit energy / V	3	3
first dynode / V	-4000	-3600
multiplier	2400	2400

Table 9.1: The multiple units, as defined in figure 9.8, in the PSM003 were tuned for an energy independent measurement and a good signal intensity. The transit energy corresponds to the axial molecule velocity in the mass filter and should not be changed.

After passing the source focus the ions enter the energy filter in form of a *Bessel Box*. Ions with higher energy than set at the parameter *energy* stay on a straight trajectory onto the centre stop in the middle of the filter. Ions of low energy are repelled by the filter, so that only ions at desired energy can pass through the Bessel Box. Finally a quadrupole sorts out the ions by charge to mass ratio. For detailed information on the mass filter the reader may refer to [256] and to [260] for understanding the trajectories in the energy filter.
Summarizing the Hiden PSM003 is able to perform energy resolving mass spectrometry for primary ions from the plasma and to analyse the neutral gas during the particle formation process. One difficulty in RGA mode is the dissociation of primary neutral species in the ionisation source by the high energetic electrons. Consequently many of the detected species are not primary but can also be secondary products, that do not originate from the plasma chamber. As no collisions are assumed to occur in the mass spectrometer the secondary species must always descend from a higher mass molecule. Typical cracking patterns of numerous molecules can be found on NIST, for example. The meaning of dissociation in the electron source is, that low amounts of radicals originating from the plasma are hidden behind great amounts of radicals originating from the electron source, and thus, are very difficult to measure.
A mass range of 0.4 to 300 amu can be scanned but in these experiments only masses from 0.4 up to 100 amu have been monitored. Two different positions of the mass spectrometer were tested in order to check for an influence in the ion energy distribution. Both positions, namely inserting the head of the spectrometer from the side or from the top, give equal results. Thereby an effect from varying particle trajectories can be excluded. However the distance between the plasma, which can vary in size, and the stationary mounted head are expected to may affect the amount of inelastic collisions to occur for particles on their way towards the orifice. Thereby an effect on the detectable chemical composition in RGA and

on the measured ion energy distribution by changing plasma size has to be considered. Principally, only the sheath chemistry can be measured by the means of mass spectrometry.
Another consideration, that needs to be taken into account, is the fact, that a mass spectrometer does not directly measure concentrations but molecule and ion fluxes through the plasma sheath. Because the flux $\Gamma = nv$ is dependent on the velocity and the density of the species, it is not only proportional to the species density in front of the sheath. For neutrals one may assume the same temperature T for all different masses, which is close to room temperature. The thermal velocity, therefore, is dependent on the mass m after

$$v_{\mathrm{th}} = \sqrt{\frac{8k_{\mathrm{B}}T}{\pi m}}, \tag{9.10}$$

and hence, the measured mass spectra must be interpreted according to $\Gamma \propto m^{-1/2}$.
Often a common Bohm velocity is assumed for ions. If that is the case, their flux is not mass dependent through the sheath, where flux continuity through the sheath has been considered. However, if each ion species is attributed its own Bohm velocity according to 2.16, the flux goes again like $\Gamma \propto m_{\mathrm{i}}^{-1/2}$ with the ion mass m_{i}, and thus, the intensity of measured ions decreases with increasing mass, even if the concentration stays constant.
For an extensive review of different challenges to mass spectrometry of reactive plasmas the reader may refer to [257]

9.3 Ion energy

For most of the tunable parameters like energy, mass, source focus etc. a scan can be performed with the mass spectrometer. This means to change its value stepwise and measuring the intensity at the particle detector at the same time. This way scanning the mass yields a traditional mass scan, scanning the energy shows the energy distribution of particles with fixed charge to mass ratio. Another kind of scan is to keep all tunable parameters fixed but measure the intensity nevertheless. This is called MID-scan and yields temporal evolution of particle fluxes at a certain charge to mass ratio and at a certain energy. In order to get information on the temporal evolution of the main species during particle growth all three scans mentioned have to be performed consecutively. They are part of a continuous recalibration process in order to adapt to changing plasma conditions throughout the growth cycles.
Before measuring in the challenging environment of dusty plasmas all the lenses and electrodes of the apparatus have to be set to good voltages. Doing so the most important aim is to achieve high countrates at the detector but also an energy independent extraction of the ions from the plasma in +ionSIMS mode. To check if this is the case the most powerful tool is the energy scan. If the instrument is set up correctly an energy scan should give a clean peak at the plasma potential. Using the Bessel Box as energy filter the peak shows a broadening of at least 0.5 V due to the filter's precision [257]. Depending on the gas pressure used in the reactor collisions on the way towards the mass spectrometer head lead to energy losses for a part of the impinging ions, so that the energy distribution should be smeared out towards low energies. Once the energy scan yields plausible results further checks can

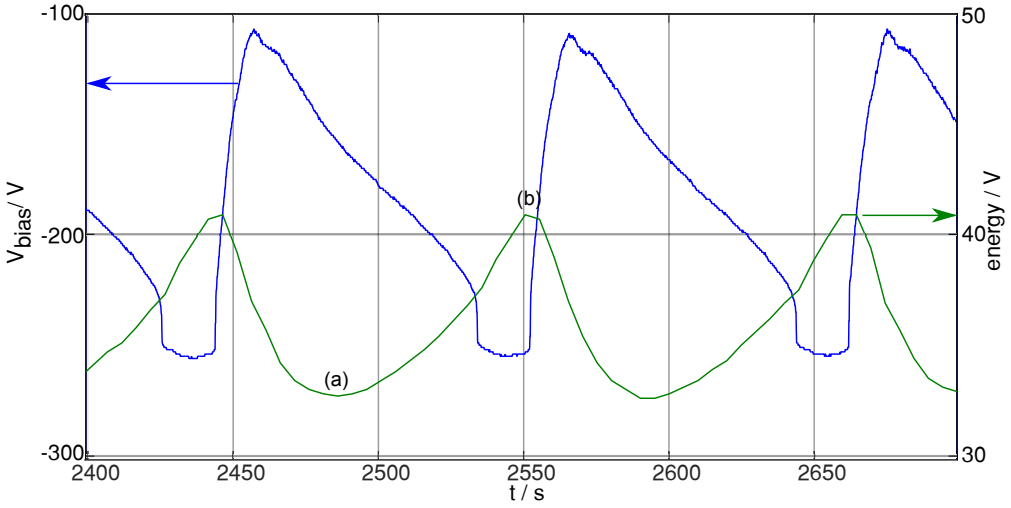

Figure 9.9: The energy of incoming ions, green line, is plotted together with the self-bias voltage, blue line, in order to correlate its evolution with the particle growth cycles. At points (a) and (b) corresponding energy distributions are shown in figure 9.10.

be done at various plasma potentials to ensure that the instrument fulfils the function of measuring energy independently.
During particle growth plasma size, plasma potential and gas composition may change continuously. In RGA mode this does not pose problems to the extraction process. However in +ionSIMS mode the changing plasma potential has to be accounted for. To ensure, that a temporal change in intensity is not caused by a misalignment of the set energy to real energy of incoming ions, energy scans have to be performed often enough. This can be implemented in a measurement loop and should be the first step of each loop, which can then be repeated as quick as possible to obtain a good time resolution.
It is useful to perform the energy scan at a mass, that has a reliably high intensity throughout the growth process. Therefore, the mass 26 amu of acetylene was chosen as this is always present in the chamber at significant density. It was further confirmed by additional tests, that all sorts of ions exhibit the same energy distribution, so that acetylene ions are representative for any ion species.
The temporal evolution of the energy distribution is obtained, as shown in figure 9.9, where the plotted energy corresponds to the maximum in the energy distribution, as shown in figure 9.10. Here, exemplary, the distributions for point (a) and (b) in figure 9.9 are shown.
The scanned energy range was kept relatively small to keep the scan duration as small as possible, and hence, to achieve a good time resolution in the measurement loop. The plotted parts of the ion energy distribution are sufficient to detect the energy maximum in order to recalibrate the instrument at the beginning of every loop. However, if the overall intensity of the ion flux is of interest actually an integration over the energy should be done. This is impossible here because for curve (a) not all of the distribution has been recorded.
As it has also been done for all other species presented in the following results, the intensity is always assumed to be proportional to the peak height of the energy distribution.

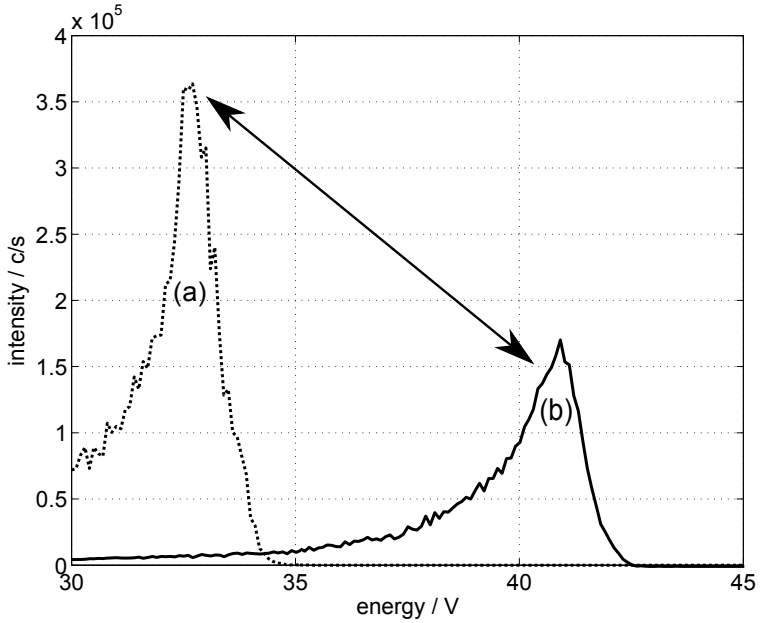

Figure 9.10: The energy of incoming ions changes strongly during particle growth. Curve (a) depicts the energy distribution at point (a) in figure 9.9 and (b) correspondingly.

Unfortunately it cannot be done differently because scanning the entire energy distribution of each species would take too much time and thus reduce the temporal resolution of the measurements to a degree, that the temporal evolution within one growth cycle could not be monitored anymore. Luckily the shape of the energy distribution does not seem to change drastically, so that the peak height should roughly be proportional to the overall ion flux.

9.4 Results and Discussion

Not only the energy shifts during particle growth but from figure 9.10 it becomes obvious, that also the intensity of many ions, here acetylene ions, varies drastically. This will be evaluated in section 9.4.4 from the MID scans, that have been done on several masses after each energy scan. But first, the most significant masses shall be introduced, which can be found from mass scans in the +ionSIMS and in the RGA mode.
Because each species' concentration is subject to variations in the related chemical reactions during particle growth, important species were identified in an acetylene / argon mixture at the same plasma power as used for particle generation but at lower precursor concentration than needed for dust synthesis. Thereby possible chemical products are formed at stable conditions, so that an entire mass scan can be performed without having trouble with the time resolution of the scan. Using the RGA mode and the +ionSIMS mode neutral species and also ions generated inside the plasma can be identified at half of the acetylene flux than that for particle generation.

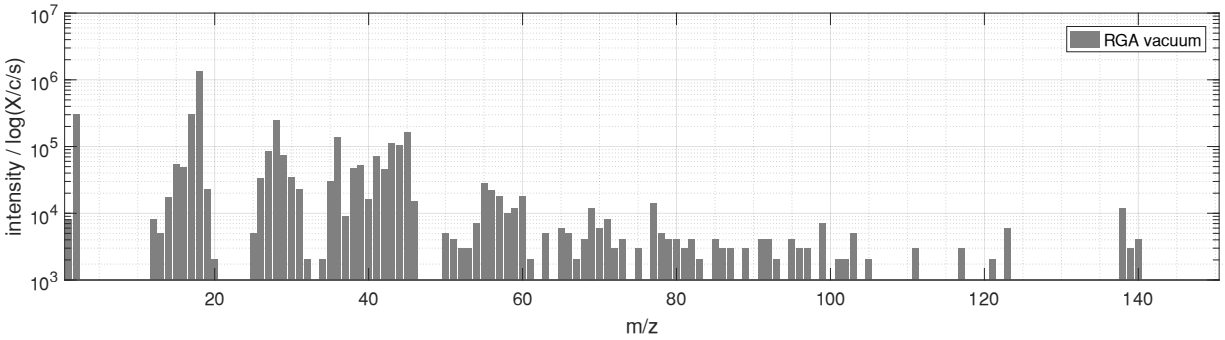

Figure 9.11: Residual gas analysis of the reactor background

9.4.1 Neutral species

Intensities measured in RGA mode are a good indicator for neutral concentrations in the reactor. Because in many reactors the plasma density is much less than neutral density, usually by some orders of magnitude, the neutrals play a crucial role in chemical reactions leading to nucleation and surface growth. In order to understand the mass spectra obtained during the process, the impurities in the reactor background gas were measured, which is presented in figure 9.11. It can be seen, that besides residual carbonaceous process chemicals like CH, CH_2 etc. a certain quantity of impurities is always present in the reactor. In table 9.2 possible explanations for several lines are suggested by impurities originating from nitrogen and oxygen containing molecules but also by carbonaceous molecules.
As some species can be masked by oxygen and nitrogen impurities, such as CH_2 by N, CH_3 by NH, CH_4 by O and C_2H_4 by N_2 and CO, the interpretation of achieved mass spectra has to be studied carefully. Further more residual chlorine from former experiments in this reactor might be present at masses 35 and 37 amu due to its two isotopes ^{35}Cl and ^{37}Cl. The ratio of the two peaks corresponds almost perfectly to the fact, that ^{35}Cl is three times more frequent than ^{37}Cl. That is why at mass 36 amu the isotope ^{36}Ar of argon can be found, but during the plasma process a certain portion of its intensity may also originate from H^{35}Cl. At 18 amu the water peak is very strong. It can be found again at $m/z = 20$ with the heavier and stable oxygen isotope ^{18}O. Contributing with 0.2 % to the worldwide amount of oxygen, the ratio of the peaks at 18 and 20 clearly indicates, that the peak measured in vacuum at 20 exclusively originates from water but not from argon in its double charged state. If necessary the water content can principally be reduced by longer conditioning time for the reactor before the experiment.
The peak at mass 44 amu is likely to be attributed to CO_2 but it could also account for propane, C_3H_8. For the masked species it is difficult to draw conclusions from measured intensities because of the complicated and mostly unknown gas mixture observed. Therefore, in many cases it is useful to do a background substraction of any taken spectrum. However it turned out to be very difficult in our studies due to continously changing reactor conditions during each experiment.
Apart from several impurities (e.g. water, nitrogen and carbon dioxide and their fragments),

chemical X	mass / amu
H	1
H_2	2
C	12
CH and / or ^{13}C	13
CH_2 and / or N	14
CH_3 and / or NH	15
CH_4 and / or NH_2 and / or O	16
NH_3 and / or OH	17
H_2O	18
H_3O	19
Ar^{++} and / or $H_2{}^{18}O$	20
C_2	24
C_2H	25
C_2H_2	26
C_2H_3 and / or HCN	27
C_2H_4 and / or N_2 and / or CO	28
CH_3CH_2 and / or CH_3N	29
C_2H_6 and / or NO	30
CH_2OH and / or CH_5N	31
CH_3OH and / or O_2	32
^{35}Cl	35
^{36}Ar	36
^{37}Cl	37
^{38}Ar	38
C_3H_3	39
Ar and / or C_3H_4	40
C_3H_5 and / or C_2H_3N	41
C_3H_6	42
C_3H_7 and / or CH_3CO and / or C_2H_5N	43
CO_2 and / or C_3H_8 and / or C_2H_4O	44
CH_3CH_2O or C_2H_7N	45
CH_3CH_2OH	46
C_4H_2 and / or CF_2	50

Table 9.2: In RGA mode many types of chemicals can be detected. Even in vacuum an abundance of compounds is present. The peaks at 35 and 37 amu point out, that chlorine from former experiments can be found. Note, that some species may not be stable in neutral form, but are created inside the mass spectrometer as positive ion.

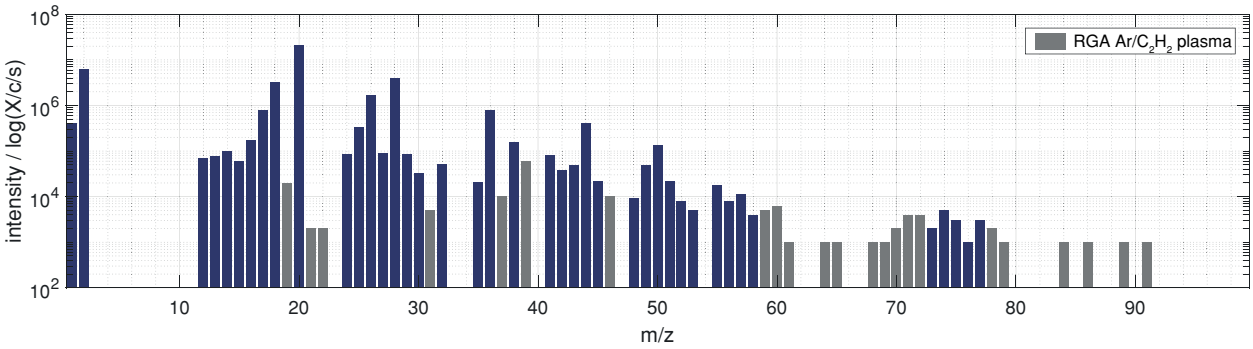

Figure 9.12: Residual gas analysis of argon / acetylene mixture at 11 / 0.5 sccm; marked in blue are those masses, which have been further investigated in the MID mode.

dominant neutral species are H, H_2, C_2H_2 and Ar, which is present at $m/z = 40$, followed by medium strong species like C, CH, C_2, C_2H, C_2H_3 and a bunch at C_4, C_4H, C_4H_2, C_4H_3 and C_4H_4. Further more small peaks at mass 58, 43 and 42 amu probably belong partwise to the impurity acetone $(CH_3)_2CO$ and its fragments C_3H_7 and C_3H_6, which originates from the acetylene pressure bottle, where it is used as a solvent to store acteylene safely [262]. Acetone fragments might also slightly affect measured intensities at masses 41, 38, 29, 28, 27, 26, 25, 16, 15 and 14 amu [263]. Also isopropyl alcohol, used for cleaning of the reactor, is probably causing corresponding peaks by fragmentation to CH_3CH_2O, CH_3CO and CH_3CH_2 at masses 45, 43, and 29 amu. At very high mass of 138 to 141 amu residuals from former experiments with parylene appear, which explains a contamination with chlorine.
By admixing argon at 11 sccm and acetylene at 0.5 sccm and igniting a plasma the main chemical compounds can be studied without generating nanoparticles, because the precursor concentration stays under a critical value. This way the discharge remains stable during the time needed to take a mass spectrum. This spectrum is presented in 9.12 up to mass 100. In comparison to a pure vacuum spectrum a clear increase can be observed for low masses, such as 1, 2, 12, 13, 16, 20, 24, 25 and 26. These correspond to atomic and molecular hydrogen, carbon, CH, CH_2, CH_4, argon, C_2, C_2H and C_2H_2, respectively, as expected from dissociation and fragmentation of acetylene. The dissociation happens in the discharge as well as in the mass spectrometer electron source. It is difficult to distinguish the two effects. Some impurities are also dissociated by the plasma, like formamide CH_3NO at mass 45, as can be seen by a loss in intensity from figure 9.11 to figure 9.12.
It shall be mentioned, that hydrocarbons with odd mass cannot be stable in neutral form. The same holds true for oxygen containing hydrocarbons. However, for nitrogen containing hydrocarbons it is the opposite. Their neutrals can only be stable with an odd quantity of hydrogen atoms, and hence, an odd mass. This may indicate, that the plasma contains a high amount of nitrogen, which is incorporated into hydrocarbons, and thus, leads to high intensities at odd values for m/z in the spectra.
However, an increase can be observed mainly for high masses like 28, 32, 36, 38, 39, 44, 49, 50 and 51 for example. It can only be explained by the presence of ethylene C_2H_4, methanol CH_3OH, ^{36}Ar, ^{38}Ar, supported by the corresponding isotope ratio of 5:1, C_3H_3, CO_2 or

CH_2NO as dissociation product of formamide and C_4H_x, respectively, as a result of polymerization processes in the plasma. The lines from $m/z = 48$ to $m/z = 52$ are attributed to C_4H_x with $x = 0 \ldots 4$ as dissociation products of C_4H_2 and C_4H_4. Mass 53 amu can only be related to C_3H_3N in the form of azete or acrylonitrile but not to fragmentation of higher order carbon compounds as indicated by the absence of a peak at mass 54 amu.
Interestingly, the absence in mass 54 clearly prooves, that no molecules of the form C_4H_6 are formed in the discharge, as all possible structures of this sum formula do exhibit a big peak at mass 54 amu. The main argon line at mass 40 amu could not be recorded due to too high intensity.
At masses greater 72 amu the next group of carbohydrates can be found each consisting of 6 C-atoms. It may be slightly mixed with molecules containing 5 C-atoms and up to 12 H-atoms. These may explain measured masses smaller than 72 amu. However, peaks at $72 \ldots 78$ should be related to C_6H_x with $x = 0 \ldots 6$. It shall also be noted, that for high masses the precision of the mass spectrometer decreases, because of a less intense signal. Therefore, the higher order carbohydrates can only be interpreted vaguely.
Resuming, besides the several observed impurities and nitrogen containing species it can clearly be confirmed, that polymerization takes place in the plasma. This leads preferably to the formation of species of kind $C_{2n}H_x$, as expected following section 3.2.2, e.g. figure 3.10. There the identified big molecules mainly are C_4H_2, C_4H_4, C_6H_2, C_6H_4, C_6H_6, C_8H_2 and C_8H_6. This can well explain the observed spectrum apart from some nitrogen containing carbohydrates. It shall be mentioned, that with higher acetylene flux, as later used for nanoparticle production, the influence of impurities is expected to decrease due to the lower relative concentration. Also the relative amount of long molecules is expected to be higher, as more collisions can occur between reactive molecules, when their partial pressure is higher. That is the reason, why no nanoparticle formation occurs at low acetylene fluxes, like here for 0.5 sccm.
In order to reduce the acquisition time of a mass spectrum and, thus, to keep the time resolution at a good level, only a few of the above shown masses have been followed throughout the particle growth process. The masses for which the evolution has been recorded in a so-called MID scan are marked in blue in figure 9.12. They will be further investigated in section 9.4.3.

9.4.2 Ionized species

In contrast to the RGA mode the ions can be measured directly, so no unwanted fragmentation by post ionization can occur. Here the same molecules are masked by impurities as for the neutrals. On the first glance some differences between the neutral and the ion spectrum in figure 9.13 can be seen. Bigger masses do have a better transmission and the spectrum seems to be shifted by 1 amu to higher masses.
Instead of H and H_2, H_2^+ and H_3^+ are present. At 19 amu the line for H_3O^+ is stronger than H_2O^+ and C_2 as well as C_2H have almost disappeared. Also the bunch of molecules with four C-atoms has shifted to higher masses in comparison to the RGA mode. Lines at 48 and 49 amu disappear in the noise but $C_4H_3^+$ is twice as strong as $C_4H_2^+$ and $C_4H_5^+$ at mass

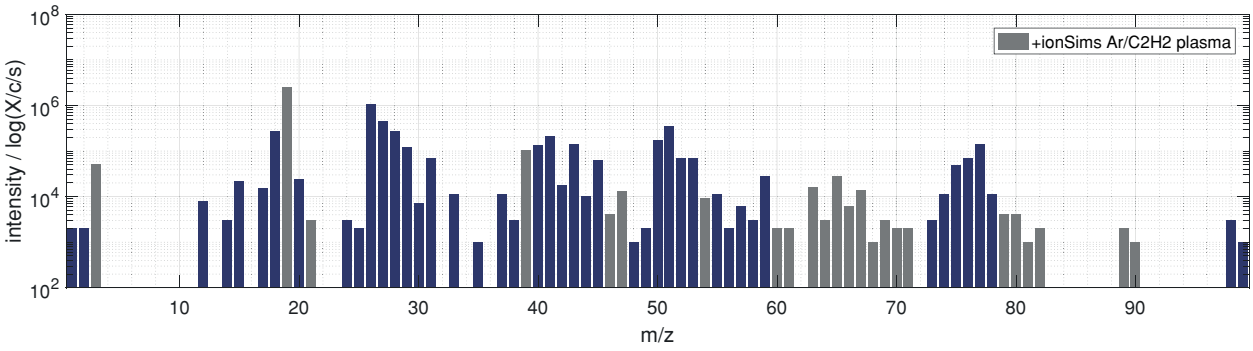

Figure 9.13: IonSIMS analysis of argon / acetylene mixture at 11 / 0.5 sccm; marked in blue are those ions, which have been further investigated in the MID mode.

53 amu as intense as $C_4H_4^+$.
Furthermore, the ions $C_4H_2^+$, $C_4H_4^+$, $C_6H_2^+$, $C_6H_4^+$ at masses 50, 52, 74, 76, repsectively do appear very well in this spectrum. They are products of the chain reaction 3.51 as possible route towards nanoparticles [179, 264]. However, their protonated forms (+1 amu) show to be equally pronounced or even more intense
Thus, some species, which do not exist as neutrals, seem to be relatively stable as protonated positive ions in the plasma. Best and most obvious examples are H_3^+ and H_3O^+, that have already widely been investigated. However the carbonium ions are less known, which is the name for protonated alkanes [265, 266].
Nevertheless, this kind of ions may exist in the argon / acetylene plasma, for example in form of the butonium cation $C_4H_{11}^+$ at mass 59 amu right next to the line of $C_4H_{10}^+$. Accordingly, the peak at mass 45 amu could be interpreted as $C_3H_9^+$. The lines at masses 45 and 59 amu could, however, also be attributed to the presence of ethylamine $C_2H_5NH_2^+$ or dimethylamine and propylamine $C_3H_7NH_2^+$ ions, respectively. The most intense signals (apart from water content) in descending order are measured for $C_2H_2^+$, $C_2H_3^+$, $C_4H_3^+$, $C_2H_4^+$ and then at mass 41 amu. The latter can be related to the fragmentation of several relatively saturated hydrocarbons in the discharge or to the formation of ArH^+. At this point no conclusion can be drawn for it. The next most important peaks in descending order are attributed to $C_4H_2^+$, $C_6H_5^+$ and then mass 43 amu, which is probably the fragmentation product of relatively saturated hydrocarbons in the discharge as well.
In the above presented figure it was possible to measure the argon ions. They can be found as single charged species at mass 40 amu, and as double charged ion at mass 20. However, the peak at $m/z = 40$ turned out to exceed the detector saturation limit during the nanoparticle growth process. Therefore, the argon ion intensity must be found from the two isotopes at masses 36 and 38 amu. The double charged argon ion is not necessarily representative for the amount of single charged ions, as their ratio may change as a function of the electron temperature inside the plasma.
Summarizing, the ions can be detected up to relatively high masses of round about 80 with good intensity. Again, the chain reaction towards bigger molecules of form $C_{2n}H_x^+$ can be confirmed to occur in the discharge by the regular appearance of bunches of carbohydrate

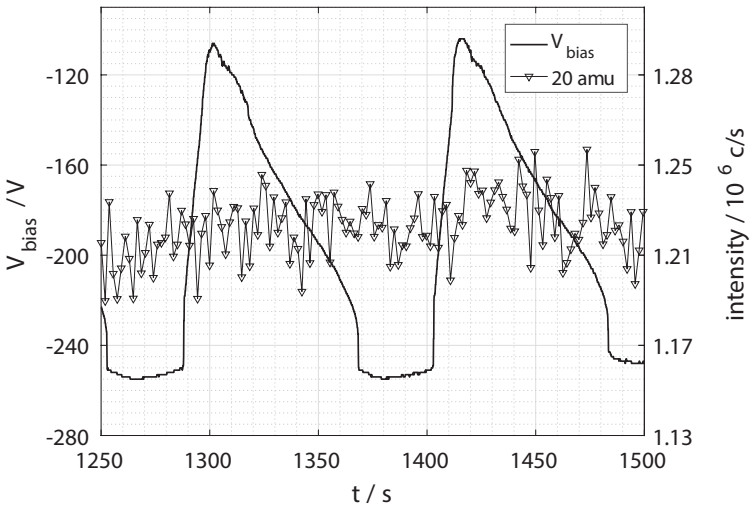

Figure 9.14: The countrate of Ar^{++} in RGA mode is not affected by the growth cycles within the measurement precision, which is expected due to the inertness of argon.

peaks each separated by the mass of round about two carbon atoms. However, the protonated variation of these molecules seems to be much more favoured than in the neutral spectrum.
Like for the neutrals, not all of the above investigated masses have been chosen to be tracked throughout the growth cycles of nanoparticles. Only for the blue marked bars in figure 9.13 the time evolution has been recorded by the help of the MID mode. At low admixtures of acetylene, the argon ion is not the most dominant ion species. Instead the acetylene ion is far more intensive. This is an indicator for low electron temperatures, that are sufficient to ionize acetylene but much less argon, although it is more frequent in the reactor. Due to the changes in the electron temperature during the nanoparticle formation, however, the argon ion signal exceeds the saturation limit of the detector and can therefore not be recorded in the MID mode.

9.4.3 Evolution of neutrals

By fixing all parameters in the mass spectrometer MID scans of several species have been performed in RGA mode, among which are the blue marked masses from figure 9.12, yielding their temporal evolution. In order to achieve a good temporal resolution not all of these masses have been recorded at the same time, but in three separate experimental runs. Due to the high amount of figures and the ease of illustration, the time evolutions of the peak intensities are all presented in the appendix A together with the correlated self-bias voltage. However, in order to explain several contexts some of these figures will be shown in this section, too.
Because the only reaction that argon is involved in as a reactant, is the formation of ArH^+, which is of very little quantity in comparison to neutral argon, it has to be of constant density over the entire particle growth cycle. This we can verify by looking at its intensity in

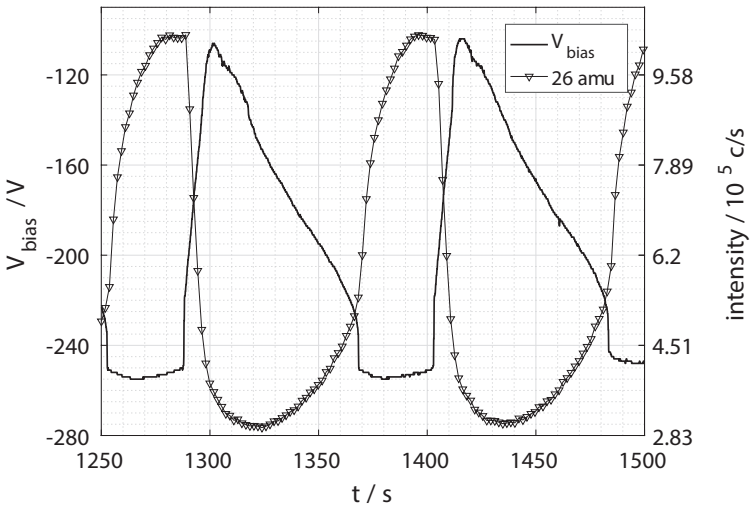

Figure 9.15: The countrate of $C_2H_2^+$ in RGA mode is strongly affected by the growth cycles. It indicates a strong dissociation of the neutral molecule during phases II and III.

the neutral spectrum. As Ar^+ is above the maximum intensity measurable with the detector the signal of double charged argon, Ar^{++}, has to be investigated at mass to charge ratio 20. In figure 9.14 indeed Ar^{++} does not show clear fluctuations correlated to the growth cycles. It confirms the time stability of the measurement signals.

Acetylene As next the evolution of acetylene from the signal at $m/z = 26$ is shown in figure 9.15, as it is the second injected gas and expected to be of high quantity. It shows the highest concentration at the end of phase I and the lowest during phase III.
Recalling equation 3.17 with the substitutions 3.28, the acetylene concentration is a function of gas flow rate R_p and loss rates R_loss. Whereas the input is fixed by the acetylene flux through the flow-controller, the loss rate strongly varies throughout the particle growth cycle. In the simplest case, when neglecting losses by deposition on nanoparticles, the loss rate can be described as

$$R_\mathrm{loss} = K_\mathrm{diss} n_\mathrm{P} n_\mathrm{e0}, \tag{9.11}$$

which is exactly described by the substitution 3.28. However, assuming irreversible deposition on the particles and considering a constant volume specific pumprate $s_\mathrm{V} = S_\mathrm{V}/V_{reactor}$, this needs to be completed with the specific loss rate of precursor onto the dust particles $K_\mathrm{loss,P}$ and the pumping losses $n_\mathrm{P} s_\mathrm{V}$, respectively:

$$R_\mathrm{loss} = \left(K_\mathrm{diss} n_\mathrm{e0} + K_\mathrm{loss,P} n_\mathrm{d} + s_\mathrm{V}\right) n_\mathrm{P}, \tag{9.12}$$

so that the substitutions become

$$\begin{aligned} n_A &\mapsto n_\mathrm{P}, \\ K_\mathrm{loss} n_\mathrm{d} &\mapsto K_\mathrm{diss} n_\mathrm{e0} + K_\mathrm{loss,P} n_\mathrm{d} + s_\mathrm{V}, \\ K_\mathrm{diss} n_\mathrm{p} n_\mathrm{e0} &\mapsto R_\mathrm{P} \\ D_{AB} &\mapsto D_{\mathrm{P}B}. \end{aligned} \tag{9.13}$$

Hence, by the help of equations 3.10 and 3.23 the qualititative dependence of the measured precursor flux into the mass spectrometer must be

$$\Gamma_{\mathrm{P}}(l/2) \propto \frac{p_{\mathrm{P}}(l/2)}{\sqrt{T}} \propto \frac{n_{\mathrm{PS}}}{T^{3/2}} \propto \frac{R_{\mathrm{P}}}{\sqrt{p_{\mathrm{tot}}(K_{\mathrm{diss}} n_{\mathrm{e0}} + K_{\mathrm{loss}} n_{\mathrm{d}} + s_{\mathrm{V}})}} \cdot T^{-1}. \tag{9.14}$$

Consequently the measured precursor intensity in the mass spectrometer, depends linearly on the precursor flow rate, which is fixed here, and inversely to the square root of the loss term. The temperature T and total pressure p_{tot} can also be assumed to be fixed here. Thus, a lower count rate during phase III must mean an increase in the losses to the square of the intensity change:

$$\frac{\Gamma_{\mathrm{P,I}}(l/2)}{\Gamma_{\mathrm{P,III}}(l/2)} = \sqrt{\frac{K_{\mathrm{diss,III}} n_{\mathrm{e0,III}} + K_{\mathrm{loss,III}} n_{\mathrm{d,III}} + s_V}{K_{\mathrm{diss,I}} n_{\mathrm{e0,I}} + K_{\mathrm{loss,I}} n_{\mathrm{d,I}} + s_V}}. \tag{9.15}$$

A reduction of the measurement signal by a factor of 4, therefore, means an increase in the losses by a factor of 16.
Whereas the pumping rate remains constant, the losses of acetylene by dissociation from electron impact and from inelastic collisions, as well as surface losses on the chamber walls and particles do vary throughout one growth cycle. The dissociation rate constant K_{diss} is expected to increase with particle presence due to higher electron temperature, whereas a lower electron density $\mathrm{n_{e0}}$ may counterbalance in the total dissociation rate. In the loss term for deposition onto the particles both parameters, the dust density n_{d} should grow with particle presence, as the specific loss rate constant K_{loss} should also do, due to the growing particle surface area. Hence one can resume:

$$\begin{aligned} K_{\mathrm{diss,I}} &< K_{\mathrm{diss,III}} \\ n_{\mathrm{e0,I}} &> n_{\mathrm{e0,III}} \\ 0 \approx K_{\mathrm{loss,I}} &< K_{\mathrm{loss,III}} \\ 0 \approx n_{\mathrm{d,I}} &< n_{\mathrm{d,III}} \\ s_{\mathrm{V,I}} &= s_{\mathrm{V,III}}. \end{aligned} \tag{9.16}$$

The losses to the particle walls require additional reactions in order for the acetylene to not desorb again and are therefore not very probable. Under the assumption of the extreme case, where the losses are dominated by the dissociation rate, equation 9.15 can be simplified, and an upper limit for the change in the specific dissociation rate K_{diss} is found to be:

$$\frac{K_{\mathrm{diss,III}}}{K_{\mathrm{diss,I}}} \approx \left(\frac{\Gamma_{\mathrm{P,I}}(l/2)}{\Gamma_{\mathrm{P,III}}(l/2)} \right)^2 \cdot \frac{n_{\mathrm{e0,I}}}{n_{\mathrm{e0,III}}}, \tag{9.17}$$

where the right hand ratios are accessible through the measurements, that have already been done at this point. The in figure 9.15 data exhibit a flux ratio of $\Gamma_{\mathrm{P,I}}(l/2)/\Gamma_{\mathrm{P,III}}(l/2) \approx 3.5$ and in chapter 7.4 it was shown, that the electron density between those two points decreases by a factor of $n_{\mathrm{e0,I}}/n_{\mathrm{e0,III}} \approx 5.5$. Hence, using a simple 1-D model, where losses and sources

are volume averaged over the entire discharge and further assuming the dissociation being the main loss process, but the precursor gas influx the main source for acetylene, one can approximate, that:

$$\frac{K_{\mathrm{diss,III}}}{K_{\mathrm{diss,I}}} \approx 67.4. \tag{9.18}$$

This is a dramatic change in the dissociation of acetylene. It may be caused by an increase of inelastic collisions with a higher density of metastable argon atoms, but probably it is mainly related to the higher amount of electrons with more than the dissociation energy due to an elevated electron temperature when nanodust is present.

Dissociation products If dissociation in the volume is the main contribution to the acetylene decrease, the products of these reactions should be detectable. The problem of detecting these, is to distinguish between dissociation products from the ion source in the mass spectrometer and from the plasma processes. However, the ratio between dissociation products from the ion source and the acetylene peak height should always stay constant.
Taking the example of CH, it means, that the peak of CH needs to evolve exactly the same way as C_2H_2, if it originates only from the ion source. In other words, when normalized to the peak of C_2H_2, it remains at a constant value. In figure 9.16 this is demonstrated and it clearly shows, that most of the measured CH is a dissociation product of acetylene in the mass spectrometer. The reason is, that the CH concentration in the reactor is very low, and thus, cannot be measured against the background from other chemicals. A low concentration of CH can originate either from high loss rates of this species in collisions and surface reactions or from very little production through dissociation in the plasma. Probably, a combination of both is the case with CH being highly reactive but difficult to produce by breaking up the C=C double bond of acetylene.
When doing a normalization to the acetylene intensity, the C peak follows the trend of the self-bias voltage almost perfectly. This does not necessarily mean, that during phase II and III the concentration of C in the plasma is higher than during phase I. Instead it only means that the concentration ratio of C to C_2H_2 is changing to a higher values during the last to phases. Therefore, it may be assumed, that the decrease in C_2H_2 originates at least partly from a high degree of fragmentation, resulting in smaller species like C.
The above described method can be applied to all possible fragmentation products of acetylene, which are C, CH, CH_2, C_2, C_2H. All fragments, that are not only a fragmentation product of acetylene in the ion source, but also originate from the plasma, as can be seen for C in figure 9.17, for example. When looking at the non-normalized evolution 9.17(a) a clear dependence on acetylene can be found, however, after normalization 9.17(b) it can be seen, that a big part of the signal originates from the plasma, actually. Hence, C originating from the plasma can be clearly identified, however, drawing conclusions about the absolute quantity is complicated. In general it can be noted, that the measured intensity I_{C} of C has two major contributions:

$$I_{\mathrm{C}} = A_{\mathrm{s}}\Gamma_{\mathrm{C}}(l/2) + \alpha_{\mathrm{C,P}} I_{\mathrm{P}}, \tag{9.19}$$

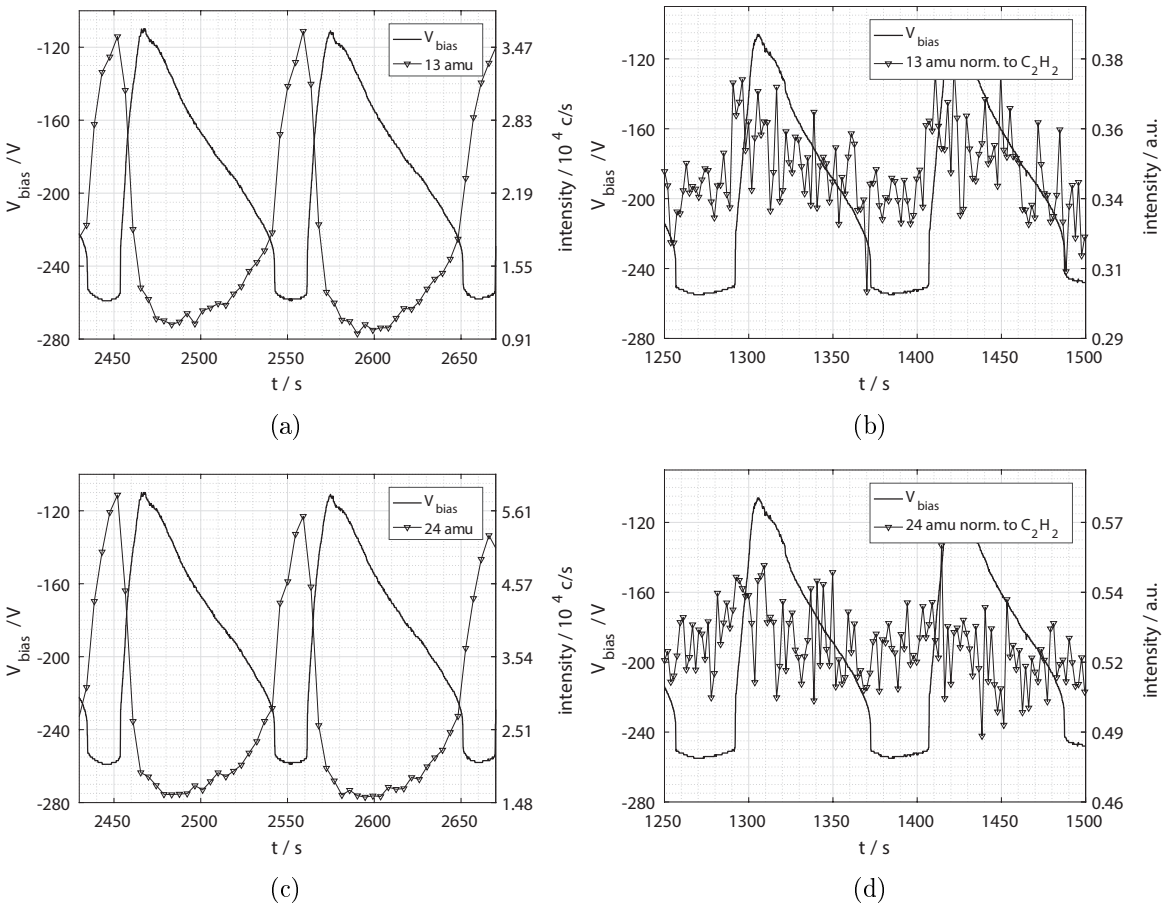

Figure 9.16: Evolution of peak at $m/z = 13\,\text{amu}$ before normalization 9.16(a) to the acetylene peak and after normalization 9.16(b). The dependence on the acetylene concentration is obvious, which indicates, that almost all measured CH originates from dissociation of acetylene in the ion source of the mass spectrometer. The same can be found for C_2 at $m/z = 24\,\text{amu}$, see 9.16(c) and 9.16(d).

the radical flux Γ_C from the reactor through the effective sampling cross section A_s and the dissociation of precursor in the mass spectrometer $\alpha_\text{C,P} I_\text{p}$, respectively. Here $\alpha_\text{C,P}$ is the line ratio, that can be found on NIST, for example, for standard RGA conditions. For the carbon peak from acetylene it is $\alpha_\text{C,P} = 7.0 \cdot 10^{-3}$.
Therefore, the plotted intensity ratio must follow:

$$\frac{I_\text{C}}{I_\text{P}} = \frac{A_\text{s}\Gamma_\text{C}(l/2)}{I_\text{P}} + \alpha_\text{C,P} = \frac{A_\text{s}\Gamma_\text{C}(l/2)}{A_\text{s}\Gamma_\text{P}(l/2)} + \alpha_\text{C,P} = \frac{\Gamma_\text{C}(l/2)}{\Gamma_\text{P}(l/2)} + \alpha_\text{C,P}. \tag{9.20}$$

From figure 9.17(b) it can be seen, that during phase I the measured line ratio is approximately 0.13 and during phase III, at its highest point the line ratio is roughly 0.23. Hence,

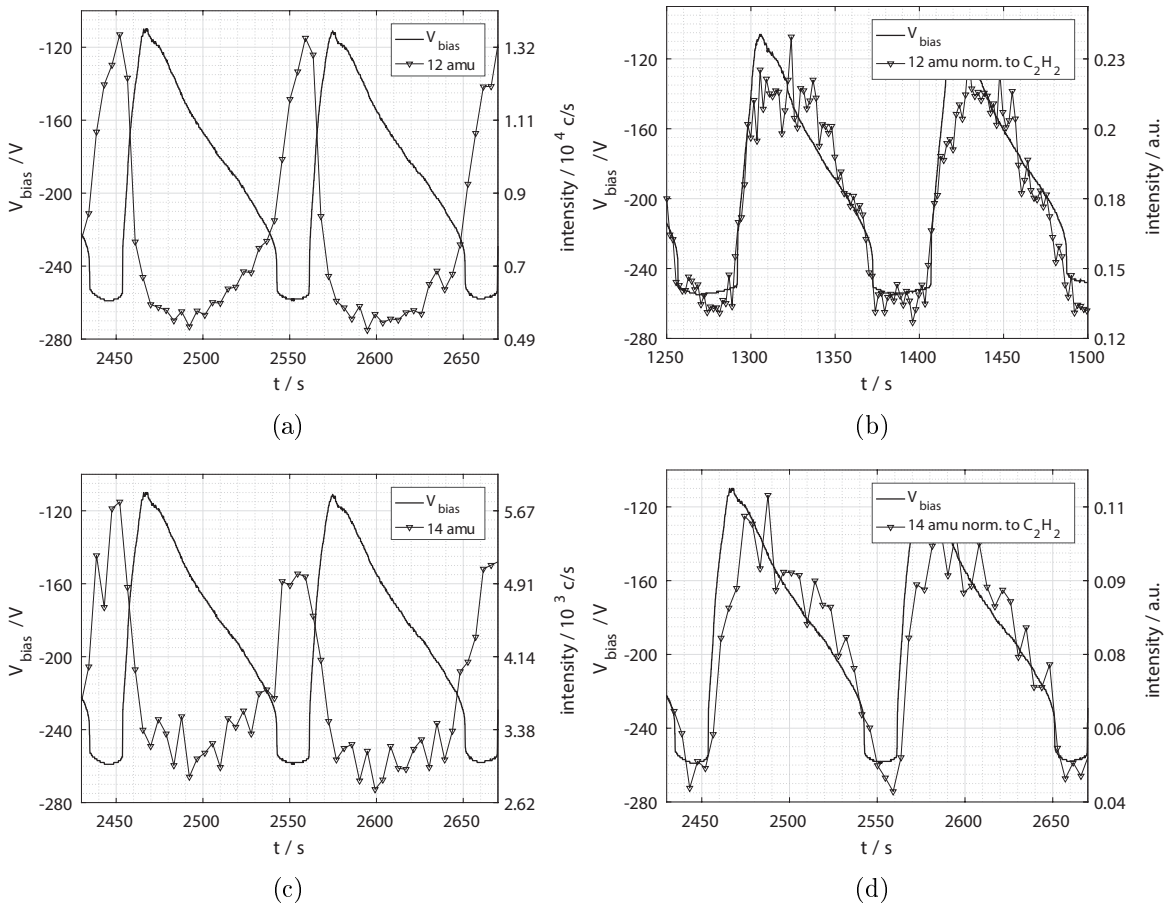

Figure 9.17: Evolution of peak at $m/z = 12\,\text{amu}$ before normalization 9.17(a) to the acetylene peak and after normalization 9.17(b). The dependence on the acetylene concentration is obvious in 9.17(a), but can be separated from fragmentation products in the plasma, as seen in 9.17(b). The same can be found for $m/z = 14\,\text{amu}$ 9.17(c), 9.17(d).

one may determine the flux ratios η to be

$$\begin{aligned} \eta_{\text{I}} &= \left.\frac{\Gamma_{\text{C}}(l/2)}{\Gamma_{\text{P}}(l/2)}\right|_{\text{I}} = 0.13 - 0.007 \approx 0.12 \\ \eta_{\text{III}} &= \left.\frac{\Gamma_{\text{C}}(l/2)}{\Gamma_{\text{P}}(l/2)}\right|_{\text{III}} = 0.23 - 0.007 \approx 0.22. \end{aligned} \tag{9.21}$$

Both radicals, C and CH_2 are the product of the same reaction, see chapter 3.2.1:

$$C_2H_2^+ + e^- \rightarrow CH_2 + C, \tag{9.22}$$

which is why they are the product of the same reaction constant K^*_{diss}. This is not the same constant as the above used overall dissociation constant K_{diss}, because the overall dissociation comprises of several paths j for dissociation by electron collisions, each with

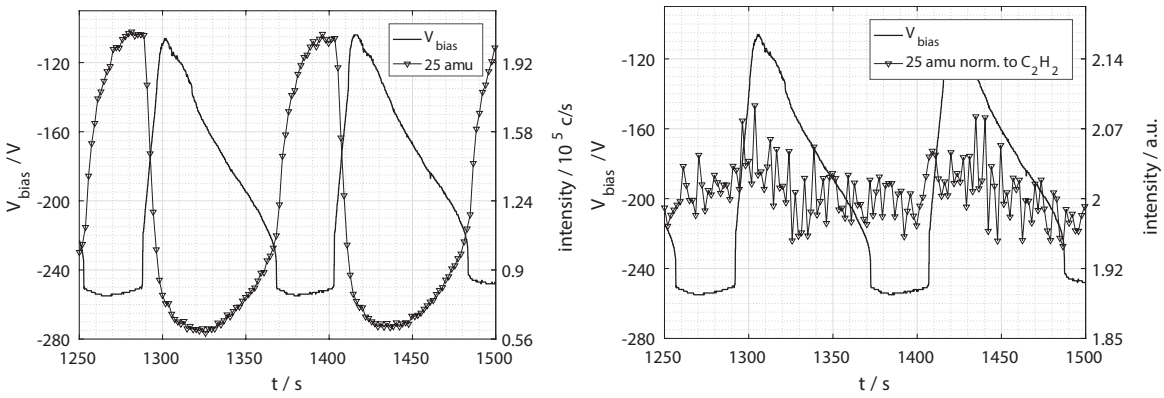

(a) (b)

Figure 9.18: Only a very small plasma contribution can be identified for the signal of C_2H 9.18(a), as shown by a small fluctuation of the to acetylene normalized evolution 9.18(b).

another dissociation rate constant K^j_{diss}.
During phase I, where no losses on particles are expected, the flux of C may be expressed according to equation 3.9, whereas during phase III estimation 3.23 needs to be applied, so that it can be written

$$\frac{\eta_{\text{I}}}{\eta_{\text{III}}} = \frac{K^*_{\text{diss,I}} n_{\text{e0,I}} n^+_{\text{P,I}}}{K^*_{\text{diss,III}} n_{\text{e0,III}} n^+_{\text{P,III}}} \sqrt{\frac{K^{\text{C}}_{\text{loss,III}} n_{\text{d,III}}}{D_{\text{C,Ar}}}} \frac{l}{2} \cdot \frac{\Gamma_{\text{P,III}}(l/2)}{\Gamma_{\text{P,I}}(l/2)} \approx \frac{0.12}{0.22}. \tag{9.23}$$

Here, the precursor intensity n_{P} needs to be replaced with the ionized precursor concentration, since it is the precursor for the dissociative recombination. By further assuming, that the volume averaged precursor density is n^+_{P} is proportional to the measured ion intensity (see following section 9.4.4)and likewise for the neutral precursor flux $\Gamma_{\text{P}}(l/2)$ to be proportional to the neutral intensity, it can be measured

$$\begin{aligned} \frac{\Gamma_{\text{P,III}}(l/2)}{\Gamma_{\text{P,I}}(l/2)} &= 0.29 \\ \frac{n^+_{\text{P,I}}}{n^+_{\text{P,III}}} &= 0.39, \end{aligned} \tag{9.24}$$

so that 9.23 simplifies to

$$0.55 \approx \frac{\eta_{\text{I}}}{\eta_{\text{III}}} = \frac{K^*_{\text{diss,I}} n_{\text{e0,I}}}{K^*_{\text{diss,III}} n_{\text{e0,III}}} \sqrt{\frac{K^{\text{C}}_{\text{loss,III}} n_{\text{d,III}}}{D_{\text{C,Ar}}}} \frac{l}{2} \cdot 0.11. \tag{9.25}$$

Taking the electron density ratio, determined from the Langmuir probe measurements in chapter 7, $n_{\text{e0,I}}/n_{\text{e0,III}} \approx 5.5$, it simplifies even further to

$$0.91 \approx \frac{K^*_{\text{diss,I}}}{K^*_{\text{diss,III}}} \sqrt{\frac{K^{\text{C}}_{\text{loss,III}} n_{\text{d,III}}}{D_{\text{C,Ar}}}} \frac{l}{2}. \tag{9.26}$$

Since CH_2 results from the exact same reaction, the same steps can be reapeated for CH_2 at $m/z = 14\,\text{amu}$, it reads from figure 9.17(d), that $\eta_\text{I} = 0.05 - 0.001$ and $\eta_\text{III} = 0.11 - 0.001$, and hence:

$$0.75 \approx \frac{K^*_\text{diss,I}}{K^*_\text{diss,III}} \sqrt{\frac{K^\text{CH2}_\text{loss,III} n_\text{d,III}}{D_\text{CH2,Ar}}} \frac{l}{2}. \tag{9.27}$$

At this point, it can already be conclude, that the loss rates on nanoparticles are similar for C and for CH_2. Unfortunately, the remaining constants are unknown. However, if one assumes, that the ratio of dissociative recombination equals the one of the total dissociation of acetylene, meaning

$$\frac{K^*_\text{diss,III}}{K^*_\text{diss,I}} \approx \frac{K_\text{diss,III}}{K_\text{diss,I}} \approx 67.4, \tag{9.28}$$

it can now be estimated, that

$$\begin{aligned} \sqrt{\frac{K^\text{C}_\text{loss,III} n_\text{d,III}}{D_\text{C,Ar}}} \frac{l}{2} &\approx 61.3 \\ \sqrt{\frac{K^\text{CH2}_\text{loss,III} n_\text{d,III}}{D_\text{CH2,Ar}}} \frac{l}{2} &\approx 50.6. \end{aligned} \tag{9.29}$$

For CH_2, however, one assumption more than for C has been done implicitly, namely that losses through dissociation in the plasma are negligible. Unfortunately, this calculation is not useful to exercise for CH, C_2 and C_2H, because the radical density in the plasma is too low compared to the radical density created in the ion source of the mass spectrometer. Nevertheless, it can now be estimated, how high losses of the radicals C and CH_2 onto the particle surface are. Probably, similar values may be assumed for the other radicals.
In order to round up the calculations performed above, the only thing that is left to do is the determination of the diffusion constants of C and CH_2 through argon. A more sophisticated method compared to equation 3.2 is the Chapman-Enskog theory [267, 268], after which the binary diffusion coefficient of A in gas B is

$$D_{AB} = \frac{3}{16} \frac{k_\text{B} T}{p_\text{tot}} \frac{2\pi k_\text{B} T / M_\text{R}}{\pi \sigma^2_{AB} \Omega_D(\Psi)} \tag{9.30}$$

with M_R again being the relative mass of A and B, the binary collision diameter

$$\sigma_{AB} = \frac{\sigma_A + \sigma_B}{2} \tag{9.31}$$

being a function of the Lennard-Jones parameter σ of the molecules A and B and the function $\Omega_D(\Psi)$:

$$\Omega_D(\Psi) = \frac{A^*}{\Psi^{B^*}} + \frac{C}{\exp(D\Psi)} + \frac{E}{\exp(F\Psi)} + \frac{G}{\exp(H\Psi)}. \tag{9.32}$$

Here, it has to be used $\Psi = T/\sqrt{\epsilon_A \epsilon_B}$, ϵ being the second Lennard-Jones parameter of A and B, and the constants $A^* = 1.06036$, $B^* = 0.15610$, $C = 0.19300$, $D = 0.47635$, $E = 1.03587$,

$F = 1.52996$, $G = 1.76474$ and $H = 3.89411$ [181]. The Lennard-Jones parameters required for the calculation are listed in table 9.3. For the radical CH_2 a lack of literature necessitates to approximate this molecule with the Lennard-Jones parameters of CH_4.
With these values, the diffusion constants can be calculated:

$$\begin{aligned} D_{\mathrm{C,Ar}} &= 0.183\,\mathrm{m^2/s} \\ D_{\mathrm{CH2,Ar}} &= 0.137\,\mathrm{m^2/s}. \end{aligned} \tag{9.33}$$

Hence, inserting this into equation 9.29 with a typical approximate reactor dimension of $l/2 \approx 25\,\mathrm{cm}$ it finally is

$$\begin{aligned} K^{\mathrm{C}}_{\mathrm{loss,III}} n_{\mathrm{d,III}} &\approx (6.74/0.25)^2 \cdot 0.183\,\mathrm{s^{-1}} = 11.0 \cdot 10^3\,\mathrm{s^{-1}} \\ K^{\mathrm{CH2}}_{\mathrm{loss,III}} n_{\mathrm{d,III}} &\approx (5.57/0.25)^2 \cdot 0.137\,\mathrm{s^{-1}} = 7.5 \cdot 10^3\,\mathrm{s^{-1}}. \end{aligned} \tag{9.34}$$

Other hydrocarbons Besides the dissociation products of acetylene and acetylene itself also longer hydrocarbons can be found in the mass spectra, see appendix A. The general trend for all of them is, that during phase I the intensity is higher than during phase III. This is similar to acetylene but also to the two above described radicals C and CH_2.
Therefore, a general conclusion may be, that during phase III the losses are stronger but the sources smaller compared to phase I. This is not surprising, when considering, that the source are smaller radicals, which do decrease in density during phase III (see above). Furthermore, the losses are expected to increase also for the bigger radicals due to capturing on the nanodust. What's more, the radicals may be dissociated in the nanodusty plasma from electron impact at elevated electron temperatures, further contributing to increased losses during phase III.

Molecular hydrogen On the contrary to the hydrocarbons molecular hydrogen evolves completely different. This is depicted in the appendix, but shall be portrayed again at this place for convenience, see figure 9.19. The H_2-behaviour is interesting and a qualitative possible explanation shall be given here.
Molecular hydrogen is not directly produced in the chamber. At low pressure, it mainly originates from reactions at surfaces through recombination of atomic hydrogen. So, a low concentration during phase I compared to the end of phase II can have three reasons:

1. a low atomic hydrogen concentration

2. a low surface area providing recombination sites

molecule	$\sigma/[\text{Å}]$	$\epsilon/k_{\mathrm{B}}[K]$	reference
C	3.55	37.2	[269]
$CH_2 \approx CH_4$	3.78	154	[267]
Ar	3.54	93.3	[175]

Table 9.3: Lennard-Jones parameters for argon, C and CH_2 from literature;

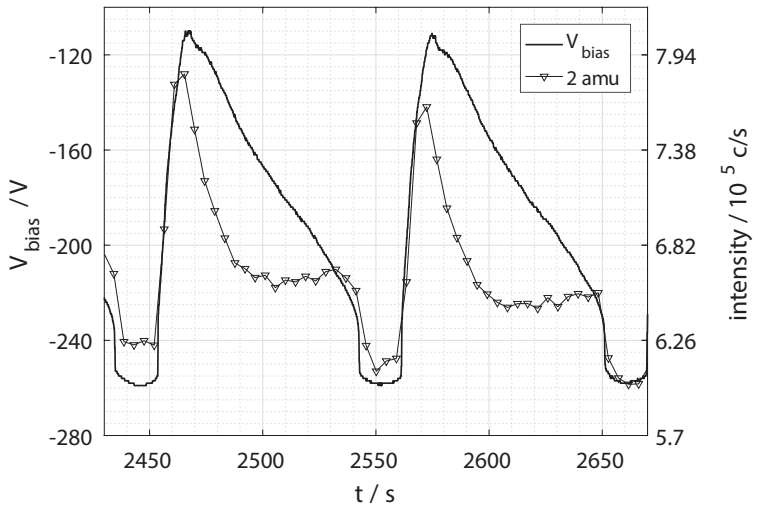

Figure 9.19: The intensity of molecular hydrogen in the RGA mode evolves different to all other species. It has a minimum during phase I and the maximum at the end of phase II.

3. a high dissociation of molecular hydrogen.

The latter is improbable, the opposite is expected, because the electron temperature is lower during this phase, also resulting in a lower dissociation of acetylene. The first argument is difficult to prove, because the measurement of atomic hydrogen is not very reliable with the Hiden PSM003. Hence, it can not be excluded as explanation. However, the measurement of atomic hydrogen, see figure A.1(a), suggests something else. It does follow the general trend, like hydrocarbons, and hence, does not provide the minimum during phase I.
Therefore, the second argument seems to be the best fitting one. It means, that the molecular hydrogen density is strongly related to the provided surface area. During phase I, where there are no dust particles in the volume, the surface area is determined by the reactor walls and the electrode. During phase II and III, however, the nanodust contributes to the overall surface area. Recombination can also occur on the dust particles.
Thus, from this consideration it may be concluded, that the overall surface area of the dust is the biggest at the end of phase II, which coincides with the highest impact of the nanodust on the discharge characteristics, as seen from the self-bias voltage. Then, during phase III it first decreases but stays stable on a lower level from the middle of phase III towards the end of the growth cycle.
This would mean, that the dust density follows

$$\begin{aligned} & n_\mathrm{d} A_\mathrm{d} = n_\mathrm{d} \cdot 4\pi r_\mathrm{d}^2 = \text{const} \\ & \Rightarrow n_\mathrm{d} \propto r_\mathrm{d}^{-2} \end{aligned} \tag{9.35}$$

in the last half of phase III. This is contradictory to the results in chapter 6, where from the scattering signal it was found, that $n_\mathrm{d} \propto r_\mathrm{d}^{-5}$. However, the LLS-signal is relatively noisy and, therefore, may be little conclusive.

Summary Summarizing this section, it was demonstrated, that all of the reactive molecules experience strong density fluctuations as a function of the nanodust presence and size. Most of them are denser during phase I of the growth cycle than during phases II and III. As quantified for acetylene, this is probably related to an elevated dissociation reaction constant during the last two growth phases. It is expected to be caused by an increase in the electron temperature.
For acetylene the increase of the dissociation reaction constant K_{diss} from phase I to III was calculated from a simple 1D-model, introduced in chapter 3. Several assumptions need to be made in order to apply it to the real discharge, among which are a homogeneously distributed precursor source and a homogeneous plasma density and temperature in the entire reactor volume. Further more, the 1D-approach may work fine in a parallel plate reactor, where the symmetry can be reduced to 1D, but in this work the reactor is highly asymmetric, so that the approach is not exact. However, in order to get a feeling for the fundamental physical processes, it may be sufficient. By the help of basic diffusion equations and the electron density from the Langmuir probe measurements it was then determined, that the specific dissociation reaction constant increases by a factor of ≈ 67 with the presence of dust particles in phase III.
As next, the radicals C and CH_2 have clearly been identified to originate from the plasma but not from the dissociation of acetylene inside the mass spectrometer. Additionally, from their evolution it is possible to roughly estimate their volume specific losses $K_{\mathrm{loss}} n_{\mathrm{d}}$ onto the dust particle surface by the use of the above determined dissociation constant K_{diss} and basic diffusion equations. The losses have been quantified to be

$$\begin{aligned} K^{\mathrm{C}}_{\mathrm{loss,III}} n_{\mathrm{d,III}} &\approx (6.74/0.25)^2 \cdot 0.183\,\mathrm{s}^{-1} = 11.0 \cdot 10^3\,\mathrm{s}^{-1} \\ K^{\mathrm{CH2}}_{\mathrm{loss,III}} n_{\mathrm{d,III}} &\approx (5.57/0.25)^2 \cdot 0.137\,\mathrm{s}^{-1} = 7.5 \cdot 10^3\,\mathrm{s}^{-1} \end{aligned} \tag{9.36}$$

at round about the middle of phase III. The reason why these two radicals can be produced in the plasma but only to very little quantity in the mass spectrometer is, that they originate mainly from the dissociative recombination of acetylene (see table 3.1), which occurs in the discharge but not in the mass spectrometer. However, it may actually be the product of dissociation of the vinylidine ion, see 3.50, which has the same mass but another structure than acetylene. The presence of the vinylidine ion is an indicator of charge exchange collisions between argon ions and acetylene [168].
The evolution of molecular hydrogen differs significantly from the other chemical species. It was concluded, that the density of hydrogen is strongly influenced by its production reactions, which mainly occur at solid surfaces. Because the nanoparticles provide an additional surface in the discharge volume, the hydrogen content increases with their presence, whereas most of the other chemicals decrease in concentration during this period.

9.4.4 Evolution of ions

As already described in section 9.3 the ion energy varies during particle growth. Hence, in order to perform a mass scan in the +ionSIMS-mode, each time an energy scan has to be done in advance. This way the correct ion energy can be adjusted for a maximum transmittance

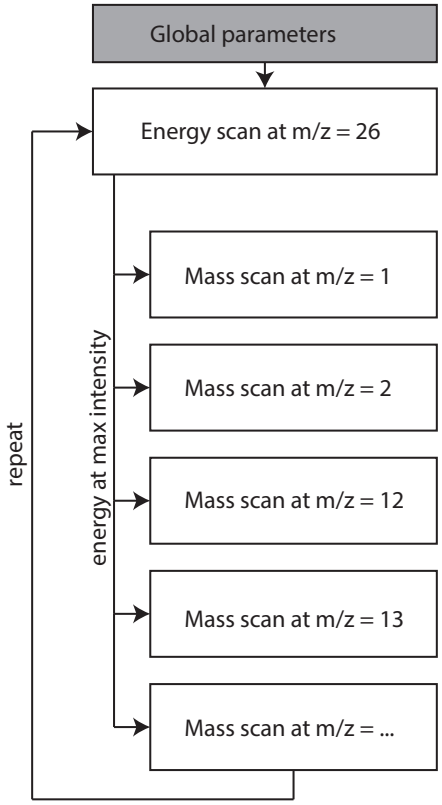

Figure 9.20: In order to adjust the ion energy parameter of the mass spectrometer to the varying plasma potential the ion energy is measured before each data point of each mass scan.

through the Bessel box. It is realized in an automatic measurement loop, schematically depicted in figure 9.20. This way it is ensured, that the measured intensity is the maximum possible intensity of each mass at any given time during the growth cycles. The evolution of these intensities is presented in the following section.
First of all, the evolution of the argon ion intensity is shown in figure 9.21(a), again plotted in the appendix B.5(c). Whereas the intensity seems to increase constantly during phase III, it experiences a sharp decrease at the beginning of growth phase II. It is the highest at the end of phase III and seems to run into an intermediate equilibrium during phase I.
The argon ion intensity is mainly a function of their density at the sheath edge $n_{\mathrm{i,s}}$ and the bohm velocity:

$$\Gamma_{\mathrm{i}} = n_{\mathrm{i,s}} v_{\mathrm{B}} = n_{\mathrm{i,s}} \sqrt{\frac{k_{\mathrm{B}} T_{\mathrm{e}}}{m_{\mathrm{i}}}} \propto n_{\mathrm{i}} T_{\mathrm{e}}^{1/2} \tag{9.37}$$

Hence, in a plasma with changing electron temperature the measured ion flux is not only proportional to the ion density at the sheath edge, which complicates the interpretation. However, the dependence on the electron temperature is weaker than on the ion density.
The ion density at the sheath edge on the other hand is a result of the ambipolar diffusion of electrons and ions from the discharge center towards it. The flux Γ_{i} of ions at any point

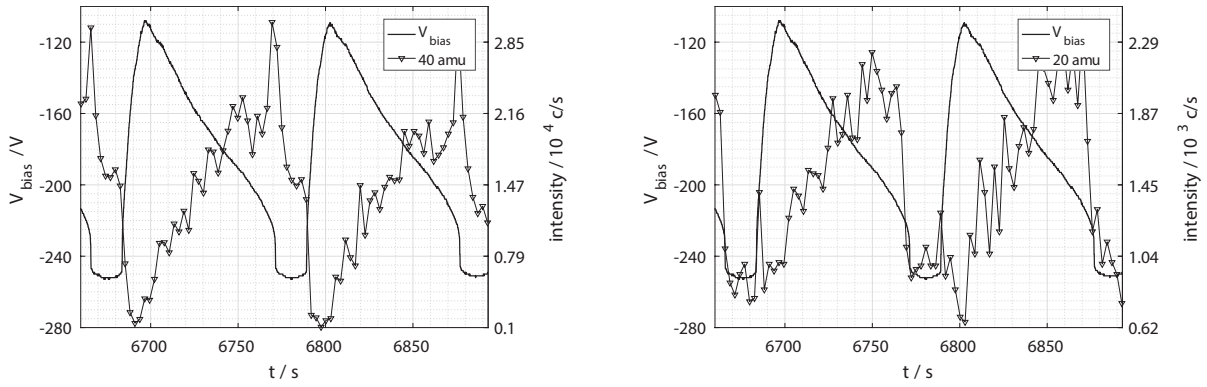

Figure 9.21: The intensity of Ar^+, see 9.21(a), varies during the growth cycles. With a constant neutral density it is a direct result of a change in the ionization and ion loss rate. The concentration of double charged argon at $m/z = 20\,\mathrm{amu}$ evolves similarly, see 9.21(b).

in the discharge, therefore, depends on the density gradient $\partial n_\mathrm{i}/\partial x$ of the ion species and on their mobility μ_i in the electric field E [90]:

$$\Gamma_\mathrm{i} = n_\mathrm{i}\mu_\mathrm{i}E - D_\mathrm{i}\frac{\partial n_\mathrm{i}}{\partial x}, \tag{9.38}$$

where the mobility is given as a function of the collision frequency with neutrals $\nu_{\mathrm{m,i}}$:

$$\mu_\mathrm{i} = \frac{e}{m_\mathrm{i}\nu_{\mathrm{m,i}}}. \tag{9.39}$$

D_i is the diffusion coefficient of the ions in a neutral background gas.
These equations can become very complicated, when considering complex geometries, several ion species and a mixture of neutral gas. Last but not least the nanodust has a strong impact of unknown kind on all these parameters. Hence, the ion density profile $n_\mathrm{i}(x)$ (in one dimension) shall be left open in this manuscript. That is why the measured intensities, shall simply be considered to represent roughly the amount of ions in the discharge instead of reflecting deeply on the spatial distribution of these ions.
Hence, the argon ion density in the entire discharge volume shall be assumed to vary roughly according to figure 9.21(a). Considering a much enhanced dissociation reaction constant during phase III it is surprising, that the ion density decreases with the onset of dust presence at the beginning of phase II. The ionization rate is actually expected to increase due to a hotter electron population like for the dissociation of acetylene. However, the opposite is observed. Thus, it can be concluded, that the losses of ions must increase even more. The change of ion losses on their way towards the mass spectrometer must be related to the losses on particles.
Interestingly, the balance of loss rate and ionization rate is in favour of the losses in the beginning of phase III, but, since the intensity overcomes the one during phase I, it is in favour

of the ionization at the end of phase III. So, the losses are dominating the ion population for small particle sizes, but for big dust sizes the ionization increase overtakes the loss processes. Usually one would expect the opposite: Big particles have a big surface, that is introduced in the plasma and may serve as recombination sites for argon ions, that are attracted onto it. Additionally, ions attracted to very small particles may describe an orbital motion, that let's them escape from the attractive potential.
Therefore, the growing Ar^+ intensity should be an indicator for a reduction in the dust density n_d. This way the overall impact of particles can decrease, although the average particle size is growing throughout phase III.
Because the formation of double charged ions Ar^{++} requires a high energy of $E_{ion}^{ArII} = 27.63\,eV$ it somehow represents the quantity of high energetic electrons in the discharge. As can be seen in figure 9.21(b), it evolves very similar to the simple argon ion intensity in figure 9.21(a) with its ionization energy of $E_{ion}^{ArI} = 15.76\,eV$. The relative intensity change during the growth cycle is smaller though, with factor of $\alpha_{Ar^{++}} \approx 3$ between the minimum and maximum for the double charged argon and a factor of $\alpha_{Ar^+} \approx 29$ for the single charged argon ion.
Provided, that all single and double charged ions are created through electron impact ionization, the amount of available electrons for such an event is given by

$$n_e^{E>E_{ion}^{ArI,II}} = n_e \int_{E_{ion}^{ArI,II}}^{\infty} f_E(E)\mathrm{d}E, \tag{9.40}$$

with $f_E(E)$ being the electron energy distribution function (EEDF) and $n_e^{E>E_{ion}^{ArI,II}}$ the amount of electrons with sufficient energy for ionization processes. For simplicity the EEDF shall be assumed to be Maxwellian:

$$f_E(E) = 2\sqrt{\frac{E}{\pi}}\left(\frac{1}{k_B T_e}\right)^{3/2} \exp\left(-\frac{E}{k_B T_e}\right). \tag{9.41}$$

Then, the integral in 9.40 becomes:

$$n_e^{E>E_{ion}^{ArI,II}} = n_e \left[\mathrm{erf}\left(\sqrt{\frac{E}{k_B T_e}}\right) - \frac{2}{\sqrt{\pi}}\sqrt{\frac{E}{k_B T_e}} \exp\left(-\frac{E}{k_B T_e}\right)\right]_{E_{ion}^{ArI,II}}^{\infty}. \tag{9.42}$$

Assuming, that the ionization energies are sufficiently large, meaning $E_{ion}^{ArI,II}/k_B T_e \gg 1$, the error function cancels out by taking the value 1. Hence, respecting the right hand side of the brackets going to zero for $E \to \infty$, the formula shrinks to

$$n_e^{E>E_{ion}^{ArI,II}} = n_e \frac{2}{\sqrt{\pi}}\sqrt{\frac{E_{ion}^{ArI,II}}{k_B T_e}} \exp\left(-\frac{E_{ion}^{ArI,II}}{k_B T_e}\right). \tag{9.43}$$

Therefore, the above mentioned intensity variation throughout one growth cycle, can be expressed via equation 9.43, using $\Gamma_{Ar^+} \propto n_{Ar^+}\sqrt{k_B T_e} \propto n_e^{E>E_{ion}^{ArI,II}}\sqrt{k_B T_e}$ with Γ_{Ar^+} being

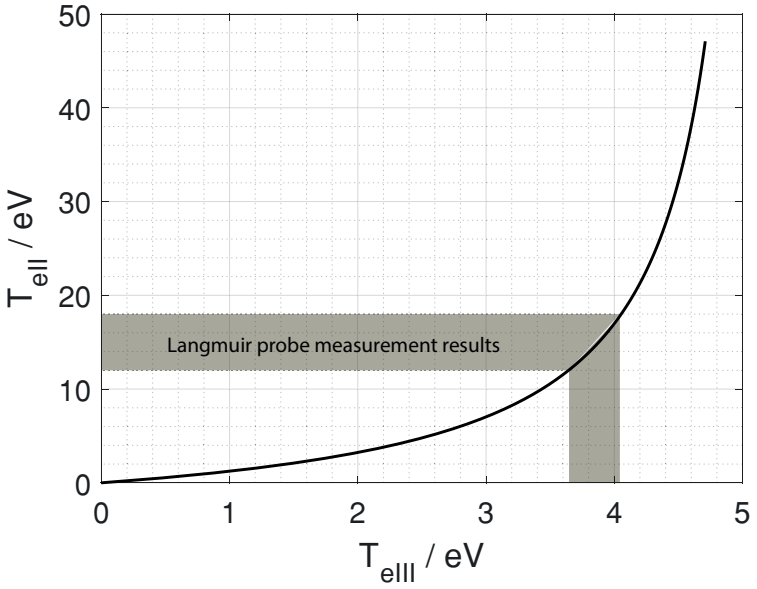

Figure 9.22: The relation between the electron temperature at the end of phase II $T_{\mathrm{e,II}}$ and at the end of phase III $T_{\mathrm{e,III}}$ can be calculated from the argon ion flux intensities into the mass spectrometer. Additionally, the Langmuir probe results are correlated to it, marked through the grey regions.

the ion flux into the mass spectrometer:

$$\begin{aligned} \alpha_{\mathrm{Ar^+}} &= \frac{\Gamma_{\mathrm{Ar^+,III}}}{\Gamma_{\mathrm{Ar^+,II}}} = \frac{n_{\mathrm{e,III}}}{n_{\mathrm{e,II}}} \exp\left(-E_{\mathrm{ion}}^{\mathrm{ArI}}\left(\frac{1}{k_{\mathrm{B}}T_{\mathrm{e,III}}} - \frac{1}{k_{\mathrm{B}}T_{\mathrm{e,II}}}\right)\right) \\ \alpha_{\mathrm{Ar^{++}}} &= \frac{\Gamma_{\mathrm{Ar^{++},III}}}{\Gamma_{\mathrm{Ar^{++},II}}} = \frac{n_{\mathrm{e,III}}}{n_{\mathrm{e,II}}} \exp\left(-E_{\mathrm{ion}}^{\mathrm{ArII}}\left(\frac{1}{k_{\mathrm{B}}T_{\mathrm{e,III}}} - \frac{1}{k_{\mathrm{B}}T_{\mathrm{e,II}}}\right)\right) \end{aligned} \tag{9.44}$$

With the ratio of the two factors $\alpha_{\mathrm{Ar^+}}$ and $\alpha_{\mathrm{Ar^{++}}}$ one can now eliminate the electron density from the equations, so that

$$\frac{\alpha_{\mathrm{Ar^+}}}{\alpha_{\mathrm{Ar^{++}}}} = \frac{\Gamma_{\mathrm{Ar^+,III}}}{\Gamma_{\mathrm{Ar^+,II}}} = \exp\left(\left(E_{\mathrm{ion}}^{\mathrm{ArII}} - E_{\mathrm{ion}}^{\mathrm{ArI}}\right) \cdot \left(\frac{1}{k_{\mathrm{B}}T_{\mathrm{e,III}}} - \frac{1}{k_{\mathrm{B}}T_{\mathrm{e,II}}}\right)\right), \tag{9.45}$$

The reader may note, that no assumptions on the mass dependency of the ion transmission in the spectrometer needs to be made here. And so it can be obtained:

$$\begin{aligned} \frac{1}{k_{\mathrm{B}}T_{\mathrm{e,III}}} - \frac{1}{k_{\mathrm{B}}T_{\mathrm{e,II}}} &= \ln\left(\frac{\alpha_{\mathrm{Ar^+}}}{\alpha_{\mathrm{Ar^{++}}}}\right)\frac{1}{E_{\mathrm{ion}}^{\mathrm{ArII}} - E_{\mathrm{ion}}^{\mathrm{ArI}}} \approx \frac{0.191}{[\mathrm{eV}]} \\ \Rightarrow \qquad \frac{k_{\mathrm{B}}T_{\mathrm{e,II}}}{[\mathrm{eV}]} &= 5.23\left(\frac{T_{\mathrm{e,II}}}{T_{\mathrm{e,III}}} - 1\right). \end{aligned} \tag{9.46}$$

One main result of equation 9.46 is, that $T_{\mathrm{e,II}} > T_{\mathrm{e,III}}$ in all cases. This is an interesting observation, because it is hard to verify by other methods in nano-dusty plasmas.

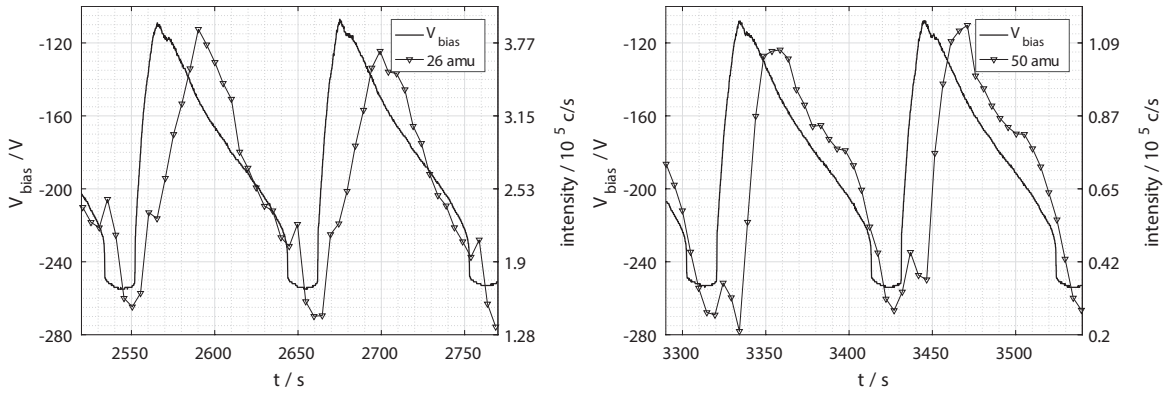

(a) (b)

Figure 9.23: The acetylene ion flux 9.23(a) evolves together with the $C_4H_2^+$ flux. Both ions are part of the chain reaction 3.51. Contrarily to the argon ion flux, the reactive ions decrease in intensity towards the end of phase III.

Furthermore, using this equation, possible values for $T_{e,II}$ and $T_{e,III}$ can be plotted against each other, as done in figure 9.22, as their relation is fixed. This may be compared to the measurement results of the Langmuir probe (see chapter 7.4). The obtained value range for those is marked in grey in figure 9.22. It shows, that both measurements can be brought to an agreement, which is a further validation of the here used methods. However, the precision of the electron temperature measurement remains low. The performed calculations are very basic with the main assumptions of a maxwellian electron energy distribution and electron impact ionization as the dominant ionization process. Furthermore, the ion losses need to be assumed to be constant throughout phase III in order perform above calculations, which may not be true.
The electron density can not be found self-consistently from these calculations. Nevertheless, its variation has a high impact on the discharge properties. This becomes obvious by the fact, that $T_{e,II} > T_{e,III}$, but the measured ion flux $\Gamma_{Ar^+,II} < \Gamma_{Ar^+,III}$. This means, that the high ion flux needs to be sustained by higher ionization rates during the end of phase III or much lower losses. Whereas the first would indicate a higher electron density, the latter would imply a drastic change in the loss mechanisms. Both may be the case, assuming, that the dust influence in front of the mass spectrometer head decreases throughout phase III. Therefore, less ions may be lost onto the nanoparticles, as there are less losses of electrons on the dust. Hence, the electron density could recover and in turn lead to a higher ionization rate even though the electron temperature decreases towards the end of phase III.
As next, the evolution of the acetylene ion flux is shown in figure 9.23(a) together with the signal at $m/z = 50\,\text{amu}$ 9.23(b), which can be attributed to $C_4H_2^+$. Both ions are part of the ionic polymerization reaction 3.51. Therefore, the bigger molecules depend on the presence of the smaller ones and, thus, evolve similarly. Contrarily to the argon ion flux, the reactive ions decrease in intensity towards the end of phase III and have their maximum somewhere in the middle of phase III.

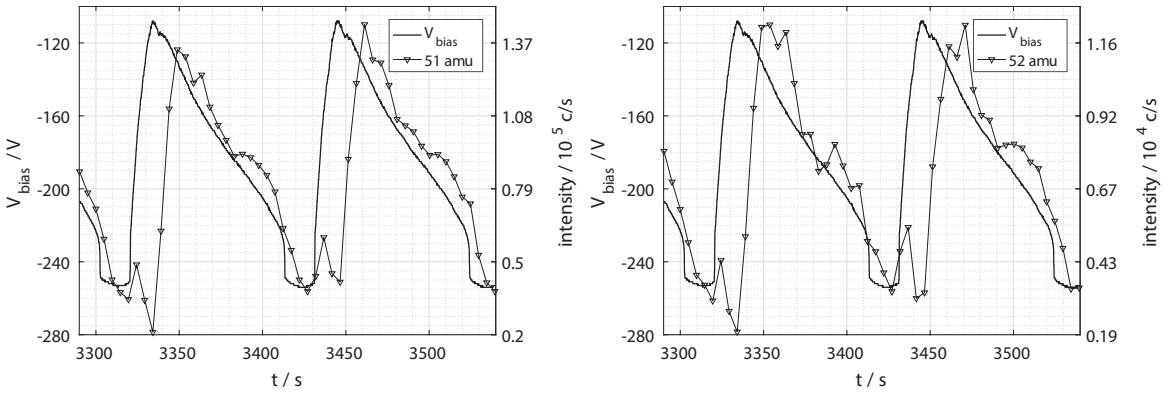

(a) (b)

Figure 9.24: The ions $m/z = 51$ amu 9.24(a) and $m/z = 52$ amu 9.24(b) evolve are products of the polymerization reaction 3.51 and, hence, evolve like the basic monomer $C_2H_2^+$.

Since the ions $C_4H_3^+$ and $C_4H_4^+$ are further products of the same chain reaction, they are expected to evolve the same way, which indeed is the case as shown in figure 9.24. The same can be found for $C_6H_2^+$, $C_6H_3^+$ and $C_6H_4^+$, as depicted in the appendix B.8 at masses 74, 75 and 76 amu.
However, a general trend can be observed. The longer the molecule becomes, meaning the greater n in $C_{2n}H_2^+$, the stronger is the difference between the minimum at the end of phase II and the maximum signal during phase III. Being 1.7 for $C_2H_2^+$ it becomes 2.9, 3.2, 4.0 and 26.7, 26.5, 34.8 for $C_4H_2^+$, $C_4H_3^+$, $C_4H_4^+$ and $C_6H_2^+$, $C_6H_3^+$, $C_6H_4^+$, respectively.
One explanation might be, that the consumption of the shorter ions is high during phase II due to the presence of dust particles. At the same time the plasma almost shuts down due to the loss of electrons. Therefore, only a little quantity of ions is left, making collisions between them less probable. Hence, the chain reaction 3.51 can not take place and the decrease in the production of heavier ions is even amplified. When the plasma recovers, but dust particles are still present (during phase III), the bigger ions can be produced thanks to a recovered light ion population. The high intensity of heavy ions may be a result of their low mobility μ_i, see equation 9.39. Hence, they can accumulate better in the discharge.
At last another class of ions shall be presented, which evolves different to the argon ions and also different to the right above discussed species. This class of ions exhibits a maximum flux during phase I in contrary to all other species as exemplarily shown in figure 9.25. While the peaks at mass to charge ratios m/z of 43, 53, 59, 77 and 78 amu show this behaviour very distinctively, there can be found some masses that don't have the absolute maximum in phase I, but show the same tendency to some degree. This concerns the masses 44, 45, and 55, that have a small local maximum during phase I. For the presentation of these masses the reader may refer to the appendix B.
The distinct evolution of the above named ions reflects the fact, that these do not take part in the same sort of chain reactions. The question is, however, if they are involved in a separate chain of polymerization reactions. The mass difference between the main peaks 43,

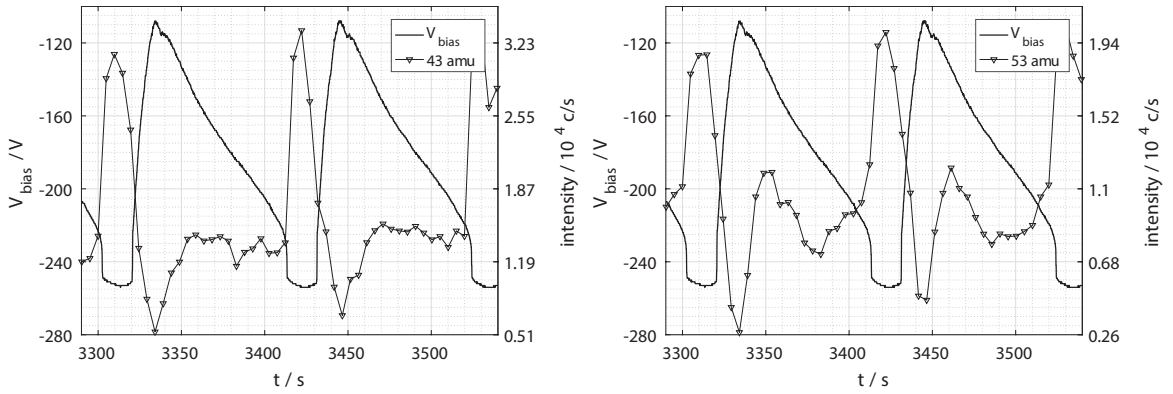

(a) (b)

Figure 9.25: The ions $m/z = 51\,\text{amu}$ 9.25(a) and $m/z = 52\,\text{amu}$ 9.25(b) evolve are products of the polymerization reaction 3.51 and, hence, evolve like the basic monomer $C_2H_2^+$.

53, 59, 77 and 78 is not regular, though. Therefore, no subsequent monomer addition can be concluded for these species.
Two points are conspicuous, firstly almost all of above ions are of odd mass to charge ratio and secondly, except for 43 they appear at 1 amu higher than a group of peaks of relatively high intensities. Considering the first point, it may indicate the presence of nitrogen in those ions, as nitrogen is always present as an impurity. The second observation could indicate a reaction of the form

$$C_xH_y + H^+ \rightarrow C_xH_{y+1}^+, \tag{9.47}$$

or

$$C_xH_y^+ + H \rightarrow C_xH_{y+1}^+, \tag{9.48}$$

in order to produce those species. However, especially mass 59 does not fit into this scheme, because it is exactly between the biggest possible hydrocarbon with 4 C-atoms, C_4H_{10}, and the smallest possible hydrocarbon with 5 C-atoms, C_5.
Anyhow, the evolution means, that the loss to production ratio of them is higher with the presence of dust than without, which is kind of inverse to the ions from reaction 3.51. For the moment the species related to those peaks remain unclear, but certainly interesting.
Summarizing ion evolution measurements, the main reaction paths towards nanoparticle formation via positive ions 3.51 has been confirmed. It seems, that these ions are most present are consumed drastically with the onset of phase II, but recover fast and remain on a high level throughout phase III. During phase I, however, these ions are of medium concentration. The argon ions represent the plasma intensity in terms of electron density and temperature. The evolution of Ar^+ indicates an almost extinguishing plasma during phase II, but an increase to more than the initial value towards the end of phase III with a maximum of the measured argon ion flux right before the end of phase III.
A third ion population has been found. It is mainly of odd mass to charge ratio and exhibits the strongest flux into the mass spectrometer during phase I. Therefore, its loss and produc-

tion channels must be completely different to those of the argon ions and also to those of the $C_{2n}H^+_{2...4}$ ions. The identification of the ion species remains unclear, although the odd masses indicate possible nitrogen content in those molecules.
Finally, it shall be mentioned, that the measurement of ion intensities remains a local measurement, which does not necessarily represent the center of the discharge. Hence, the time evolution in the center may differ to the measured one, especially if the dust density in front of the mass spectrometer measurement is not the same.

Chapter 10

Deposition rate measurements

Deposition rate measurements are a fundamental part of any deposition or etching process analysis. The thinner the films are, the more difficult it can become. Common instruments to analyse thin films are profilometer measurements, electron microscopy, ellipsometry and quartz crystal microbalances (QCM). The latter is the cheapest of above named methods and under certain conditions also the most precise one with resolutions down to atom monolayers. Additionally, it allows easily to retrieve in-situ data with a high time resolution.
Therefore, it has been applied to this experiment, too. Quartz crystals have first been described as balancing tool by Sauerbrey in 1959 [270], who investigated their use during his PhD studies. Their principle bases on a frequency shift of a vibrating piezo-quartz crystal after the formation of a thin film on its surface. In first order the deposited mass Δm is measured, from which the film thickness can be calculated. Sauerbrey already worked out an approximative mathematical description, which is used until today, the Sauerbrey equation:

$$\Delta f = -\frac{2f_0^2}{A\sqrt{\rho_q \mu_q}} \cdot \Delta m. \tag{10.1}$$

Hence, the shift Δf of the eigenfrequency f_0 is directly proportional to the deposited mass Δm per crystal area A. The units ρ_q and μ_q denote the mass density and shear modulus of the quartz, respectively. By assuming a density ρ_f for the deposited material, the thickness d can be calculated according to

$$\Delta f = -\frac{2f_0^2\rho_f}{\sqrt{\rho_q \mu_q}} \cdot d \tag{10.2}$$

In most instruments the thin films are assumed to have a clean surface. However, a rough surface makes the conversion of mass into thickness non-trivial. For this purpose the viscoelastic properties of the film can be measured by the damping of the crystal. However, this has not been done in this study. Hence, the measured thickness can be regarded as an average measure. If nanoparticles are deposited on the surface, the roughness is high, so that the interpretation of thickness does not correspond directly to the height of the particle film.
Besides, the material density is completely unknown for the here produced hydrocarbon film

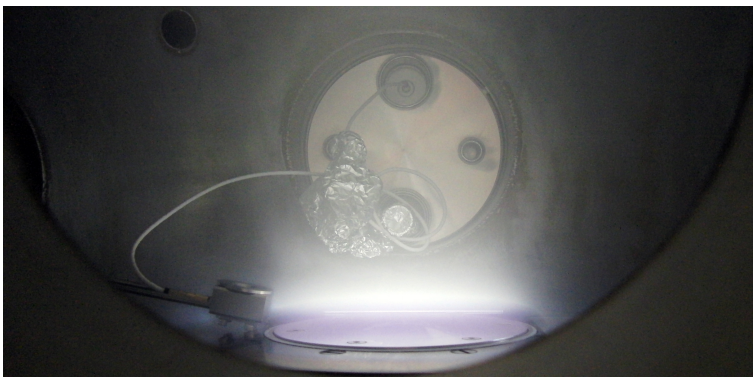

Figure 10.1: The quartz crystal micro-balance was positioned at the bottom next to the powered electrode. It measures a frequency shift as a function of deposited mass on top of the crystal.

and nanoparticles. Hence, for simplicity it has been set to $\rho_f = 1\,\mathrm{g/cm^3}$ in the here presented data. The other constants are crystal dependent and set by the manufacturer. What also needs to be taken care of is to keep the thickness of the deposited material on the crystal small. If the film becomes too thick, its viscoelastic properties need to be considered for correct frequency shift calculations. That is why the quartz crystal needs to be cleaned with an oxygen plasma from time to time.
The used setup is shown in the photograph 10.1. The QCM was placed as low as possible next to the powered electrode. It is fixed by two stainless steel tubes, that can serve as water cooling for processes with a high heat load on the crystal. However, during these measurements it was not necessary to actively cool the crystal thanks to the low plasma power of 9 W.
The quartz crystal surface is directed upward. Hence, not only the thin film deposition by radicals and ions is supposed to be measured but also nanoparticles can be collected and measured with the crystal. Thus, both, molecules and nanoparticles are always measured simultaneously and their contributions can not be distinguished.
The signal was retrieved from the controller box by the help of its analog output. The analog signal was detected by a digital multimeter with a connection to the computer for in-situ recording of the signal evolution. This way the time resolution of the deposition rate measurement was 1 Hz and can easily be correlated to the self-bias voltage, as already done with the other measurements in previous chapters.
The obtained measurement is shown in figure 10.2 together with several linear curves, that have been fitted to the deposition thickness d_f. Their slope $\Delta \mathrm{d_f}/\mathrm{d}t$ yields the deposition rate in nm/s at the corresponding times. The results of the fits are summarized in table 10.1.
As can be seen, the deposition rate is the highest with 0.086 nm/s at the transition from phase III to I and during the first half of phase III. The first is not surprising as the transition is linked to the falling out of the nanoparticles and the void explosion. Hence, a high nanoparticle deposition rate may be expected here. The latter is less trivial.
During the second half of phase I and the first moments in phase II the deposition rate

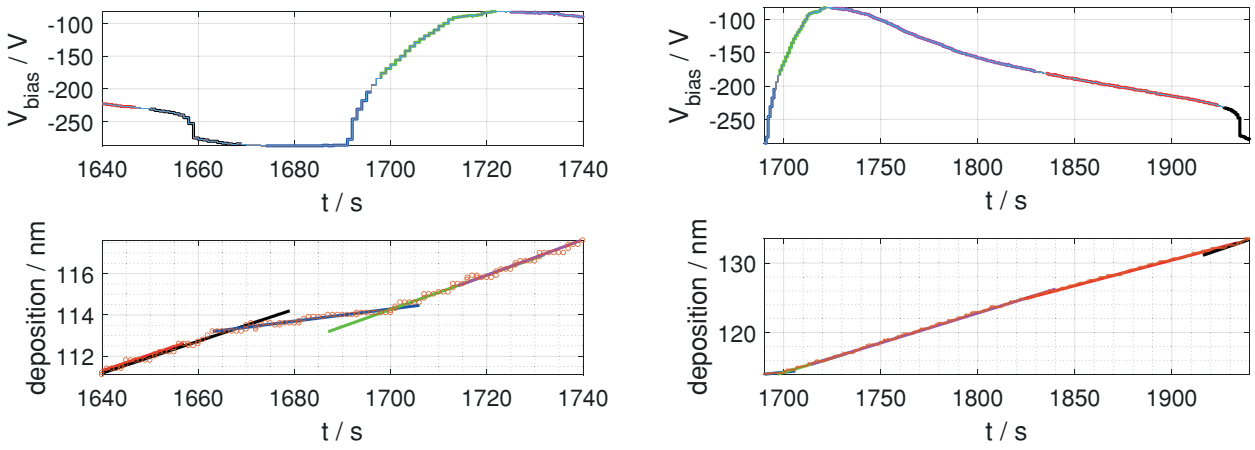

(a) (b)

Figure 10.2: The deposition rate is lower during the end of phase I and the beginning of phase II, here fitted with the blue line in 10.2(a). The fit region is equally plotted in the corresponding self-bias voltage curve. During the rest of the cycle the deposition rate stays almost perfectly constant 10.2(b), as several linear fits prove (green, purple, red and black).

then reaches a significantly lower value of 0.030 nm/s. This comes as a surprise, because this is the time, when the neutral flux into the mass spectrometer is the highest. Hence, measured rate does not correlate with the neutral flux. It may still be, though, that only a small fraction of the neutrals is effectively contributing to a thin film deposition on the quartz crystal. Another possibility might be, that the deposition is strongly dominated by the deposition of nanoparticles.
If nanoparticles are the main contributor to the thin film on top of the quartz, it would mean, that during this time almost no particles leave the plasma, or that they are so small but not of sufficient quantity, that the deposition rate remains low.
This changes abruptly during phase II, where suddenly the deposition rate goes up to 0.083 nm/s. It then stays almost stable until the transition between phases III and I again occurs. During the end of phase III it decreases slightly to 0.076 nm/s, though.
It is worth mentioning, that the flux of the positive ions involved in the polymerization reac-

fit colour	growth phase	slope / nm/s
red	end of III	0.076
black	transition from III to I	0.086
blue	end of I and beginning of II	0.030
green	end of II	0.083
purple	beginning III	0.086

Table 10.1: Obtained deposition rates during different point of times of the growth cycle by linear fitting.

tion 3.51 has a similar characteristics as the measured deposition rate. It remains low until somewhere in phase II and has its maximum in the first half of phase III, see figures 9.23. Therefore it might also be considered, that the ions play an important role in the deposition of thin films by either direct deposition or ion assisted thin film deposition. The high rate at the transition from phase III to I can still be due to nanoparticle deposition.
What could also make the impression of a correlation between the ion flux and thin film deposition is the fact, that both can have the same origin, which would be a higher electron temperature. This would lead to a high dissociation rate and the enhanced formation of radicals, that then stick to the surface. It somehow remains difficult to match with the mass spectrometric results, which show a strong decrease of all masses during phase II and III and is not much more than another technique to measure flow rates to a surface.
A judicious experiment in order to distinguish between the contributions from ions, neutral radicals and nanoparticles would be to place the QCM at different places in the chamber and with different orientations, e.g. upward and downward directed. This, however, remains a task for the future.
Nevertheless, in the following the particle flux density through the sheath can be calculated under the assumption, that 100 % of the deposited material of thickness d_f is made up of nanoparticles, in other words neglecting completely the contributions to film growth from neutral molecules and ions. The calculation may serve as an upper possible limit for the nanoparticle flux during phase III, where the dust size is more or less well known.
The deposition rate R_f must equal the total particle volume flow per time and surface area A:

$$R_\mathrm{f} = \frac{\Delta d_\mathrm{f}}{\Delta t} = \frac{\Delta V_\mathrm{f}}{A\Delta t} = \frac{\Delta N V_\mathrm{d}}{A\Delta t}. \tag{10.3}$$

Here V_f denotes the thin film volume over surface A and $\Delta N V_\mathrm{d}$ is the amount of particle volume reaching the surface A during time Δt. The dust particle number flux density Γ_d must therefore be

$$\Gamma_\mathrm{d} = \frac{\Delta N}{A\Delta t} = \frac{R_\mathrm{f}}{V_\mathrm{d}} = \frac{3R_\mathrm{f}}{4\pi r_\mathrm{d}^3}. \tag{10.4}$$

Now, using the values at the beginning and end of phase III, knowing, that the dust radius is roughly 25 and 75 nm, respectively, the following values for the particle number flux density may be calculated:

- beginning of phase III: $\Gamma_d \approx 1.3 \cdot 10^6\,\mathrm{mm^{-2}s^{-1}}$
- end of phase III: $\Gamma_d \approx 4.3 \cdot 10^4\,\mathrm{mm^{-2}s^{-1}}$

Hence, a decrease in the particle flux of a factor of 30 can be found as a result of an almost constant deposition rate at growing particle size. In other words, the overall deposited mass remains almost constant, but it reaches the surface in bigger packages.
Assuming a monolayer of closest packed nanoparticles, the projected covered area equals 90.7 % of the total surface area. Thus, on the surface area A as many dust particles as

$$N = 0.907 \cdot \frac{A}{4\pi r_\mathrm{d}^2} \tag{10.5}$$

find place in a monolayer. Using the particle number flux density of equation 10.4 it can be estimated, that a complete coverage of the surface is reached after a time T according to

$$\Gamma_\mathrm{d} = \frac{N}{AT} = \frac{0.907}{4\pi r_\mathrm{d}^2 T} \Leftrightarrow T = \frac{0.907}{\Gamma_\mathrm{d} 4\pi r_\mathrm{d}^2}. \tag{10.6}$$

Using the above obtained values for Γ_d, one finally finds:

- beginning of phase III: $T \approx 88\,\mathrm{s}$
- end of phase III: $T \approx 298\,\mathrm{s}$

These are reasonable values, as collection experiments, where the collection process may take a few seconds, usually do not show a complete coverage of the sample. The reader may keep in mind, that the values for T are the low limit estimates, as it has been assumed, that no other deposition mechanism rivals with the flux of nanoparticles towards the surface.
Also, the bias voltage of the surface plays a crucial role. If the surface is biased more positive than the plasma potential particles are actively attracted, when biased more negative they are less likely to cross the plasma sheath due to the confining plasma potential. In the latter case all possible forces, as described in chapter 2.3.3 need to be considered in order to determine the nanoparticle motion. This is a non-trivial task, because the forces depend badly known parameters like the particle charge and, additionally, the forces change during the crossing of the sheath due to variations in potential, ion velocity and density, electron density and temperature and particle charge and speed.

Chapter 11

Summary

In this thesis a dust forming capacitively coupled Ar/C_2H_2 plasma was investigated. The process parameters were kept almost fixed for all sets of experiments, that have been performed. They were chosen in such a way, that consecutive generations of nanoparticles were formed. These generations leave characteristic cyclic marks in various time resolved measurements. All of those measurements have been correlated to each other in the course of this work.
This thesis gives an inside into basic physical principles and chemical pathways, that lead to nanoparticle synthesis. Basic plasma concepts, dust charging and forces on the dust have been introduced. Further more a simple but efficient view on the concentration profiles of reactive species in the reactor chamber has been presented in order to give a simplified picture on how to interpret mass spectrometric data. One of the main questions throughout the work, was the impact of the nanoparticle presence on the discharge and vice versa.

Electrical measurements and LLS To start off, some electrical measurements were presented, which give a good impression on the repetitive growth cycles and their drastic impact on the discharge. They have been correlated to size distribution measurements of the collected dust at specific times The electrical measurements served in the following to be able to compare different measurement techniques by using the self-bias voltage as a measure of the growth process progress. Each growth cycle has been separated into three different growth phases, a first one, where the plasma is basically unaffected of the nanodust, a second, where the plasma undergoes a rapid change and a third one, during which the plasma slowly recovers to its initial conditions.
In the following laser light scattering was applied in order to evidence the generations by making the dust visible. It was found, that with this method the dust can be seen from sizes of 40 to 50 nm in diameter and upward. Therefore, the dust cloud can be studied from the end of growth phase II on. Simultaneously the plasma luminosity in the green region has been recorded. The experiment evidences an inhomogeneous dust cloud, that is brighter in the lower region towards the end of each growth cycle and also exhibits a void in the plasma centre.
From the LLS a hypothesis was developed, which is based on the observation of the dust

size distribution compared with the duration of phase I in the growth cycle. It was found a linear dependence. In the contrary for the duration of phases II and III no such dependency was found. Thus, the hypothesis states, that new dust nuclei are formed throughout phase I. It is a major statement of this thesis and refers to the question if simultaneous coagulation and nucleation can take place. Here, it was proposed, that the nucleation and coagulation indeed take place at the same time but perhaps in different regions of the discharge.
Further more, the visible dust cloud can be used to detect the plasma sheath, which is located at the dust cloud edge. Thus, the sheath thickness was evaluated for phase III, where the particles are visible, in front of the powered electrode. In combination with the self-bias voltage and the Child-Langmuir law it was used to determine the ion current density through the sheath. The ion current density was calculated to decrease during phase III.

Langmuir probe measurements After discussing the most basic Langmuir probe theory, using the OML-model, another approach to calculate the ion current was introduced. It uses the Child-Langmuir law for cylindrical geometries and the main assumption of an ion current determined by the ion flux through the sheath edge. The main challenges of applying Langmuir probes in nanodusty reactive plasmas are discussed and a solution proposed, which was realized in the subsequently described setup. It utilizes a passive RF compensating pick-up probe, a fast modulation of the probe voltage and heating by electron current as well as ion bombardment in order to keep the probe tip clean.
The results were cross checked by applying two slightly different methods to calculate the electron temperature. Both methods yield similar values, that are exceptionally high. Hence, without any further confirmation of such high electron temperatures from other experiments, the measured temperature must be interpreted cautiously. Nevertheless, the ion and electron density as well as the floating and plasma potential may be taken as reliable. They exhibit strong modulations throughout the nanodust growth cycles.
The Langmuir probe measurements are a key for the understanding of any process in the nanodusty plasma, as it can reveal the most crucial parameters, like electron temperature and density, that affect substantially the discharge behaviour, but also the potentials, that affect the dust trapping and movement. Additionally it was proposed, that the simultaneous measuring of dust plasma frequency, electron density and temperature may allow to calculate the dust charge and density. Hence, a rough approximation of these parameters has been made and a dust charge of $Q_\mathrm{d} \approx -12e$ and a dust density of $n_\mathrm{d} = 10^{14}\,\mathrm{m}^{-3}$ for the beginning of phase III has been calculated, leading to an Havnes parameter of $P \approx 73$.

Phase resolved camera imaging In order to better understand the detailed electron processes in the sheath region above the powered electrode a fast camera was installed. It allows to resolve the emission intensity as a function of time during one RF-cycle. This way emission patterns can be created by reducing each image to one intensity profile along the vertical axis and then plotting it against time. Emission patterns have been obtained for different points of time during the particle growth in the following.
A strong variation of the emission pattern throughout the nanodust growth cycle was observed. Generally, one emission region at roughly 10 to 11 mm above the powered electrode

remained constantly present without major changes during particle growth. However, a second brighter glow region closer to the electrode appears with the onset of phase II. It then approaches the electrode to a minimum distance of 5 mm at the transition between phase II and III. A comparison to the previously by LLS determined sheath edge evolution was made and found to be in good agreement, if the sheath edge is defined as the point, where the lower glow intensity decreased to e^{-1} of its maximum value.
Hence, the Child-Langmuir law could be applied to the entire growth cycle. The result shows a maximum ion current, when the self-bias is the less negative, at the transition between phase II and III. The lower glow region may strongly be related to what is called the α-γ' transition. The de-excitation in the vicinity of the powered electrode speaks for electron energy losses in this region, which may dominate the losses in the bulk plasma.

Energy resolved mass spectrometric measurements A big part of this work was dedicated to mass spectrometry. It allows to identify important molecules and ions in the plasma. Already known polymerization reactions in the gas volume were confirmed. The acetylene density was found to decrease drastically with the onset of phase II and to recover during phase I. Usually, neutral radicals are very difficult to measure, since they are masked by the dissociation of the monomer in the mass spectrometer. However, pure carbon and CH_2 have been identified to originate at least to parts from the discharge but not from the inside of the mass spectrometer. Some calculations based on diffusion theory have been performed on these two species and their diffusion constants as well as their loss rates onto the particles during phase III have been estimated.
Exhibiting a very interesting evolution, molecular hydrogen has been discussed, too. It was proposed, that the density of molecular hydrogen is influenced by the additionally provided surface of the nanodust, that increases overall recombination rate of atomic hydrogen.
The ion spectra involve a detailed study of their energies onto the grounded chamber walls. All ions seem to possess the same energy, however it varies significantly during the particle growth cycles. The ion energy represents the plasma potential close to the plasma sheath edge in front of the mass spectrometer. Curiously, the highest energy is reached at the end of phase I and the lowest during phase III. This is contradictory to the plasma potential measured by means of the Langmuir probe.
During the growth of nanoparticles not only the ion energy was found to fluctuate but also the ion flux density into the mass spectrometer. Whereas argon ions were found to be most intense at the end of phase III and lowest during phase II, the acetylene ions were measured to be of highest density in the first half of phase III. Most of the reactive ions follow the same trend, especially those connected to the well known ionic polymerization reaction $C_{2n}H_{2...4}$. Hence, generally speaking, the reactive positive ions are much more frequent in a dusty plasma than in an argon/acetylene mixture without dust.
A few ions show a distinctively different evolution. They are most intensive during phase I and have a minimum during phase II. These ions are mostly of odd mass to charge ratio. Their nature was not determined confidently but a nitrogen content is imaginable.

QCM measurements Finally, in the last chapter deposition rate measurements by the help of a quartz crystal microbalance have been presented. It can not be distinguished between the contributions of nanodust and radicals or ions to the thin film growth on top of the crystal. However, the results show, that the growth rate is high in the first half of phase III and during the transition of phase III to I. Whereas the latter may be connected to the falling out of nanodust and to the void explosion, the first is less trivial to understand. It is, however, remarkable, that it coincides with the maximum in the reactive hydrocarbon ion flux towards the grounded surfaces. One may therefore speculate, that these ions due play a crucial role in the thin film growth. Either due to a high sticking coefficient or due to opening up bonds at the surface of the substrate, their contribution to the thin film can be direct or indirect. The latter case would correspond to an ion assisted type of film growth. Under the assumption, that the measured film is solely made up of nanoparticles, e.g. the ion and radical contribution being neglected, a nanoparticle flux of 1.3 particles per μm^2 and per second was calculated for the beginning of phase III and a flux of 0.043 particles per μm^2 and per second for the end of phase III.

In this thesis it was successfully demonstrated, that the correlation of several measurements can complement each other in a beneficial way. In order to be able to do so, the experiment needs to be highly reproducible. Here, the cyclic single generation nanoparticle growth was chosen as stable and reproducible system. It has the further advantage of enabling the systematic influence of different dust sizes in one experiment.
Although the transfer of results from this work to other reactors and processes is not trivial, some of them have a general character. Mechanisms like the cyclic behaviour of nanodust forming pasmas, void formation and reaction pathways have been reported in various reactor designs and pressure ranges. Thus, this thesis may contribute to the understanding in the fundamental processes involved in reactive and in nanodust forming plasmas.

Appendix A

Appendix - Evolution of neutral species

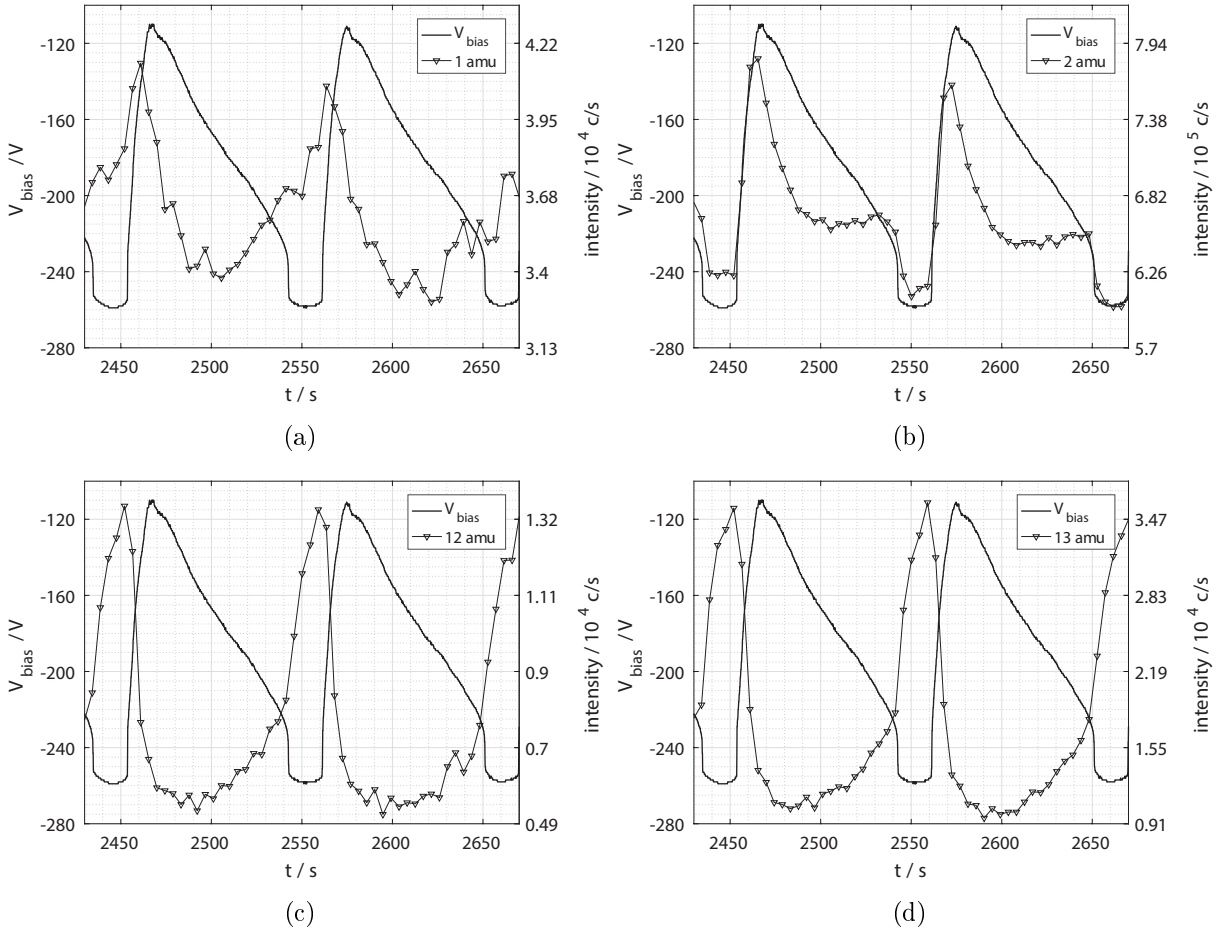

Figure A.1: Evolution of neutrals measured in RGA mode, time correlated to the self-bias voltage.

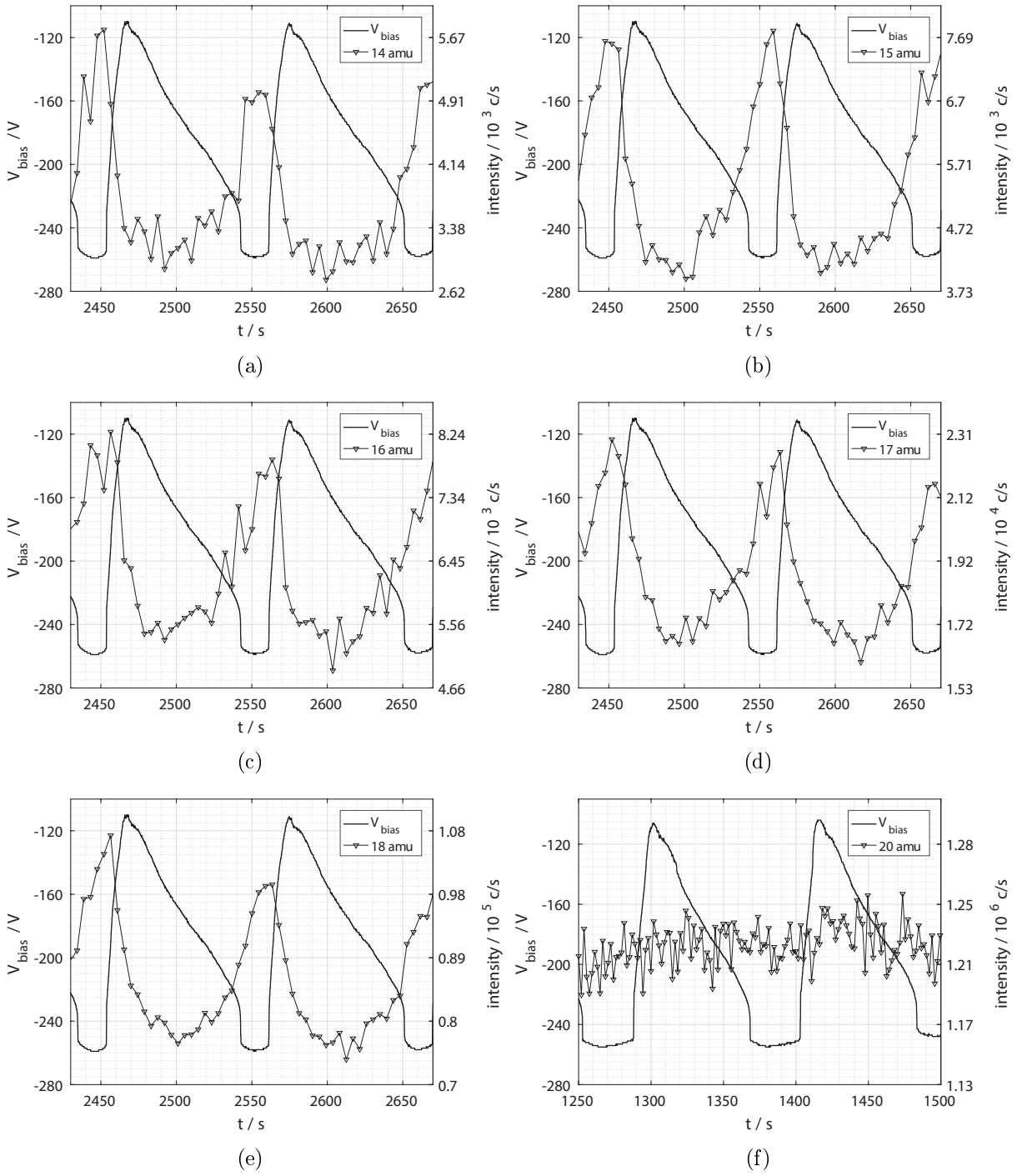

Figure A.2: Evolution of neutrals measured in RGA mode, time correlated to the self-bias voltage.

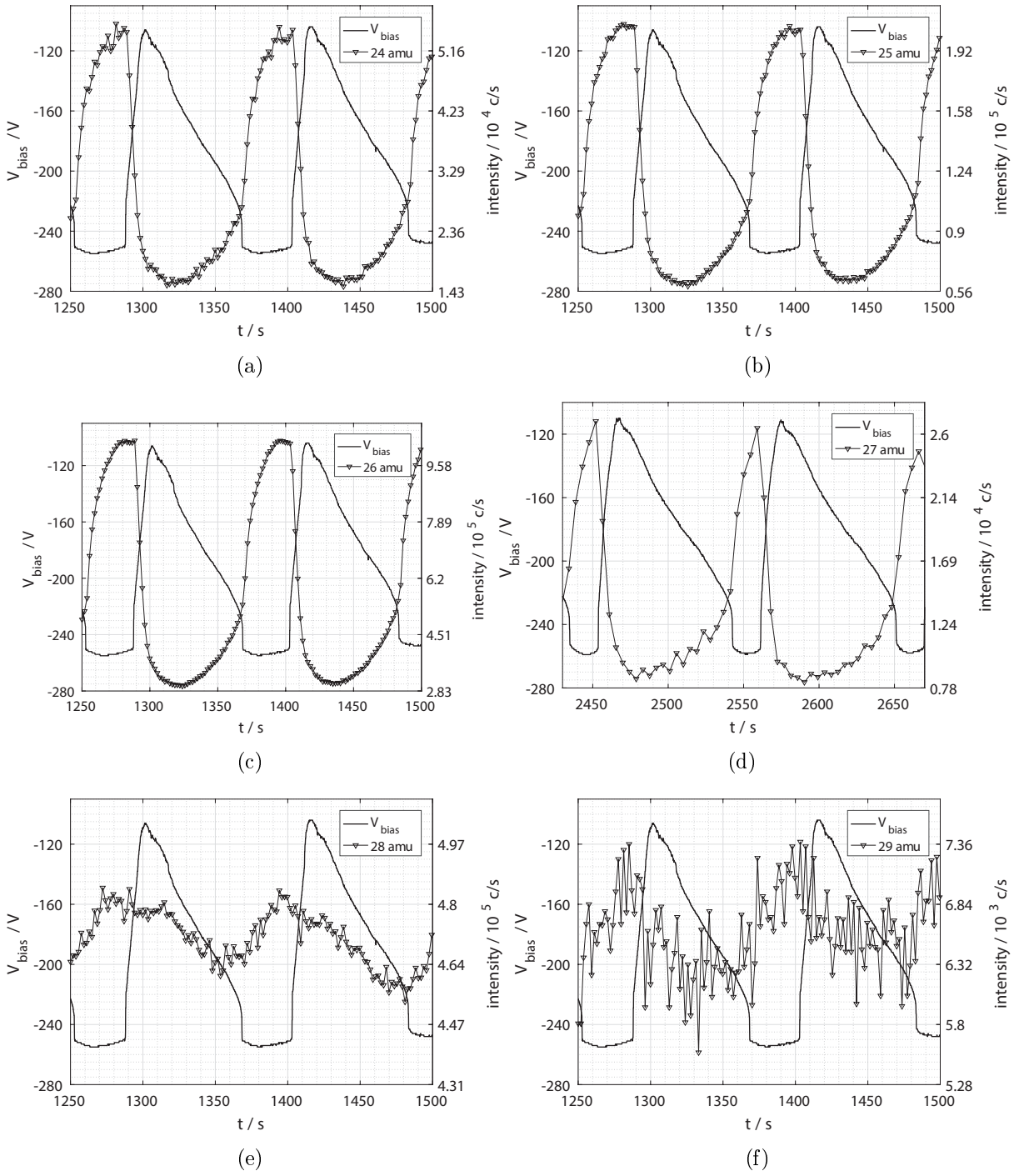

Figure A.3: Evolution of neutrals measured in RGA mode, time correlated to the self-bias voltage.

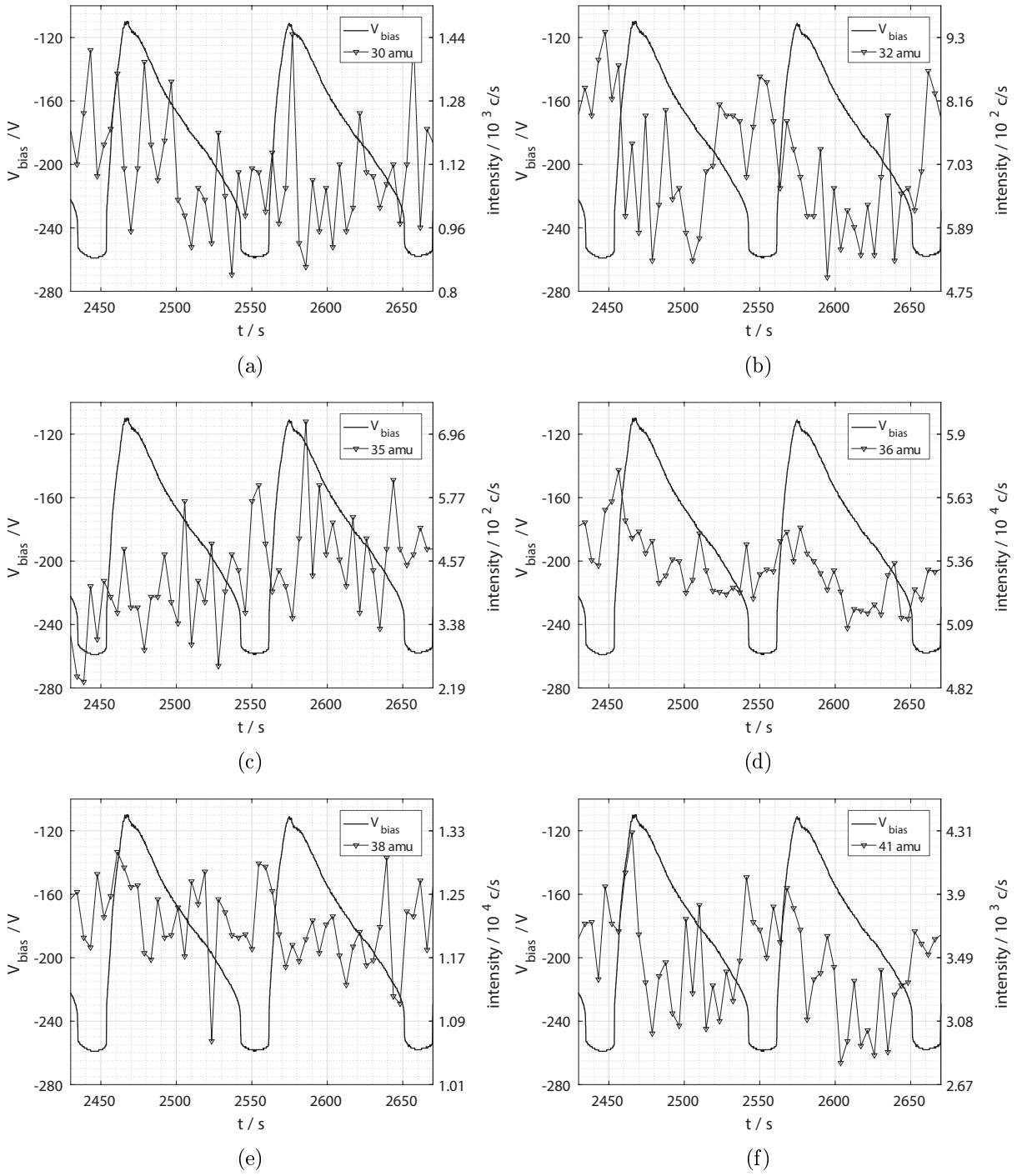

Figure A.4: Evolution of neutrals measured in RGA mode, time correlated to the self-bias voltage.

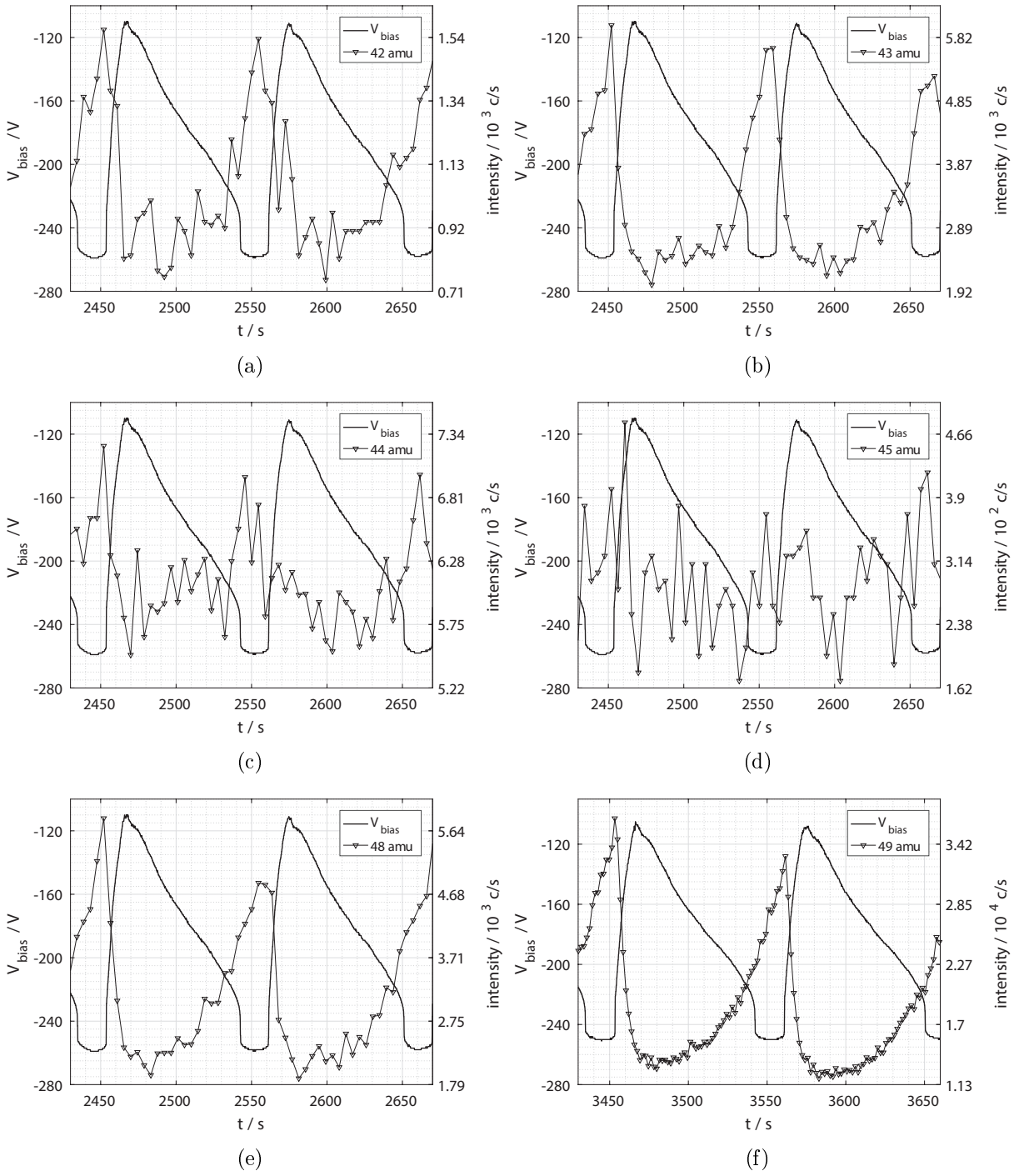

Figure A.5: Evolution of neutrals measured in RGA mode, time correlated to the self-bias voltage.

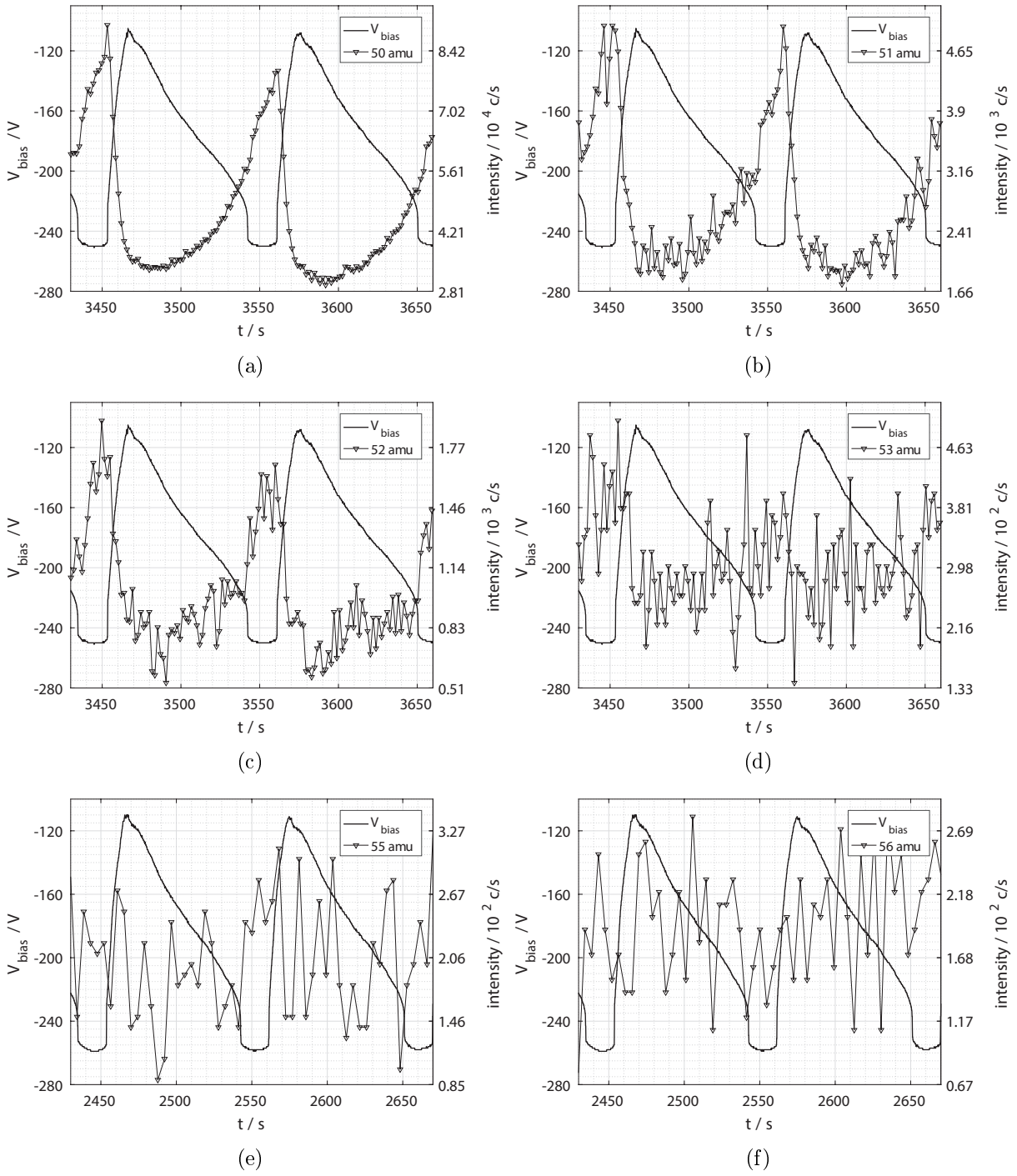

Figure A.6: Evolution of neutrals measured in RGA mode, time correlated to the self-bias voltage.

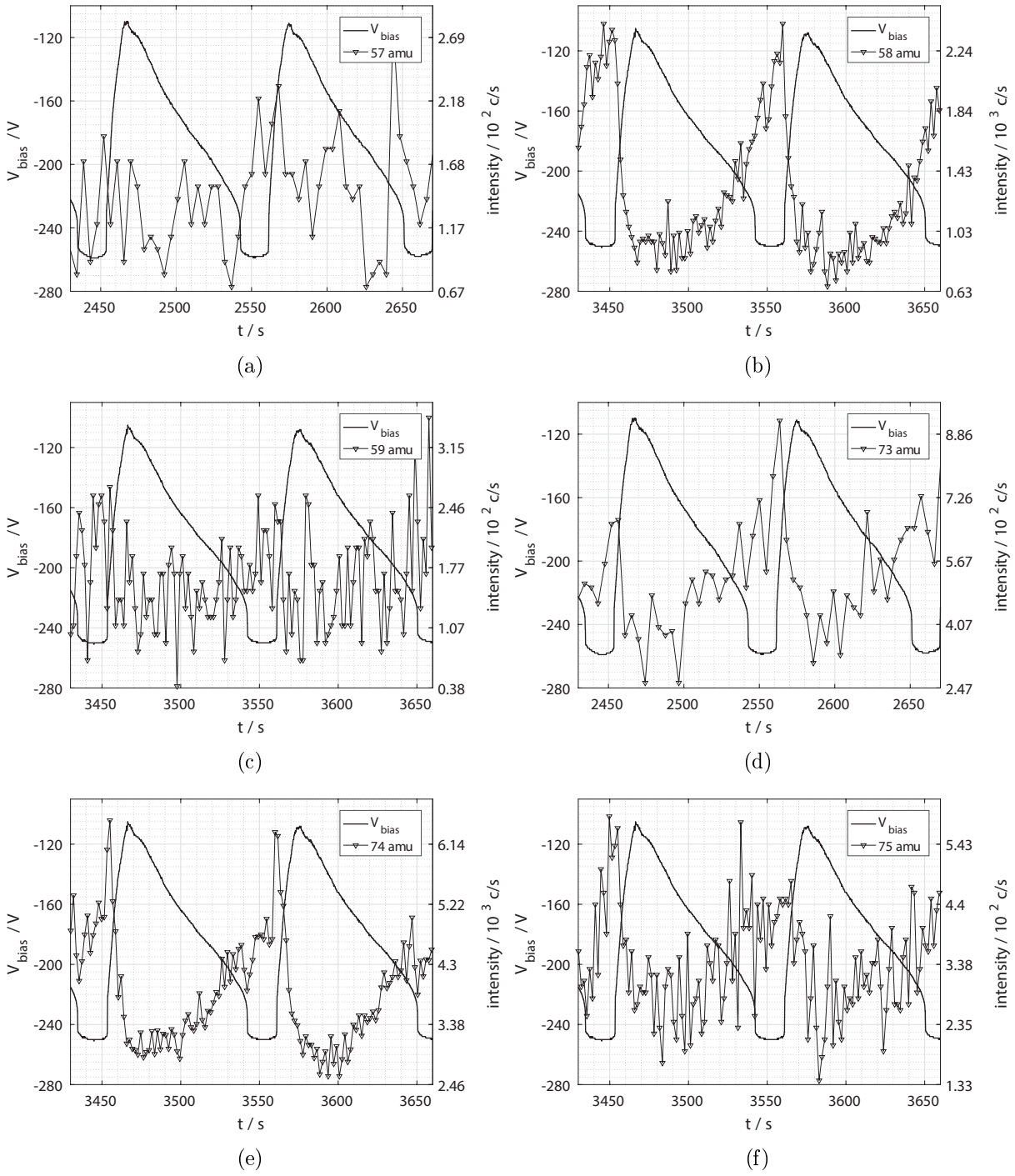

Figure A.7: Evolution of neutrals measured in RGA mode, time correlated to the self-bias voltage.

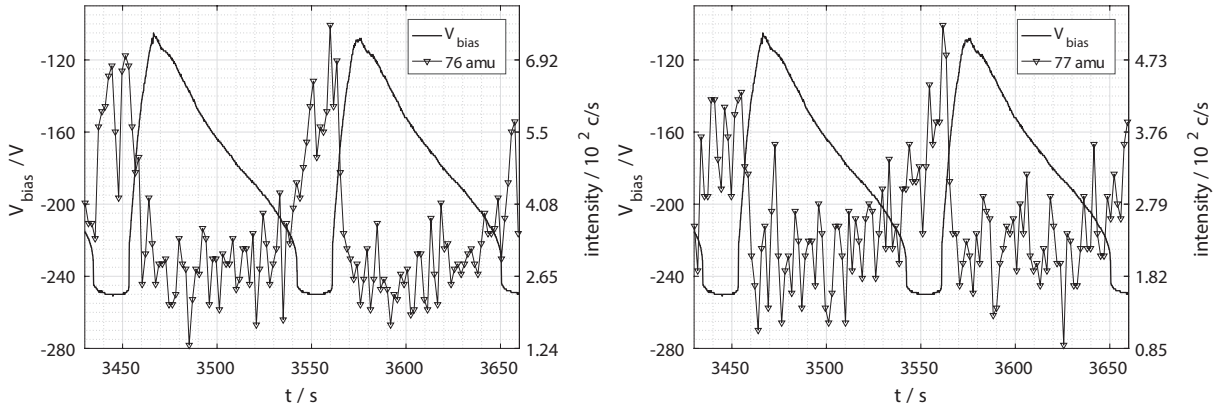

Figure A.8: Evolution of neutrals measured in RGA mode, time correlated to the self-bias voltage.

Appendix B

Appendix - Evolution of ionized species

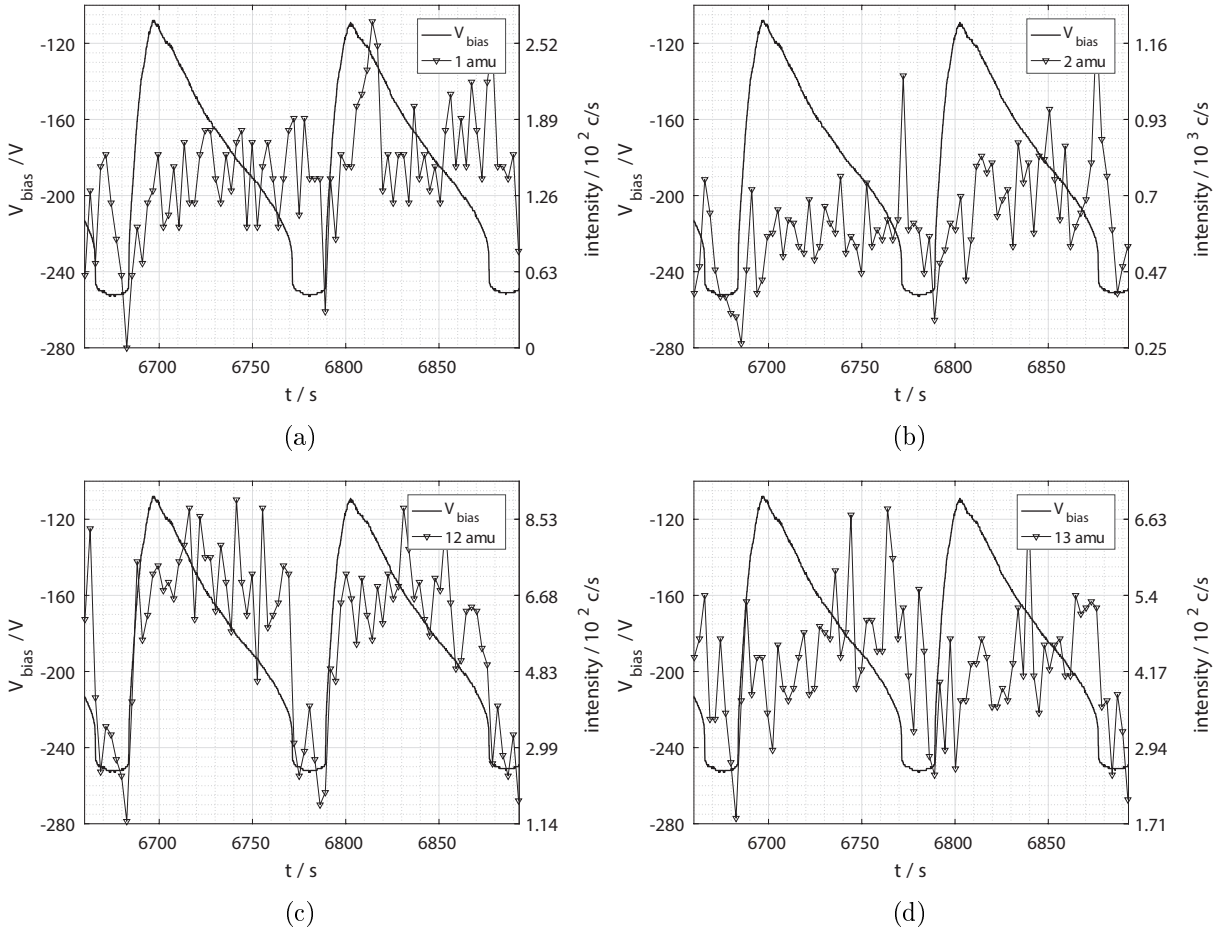

Figure B.1: Evolution of ions measured in +ionSIMS mode, time correlated to the self-bias voltage.

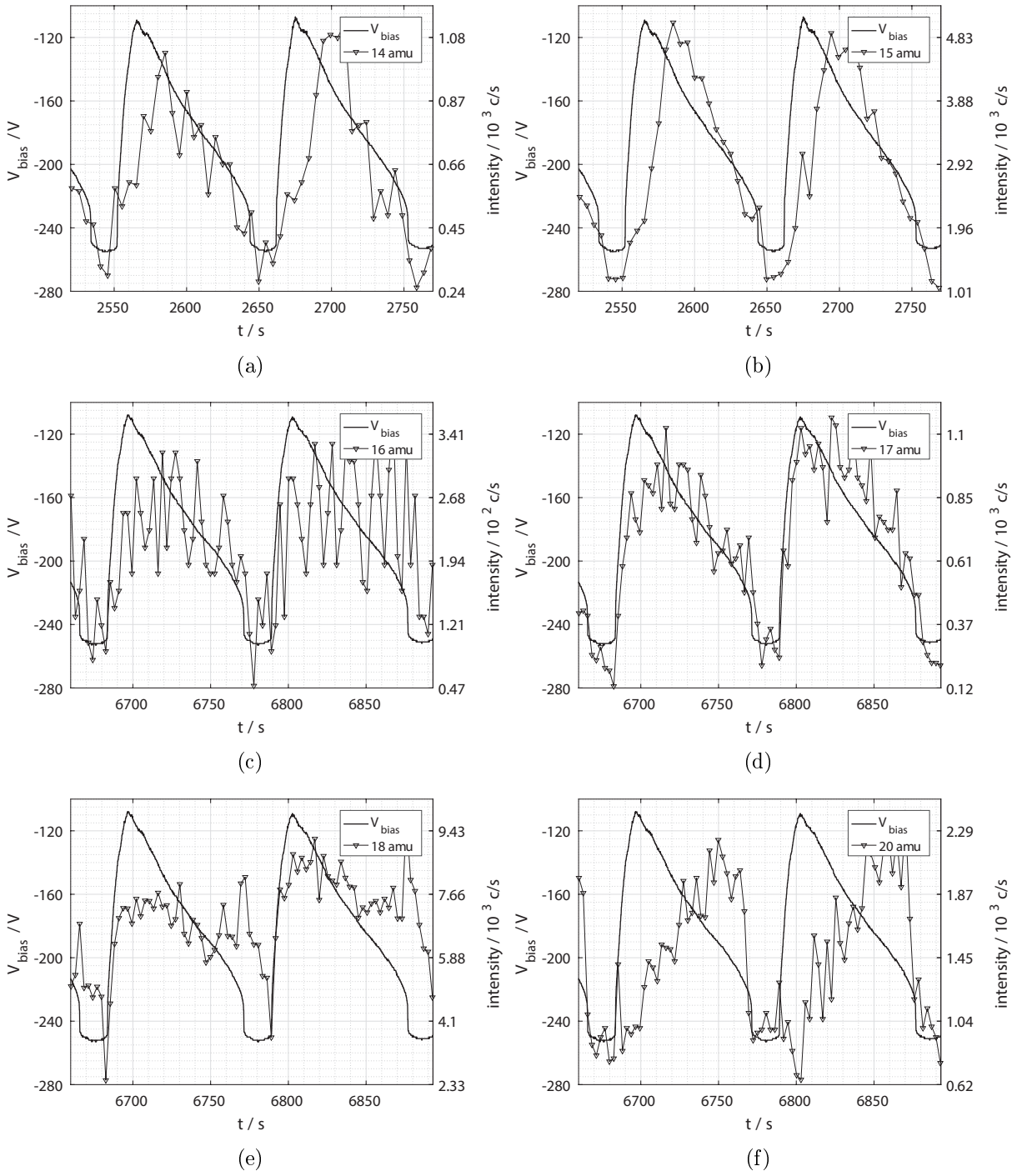

Figure B.2: Evolution of ions measured in +ionSIMS mode, time correlated to the self-bias voltage.

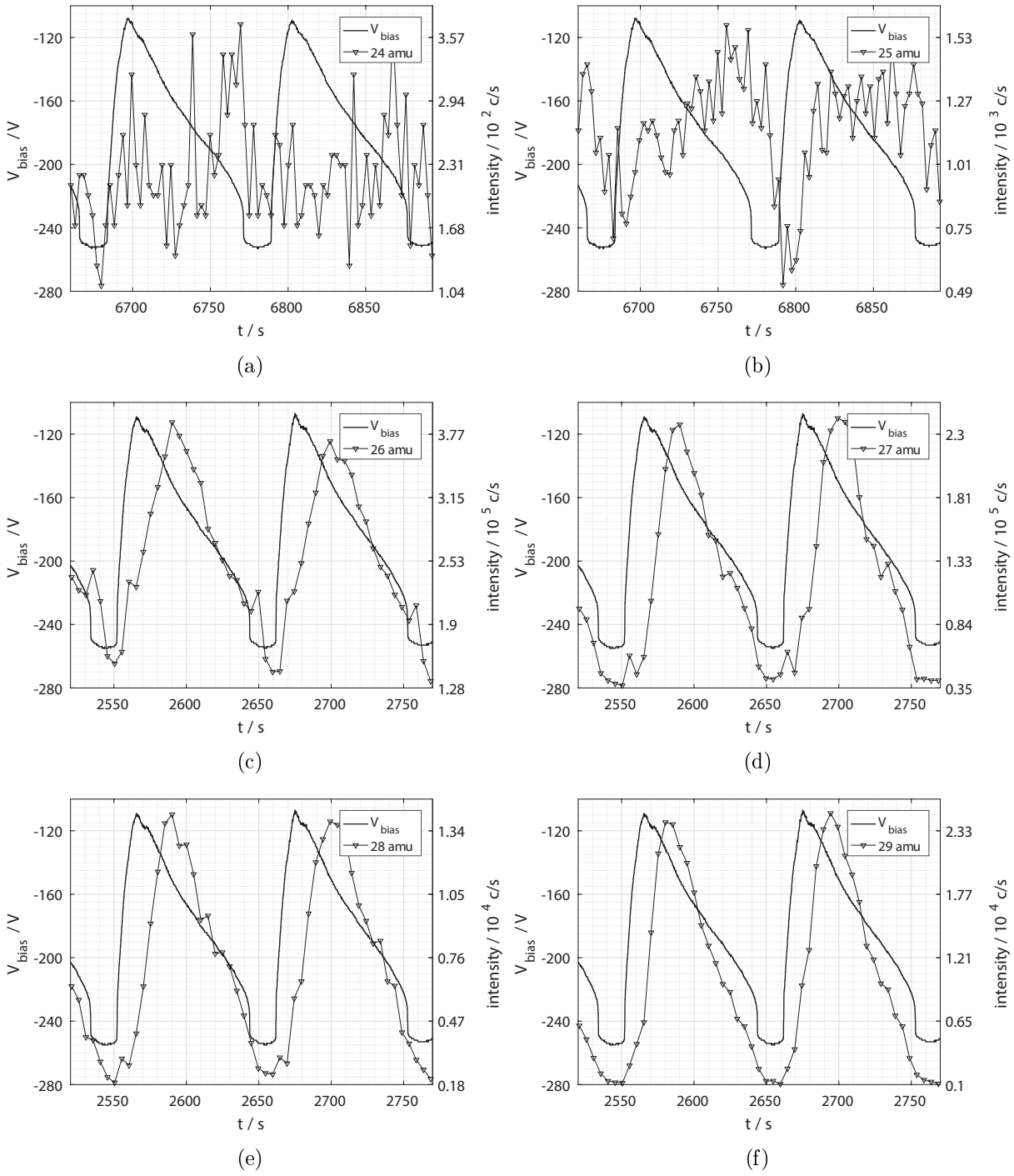

Figure B.3: Evolution of ions measured in +ionSIMS mode, time correlated to the self-bias voltage.

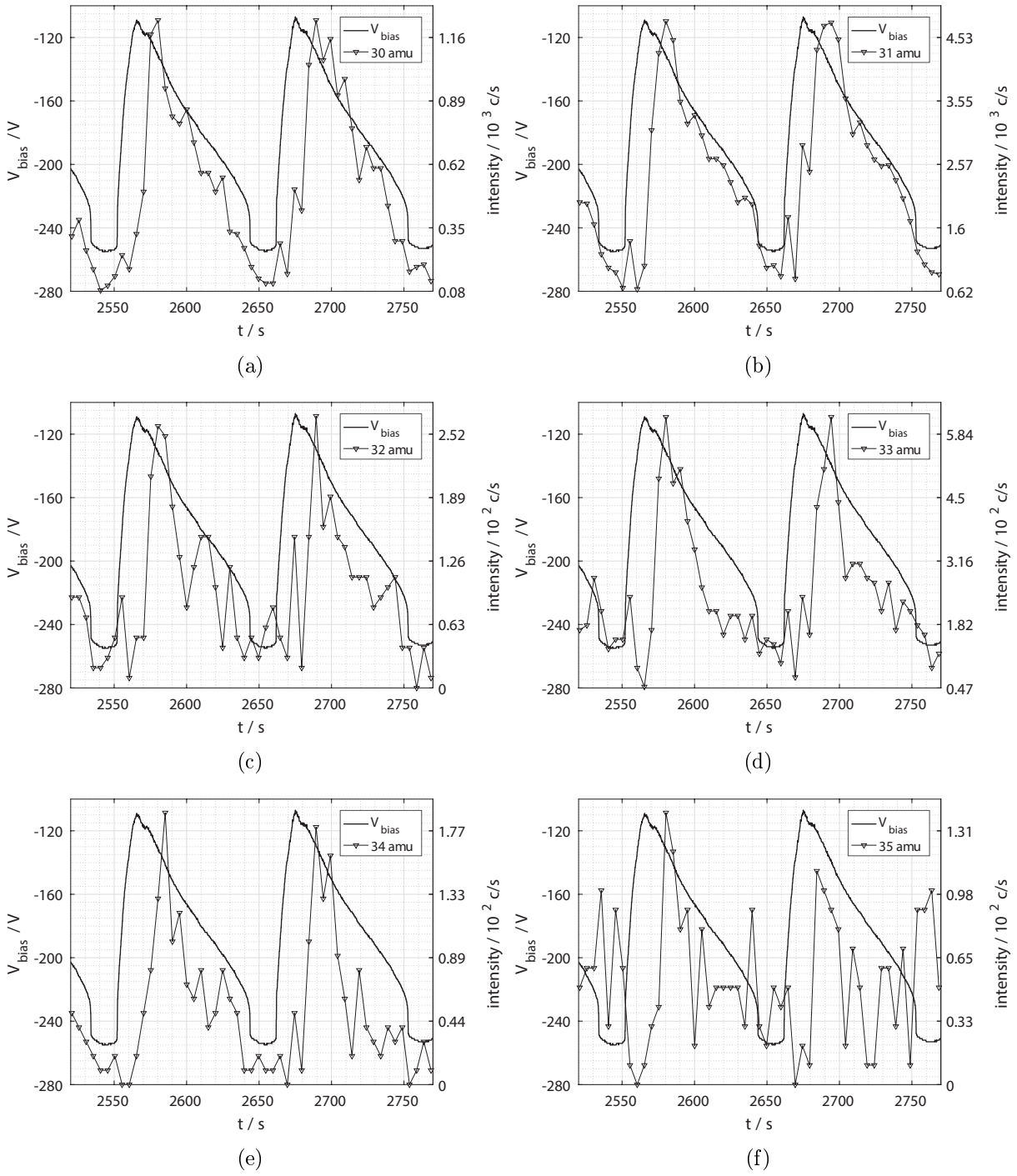

Figure B.4: Evolution of ions measured in +ionSIMS mode, time correlated to the self-bias voltage.

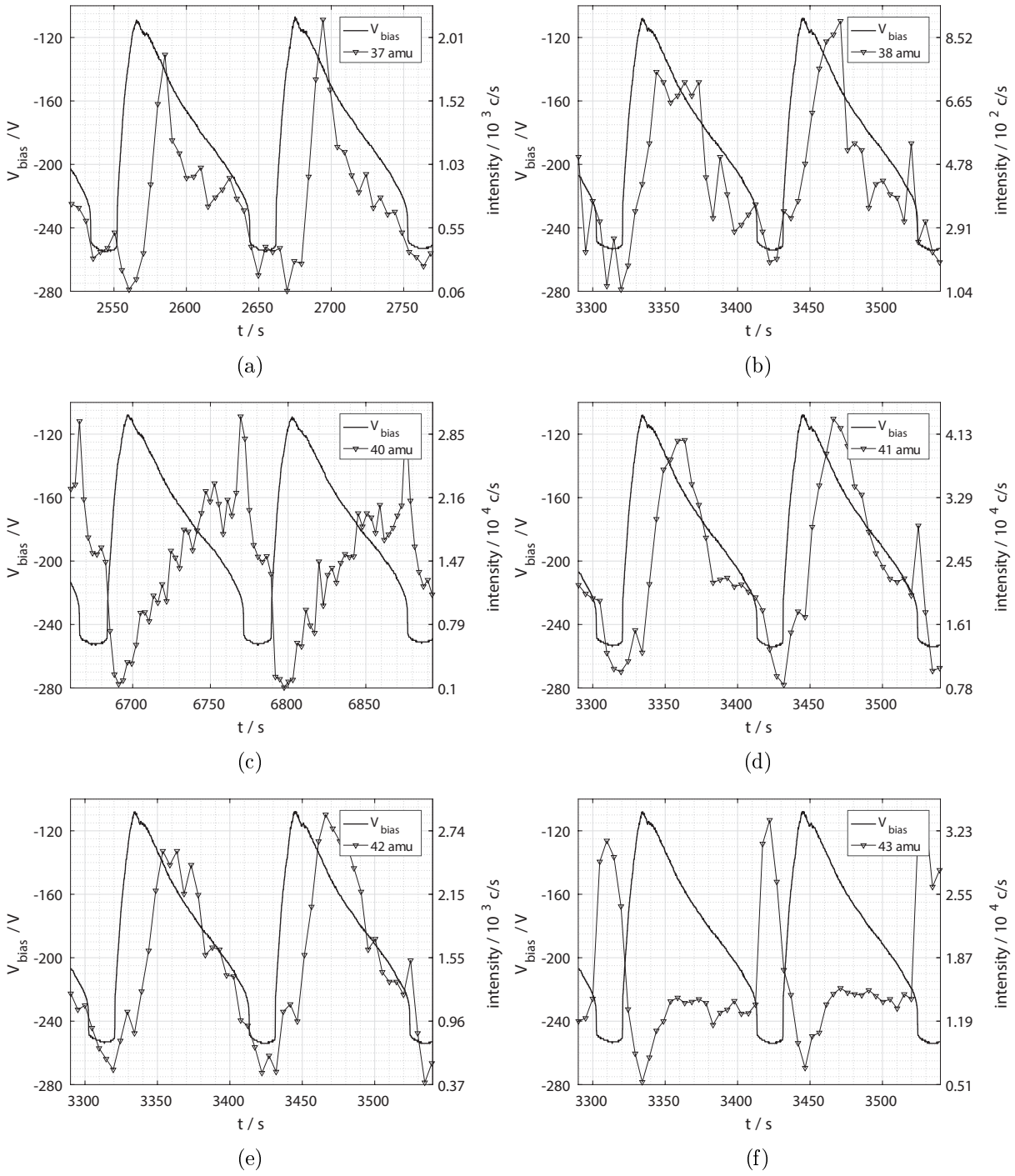

Figure B.5: Evolution of ions measured in +ionSIMS mode, time correlated to the self-bias voltage.

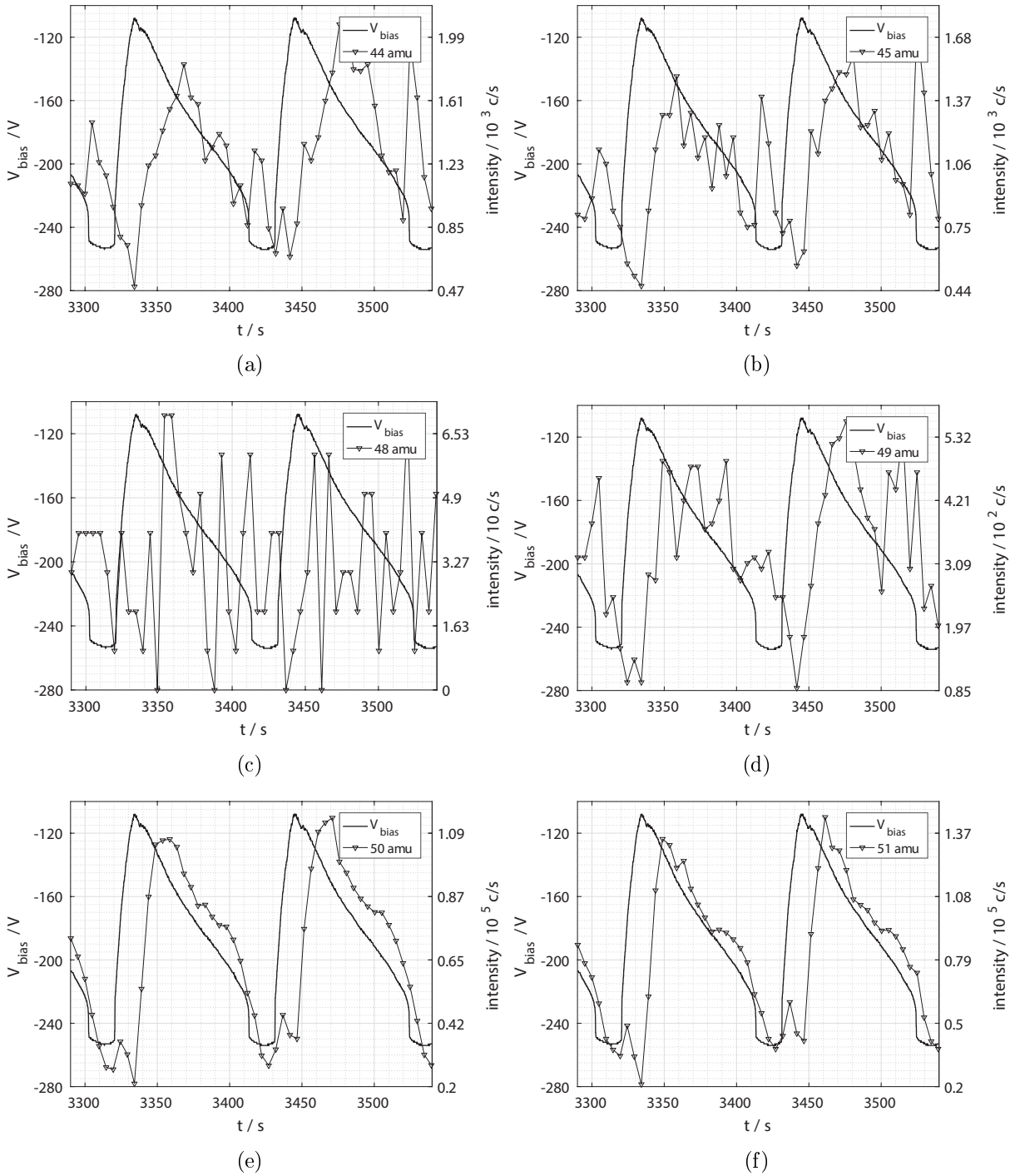

Figure B.6: Evolution of ions measured in +ionSIMS mode, time correlated to the self-bias voltage.

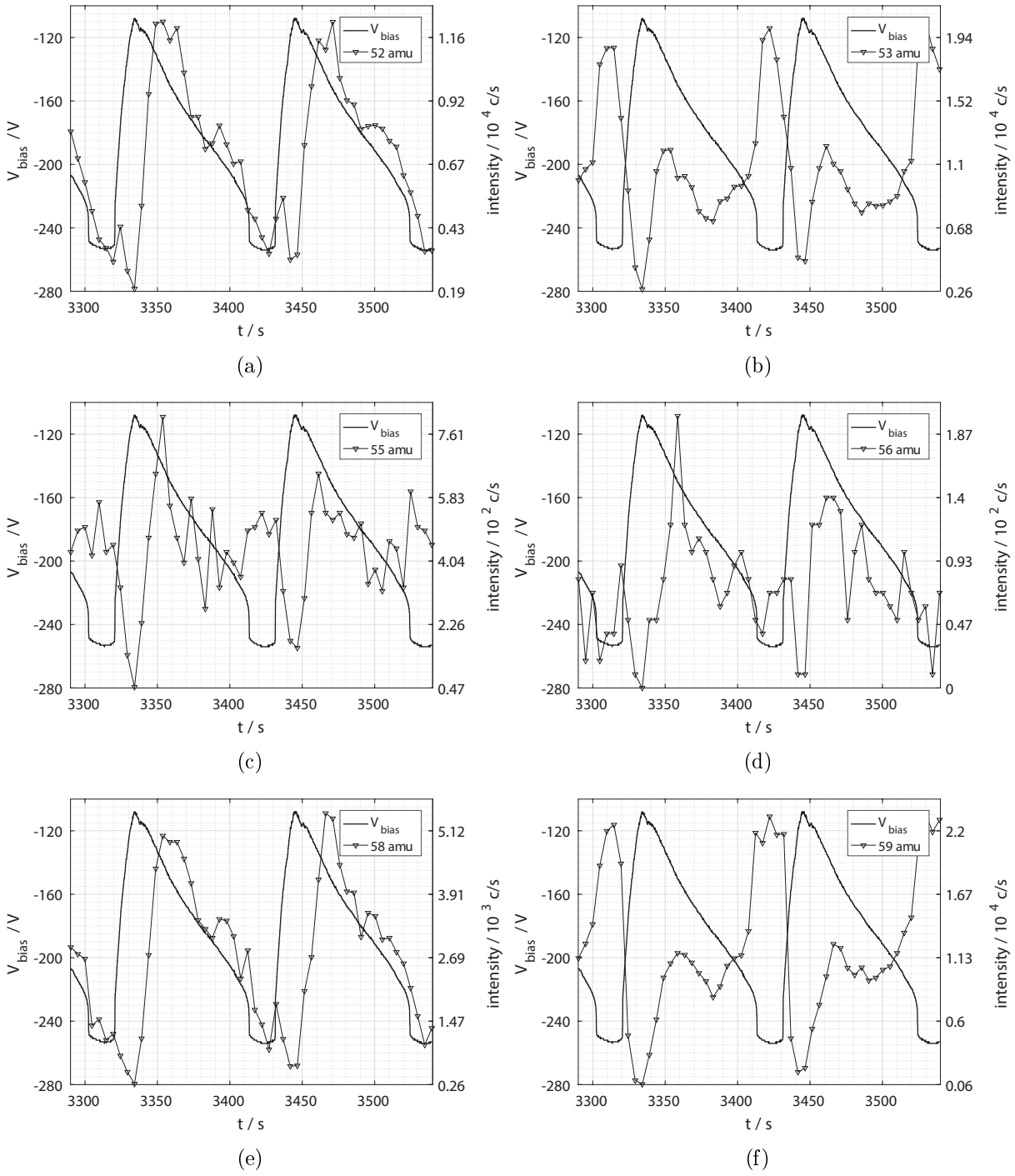

Figure B.7: Evolution of ions measured in +ionSIMS mode, time correlated to the self-bias voltage.

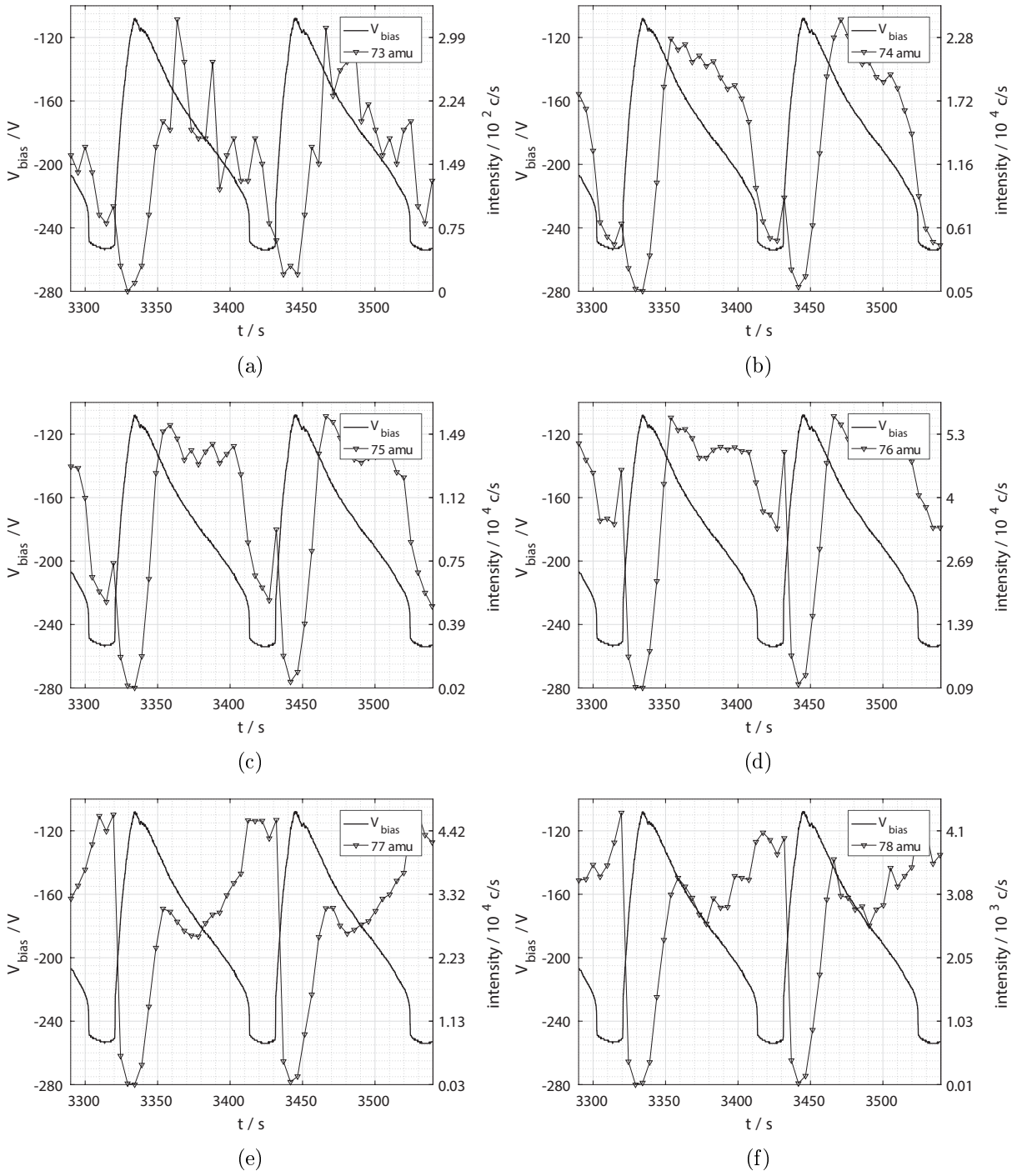

Figure B.8: Evolution of ions measured in +ionSIMS mode, time correlated to the self-bias voltage.

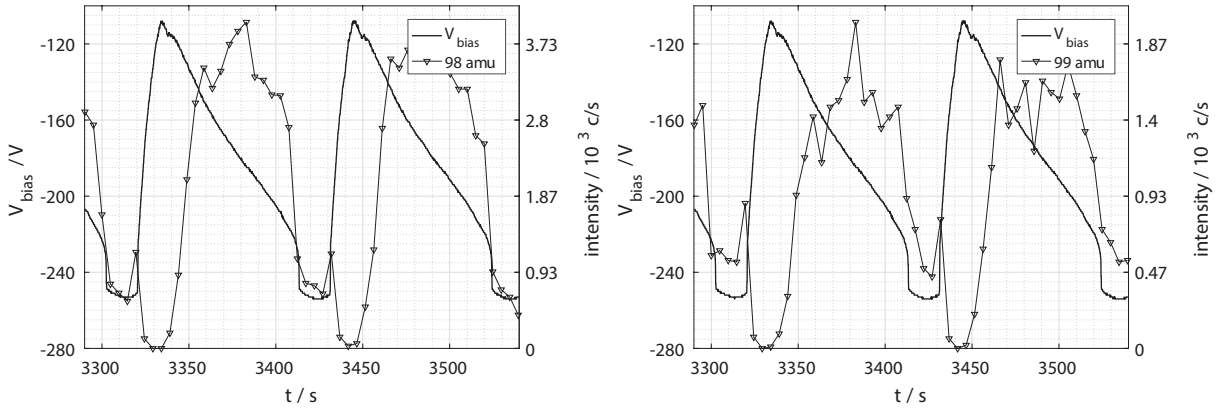

Figure B.9: Evolution of ions measured in +ionSIMS mode, time correlated to the self-bias voltage.

List of Tables

List of Figures

Bibliography

[1] Julia Cipo and Holger Kersten. Die Geschichte der Gasentladungsphysik. *Vakuum in Forschung und Praxis*, 30(2):34–42, 2018.

[2] I. Langmuir. Positive ion currents from the positive column of mercury arcs. *Science*, 58(1502):290, Oktober 1923.

[3] I. Langmuir. Oscillations in ionized gases. *Proc. Nat. Acad. Sci.*, 14:627, 07 1928.

[4] L. Tonks and I. Langmuir. Oscillations in ionized gases. *Phys. Rev.*, 33(2):195–210, Feb 1929.

[5] C. K. Goertz and G. E. Morfill. A model for the formation of spokes in Saturn's ring. *Icarus*, 53:219–229, 1983.

[6] C. K. Goertz. Dusty plasmas in the solar system. *Rev. Geophys.*, 27:271–292, 1989.

[7] M. Horányi and T. E. Cravens. The structure and dynamics of jupiter's ring. *Nature*, 381:293–295, 1996.

[8] André Anders. Tracking down the origin of arc plasma science. i. early pulsed and oscillating discharges. *IEEE Trans. Plasma Sci.*, 31:1052, 2003.

[9] Howard B. Rockman. *Intellectual Property Law for Engineers and Scientists*. 2004.

[10] R. Michaud, V. Felix, A. Stolz, O. Aubry, P. Lefaucheux, S. Dzikowski, V. Schulz von der Gathen, L. J. Overzet, and R. Dussart. Direct current microhollow cathode discharges on silicon devices operating in argon and helium. *Plasma Sources Sci. Technol.*, 27:025005, 2018.

[11] Karl H. Schoenbach and Kurt Becker. 20 years of microplasma research: a status report. *Eur. Phys. J. D*, 70:29, 2016.

[12] S. I. Krasheninnikov A. Yu, Pigarov, R. D. Smirnov, M. Rosenberg, Y. Tanaka, D. J. Benson, T. K. Soboleva, T. D. Rognlien, D. A. Mendis, B. D. Bray, D. L. Rudakov, J. H. Yu, W. P. West, A. L. Roquemore, C. H. Skinner, J. L. Terry, B. Lipschultz, A. Bader, R. S. Granetz, C. S. Pitcher, N. Ohno, S. Takamura, S. Masuzaki, N. Ashikawa, M. Shiratani, M. Tokitani, R. Kumazawa, N. Asakura, T. Nakano, A. M. Litnovsky,

R. Maqueda, and the LHD Experimental Group. Recent progress in understanding the behavior of dust in fusion devices. *Plasma Phys. Control. Fusion*, 50:124054, 2008.

[13] F. Farmer, V. Bykov, M. Drevlak, A. Häußler, U. Fischer, T. Stange, C.D. Beidler, R.C. Wolf, and W7-X Team. From W7-X to a HELIAS fusion power plant: On engineering considerations for the next-step stellarator devices. *Fusion Eng. Des.*, 123:47–53, 2017.

[14] Mounir Laroussi and Tamer Akan. Arc-free atmospheric pressure cold plasma jets: A review. *Plasma Processes and Polymers*, 4:777–788, 2007.

[15] M. A. Lieberman and A. J. Lichtenberg. *Principles of plasma discharges and material processing.* John Wiley & Sons Inc., New York, 1994.

[16] Vincent M. Donnelly and Avinoam Kornblit. Plasma etching: Yesterday, today, and tomorrow. *J. Vac. Sci. Technol. A*, 31(5):050825, 2013.

[17] Chi-Ming Chan. *Polymer surface modification and characterization.* Carl Hanser Verlag, Germany, 1993.

[18] Riccardo d'Agostino. *Plasma Deposition, Treatment, and Etching of Polymers.* Acadamic Press Inc., New York, 1990.

[19] E. M. Liston, L. Martinu, and M. R. Wertheimer. Plasma surface modification of polymers for improved adhesion: a critical review. *J. Adhesion Sci. Technol.*, 7:1091, 1993.

[20] Jörg Friedrich. *The Plasma Chemistry of Polymer Surfaces.* WILEY-VCH, 1 edition, 2012.

[21] Hiroaki Kobayashi, Alexis T. Bell, and Mitchel Shen. Formation of an amorphous powder during the polymerization of ethylene in a radio-frequency discharge. *J. Appl. Polym. Sci.*, 17:885, 1973.

[22] G. S. Selwyn, J. Singh, and R. S. Bennett. In situ laser diagnostic studies of plasma–generated particulate contamination. *J. Vac. Sci. Technol. A*, 7:2758–2765, 1989.

[23] E. Stoffels, W. W. Stoffels, H. Kersten, G. H. P. M. Swinkels, and G. M. W. Kroesen. Surface processes of dust particles in low pressure plasmas. *Phys. Scr.*, T89:168–172, 2001.

[24] J. Winter. Dust in fusion devices - a multi-faceted problem connecting high- and low-temperature plasma physics. *Plasma Phys. Control. Fusion*, 46:B583–B592, 2004.

[25] A. Bouchoule. *Dusty Plasmas - Physics, Chemistry and Technological Impacts in Plasma Processing.* Wiley-VCH, 1999.

[26] H. Thomas, G. E. Morfill, V. Demmel, J. Goree, B. Feuerbacher, and D. Möhlmann. Plasma crystal: Coulomb crystallization in a dusty plasma. *Phys. Rev. Lett.*, 73:652–655, 1994.

[27] A. A. Fridman, L. Boufendi, T. Hbid, B. V. Potapkin, and A. Bouchoule. Dusty plasma formation: Physics and critical phenomena. Theoretical approach. *J. Appl. Phys*, 79:1303, 1996.

[28] A. Piel and A. Melzer. Dynamical processes in complex plasmas. *Plasma Phys. Control. Fusion*, 44:R1–R26, 2002.

[29] J. Berndt, E. Kovačević, I. Stefanović, O. Stepanović, S. H. Hong, L. Boufendi, and J. Winter. Some aspects of reactive complex plasmas. *Contributions to Plasma Physics*, 49:107, 2009.

[30] M. Bonitz, C. Henning, and D. Block. Complex plasmas: a laboratory for strong correlations. *Rep. Prog. Phys.*, 73:1, 2010.

[31] M. Mikikian, L. Couëdel, M. Cavarroc, Y. Tessier, and L. Boufendi. Dusty plasmas: synthesis, structure and dynamics of a dust cloud in a plasma. *Eur. Phys. J. Appl. Phys.*, 49:13106, 2010.

[32] H. R. Maurer and H. Kersten. On the heating of nano- and microparticles in process plasmas. *J. Phys. D: Appl. Phys.*, 44:174029, 2011.

[33] F. X. Bronold, H. Fehske, H. Kersten, and H. Deutsch. Surface states and the charge of a dust particle in plasma. *Phys. Rev. Lett.*, 17:175002, 2008.

[34] H. R. Maurer, Viktor Schneider, Matthias Wolter, R. Basner, Thomas Trottenberg, and Holger Kersten. Microparticles as plasma diagnostic tools. *Contributions to Plasma Physics*, 51:218–227, 2011.

[35] O. Kylian, A. Choukourov, and H. Biederman. Nanostructured plasma polymers. *Thin Solid Films*, 548:1, 2013.

[36] Laïfa Boufendi and André Bouchoule. Industrial developments of scientific insights in dusty plasmas. *Plasma Sources Sci. Technol.*, 11:A211–A218, 2002.

[37] M. Quitzau, M. Wolter, V. Zaporojtchenko, Holger Kersten, and Franz Faupel. Modification of polyethylene powder with an organic precursor in a spiral conveyor by hollow cathode glow discharge. *The European Physical Journal D*, 58:305–310, 2010.

[38] Jiachun Feng and Wei Huang. Nanostructured ultra-low-κ porous fluoropolymer composite films via plasma co-polymerization of hydrophobic and hydrophilic monomers and subsequent hydrolysis treatment. *European Polymer Journal*, 43:3773, 2007.

[39] Virginie Bouchat, Olivier Feron, Bernard Gallez, Bernard Masereel, Carine Michiels, Thierry Vander Borght, and Stéphane Lucas. Carbon nanoparticles synthesized by sputtering and gas condensation inside a nanocluster source of fixed dimension. *Surf. Coat. Technol.*, 205:577, 2011.

[40] Gudrun Schmidt and Matthew M. Malwitz. Properties of polymer-nanoparticle composites. *Current Opinion in Colloid and Interface Science*, 8:103–108, 2003.

[41] Amir H. Faraji and Peter Wipf. Nanoparticles in cellular drug delivery. *Bioorganic & Medicinal Chemistry*, 17:2950–2962, 2009.

[42] Alessio Becheri, Maximilian Dürr, Pierandrea Lo Nostro, and Piero Baglioni. Synthesis and characterization of zinc oxide nanopartilces: application to textiles as uv-absorbers. *J Nanopart Res*, 10:679–689, 2007.

[43] H. J. Klasen. Historical review of the use of silver in the treatment of burns. I. Early uses. *Burns*, 26:117–130, 2000.

[44] Yun Kee Jo, Jeong Hyun Seo, Bong-Hyuk Choi, Bum Jin Kim, Hwa Hui Shin, Byeong Hee Hwang, and Hyung Joon Cha. Surface-independent antibacterial coating using silver nanoparticle-generating engineered mussel glue. *ACS Appl. Mater. Interfaces*, 6:20242–20253, 2014.

[45] J. Xiong, M. Z. Ghori, B. Henkel, T. Strunskus, U. Schürmann, M. Deng, L. Kienle, and F. Faupel. Tuning silver ion release properties in reactively sputtered Ag/TiOx nanocomposites. 123:470, 2017.

[46] Jun-Hong Liu, Ai-Qin Wang, Yu-Shan Chi, Hong-Ping Lin, and Chung-Yuan Mou. Synergistic effect in an Au-Ag alloy nanocatalyst: CO oxidation. *J. Phys. Chem. B*, 109:40–43, 2005.

[47] Mehdi Keshavarz Hedayati, Franz Faupel, and Mady Elbahri. Review of plasmonic nanocomposite metamaterial absorber. *Materials*, 7:1221–1248, 2014.

[48] Chin-Yi Liu, Zachary C Holman., and Uwe R. Kortshagen. Hybrid solar cells from P3HT and silicon nanocrystals. *Nano Letters*, 9(1):449–452, 2009.

[49] Michael Holzinger, Alan Le Goff, and Serge Cosnier. Nanomaterials for bionsensing applications: a review. *Front Chem.*, 2:63, 2014.

[50] L. Boufendi, M. Ch. Jouanny, E. Kovačević, J. Berndt, and M. Mikikian. Dusty plasma for nanotechnology. *J. Phys. D: Appl. Phys.*, 44(17):174035, 2011.

[51] Y. Watanabe. Formation and behavior of nano/micro-particles in low pressure plasmas. *J. Phys. D: Appl. Phys.*, 39:R329–R361, 2006.

[52] G. M. Jellum, J. E. Daugherty, and D. B. Graves. Particle thermophoresis in low pressure glow discharges. *J. Appl. Phys.*, 69:6923, 1991.

[53] Y. Watanabe, M. Shiratani, T. Fukuzawa, and H. Kawasaki. Effects of particles on He-SiH_4 modulated rf discharges. *Plasma Sources Sci. Technol.*, 3(3):355, 1994.

[54] E. V. Johnson, Y. Djeridane, A. Abramov, and P. Roca i Cabarrocas. Experiment and modelling of very low frequency oscillations in RF-PECVD: a signature for nanocrystal dynamics. *Plasma Sources Sci. Technol.*, 17(3):035029, 2008.

[55] Morten Hundt, Patrick Sadler, Igor Levchenko, Matthias Wolter, and Holger Kersten Kostya (Ken) Ostrikov. Real-time monitoring of nucleation-growth cycle of carbon nanoparticles in acetylene plasmas. *J. Appl. Phys.*, 109:123305, 2011.

[56] J.-C. Schauer, S. Hong, and J. Winter. Electrical measurements in dusty plasmas as a detection method for the early phase of particle formation. *Plasma Sources Sci. Technol.*, 13(4):636, 2004.

[57] J. F. Lagrange, I. Géraud-Grenier, F. Faubert, and V. Massereau-Guilbaud. Optical diagnostic and electrical analysis in dusty rf discharges containing plasmoids. *J. Appl. Phys.*, 118:163302, 2015.

[58] Maxime Mikikian, Marjorie Cavarroc, Lénaïc Couëdel, Yves Tessier, and Laïfa Boufendi. Dust particles in low-pressure plasmas: Formation and induced phenomena. *Pure Appl. Chem.*, 82(6):1273–1282, 2010.

[59] R. M. Roth, K. G. Spears, G. D. Stein, and G. Wong. Spatial dependence of particle light scattering in an rf silane discharge. *Applied Physics Letters*, 46:253–255, 1985.

[60] T. Schlebrowski, H. Bahre, M. Böke, and J. Winter. Monitoring particle growth in deposition plasmas. *Plasma Sources Sci. Technol.*, 22(065014), 2013.

[61] Eva Kovačević, Ilja Stefanović, and Johannes Berndt. Infrared fingerprints and periodic formation of nanoparticles in Ar/C_2H_2 plasmas. *J. Appl. Phys.*, 39:2924, 2003.

[62] Iris Pilch and Franko Greiner. Diagnostics of void expansion during cyclic growth and formation of layered nanoparticle clouds. *J. Appl. Phys.*, 121:113302, 2017.

[63] Benjamin Tadsen, Franko Greiner, Sebastian Groth, and Alexander Piel. Self-excited dust-acoustic waves in an electron-depleted nanodusty plasma. *Pysics of Plasmas*, 22:113701, 2015.

[64] Ch. Hollenstein, J-L. Dorier, J. Dutta, L. Sansonnens, and A. A. Howling. Diagnostics of particle genesis and growth in rf silane plasmas by ion mass spectrometry and light scattering. *Plasma Sources Sci. Technol.*, 3:278–285, 1994.

[65] Yasuaki Hayashi and Kunihide Tachibana. Mie-scattering ellipsometry for analysis of particle behaviours in processing plasmas. *Japanese Journal of Applied Physics*, 33(3B):L476, 1994.

[66] Sebastian Groth, Franko Greiner, Benjamin Tadsen, and Alexander Piel. Kinetic Mie ellipsometry to determine the time-resolved particle growth in nanodusty plasmas. *J. Phys. D: Appl. Phys.*, 48:465203, 2015.

[67] Ch. Deschenaux, A. Affolter, D. Magni, Ch. Hollenstein, and P. Fayet. Investigations of CH_4, C_2H_2 and C_2H_4 dusty rf plasmas by means of FTIR absorption spectroscopy and mass spectrometry. *J. Phys. D: Appl. Phys.*, 32:1876–1886, 1999.

[68] S. Stoykov, C. Eggs, and U. Kortshagen. Plasma chemistry and growth of nanosized particles in a C_2H_2 rf discharge. *J. Phys. D: Appl. Phys.*, 34(14):2160, 2001.

[69] M. Mikikian, L. Couëdel, M. Cavarroc, Y. Tessier, and L. Boufendi. Self-excited void instability in dusty plasmas: plasma and dust cloud dynamics during the heartbeat instability. *New Journal of Physics*, 9:268, 2007.

[70] A. Pastol and Y. Catherine. Optical emission spectroscopy for diagnostic and monitoring of CH_4 plasmas used for a-C:H deposition. *Journal of Physics D: Applied Physics*, 23(7):799, 1990.

[71] Jérémy Pereira, Véronique Masserau-Guilbaud, Isabelle Géraud-Grenier, and André Plain. CH and CN radical contribution in the particle formation generated in a radiofrequency CH_4/N_2 plasma. *Plasma Processes Polym.*, 2:633–640, 2005.

[72] Ann-Pierra Herrendorf, Vladimir Sushkov, and Rainer Hippler. Mass spectrometric investigations of plasma chemical reactions in a radiofrequency discharge with Ar/C_2H_2 and $Ar/C_2H_2/O_2$ gas mixtures. *J. Appl. Phys.*, 121:123303, 2017.

[73] J. Perrin, C. Bohm, R. Etemadi, and A. Lloret. Possible routes for cluster growth and particle formation in rf silane discharges. *Plasma Sources Sci. Technol.*, 3(3):252, 1994.

[74] James R. Doyle. Chemical kinetics in low pressure acetylene radio frequency glow discharges. *Journal of Applied Physics*, 82:4763–4771, 1997.

[75] Petr Pokorný, Jindřich Musil, Michal Novotný, Ján Lančok, Přemysl Fitl, and Jan Vlček. Creation and behavior of radicals and ions in the acetylene/argon microwave ECR discharge. *Plasma Processes Polym.*, page e1700062, 2017.

[76] A. Consoli, J. Benedikt, and A. von Keudell. Initial polymerization reactions in particle-forming $Ar/He/C_2H_2$ plasmas studied via quantitative mass spectrometry. *J. Phys. Chem. A*, 112:11319–11329, 2008.

[77] Th. Wegner, A. M. Hinz, F. Faupel, T. Strunskus, H. Kersten, and J. Meichsner. Influence of nanoparticle formation on discharge properties in argon-acetylene capacetively coupled radio frequency plasmas. *Appl. Phys. Lett.*, 108:063108, 2016.

[78] Masaharu Shiratani, Tsuyoshi Fukuzawa, Kenji Eto, and Yukio Watanabe. Detection of negative ions in a helium-silane rf plasma. *Japanese Journal of Applied Physics*, 31(12B):L1791, 1992.

[79] J. Berndt, E. Kovačević, I. Stefanović, and J. Winter. Anomalous behaviour of the electron density in a pulsed complex plasma. *Plasma Sources Sci. Technol.*, 15(1):18, 2005.

[80] M. Klindworth, O. Arp, and A. Piel. Langmuir probe system for dusty plasmas under microgravity. *Rev. Sci. Instrum.*, 78:033502, 2007.

[81] D. Samsonov and J. Goree. Instabilities in a dusty plasma with ion drag and ionization. *Phys. Rev. E*, 59(1):1047–1058, 1999.

[82] A. Barkan, N. D'Angelo, and R. L. Merlino. Charging of dust grains in a plasma. *Phys. Rev. Lett.*, 73:3093, 1994.

[83] N. Bilik, R. Anthony, B. A. Merritt, E. S. Aydil, and U. R. Kortshagen. Langmuir probe measurements of electron energy probability functions in dusty plasmas. *J. Phys. D: Appl. Phys.*, 48(10):105204, 2015.

[84] A. M. Hinz, E. von Wahl, F. Faupel, T. Strunskus, and H. Kersten. Versatile particle collection concept for correlation of particle growth and discharge parameters in dusty plasmas. *J. Phys. D: Appl. Phys*, 48(055203), 2015.

[85] Eva Kovačević, Johannes Berndt, Thomas Strunskus, and Laifa Boufendi. Size dependent characteristics of plasma synthesized carbonaceous nanoparticles. *J. Appl. Phys.*, 112:013303, 2012.

[86] E. Kovačević, J. Berndt, I. Stefanović, H.-W. Becker, C. Godde, Th. Strunskus, J. Winter, and L. Boufendi. Formation and material analysis of plasma polymerized carbon nitride nanoparticles. *Journal of Applied Physics*, 105:104910, 2009.

[87] Alexander Martin Hinz. *Nanoparticle Forming Reactive Plasmas: A Multidiagnostic Approach*. PhD thesis, 2018.

[88] Peter Debye and Erich Hückel. Zur Theorie der Elektrolyte. I. Gefrierpunktserniedrigung und verwandte Erscheinungen. *Phys. Z.*, 24(9):185, 1923.

[89] Hideki Yukawa. On the interaction of elementary particles I. *Proceedings of the Physico-Mathematical Society of Japan*, 17:48–57, 1935.

[90] Alexander Piel. *Plasma Physics, An Introduction to Laboratory, Space and Fusion Plasmas*. Springer-Verlag, 1 edition, 2010.

[91] A. Melzer, T. Trottenberg, and A. Piel. Experimental determination of the charge on dust particles forming Coulomb lattices. *Phys. Lett. A*, 191:301–308, 1994.

[92] S. Peters, A. Homann, A. Melzer, and A. Piel. Measurement of dust particle shielding in a plasma from oscillations of a linear chain. *Phys. Lett. A*, 223:389–393, 1996.

[93] A. Homann, A. Melzer, S. Peters, R. Madani, and A. Piel. Determination of the dust screening length by laser-excited lattice waves. *Phys. Rev. E*, 56:7138–7141, 1997.

[94] U. Konopka, L. Ratke, and H. M. Thomas. Central collisions of charged dust particles in a plasma. *Phys. Rev. Lett.*, 79:1269–1272, 1997.

[95] Alexander Piel. Plasma crystals - structure and dynamics. *Plasma and Fusion Research: Review Articles*, 4:013, 2009.

[96] E. R. Harrison and W. B. Thompson. The low pressure plane symmetric discharge. *Proc. Phys. Soc.*, 74(2):145, 1959.

[97] C. D. Child. Discharge from hot CaO. *Phys. Rev.*, 32:492, 1911.

[98] Irving Langmuir. The effect of space charge and residual gases on thermionic currents in high vacuum. *Phys. Rev.*, 2:450, 1913.

[99] M. S. Benilov. The Child-Langmuir law and analytical theory of collisionless to collision-dominated sheaths. *Plasma Sources Sci. Technol.*, 18:014005, 2009.

[100] A. von Keudell. Vorlesungsskript - Einführung in die Plasmaphysik, 2012.

[101] Rainer Hippler, Holger Kersten, Martin Schmidt, and Karl H. Schoenbach, editors. *Low Temperature Plasmas, Fundamentals, Technologies and Techniques*. Wiley-VCH, 2 edition, 2008.

[102] Pascal Chabert and Nicholas Braithwaite. *Physics of Radio-Frequency Plasmas*. Cambridge University Press, 2011.

[103] Irving Langmuir and Katharine B. Blodgett. Current limited by space charge between coaxial cylinders. *Phys. Zeits.*, 15:348, 1914.

[104] Irving Langmuir and Katharine B. Blodgett. Currents limited by space charge between concentric spheres. *Phys. Rev.*, 24:49, 1924.

[105] Francis F. Chen. Lecture notes on Langmuir probe diagnostics. IEEE-ICOPS meeting, 2003.

[106] M. A. Lieberman. Spherical shell model of an asymmetric rf discharge. *J. Appl. Phys.*, 65:4186, 1989.

[107] A. A. Howling, Ch. Hollenstein, and P.-J. Paris. Direct visual observation of powder dynamics in rf plasma-assisted deposition. *Appl. Phys. Lett.*, 59:1409, 1991.

[108] Kenneth G. Spears, Rodger P. Kampf, and Timothy J. Robinson. Particle densities in radio-frequency discharges of silane. *J. Phys. Chem.*, 92:5297–5302, 1988.

[109] A. Bouchoule, A. Plain, L. Boufendi, J. Ph. Blondeau, and C. Laure. Particle generation and behavior in a silane-argon low-pressure discharge under continuous or pulsed radio-frequency excitation. *J. Appl. Phys.*, 70:1991, 1991.

[110] Gary S. Selwyn, John E. Heidenreich, and Kurt L. Haller. Particle trapping phenomena in radio frequency plasmas. *Appl. Phys. Lett.*, 57:1876, 1990.

[111] E. C. Whipple. Potentials of surfaces in space. *Rep. Prog. Phys.*, 44:1197–1250, 1981.

[112] B. T. Draine and E. E. Salpeter. On the physics of dust grains in hot gas. *Astrophys. J.*, 231:77–94, 1979.

[113] M. K. Wallis and M. H. A. Hassan. Electrodynamics of submicron dust in the cometary coma. *Astron. Astrophys.*, 121:10–14, 1983.

[114] H. M. Mott-Smith and Irving Langmuir. The theory of collectors in gaseous discharges. *Phys. Rev.*, 28:727–763, 1926.

[115] T. Trottenberg, A. Melzer, and A. Piel. Measurement of the electric charge on particulates forming Coulomb crystals in the sheath of an rf plasma. *Plasma Sources Sci. Technol.*, 4:450–458, 1995.

[116] U. Konopka, G. E. Morfill, and L. Ratke. Measurement of the interaction potential of microspheres in the sheath of a rf discharge. *Phys. Rev. Lett.*, 84:891–894, 2000.

[117] A. V. Zobnin, A. P. Nefedov, V. A. Sinel'shchikov, and V. E. Fortov. On the charge of dust particles in a low-pressure gas discharge plasma. *JETP*, 91:483–487, 2000.

[118] M. Lampe, Valeriy Gavrishchaka, G. Ganguli, and G. Joyce. Effect of trapped ions on shielding of a charged spherical object in a plasma. *Phys. Rev. Lett.*, 86:5278–5281, 2001.

[119] R. N. Varney. Drift velocities of ions in krypton and xenon. *Phys. Rev.*, 88(2):362–364, Oktober 1952.

[120] S. A. Khrapak, S. V. Ratynskaia, A. V. Zobnin, A. D. Usachev, V. V. Yaroshenko, M. H. Thoma, M. Kretschmer, H. Höfner, G. E. Morfill, O. F. Petrov, and V. E. Fortov. Particle charge in the bulk of gas discharges. *Phys. Rev. E*, 72:016406, 07 2005.

[121] O. Havnes, G. E. Morfill, and C. K. Goertz. Plasma potential and grain charge in a dust cloud embedded in a plasma. *J. Geophys. Res.*, 89:10999–11003, 1984.

[122] Ove Havnes, Torsten K. Aanesen, and Frank Melandsø. On dust charges and plasma potentials in a dusty plasma with dust size distribution. *J. Geophys. Res.*, 95:6581–6585, 1990.

[123] I. B. Denysenko, H. Kersten, and N. A. Azarenkov. Electron energy distribution in a dusty plasma: Analytical approach. *Physical Review E*, 92:033102, 2015.

[124] F. X. Bronold, H. Deutsch, and H. Fehske. Physisorption kinetics of electrons at plasma boundaries. *Eur. Phys. J. D*, 54:519–544, 2009.

[125] Chunshi Cui and J. Goree. Fluctuations of the charge on a dust grain in a plasma. *IEEE Transactions on Plasma Science*, 22(2):151, 1994.

[126] J. E. Daugherty, R. K. Porteous, and D. B. Graves. Electrostatic forces on small particles in low-pressure discharges. *Journal of Applied Physics*, 73:1617, 1993.

[127] O. Arp. *Coulomb balls - Structure and confinement of spherical dust crystals in a plasma.* Dissertation, Christian-Albrechts-Universität zu Kiel, 2006.

[128] V. N. Salimgareeva, N. S. Sannikova, S. V. Kolesov, and Z. Kh. Kuvatov. Some properties of crystalline polyacetylenes of various density. *Russian Journal of Applied Chemistry*, 47:478, 2001.

[129] T. Nitter. Levitation of dust in rf and dc glow discharges. *Plasma Sources Sci. Technol.*, 5:93, Februar 1996.

[130] H. Rothermel, T. Hagl, G. E. Morfill, M. H. Thoma, and H. M. Thomas. Gravity compensation in complex plasmas by application of a temperature gradient. *Phys. Rev. Lett.*, 89:175001–1–1, 2002.

[131] L. Talbot, R. K. Cheng, R. W. Schefer, and D. R. Willis. Thermophoresis of particles in a heated boundary layer. *J. Fluid Mech.*, 101:737–758, 1980.

[132] Kathleen De Bleecker and Annemie Bogaerts. Role of the thermophoretic force on the transport of nanoparticles in silane plasmas. *Physical Review E*, 71:066405, 2005.

[133] M. S. Barnes, J. H. Keller, J. C. Forster, J. A. O'Neill, and D. K. Coultas. Transport of dust particles in glow–discharge plasmas. *Phys. Rev. Lett.*, 68:313–316, 1992.

[134] M. Mikikian, L. Boufendi, A. Bouchoule, H. M. Thomas, G. E. Morfill, A. P. Nefedov, and V. E. Fortov. Formation and behaviour of dust particle clouds in a radio-frequency discharge: results in the laboratory and under microgravity conditions. *New J. Phys.*, (5):19.1–19.2, März 2003.

[135] G. Praburam and J. Goree. Experimental observation of very low-frequency macroscopic modes in a dusty plasma. *Phys. Plasmas*, 3:1212–1219, 1996.

[136] Phil Morten Hundt. Spektroskopische Diagnostik an Prozessplasmen. Master's thesis, Christian-Albrechts-Universität zu Kiel, 2009.

[137] I. H. Hutchinson. Ion collection by a sphere in a flowing plasma: 3. floating potential and drag force. *Plasma Phys. Control. Fusion*, 47(47):71, Dezember 2005.

[138] G. A. Hebner. Metastable chlorine ion temperature and drift velocity in an inductively coupled plasma. *Journal of Applied Physics*, 80:3215, 1996.

[139] S. A. Maiorov, S. K. Kodanova, M. K. Dosbolayev, T. S. Ramazanov, R. I. Golyatina, n. Kh. Bastykova, and A. U. Utegenov. The role of gas composition in plasma-dust structures in rf discharge. *Physics of Plasmas*, 22:033705, 2015.

[140] S. Chandrasekhar. Dynamical friction. i. general considerations: The coefficient of dynamical friction. *Astrophysical Journal*, 97:255, 1943.

[141] S. A. Khrapak, A. V. Ivlev, G. E. Morfill, and H. M. Thomas. Ion drag force in complex plasmas. *Phys. Rev. E*, 66(4):046414, 10 2002.

[142] Kathleen De Bleecker, Annemie Bogaerts, and Wim Goedheer. Modeling of the formation and transport of nanoparticles in silane plasmas. *Physical Review E*, 70:056407, 2004.

[143] G. G. Stokes. On the effect of the internal friction of fluids on the motion of pendulums. *Cambridge Philos. Trans.*, 9:8–106, 1851.

[144] A. Einstein. Über die von der molekularkinetischen Theorie der Wärme geforderte Bewegung von in ruhenden Flüssigkeiten supendierten Teilchen. *Annalen der Physik*, 17:549–560, 1905.

[145] P. S. Epstein. On the resistance experienced by spheres in their motion through gases. *Phys. Rev.*, 23:710–733, 1924.

[146] R. A. Millikan. The isolation of an ion, a precision measurement of its charge, and the correction of Stokes's law. *Science*, 32:436–448, 1910.

[147] Kathleen De Bleecker, Annemie Bogaerts, and Wim Goedheer. Modelling of nanoparticle coagulation and transport dynamics in dusty silane discharges. *New J. Phys.*, 8:178, 2006.

[148] Michael Deilmann. *Silicon oxide permeation barrier coating and sterilization of PET bottles by pulsed low-pressure plasmas.* PhD thesis, Ruhr-Universität Bochum, 2008.

[149] Ludvik Martinu and Daniel Poitras. Plasma deposition of optical films and coatings: A review. *J. Vac. Sci. Technol. A*, 18:2619, 2000.

[150] Mitsuharu Konuma. *Film Deposition by Plasma Techniques*, volume 10 of *Springer Series on Atoms+Plasmas*. Springer Verlag Berlin Heidelberg, 1 edition, 1992.

[151] Beat Urs Borer. *SiO_x Thin Film Deposition on Particles by Plasma Enhanced Chemical Vapor Deposition in a Circulating Fluidized Bed Reactor.* PhD thesis, Swiss Federal Institute of Technology Zurich, 1974.

[152] Ernst Bauer. Phänomenologische Theorie der Kristallabscheidung an Oberflächen. I. *Zeitschrift für Kristallographie*, 110:372–394, 1958.

[153] André Anders. A structure zone diagram including plasma-based deposition and ion etching. *Thin Solid Films*, 518:4087–4090, 2010.

[154] John A. Thornton. Influence of apparatus geometry and deposition conditions on the structure and topography of thick sputtered coatings. *Journal of Vacuum Science and Technology*, 11:666, 1974.

[155] Akiyoshi Chayahara, Haruki Yokoyama, Takeshi Imura, and Yukio Osaka. Function of substrate bias potential for formation of cubic boron nitride films in plasma CVD technique. *Jpn. J. Appl. Phys.*, 26:L1435, 1987.

[156] Yukio Ichinose, Hidetoshi Saitoh, and Yoshihiko Hirotsu. Synthesis of cubic BN from the gas phase by a new plasma chemical vapour deposition method using R.F. waves and a tungsten filament. *Surf. Coat. Technol.*, 43/44:116, 1990.

[157] J. A. Venables, G. D. T. Spiller, and M. Hanbücken. Nucleation and growth of thin films. *Reg. Prog. Phys.*, 47:399–459, 1984.

[158] Meng Tao. Growth kinetics and reaction mechanism of silicon chemical vapour deposition from silane. *Thin Solid Films*, 223:201–211, 1993.

[159] P. K. Chantry. A simple formula for diffusion calculations involving wall reflection and low density. *Journal of Applied Physics*, 62:1141, 1987.

[160] Nils Lukat. Energieaufgelöste Massenspektrometrie an präkursorhaltigen Prozessplasmen. Master's thesis, University of Kiel, 2016.

[161] Erik von Wahl. Experimentelle Untersuchungen zur Plasmapolymerisation und Partikelsynthese. Master's thesis, Christian-Albrechts-Universität zu Kiel, 2014.

[162] Christian Soll. *Plasmapolymerisation von Hexamethyldisiloxan zur Abscheidung von quarzähnlichen Schichten bei gepulster Leistungszufuhr*. PhD thesis, Bergische Universität, 2000.

[163] P. Plessis and P. Marmet. Electronionization study of acetylene and fragment ions. *Int. J. Mass Spectrom. Ion Processes*, 70:23, 1986.

[164] Hoang Tung Do, G. Thieme, M. Fröhlich, Holger Kersten, and Rainer Hippler. Ion molecule and dust particle formation in Ar/CH_4, Ar/C_2H_2 and Ar/C_3H_6 radio-frequency plasmas. *Contrib. Plasma Phys.*, 45(5-6):378–384, 2005.

[165] Hoang Tung Do, Gabriele Thieme, and Rainer Hippler. Energy distribution of ion species in Ar/CH_4, Ar/C_2H_2, and Ar/C_3H_6 radio-frequency plasmas. *AIP Conference Proceedings*, 799:375, 2005.

[166] S. Hong, J. Berndt, and J. Winter. Growth precursors and dynamics of dust particle formation in the Ar/CH_4 and Ar/C_2H_2 plasmas. *Plasma Sources Sci. Technol.*, 12:46, 2003.

[167] J. Benedikt, A. Consoli, M. Schulze, and A. von Keudell. Time-resolved molecular beam mass spectrometry of the initial stage of particle formation in an Ar/He/C_2H_2 plasma. *J. Phys. Chem. A*, 111:10453–10459, 2007.

[168] J. Benedikt. Plasma-chemical reactions: low pressure acetylene plasmas. *J. Phys. D: Appl. Phys.*, 43:043001, 2010.

[169] R. K. Janev and D. Reiter. Collision processes of $C_{2,3}H_y$ and $C_{2,3}H_y^+$ hydrocarbons with electrons and protons. *Phys. Plasmas*, 11(2):780–829, 2004.

[170] J. Rutkowsky, H. Drost, and H.-J. Spangenberg. Untersuchung der unelastischen Wechselwirkung langsamer monoenergetischer Elektronen mit einfachen Kohlenwasserstoff-Molekülen I. Elektronenanlagerungs-Wirkungsquerschnitte in Abhängigkeit von der Elektronenenergie und vom Molekül. *Ann. Phys.*, 492:259–270, 1980.

[171] Ming Mao, Jan Benedikt, Angelo Consoli, and Annemie Bogaerts. New pathways for nanoparticle formation in acetylene dusty plasmas: a modelling investigation and comparison with experiments. *J. Phys. D: Appl. Phys.*, 41:225201, 2008.

[172] J. S. Knight, C. G. Freeman, M. J. McEwan, V. G. Anicich, and Jr. W. T. Huntress. A flow tube study of ion-molecule reactions of acetylene. *J. Phys. Chem.*, 91:3898–3902, 1987.

[173] Vincent G. Anicich and Murray J. McEwan. Ion-molecule chemistry in Titan's ionosphere. *Planet. Space Sci.*, 45(8):897–921, 1997.

[174] P. M. Mul and J. W. McGowan. Dissociative recombination of C_2^+, C_2H^+, $C_2H_2^+$ and $C_2H_3^+$. *Astrophys. J.*, 237:749–751, 1980.

[175] I. V. Schweigert, A. L. Alexandrov, and D. A. Ariskin. Effect of nanoparticles on discharge plasma and first steps of their formation. *Plasma Chem. Plasma Process*, 34:671–702, 2014.

[176] F. J. Gordillo-Vázquez and J. M. Albella. Distinct nonequilibrium plasma chemistry of C_2 affecting the synthesis of nanodiamond thin films from C_2H_2 (1 %)/H_2/Ar-rich plasmas. *J. Appl. Phys.*, 94(9):6085–6090, 2003.

[177] Julianne I. Moses and Stephen F. Bass. The effects of external material on the chemistry and structure of saturn's ionosphere. *J. Geophys. Res.*, 105(E3):7013–7052, 2000.

[178] P. G. Miasek and J. L. Beauchamp. A novel trapped-ion mass spectrometer for the study of ion-molecule reactions. *Int. J. Mass Spectrom. Ion Phys.*, 15:49–66, 1974.

[179] Kathleen De Bleecker, Annemie Bogaerts, and Wim Goedheer. Detailed modeling of hydrocarbon nanoparticle nucleation in acetylene discharge. *Physical Review E*, 73:026405, 2006.

[180] Cynthia Barckholtz, Theodore P. Snow, and Veronica M. Bierbaum. Reactions of C_n^- and C_nH^- with atomic and molecular hydrogen. *Astrophys. J.*, 547:L171–L174, 2001.

[181] D. A. Ariskin, Irina Schweigert, A. L. Alexandrov, Annemie Bogaerts, and F. M. Peeters. Modeling of chemical processes in the low pressure capacitive rf discharges in a mixture of Ar/C_2H_2. *J. Appl. Phys.*, 105(6):063305–063305–9, 2009.

[182] A. Akhoundi and G. Foroutan. The effects of gas dilution on the nanoparticles nucleation in a low pressure capacitively coupled acetylene discharge. *Phys. Plasmas*, 24:053516, 2017.

[183] Xiang-Mei Liu, Qi-Nan Li, and Rui Li. Simulation of nanoparticle coagulation in radio-frequency C_2H_2/Ar microdischarges. *Chin. Phys. B*, 25(6):065203, 2016.

[184] Igor Denysenko, Kostya Ostrikov, Uroš Cvelbar, Miran Mozetic, and N. A. Azarenkov. Carbon nanofiber growth in plasma-enhanced chemical vapor deposition. *J. Appl. Phys.*, 104(7):073301–073301–9, 2008.

[185] Toshihiro Fujii. Diagnostics of microwave plasmas of C_2H_2: Mass spectrometric investigations of ionic and neutral species. *Phys. Rev. E*, 58(5):6495, 1998.

[186] Johannes Berndt, Eva Kovačević, Ilja Stefanović, and L. Boufendi. Controlled dust formation in pulsed rf plasms. *J. Appl. Phys.*, 106:063309, 2009.

[187] Olivier May, Juraj Fedor, Bogdan C. Ibaňescu, and Michael Allan. Absolute cross sections for dissociative electron attachement to acetylene and diacetylene. *Phys. Rev. A*, 77:040701, 2008.

[188] A. Consoli, J. Benedikt, and A. von Keudell. The role of C_2H_4 for the acetylene chemistry in particle forming $Ar/He/C_2H_2$ plasmas studied via quantitative mass spectrometry. *Plasma Sources Sci. Technol.*, 18:034004, 2009.

[189] Ilja Stefanović, Eva Kovačević, Johannes Berndt, Yvonne Pendleton, and Jörg Winter. Hdrocarbon nanoparticles as a diffuse ISM analogue: morphology and infrared absorption in the 2000-500 cm^{-1} region. *Plasma Phys. Control. Fusion*, 47:A179–A189, 2005.

[190] Kathleen De Bleecker, Annemie Bogaerts, and Wim Goedheer. Aromatic ring generation as a dust precursor in acetylene discharges. *Appl. Phys. Lett.*, 88:151501, 2006.

[191] A. Bouchoule and L. Boufendi. Particulate formation and dusty plasma behaviour in argon-silane rf discharge. *Plasma Sources Sci. Technol.*, 2:204–213, 1993.

[192] Ch. Hollenstein, A. A. Howling, C. Courteille, D. Magni, S. M. Scholz, G. M. W. Kroesen, N. Simons, W. de Zeeuw, and W. Schwarzenbach. Silicon oxide particle formation in rf plasmas investigated by infrared absorption spectroscopy and mass spectrometry. *J. Phys. D: Appl. Phys.*, 31:74, 1998.

[193] Ch. Hollenstein. The physics and chemistry of dusty plasmas. *Plasma Phys. Control. Fusion*, 42:R93, 2000.

[194] Morten Hundt, Patrick Sadler, Igor Levchenko, Matthias Wolter, Holger Kersten, and Kostya (Ken) Ostrikov. Real-time monitoring of nucleation-growth cycle of carbon nanoparticles in acetylene plasmas. *J. Appl. Phys.*, 109:123305, 2011.

[195] U. Kortshagen and U. Bhandarkar. Modeling of particulate coagulation in low pressure plasmas. *Physical Review E*, 60(1):887, 1999.

[196] Christian Böhm and Jérôme Perrin. Spatially resolved optical emission and electrical properties of SiH_4 rf discharges at 13.56 MHz in a symmetric parallel-plate configuration. *J. Phys. D: Appl. Phys*, 24:865–881, 1991.

[197] Helge Ketelsen. Mie-Ellipsometrie an staubigen Plasmen. Master's thesis, Christian-Albrechts-Universität, Kiel, 2009.

[198] Franko Greiner, Jan Carstensen, Nils Köhler, Helge Ketelsen, Sascha Knist, and Alexander Piel. Imaging Mie ellipsometry: dynamics of nanodust clouds in an argon-acetylene plasma. *Plasma Sources Sci. Technol.*, 21(065005), 2012.

[199] David Falk, Dieter Brill, and David Stork. *Seeing the Light: Optics in Nature, Photography, Color, Vision, and Holography.* Harper and Row, 1986.

[200] Gustav Mie. 1. Beiträge zur Optik trüber Medien, speziell kolloidaler Metallösungen. *Ann. Phys.*, 25:377, 1908.

[201] Yasuaki Hayashi and Akio Sanpei. *Ellipsometry - Principles and Techniques for Materials Characterization.* InTech, 2017.

[202] Suk-Ho Hong and Jörg Winter. Size dependence of optical properties and internal structure of plasma grown carboncarbon nanoparticles studied by in situ Rayleigh-Mie scattering ellipsometry. *Journal of Applied Physics*, 100(064303), 2006.

[203] S. Barbosa, F. R. A. Onofri, L. Couëdel, M. Wozniak, C. Montet, C. Pelcé, C. Arnas, L. Boufendi, E. Kovačević, J. Berndt, and C. Grisolia. An introduction to light extinction spectrometry as a diagnostic for dust particle characterisation in dusty plasmas. *J. Plasma Phys.*, 82:615820403, 2016.

[204] Micheal Bass, Eric W. Stryland, David R. Williams, and William L. Wolfe. *Handbook of optics, devices, measurements, and properties*, volume 2. 2 edition, 1995.

[205] M. Kerker. *The scattering of light and other electromagnetic radiation.* Academic, New York, 1969.

[206] H. C. van de Hulst. *Light scattering by small particles.* John Wiley & Sons, New York, 1957.

[207] F. Kirchschlager, S. Wolf, F. Greiner, S. Groth, and A. Labdon. In-situ analysis of optically thick nanoparticle clouds. *Appl. Phys. Lett.*, 110(17):173106, 2017.

[208] J. Vlcek. A collisional-radiative model applicable to argon discharges over a wide range of conditions. I. Formulation and basic data. *J Phys D: Appl Phys*, 22:623, 1989.

[209] J. Vlcek. A collsional-radiative model applicable to argon discharges over a wide range of conditions. II. Application to low-pressure, hollow-cathode ard and low-pressure glow discharges. *J. Phys. D: Appl. Phys.*, 22:632, 1989.

[210] Annemie Bogaerts, Renaat Gijbels, and Jaroslav Vlcek. Collisional-radiative model for an argon glow discharge. *J. Appl. Phys.*, 84:121, 1998.

[211] K. Kano, M. Suzuki, and H. Akatsuka. Spectroscopic measurement of electron temperature and density in argon plasmas based on collisional-radiative model. *Plasma Sources Sci Technol*, 9:314–322, 2000.

[212] S. Iordanova and I. Koleva. Optical emission spectroscopy diagnostics of inductively-driven plasmas in argon gas at low pressures. *Spectrochimica Acta Part B*, 62:344–356, 2007.

[213] D. L. Crintea, U. Czarnetzki, S. Iordanova, I. Koleva, and D. Luggenhölscher. Plasma diagnostics by optical emission spectroscopy on argon and comparison with Thomson scattering. *J Phys D: Appl Phys*, 42:045208, 2009.

[214] T. I. Cox, V. G. I. Deshmukh, D. A. O. Hope, A. J. Hydes, N. St. J. Braithwaite, and N. M. P. Benjamin. The use of Langmuir probes and optical emission spectroscopy to measure electron energy distribution function in rf-generated argon plasmas. *J Phys D: Appl Phys*, 20:820–831, 1987.

[215] G. Crolly and H. Oechsner. Comparative determination of the electron temperature in Ar- and N_2-plasmas with electrostatic probes, optical emission spectroscopy OES and energy dispersive mass spectrometry EDMS. *Eur. Phys. J. AP*, 15:49–56, 2001.

[216] John B. Boffard, R. O. Jung, Chun C. Lin, L. E. Aneskavich, and A. E. Wendt. Argon 420.1-419.-8 nm emission line ratio for measuring plasma effective electron temperatures. *J Phys D: Appl Phys*, 45:045201, 2012.

[217] David. R. Lide. *CRC Handbook of Chemistry and Physics.* CRC Press, 90 edition, 2010.

[218] M. Mikikian, S. Labidi, E. von Wahl, J. F. Lagrange, T. Lecas, V. Massereau-Gilbaud, I. Géraud-Grenier, E. Kovačević, J. Berndt, H. Kersten, and T. Gibert. Optical diagnostics of dusty plasmas during nanoparticle growth. *Plasma Phys. Controlled Fusion*, 59:014034, 2017.

[219] Igor Odrobina and Masashi Kando. Discontinuous transitions between alpha and gamma regimes of rf capacitive discharge. *Plasma Sources Sci. Technol.*, 5:517, 1996.

[220] F. M. J. H. van de Wetering, R. J. C. Brooimans, J. Beckers, and G. M. W. Kroesen. Fast and interrupted expansion in cyclic void growth in dusty plasma. *J. Phys. D: Appl. Phys.*, 48:035204, 2015.

[221] I. Stefanović, B. Sikimić, A. Aschinger, E. Kovačević, and J. Winter. Development of voids in pulsed and CW- driven reactive plasmas with large nanoparticle density. *J. Phys. D: Appl. Phys.*, 48:385202, 2015.

[222] Benjamin Tadsen, Franko Greiner, and Alexander Piel. Probing a dusty magnetized plasma with self-excited dust-density waves. *Phys. Rev. E*, 97:033203, 2018.

[223] J. Beckers and G. M. W. Kroesen. Surprising temperature dependence of the dust particle growth rate in low pressure Ar/C_2H_2 plasmas. *Appl. Phys. Lett.*, 99:181503, 2011.

[224] Alexander Hinz, Erik von Wahl, Franz Faupel, Thomas Strunskus, and Holger Kersten. Nanoparticle forming reactive plasmas: a multidiagnostic approach. *Eur Phys J D*, 72:91, 2018.

[225] L. Boufendi and A. Bouchoule. Particle nucleation and growth in a low-pressure argon-silane discharge. *Plasma Sources Science and Technology*, 3:262, 1994.

[226] M. Cavarroc, M. Mikikian, G. Perrier, and L. Boufendi. Single-crystal silicon nanoparticles: An instability to check their synthesis. *Appl. Phys. Lett.*, 89:013107, 2006.

[227] M. Lapke, T. Mussenbrock, and R. P. Brinkmann. The multipole resonance probe: A concept for simultaneous determination of plasma density, electron temperature, and collision rate in low-pressure plasmas. *Appl. Phys. Lett.*, 93:051502, 2008.

[228] M. Friedrichs and J. Oberrath. The planar multipole resonance probe: a functional analytic approach. *EPJ Techniques and Instrumentation*, 5(7), 2018.

[229] J. E. Allen. Probe theory - the orbital motion approach. *Phys. Scr.*, 45:497, 1992.

[230] I. H. Hutchinson. *Principles of Plasma Diagnostics*. Cambridge University Press, 1987.

[231] Francis F. Chen. Saturation ion currents to Langmuir probes. *J. Appl. Phys*, 36:675–678, 1965.

[232] F. F. Chen. Numerical computations for ion probe characteristics in a collisionless plasma. *J. Nucl. Energy, Part C Plasma Phys.*, 7:47, 1965.

[233] Francis F. Chen. Langmuir probe analysis for high density plasmas. *Phys. Plasmas*, 8:3029, 2001.

[234] Francis F. Chen and Donald Arnush. The floating potential of cylindrical Langmuir probes. *Phys Plasmas*, 8(11):5051, 2001.

[235] I. B. Denysenko, E. von Wahl, S. Labidi, M. Mikikian, H. Kersten, T. Gibert, E. Kovačević, and N. A. Azarenkov. Modelling of argon-acetylene dusty plasma. *Plasma Phys. Control. Fusion*, 61:014014, 2018.

[236] N. St. J. Braithwaite and J. E. Allen. Boundaries and probes in electronegative plasmas. *J. Phys. D: Appl. Phys.*, 21, 1988.

[237] Robert Lewis Fullarton Boyd and J. B. Thompson. The operation of Langmuir probes in electronegative plasmas. *Proc. R. Soc. Lond. A*, 252:102–119, 1959.

[238] Paul Bryant, Anthony Dyson, and John E. Allen. Langmuir probe measurements of weakly collisional electronegative rf discharge plasmas. *J. Phys. D: Appl. Phys.*, 34, 2001.

[239] V. Straňák, J. Blažek, S. Wrehde, P. Adámek, Z. Hubička, M. Tichý, P. Špatenka, and R. Hippler. Study of electronegative Ar/O_2 discharge by means of Langmuir probe. *Contrib. Plasma Phys.*, 48(5-7):503–508, 2008.

[240] E. Stoffels, W. W. Stoffels, D. Vender, M. Haverlag, G. M. W. Kroesen, and F. J. De Hoog. Negative ions in low pressure discharges. *Contrib. Plasma Phys.*, 35(4-5):331–357, 1995.

[241] Marjorie Cavarroc, Maxime Mikikian, Yves Tessier, and Laïfa Boufendi. Successive generations of dust in complex plasmas: A cyclic phenomenon in the void region. *Phys. Rev. Lett.*, 100(045001), 2008.

[242] Gilles de Rosny, Earl R. Mosburg Jr., John R. Abelson, Genevieve Devaud, and Ralph C. Kerns. Edischarges a time dependent excitation process in silane radio frequency glow discharges. *J. Appl. Phys.*, 54(2272), 1983.

[243] T. Gans, V. Schulz von der Gathen, and H. F. Döbele. Prospects of phase resolved optical emission spectroscopy as a powerful diagnostic tool for rf-discharges. *Contrib. Plasma Phys.*, 44(5-6):523–528, 2004.

[244] Sebastian Nemschokmichal, Kristian Dittmann, and Jürgen Meichsner. Spatial and phase-resolved optical emission patterns in capacitively coupled radio-frequency plasmas. *IEEE Transactions on Plasma Science*, 36(4):1360–1361, 2008.

[245] K. Dittmann, K. Matyash, S. Nemschokmichal, J. Meichsner, and R. Schneider. Excitation mechanisms and sheath dynamics in capacitively coupled radio-frequency oxygen plasmas. *Contrib. Plasma Phys.*, 50(10):942–953, 2010.

[246] C. M. O. Mahony and W. G. Graham. Heating modes in capacitively coupled rf plasmas observed with emission spectroscopy. *IEEE Transactions on Plasma Science*, 27(1), 1999.

[247] C. M. O. Mahony, R. Al Wazzan, and W. G. Graham. Sheath dynamics observed in a 13.56 MHz-driven plasma. *Appl. Phys. Lett.*, 71(5):608–610, 1997.

[248] T. Gans, Chun C. Lin, V. Schulz von der Gathen, and H. F. Döbele. Phase-resolved emission spectroscopy of a hydrogen rf discharge for the determination of quenching coefficients. *Physical Review A*, 67(012707), 2003.

[249] T. Gans, Chun C. Lin, V. Schulz von der Gathen, and H.F. Döbele. Determination of quenching coefficients in a hydrogen rf discharge by time-resolved optical emission spectroscopy. *J. Phys. D: Appl. Phys*, 34:L39–L42, 2001.

[250] U. Czarnetzki, D. Luggenhölscher, and H.F. Döbele. Space and time resolved electric field measurements in helium and hydrogen rf-discharges. *Plasma Sources Sci. Technol.*, 8:230–248, 1999.

[251] J. Schulze, E. Schüngel, Z. Donkó, D. Luggenhölscher, and U. Czarnetzki. Phase resolved optical emission spectroscopy: a non-intrusive diagnostic to study electron dynamics in capacitive radio frequency discharges. *J. Phys. D: Appl. Phys.*, 43(124016), 2010.

[252] *User's manual - New iStar ICCD*, 2012.

[253] R. W. Pearse and A. G. Gaydon. *The identification of molecular spectra.* Chapman and Hall Ltd, 3 edition, 1963.

[254] http://physics.nist.gov/PhysRefData/Handbook/Tables/argontable2.htm. Nist basic atomic spectroscopic data - strong lines of argon.

[255] J. J. Thomson. Xl. cathode rays -. *Philos. Mag. Lett.*, 44(269):303–326, 1897.

[256] Jürgen H. Gross. *Mass Spectrometry.* Springer-Verlag Berlin Heidelberg, 2nd edition, 2013.

[257] J. Benedikt, A. Hecimovic, D. Ellerweg, and A. von Keudell. Quadrupole mass spectrometry of reactive plasmas. *J. Phys. D: Appl. Phys.*, 45:403001, 2012.

[258] J. Throck Watson and O. David Sparkman. *Introduction to Mass Spectrometry: Instrumentation, Applications, and Strategies for Data Interpretation.* New York: Wiley, 4th edition, 2007.

[259] Wolfgang Demtröder. *Atome, Moleküle und Festkörper*. Experimentalphysik 3. Springer, Berlin Heidelberg, 3 edition, 2005.

[260] G. Schiwietz, Martin Beye, D. Kühn, and G. Xiao. The retarding Bessel-box - an electron-spectrometer designed for pump/probe experiments. *J. Electron Spectrosc. Relat. Phenom.*, 203:51–59, 2015.

[261] Wolfgang Paul. Elektromagnetische Käfige für geladene und neutrale Teilchen. *Phys. Bl.*, 46(7):227–236, 1990.

[262] Air liquide s. a., oral information on acetylene storage. telephone call, april 2017.

[263] S. E. Stein. Nist database on mass spectrometry: Acetone, april 2017.

[264] Kathleen De Bleecker and Annemie Bogaerts. Modeling of the synthesis and subsequent growth of nanoparticles in dusty plasmas. *High Temperature Material Processes (An International Quarterly of High-Technology Plasma Processes)*, 11:21–36, 2007.

[265] K. Hiraoka and P. Kebarle. Ion molecule reactions in ethane. thermochemistry and sstructure of the intermediate complex: $C_4H_{11}^+$ and $C_4H_{10}^+$ formed in the reactions of $C_2H_5^+$ and $C_2H_4^+$ with C_2H_6. *Can. J. Chem.*, 58:2262–2270, 1980.

[266] Pierre M. Esteves, Gabriel G. P. Alberto, Alejandro Ramirez-Solis, and Claudio J. A. Mota. The n-butionium cation (n-$C_4H_{11}^+$): The potential energy surface of protonated n-butane. *J. Phys. Chem. A*, 104:6233–6240, 2000.

[267] Joseph O. Hirschfelder, Charles Francis Curtiss, and Robert Byron Bird. *Molecular Theory of Gases and Liquids*. 1954.

[268] Robert C. Reid. *The Properties of Gases and Liquids*. 1987.

[269] S. Palucha, Z. Giburski, and J. Biesiada. A molecular dynamics study of fullerene - carbon monoxide mixture. *J. Mol. Struct.*, 704:269–273, 2004.

[270] Günter Sauerbrey. Verwendung von Schwingquarzen zur Wägung dünner Schichten und zur Mikrowägung. *Zeitschrift für Physik*, 155:206–222, 1959.

Acknowledgements

This thesis would not have been possible without the help of family, friends and colleagues. I am especially grateful to my dear wife, who showed an incredible amount of patience. The times of my PhD thesis have been full of work and she accepted it without any questioning, even though I could not always give her the full attention, that she deserves. It was the contrary, she always was helpful and supporting me wherever she could.
Of course, I also owe my parents a dept of gratitude. They always believe in me more than I do. It gave me a tremendous amount of confidence to finish this project in my life. Their help is something I can always rely on without the need to ask. Similarly, being far away or close, I know that my brother and my sister are always there for me, if I am in trouble.
Holger Kersten integrated me into his workgroup early and kept me for the PhD thesis by offering the necessary financial and professional support. No matter if a physical, administration or soft skill problem, he was always a great help throughout the years of work. I thank him a thousand times for this great opportunity, which also let me travel around Europe and even the world in order to come into contact to other scientists and to broaden my horizon.
In this sense, I also thank to my other colleagues, with whom i passed some formidable years, never stopped learning on a personal and professional level. I am especially thankful to Thomas Trottenberg, who is so patient and excited at the same time, when it comes to discussing results and ideas, to Michael Poser, who is of a great help in the design of new experiments, to Volker Rohwer, who makes experiment designs become reality, to Fabian Haase and Sven Gauter, who were not only there as colleagues but also as close friends, who made life so much easier, to Viktor Schneider, my friend and colleague, who always kept everyone together. Many thanks to Nils Lukat and Christian Schulze, too, who were formidable master students at that time and from whom I learned a lot from working with them.
In further cooperation I also had the pleasure to work with scientists from other institutes and nations, who contributed to the presented experiments. With Jean-François Lagrange I had the opportunity to be introduced into advanced optical emission spectroscopy, with Alexander Hinz I measured the size distribution of the nanoparticles, with Safa Labidi I did the mass spectrometric investigations, with Yerbolat Ussenov the Langmuir probe system was developped and applied and last but not least Zahra Marvi was a great help for the acquisition of the laser light scattering experiments and further not in this thesis presented experiments. Thanks a lot to all of these nice colleagues, with whom I spent a nice time working together.
I also shall not forget to mention my new colleagues from the GREMI in Orléans, where Maxime Mikikian offered me a job without having finished my thesis yet. Without the financial and professional support from him I could neither have finished the thesis nor could I have passed to the new contract with Chantal Leborgne, who was equally supportive, always pushing me to finish the manuscript. Very fruitful discussions together with Johannes Berndt and Igor Denysenko contributed to a great deal to the interpretation of several results. Thank you very much.

List of Publications

In chronologically descending order:

1. *I. B. Denysenko,* ***E. von Wahl****, S. Labidi, M. Mikikian, H. Kersten, T. Gibert*, Plasma Process. Polym. **16** (6), 1800209 (2019), Effects of process conditions on the chemistry of an Ar/C_2H_2 dust-forming plasma
doi: 10.1002/ppap.201800209

2. *Y. A. Ussenov,* ***E. von Wahl****, Z. Marvi, T. S. Ramazanov, H. Kersten*,Vacuum **166**, 15-25 (2019), Langmuir probe measurements in nanodust containing argon-acetylene plasmas
doi: 10.1016/j.vacuum.2019.04.051

3. *I. B. Denysenko,* ***E. von Wahl****, S. Labidi, M. Mikikian, H. Kersten, T. Gibert, E. Kovačević, N. A. Azarenkov*, Plasma Phys. Control. Fusion **61**, 014014 (2019), Modelling of argon-acetylene dusty plasma
doi: 10.1088/1361-6587/aade2d

4. *A. M. Hinz,* ***E. von Wahl****, F. Faupel, T. Strunskus, H. Kersten*, EPJ D **72**, 91 (2018), Nanoparticle forming reactive plasmas: a multidiagnostic approach
doi: 10.1140/epjd/e2017-80372-6

5. *J. Röpcke, D. Loffhagen,* ***E. von Wahl****, A. S. C. Nave, J.-P. H. van Helden, N. Lang, H. Kersten*, EPJ D **72**, 87 (2018), On improved understanding of plasma-chemical processes in complex low-temperature plasmas
doi: 10.1140/epjd/e2017-80363-7

6. *M. Mikikian, S. Labidi,* ***E. von Wahl*** *J.-F. Lagrange, T. Lecas, V. Massereau-Guilbaud, I. Géraud-Grenier, E. Kovačević, J. Berndt, H. Kersten, T. Gibert*, Plasma Phys. Control. Fusion **59**, 014034 (2017), Optical diagnostics of dusty plasmas during nanoparticle growth
doi: 10.1088/0741-3335/59/1/014034

7. *A. M. Hinz,* ***E. von Wahl****, F. Faupel, T. Strunskus, H. Kersten*, Journal of Physics D: Applied Physics **48**, 055203 (2015), Versatile particle collection concept for correlation of particle growth and discharge parameters in dusty plasmas
doi: 10.1088/0022-3727/48/5/055203